

# **B-N LEWIS PAIR-FUNCTIONALIZED ANTHRACENES**

by

KANGLEI LIU

A Dissertation submitted to the

Graduate School - Newark

Rutgers, The State University of New Jersey

in partial fulfillment of requirements

for the degree of

Doctor of Philosophy

Graduate Program in Chemistry

written under the direction of

Professor Frieder Jäkle

and approved by

---

---

---

---

Newark, New Jersey

January, 2020

© 2019

Kanglei Liu

ALL RIGHTS RESERVED

## ABSTRACT OF THE THESIS

### B-N LEWIS PAIR-FUNCTIONALIZED ANTHRACENES

*By Kanglei Liu*

Dissertation Director: Professor Frieder Jäkle

The functionalization of  $\pi$ -conjugated polycyclic aromatic hydrocarbons (PAHs) with main group elements (i.e., B, Si, P) has been a topic of intense interest over the past several years. Especially conjugated organoboron compounds have attracted considerable attention owing to their unusual optical and electronic properties. Recently, tetra-coordinated organoboron compounds have attracted increasing attention for applications in organic field effect transistors (OFETs), organic light emitting diodes (OLEDs), solar cells, sensory and biological imaging materials, and as photoresponsive materials. This dissertation focuses on the investigation of the effects of the B-N Lewis pair functionalization on larger  $\pi$ -conjugated scaffolds based on anthracene. Several new types of BN-substituted anthracenes were targeted as new low band gap materials for use as optoelectronic materials, as well as for singlet oxygen uptake and release applications.

We developed a new class of B-N functionalized PAHs by electrophilic aromatic borylation of pyridylanthracenes. The formation of B-N Lewis pairs at the periphery of anthracene results in unique structural features and electronic properties. In addition, we discovered that the BN-fused anthracenes undergo self-sensitized uptake of singlet oxygen and subsequent controlled release by thermolysis. The controlled capture/release of singlet oxygen opens the possibility for applications in photodynamic therapy (PDT) and sensing.

In continuation of this work, we investigated the effects of substituents on the structural features and electronic properties. A series of BN-fused dipyridylanthracenes with Me groups in different positions of the pyridyl rings were synthesized. The results suggest that minor structural modifications on the pyridyl moiety can alter dramatically the reactivity of the BN-anthracenes, which can be exploited for applications as singlet oxygen sensitizers on one hand and materials for delivery of singlet oxygen on demand on the other hand.

To achieve a further decrease in the band gap of BN Lewis pair-functionalized PAHs, we designed the borane-modified dianthracenylpyrazine derivatives. DFT calculations indicated that BN-fused dianthracenylpyrazine compounds show a large decrease in the HOMO-LUMO gap compared to the previously described BN-fused dipyridylanthracenes. The B-N doped polycyclic species have significant absorbance at greater than 700 nm. Thus, the attachment of BN Lewis pairs to PAHs is also a promising strategy toward low band gap materials.



## Acknowledgments

I am deeply grateful to many people who have helped me to complete this thesis, both within and outside of the lab. This work would not be possible without them. First and foremost I would like to thank my supervisor and mentor, Prof. Frieder Jäkle, for his continuous support and guidance over the past six years. His door was always open for a discussion about research, careers, or anything I needed help with. His passion for research and his relentless pursuit of new discoveries inspired and motivated me when I encountered difficulties during the project. He helped me to become a better researcher. I would also like to thank my research committee members Prof. Elena Galoppini, Prof. Michal Szostak and Prof. Thomas Baumgartner (York University) for their help, advice and corrections to my thesis.

I am also grateful to many of the faculty and staff at Rutgers University, especially Prof. Roger Lalancette for his help with single-crystal X-ray crystallography, Dr. Lazaros Kakalis for his expertise in NMR spectroscopy. I am also grateful for the wonderful time with everyone in the Jäkle group. I would like to thank Dr. Xiaodong Yin who gave me patient guidance when I first came to this lab. Thanks to Dr. Jiawei Chen, Dr. Yi Ren and Dr. Fernando Vidal for their help with my research and interview. In addition, I am grateful to all the past and present group members for their friendship and encouragement throughout my time in the Jäkle lab.

Last and certainly not least, I would like to thank my family and friends for their support. Mon and dad always supported and encouraged me throughout all the good and bad times. Chao gave me a place to escape from a busy scientific life. I would also like to thank my friends Huina, Jingyao and plenty of friends in China for their encouragement and support.

**To Mom and Dad**

## Table of Contents

|  |           |
|--|-----------|
| Abstract of the Thesis   | ii        |
| Acknowledgement  | iv        |
| Table of Content   | vi        |
| List of Figures  | viii      |
| List of Schemes  | xxi       |
| List of Tables   | Xxii      |
| <b>Chapter 1 General Introduction</b>  | <b>1</b>  |
| 1.1 $\pi$ -Conjugated Systems  | 1         |
| 1.1.1 Polycyclic Aromatic Hydrocarbons (PAHs)                                  | 1         |
| 1.1.1.1 Electronic Structure   | 2         |
| 1.1.1.2 Reactivity   | 3         |
| 1.2 Boron Doping of Conjugated Materials                                       | 5         |
| 1.2.1 Conjugated Systems with Tri-coordinated Boron                            | 6         |
| 1.2.2 Replacement of BN for CC Units in Conjugated Materials                   | 7         |
| 1.2.3 Conjugated Systems with Tetra-coordinated Boron via Lewis Pair Formation | 8         |
| 1.3 Applications of BN Lewis Pair Functionalized Conjugated Materials          | 12        |
| 1.3.1 Luminescent Materials  | 13        |
| 1.3.2 Materials for Singlet Fission and Triplet Fusion Upconversion            | 27        |
| 1.3.3 Photodynamic Therapy   | 33        |
| 1.4 References   | 36        |
| <b>Chapter 2 BN Lewis Pair Functionalization of Anthracene</b>                 | <b>51</b> |
| 2.1 Introduction   | 51        |

|                  |   |     |
|------------------|---|-----|
| 2.2              | Results and Discussion  | 52  |
| 2.3              | Experimental  | 64  |
| 2.4              | Conclusions   | 75  |
| 2.5              | References  | 76  |
|                  | Appendix  | 79  |
| <b>Chapter 3</b> | <b>Steric and Electronic Effects of Pyridyl Substituents and Implications on the Self-Sensitized Reactivity with Singlet Oxygen</b> | 120 |
| 3.1              | Introduction  | 120 |
| 3.2              | Results and Discussion  | 123 |
| 3.3              | Experimental  | 142 |
| 3.4              | Conclusions   | 152 |
| 3.5              | References  | 154 |
|                  | Appendix  | 162 |
| <b>Chapter 4</b> | <b>Boron Complexes of a Pyrazine-Bridged Anthracene Dimer as Low Band Gap Materials</b>   | 197 |
| 4.1              | Introduction  | 197 |
| 4.2              | Results and Discussion  | 199 |
| 4.3              | Experimental  | 207 |
| 4.4              | Conclusions   | 213 |
| 4.5              | References  | 214 |
|                  | Appendix  | 216 |
|                  | Overall Conclusions   | 230 |

## List of Figures

|                     |   |    |
|---------------------|---|----|
| <b>Figure 1-1.</b>  | (a) Sextet rings in anthracene and phenanthrene; (b) Sextet rings in linear acenes  | 3  |
| <b>Figure 1-2.</b>  | Example of Diels-Alder adducts in “smart” materials by Sumerlin   | 4  |
| <b>Figure 1-3.</b>  | Preparation of oxygen self-carrying nanoparticles (PMT NPs) by Ling   | 5  |
| <b>Figure 1-4.</b>  | Schematic representation of common organoborane structures  | 6  |
| <b>Figure 1-5.</b>  | Isoelectronic relationship between CC and BN  | 7  |
| <b>Figure 1-6.</b>  | Examples of BN-substituted heterocycles by Stock (a), Dewar (b), Liu (c), and Pei (d)   | 8  |
| <b>Figure 1-7.</b>  | General structure of tetra-coordinated boron compounds with $\pi$ -conjugated chelate ligands                                     | 9  |
| <b>Figure 1-8.</b>  | Examples of BN compounds obtained via electrophilic borylation with BBr <sub>3</sub> by Fu (a), Tang (b), Patil (c), and Fang (d) | 11 |
| <b>Figure 1-9.</b>  | Examples of BN compounds obtained via electrophilic borylation with BCl <sub>3</sub> by Ingleson                                  | 12 |
| <b>Figure 1-10.</b> | The basic structure of OLEDs  | 14 |
| <b>Figure 1-11.</b> | Jablonski diagram showing the various emission processes utilized in OLEDs  | 15 |
| <b>Figure 1-12.</b> | Four-coordinate boron TADF emitters by Chou   | 16 |
| <b>Figure 1-13.</b> | TADF molecule using a phenylpyridine coordinated boryl group as an acceptor by Matsuo   | 18 |

|                     |   |    |
|---------------------|---|----|
| <b>Figure 1-14.</b> | Four-coordinate boron complexes by Clark  | 18 |
| <b>Figure 1-15.</b> | TADF molecules introduced by Adachi (a) and Yam (b)   | 19 |
| <b>Figure 1-16.</b> | BODIPY-based bioprobes in visible wavelengths by Li (a), Cosa (b) and Kim (c)                                   | 21 |
| <b>Figure 1-17.</b> | Asymmetric boron-cored AIE luminogen by Zhang   | 21 |
| <b>Figure 1-18.</b> | Fluorescent probes with NIR emission by Cao (a), Chan (b) and Wang (c)  | 23 |
| <b>Figure 1-19.</b> | Photochromic N,C-chelated organoboron compounds by Kawashima (a) and Wang (b)                                   | 24 |
| <b>Figure 1-20.</b> | Photochromic N,C-chelated organoboron compounds by Murata (a) and Wang (b, c)                                   | 25 |
| <b>Figure 1-21.</b> | Organoboron compounds that exhibit circularly polarized luminescence (CPL) by Ema (a), Crassous (b) and Ros (c) | 27 |
| <b>Figure 1-22.</b> | Schematic representation of the singlet fission process   | 28 |
| <b>Figure 1-23.</b> | Examples of B-N substitution compounds in organic solar cells by Liu (a) and Pammer (b)                         | 29 |
| <b>Figure 1-24.</b> | Examples of B-N substitution compounds in organic solar cells by Leo (a), Huang (b), and Wang (c)               | 30 |
| <b>Figure 1-25.</b> | Simplified scheme of triplet fusion upconversion  | 31 |
| <b>Figure 1-26.</b> | Heterocyclic Compounds As Annihilators by Castellano (a) and Congreve (b)                                       | 32 |
| <b>Figure 1-27.</b> | The process of photodynamic cancer therapy  | 33 |

|                     |  |    |
|---------------------|--|----|
| <b>Figure 1-28.</b> | Examples of BODIPY dyads as photosensitizers for PDT by O'Shea (a), Zhao (b), and Senge (c)  | 35 |
| <b>Figure 1-29.</b> | Examples of N,C-chelate organoboron compounds as photosensitizers for PDT by Pischel (a) and Jäkle (b)   | 36 |
| <b>Figure 2-1.</b>  | H,H-EXSY NMR spectrum of 9,10-bis(6-methylpyrid-2-yl)anthracene ( <b>2</b> )   | 53 |
| <b>Figure 2-2.</b>  | VT <sup>1</sup> H NMR spectra of <b>2</b>  | 53 |
| <b>Figure 2-3.</b>  | X ray crystal structure plot of <b>2</b>   | 54 |
| <b>Figure 2-4.</b>  | X-ray structure plots of a,b) <b>3-Et</b> and c) <b>4-Et</b>   | 55 |
| <b>Figure 2-5.</b>  | Proposed structural inversion of compounds <b>3-R</b> (R = Et, Ph) via a planarized trans-isomer as an intermediate  | 56 |
| <b>Figure 2-6.</b>  | a) UV-Vis absorption (left) and fluorescence (right) spectra in DCM; b) Photographs of <b>3-Ph</b> in DCM solutions under daylight (left) and under UV irradiation (middle); solid-state fluorescence under UV irradiation (right) | 57 |
| <b>Figure 2-7.</b>  | Calculated orbital energy levels and HOMO/LUMO orbital plots of <b>3-Et</b> and <b>4-Et</b> in comparison to their all-carbon analogs <b>3C-Et</b> and <b>4C-Et</b>  | 59 |
| <b>Figure 2-8.</b>  | Cyclic voltammetry (CV) data for the oxidation and reduction of BN-functionalized anthracenes  | 60 |
| <b>Figure 2-9.</b>  | Square wave voltammetry (SWV) data for the oxidation and reduction of BN-functionalized anthracenes  | 61 |

|                      |   |    |
|----------------------|---|----|
| <b>Figure 2-10.</b>  | a) Endoperoxides <b>3-R-O2</b> ; b) X-ray crystal structure of <b>3-Ph-O2</b> ;<br>c) absorption and emission color changes upon uptake and release of O <sub>2</sub>                             | 62 |
| <b>Figure 2-11.</b>  | a) Formation of EPOs from oligoacenes by type I and type II mechanisms; b) The energy for the ground singlet and triplet states of <b>3-Et</b>  | 63 |
| <b>Figure 2-12.</b>  | Illustration of spin densities in the T <sub>1</sub> state for (a) <b>3-Et</b> , (b) <b>3-Ph</b> , and (c) <b>4-Et</b>  | 64 |
| <b>Figure 2-13.</b>  | H,H-EXSY (NOESY) NMR spectrum of <b>3-Ph</b>  | 79 |
| <b>Figure 2-14a.</b> | Full H,H-EXSY (NOESY) NMR spectrum of <b>3-Et</b>   | 79 |
| <b>Figure 2-14b.</b> | Expansions of H,H-EXSY (NOESY) NMR spectrum of <b>3-Et</b>  | 81 |
| <b>Figure 2-15a.</b> | Full H,H-EXSY (NOESY) NMR spectrum of <b>4-Et</b>   | 81 |
| <b>Figure 2-15b.</b> | Expansions of the H,H-EXSY (NOESY) NMR spectrum of <b>4-Et</b>  | 82 |
| <b>Figure 2-16.</b>  | VT <sup>1</sup> H NMR spectra of <b>3-Et</b>  | 83 |
| <b>Figure 2-17.</b>  | VT <sup>1</sup> H NMR spectra of <b>3-Ph</b>  | 83 |
| <b>Figure 2-18.</b>  | VT <sup>1</sup> H NMR spectra of <b>4-Et</b>  | 84 |
| <b>Figure 2-19.</b>  | Projection of <sup>1</sup> H NMR chemical shifts for CH <sub>3</sub> groups of compound <b>3-Et</b> by extrapolation of low temperature data to 50 °C for determination of Δv at T <sub>c</sub> . | 85 |
| <b>Figure 2-20.</b>  | Projection of <sup>1</sup> H NMR chemical shifts for CH <sub>3</sub> groups of compound <b>4-Et</b> by extrapolation of low temperature data to 20 °C for determination of Δv at T <sub>c</sub> . | 85 |
| <b>Figure 2-21a.</b> | X-ray crystal structure of <b>3-Et</b>  | 86 |



|                      |   |     |
|----------------------|---|-----|
| <b>Figure 2-21b.</b> | X-ray crystal structure plot of <b>4-Et</b>   | 86  |
| <b>Figure 2-22.</b>  | Optimized structures of (a) <b>2</b> (trans), (b) <b>2M</b> , (c) <b>3-Et</b> (cis), (d) <b>3C-Et</b> (cis), (e) <b>3-Et</b> (trans), (f) <b>3-Ph</b> (cis), (g) <b>4-Et</b> , (h) <b>4C-Et</b> | 87  |
| <b>Figure 2-23a.</b> | Single-exponential fit of fluorescence decay of <b>2</b>  | 90  |
| <b>Figure 2-23b.</b> | Single-exponential fit of fluorescence decay of <b>2M</b>   | 90  |
| <b>Figure 2-23c.</b> | Single-exponential fit of fluorescence decay of <b>3-Et</b>   | 91  |
| <b>Figure 2-23d.</b> | Single-exponential fit of fluorescence decay of <b>3-Ph</b>   | 91  |
| <b>Figure 2-23e.</b> | Single-exponential fit of fluorescence decay of <b>4-Et</b>   | 92  |
| <b>Figure 2-24.</b>  | Illustration of changes in the absorption for an oxygen-saturated solution of compound <b>3-Ph</b> (right) in DCM   | 98  |
| <b>Figure 2-25.</b>  | Normalized UV-Vis absorption spectra in DCM of endoperoxides <b>3-R-O2</b> in comparison to the O <sub>2</sub> -free species <b>3-R</b>   | 98  |
| <b>Figure 2-26.</b>  | X-ray crystal structure of one of three independent molecules of <b>3-Ph-O2</b>   | 99  |
| <b>Figure 2-27.</b>  | Optimized structures of (a) <b>3-Et-O2</b> , (b) <b>3-Ph-O2</b> , (c) <b>4-Et-O2</b>  | 99  |
| <b>Figure 2-28.</b>  | <sup>1</sup> H NMR spectrum of 9,10-bis(6-methylpyrid-2-yl)anthracene ( <b>2</b> ) in CDCl <sub>3</sub>   | 101 |
| <b>Figure 2-29.</b>  | <sup>13</sup> C NMR spectrum of 9,10-bis(6-methylpyrid-2-yl)anthracene ( <b>2</b> ) in CDCl <sub>3</sub>  | 101 |
| <b>Figure 2-30.</b>  | MALDI-TOF mass spectrum of 9,10-bis(6-methylpyrid-2-yl)anthracene ( <b>2</b> )  | 102 |
| <b>Figure 2-31.</b>  | <sup>1</sup> H NMR spectrum of 9-(6-methylpyrid-2-yl)anthracene ( <b>2M</b> ) in CDCl <sub>3</sub>  | 102 |

|                      |   |     |
|----------------------|---|-----|
| <b>Figure 2-32.</b>  | $^{13}\text{C}$ NMR spectrum of 9-(6-methylpyrid-2-yl)anthracene ( <b>2M</b> ) in $\text{CDCl}_3$ | 103 |
| <b>Figure 2-33.</b>  | MALDI-TOF mass spectrum of 9-(6-methylpyrid-2-yl)anthracene ( <b>2M</b> )                         | 103 |
| <b>Figure 2-34.</b>  | $^1\text{H}$ NMR spectrum of <b>3-Ph</b> in $\text{CDCl}_3$                                       | 104 |
| <b>Figure 2-35.</b>  | $^{11}\text{B}$ NMR spectrum of <b>3-Ph</b> in $\text{CDCl}_3$                                    | 104 |
| <b>Figure 2-36.</b>  | $^{13}\text{C}$ NMR spectrum of <b>3-Ph</b> in $\text{CDCl}_3$                                    | 105 |
| <b>Figure 2-37.</b>  | gCOSY NMR spectrum of <b>3-Ph</b>   | 106 |
| <b>Figure 2-38.</b>  | HMQC NMR spectrum of <b>3-Et</b>  | 106 |
| <b>Figure 2-39.</b>  | MALDI-TOF mass spectrum of <b>3-Ph</b>  | 107 |
| <b>Figure 2-40.</b>  | $^1\text{H}$ NMR spectrum of <b>3-Et</b> in $\text{CDCl}_3$                                       | 107 |
| <b>Figure 2-41.</b>  | $^{11}\text{B}$ NMR spectrum of <b>3-Et</b> in $\text{CDCl}_3$                                    | 108 |
| <b>Figure 2-42.</b>  | $^{13}\text{C}$ NMR spectrum of <b>3-Et</b> in $\text{CDCl}_3$                                    | 108 |
| <b>Figure 2-43.</b>  | MALDI-TOF mass spectrum of <b>3-Et</b>  | 109 |
| <b>Figure 2-44.</b>  | $^1\text{H}$ NMR spectrum of <b>4-Et</b> in $\text{CDCl}_3$                                       | 109 |
| <b>Figure 2-45.</b>  | $^{11}\text{B}$ NMR spectrum of <b>4-Et</b> in $\text{CDCl}_3$                                    | 110 |
| <b>Figure 2-46.</b>  | $^{13}\text{C}$ NMR spectrum of <b>4-Et</b> in $\text{CDCl}_3$                                    | 110 |
| <b>Figure 2-47.</b>  | MALDI-TOF mass spectrum of <b>4-Et</b>  | 111 |
| <b>Figure 2-48.</b>  | $^1\text{H}$ NMR spectrum of <b>3-Ph-O2</b> in $\text{CDCl}_3$                                    | 111 |
| <b>Figure 2-49.</b>  | $^{11}\text{B}$ NMR spectrum of <b>3-Ph-O2</b> in $\text{CDCl}_3$                                 | 112 |
| <b>Figure 2-50.</b>  | $^{13}\text{C}$ NMR spectrum of <b>3-Ph-O2</b> in $\text{CDCl}_3$                                 | 113 |
| <b>Figure 2-51.</b>  | gCOSY NMR spectrum of <b>3-Ph-O2</b>  | 114 |
| <b>Figure 2-52a.</b> | Full H,H-NOESY NMR spectrum of <b>3-Ph-O2</b>   | 115 |

|                      |  |     |
|----------------------|--|-----|
| <b>Figure 2-52b.</b> | Expansions of H,H-NOESY NMR spectrum of <b>3-Ph-O2</b>   | 116 |
| <b>Figure 2-53.</b>  | MALDI-TOF mass spectrum of <b>3-Ph-O2</b>  | 117 |
| <b>Figure 2-54.</b>  | $^1\text{H}$ NMR spectrum of <b>3-Et-O2</b> in $\text{CDCl}_3$   | 117 |
| <b>Figure 2-55.</b>  | $^{11}\text{B}$ NMR spectrum of <b>3-Et-O2</b> in $\text{CDCl}_3$  | 118 |
| <b>Figure 2-56.</b>  | $^{13}\text{C}$ NMR spectrum of <b>3-Et-O2</b> in $\text{CDCl}_3$  | 118 |
| <b>Figure 2-57.</b>  | MALDI-TOF mass spectrum of <b>3-Et-O2</b>  | 119 |
| <b>Figure 3-1.</b>   | Structure, orbital energies, and LUMO plot of borylated BN-anthracene ( <b>B</b> ) in comparison to the all-carbon analog ( <b>C</b> ) and the boron-free ligand ( <b>A</b> )                                      | 122 |
| <b>Figure 3-2.</b>   | Structures of BN-anthracenes investigated by DFT methods   | 123 |
| <b>Figure 3-3.</b>   | Illustration of geometric parameters discussed for BN-anthracenes  | 126 |
| <b>Figure 3-4.</b>   | Comparison of HOMO and LUMO energies of BN-anthracenes   | 126 |
| <b>Figure 3-5.</b>   | Ball-and-stick illustrations of the X-ray structures of a) <b>BDPA-4Me</b> and b) <b>BDPA-5Me</b>  | 128 |
| <b>Figure 3-6.</b>   | VT $^1\text{H}$ NMR spectra of <b>BDPA-3Me</b> and <b>BDPA-4Me</b>   | 130 |
| <b>Figure 3-7.</b>   | a) UV-vis absorption and b) emission spectra in $\text{CH}_2\text{Cl}_2$ solution  | 132 |
| <b>Figure 3-8.</b>   | Cyclic and square wave voltammetry data  | 134 |
| <b>Figure 3-9.</b>   | Self-sensitized formation of endoperoxides and photographs under ambient light and UV-irradiation illustrating color changes for the reversible conversion of <b>BDPA-5Me</b> to its endoperoxide <b>BPO-5Me</b> . | 137 |

|                     |   |     |
|---------------------|---|-----|
| <b>Figure 3-10.</b> | a) Pseudo first-order kinetics and structures of proposed intermediates for the reaction of BN-functionalized anthracenes with oxygen upon photoirradiation with a Xe lamp in CH <sub>2</sub> Cl <sub>2</sub> solution. b) Kinetics for the thermolysis of the endoperoxides at 100 °C and structures of proposed intermediates | 139 |
| <b>Figure 3-11.</b> | Photoirradiation of 9,10-dimethylantracene (DMA) in the presence of 10 mol% <b>BDPA-5Me</b> with a Xe lamp in oxygen-saturated CH <sub>2</sub> Cl <sub>2</sub> solution followed by UV-Vis spectroscopy   | 142 |
| <b>Figure 3-12.</b> | Crystal packing of <b>BDPA-2Me</b>  | 162 |
| <b>Figure 3-13.</b> | Crystal packing of <b>BDPA-4Me</b>  | 162 |
| <b>Figure 3-14.</b> | Crystal packing of <b>BDPA-5Me</b>  | 162 |
| <b>Figure 3-15.</b> | Different views of the optimized structures of <b>BDPA-2Me</b> , <b>BDPA-3Me</b> , <b>BDPA-4Me</b> , and <b>BDPA-5Me</b>  | 164 |
| <b>Figure 3-16.</b> | Optimized structures of (a) <b>BPO-2Me</b> , (b) <b>BPO-3Me</b> , (c) <b>BPO-4Me</b> , (d) <b>BPO-5Me</b>   | 169 |
| <b>Figure 3-17.</b> | Pseudo first-order kinetics for the reaction of BN-functionalized anthracenes with oxygen upon photoirradiation to give the respective endoperoxides in DCM   | 170 |
| <b>Figure 3-18.</b> | Thermolysis of the endoperoxides at 100 °C  | 171 |
| <b>Figure 3-19.</b> | Competition of BN-functionalized anthracenes and dimethylantracene (DMA) in the reaction with oxygen upon photoirradiation by a Xe lamp at room temperature   | 173 |

|                     |  |     |
|---------------------|--|-----|
| <b>Figure 3-20.</b> | $^1\text{H}$ NMR spectrum of 9,10-bis(3-methylpyrid-2-yl)anthracene ( <b>DPA-3Me</b> ) in $\text{CDCl}_3$                  | 174 |
| <b>Figure 3-21.</b> | $^{13}\text{C}\{^1\text{H}\}$ NMR spectrum of 9,10-bis(3-methylpyrid-2-yl)anthracene ( <b>DPA-3Me</b> ) in $\text{CDCl}_3$ | 174 |
| <b>Figure 3-22.</b> | MALDI-TOF mass spectrum of 9,10-bis(3-methylpyrid-2-yl)anthracene ( <b>DPA-3Me</b> )                                       | 175 |
| <b>Figure 3-23.</b> | $^1\text{H}$ NMR spectrum of 9,10-bis(4-methylpyrid-2-yl)anthracene ( <b>DPA-4Me</b> ) in $\text{CDCl}_3$                  | 175 |
| <b>Figure 3-24.</b> | $^{13}\text{C}\{^1\text{H}\}$ NMR spectrum of 9,10-bis(4-methylpyrid-2-yl)anthracene ( <b>DPA-4Me</b> ) in $\text{CDCl}_3$ | 176 |
| <b>Figure 3-25.</b> | MALDI-TOF mass spectrum of 9,10-bis(4-methylpyrid-2-yl)anthracene ( <b>DPA-4Me</b> )                                       | 176 |
| <b>Figure 3-26.</b> | $^1\text{H}$ NMR spectrum of 9,10-bis(5-methylpyrid-2-yl)anthracene ( <b>DPA-5Me</b> ) in $\text{CDCl}_3$                  | 177 |
| <b>Figure 3-27.</b> | $^{13}\text{C}\{^1\text{H}\}$ NMR spectrum of 9,10-bis(5-methylpyrid-2-yl)anthracene ( <b>DPA-5Me</b> ) in $\text{CDCl}_3$ | 177 |
| <b>Figure 3-28.</b> | MALDI-TOF mass spectrum of 9,10-bis(5-methylpyrid-2-yl)anthracene ( <b>DPA-5Me</b> )                                       | 178 |
| <b>Figure 3-29.</b> | $^1\text{H}$ NMR spectrum of <b>BDPA-3Me</b> in $\text{CDCl}_3$  | 179 |
| <b>Figure 3-30.</b> | Aromatic region of the gCOSY NMR spectrum of <b>BDPA-3Me</b> in $\text{CDCl}_3$  | 179 |
| <b>Figure 3-31.</b> | $^{13}\text{C}\{^1\text{H}\}$ NMR spectrum of <b>BDPA-3Me</b> in $\text{CDCl}_3$   | 180 |
| <b>Figure 3-32.</b> | $^{11}\text{B}\{^1\text{H}\}$ NMR spectrum of <b>BDPA-3Me</b> in $\text{CDCl}_3$   | 180 |

|                      |  |     |
|----------------------|--|-----|
| <b>Figure 3-33.</b>  | MALDI-TOF mass spectrum of <b>BDPA-3Me</b>                                       | 181 |
| <b>Figure 3-34.</b>  | $^1\text{H}$ NMR spectrum of <b>BDPA-4Me</b> in $\text{CDCl}_3$                  | 182 |
| <b>Figure 3-35.</b>  | Aromatic region of the gCOSY NMR spectrum of <b>BDPA-4Me</b> in $\text{CDCl}_3$  | 182 |
| <b>Figure 3-36a.</b> | Expansions of the HH-NOESY NMR spectrum of <b>BDPA-4Me</b> in $\text{CDCl}_3$    | 183 |
| <b>Figure 3-36b.</b> | Expansion of the HH-NOESY NMR spectrum of <b>BDPA-4Me</b> in $\text{CDCl}_3$     | 184 |
| <b>Figure 3-37.</b>  | $^{13}\text{C}\{^1\text{H}\}$ NMR spectrum of <b>BDPA-4Me</b> in $\text{CDCl}_3$ | 184 |
| <b>Figure 3-38.</b>  | $^{11}\text{B}\{^1\text{H}\}$ NMR spectrum of <b>BDPA-4Me</b> in $\text{CDCl}_3$ | 185 |
| <b>Figure 3-39.</b>  | MALDI-TOF mass spectrum of <b>BDPA-4Me</b>                                       | 185 |
| <b>Figure 3-40.</b>  | $^1\text{H}$ NMR spectrum of <b>BDPA-5Me</b> in $\text{CDCl}_3$                  | 186 |
| <b>Figure 3-41a.</b> | Expansion of the HH-NOESY NMR spectrum of <b>BDPA-5Me</b> in $\text{CDCl}_3$     | 186 |
| <b>Figure 3-41b.</b> | Expansions of the HH-NOESY NMR spectrum of <b>BDPA-5Me</b> in $\text{CDCl}_3$    | 187 |
| <b>Figure 3-42.</b>  | $^{13}\text{C}\{^1\text{H}\}$ NMR spectrum of <b>BDPA-5Me</b> in $\text{CDCl}_3$ | 188 |
| <b>Figure 3-43.</b>  | $^{11}\text{B}\{^1\text{H}\}$ NMR spectrum of <b>BDPA-5Me</b> in $\text{CDCl}_3$ | 188 |
| <b>Figure 3-44.</b>  | MALDI-TOF mass spectrum of <b>BDPA-5Me</b> in $\text{CDCl}_3$                    | 189 |
| <b>Figure 3-45.</b>  | $^1\text{H}$ NMR spectrum of <b>BPO-3Me</b> in $\text{CDCl}_3$                   | 190 |
| <b>Figure 3-46.</b>  | $^{13}\text{C}\{^1\text{H}\}$ NMR spectrum of <b>BPO-3Me</b> in $\text{CDCl}_3$  | 190 |
| <b>Figure 3-47.</b>  | $^{11}\text{B}\{^1\text{H}\}$ NMR spectrum of <b>BPO-3Me</b> in $\text{CDCl}_3$  | 191 |
| <b>Figure 3-48.</b>  | MALDI-TOF mass spectrum of <b>BPO-3Me</b>  | 191 |

|                     |  |     |
|---------------------|--|-----|
| <b>Figure 3-49.</b> | $^1\text{H}$ NMR spectrum of <b>BPO-4Me</b> in $\text{CDCl}_3$                                       | 192 |
| <b>Figure 3-50.</b> | Aromatic region of the gCOSY NMR spectrum of <b>BPO-4Me</b> in $\text{CDCl}_3$                       | 192 |
| <b>Figure 3-51.</b> | Aromatic region of the HH-NOESY NMR spectrum of <b>BPO-4Me</b> in $\text{CDCl}_3$                    | 193 |
| <b>Figure 3-52.</b> | $^{13}\text{C}\{^1\text{H}\}$ NMR spectrum of <b>BPO-4Me</b> in $\text{CDCl}_3$                      | 193 |
| <b>Figure 3-53.</b> | $^{11}\text{B}\{^1\text{H}\}$ NMR spectrum of <b>BPO-4Me</b> in $\text{CDCl}_3$                      | 194 |
| <b>Figure 3-54.</b> | MALDI-TOF mass spectrum of <b>BPO-4Me</b>  | 194 |
| <b>Figure 3-55.</b> | $^1\text{H}$ NMR spectrum of <b>BPO-5Me</b> in $\text{CDCl}_3$                                       | 195 |
| <b>Figure 3-56.</b> | $^{13}\text{C}\{^1\text{H}\}$ NMR spectrum of <b>BPO-5Me</b> in $\text{CDCl}_3$                      | 195 |
| <b>Figure 3-57.</b> | $^{11}\text{B}\{^1\text{H}\}$ NMR spectrum of <b>BPO-5Me</b> in $\text{CDCl}_3$                      | 196 |
| <b>Figure 3-58.</b> | MALDI-TOF mass spectrum of <b>BPO-5Me</b>  | 196 |
| <b>Figure 4-1.</b>  | Examples of borylation of pyrazine-derived substrates  | 198 |
| <b>Figure 4-2.</b>  | Optimized structures of (a) <b>4-Et</b> and (b) <b>4-Pf</b>  | 201 |
| <b>Figure 4-3.</b>  | UV-vis absorption spectra of <b>3</b> , <b>4-Et</b> and <b>4-Pf</b> in DCM                           | 202 |
| <b>Figure 4-4.</b>  | UV-vis absorption spectra of (a) <b>4-Et</b> and (b) <b>4-Pf</b> in solvents of varying polarity     | 204 |
| <b>Figure 4-5.</b>  | Cyclic voltammetry (CV) data   | 205 |
| <b>Figure 4-6.</b>  | Calculated frontier orbital energy levels and HOMO/LUMO orbital plots of <b>4-Et</b> and <b>4-Pf</b> | 207 |
| <b>Figure 4-7.</b>  | VT $^{19}\text{F}$ NMR spectra of <b>4-Pf</b>  | 216 |
| <b>Figure 4-8.</b>  | Square wave voltammetry (SWV) data   | 217 |

|                     |  |     |
|---------------------|--|-----|
| <b>Figure 4-9.</b>  | <sup>1</sup> H NMR spectrum of 2-(10-(4-tert-butylphenyl)anthracen-9-yl)-<br>4,4,5,5- tetramethyl-1,3,2-dioxaborolane ( <b>2</b> ) in CDCl <sub>3</sub>  | 221 |
| <b>Figure 4-10.</b> | <sup>13</sup> C NMR spectrum of 2-(10-(4-tert-butylphenyl)anthracen-9-<br>yl)-4,4,5,5- tetramethyl-1,3,2-dioxaborolane ( <b>2</b> ) in CDCl <sub>3</sub> | 221 |
| <b>Figure 4-11.</b> | MALDI-TOF mass spectrum of 2-(10-(4-tert-<br>butylphenyl)anthracen-9-yl)-4,4,5,5-tetramethyl-1,3,2-<br>dioxaborolane ( <b>2</b> )                        | 222 |
| <b>Figure 4-12.</b> | <sup>1</sup> H NMR spectrum of 2,5-bis(10-(4-tert-butylphenyl)anthracen-<br>9-yl)pyrazine ( <b>3</b> ) in CDCl <sub>3</sub>                              | 222 |
| <b>Figure 4-13.</b> | <sup>13</sup> C NMR spectrum of 2,5-bis(10-(4-tert-butylphenyl)anthracen-<br>9-yl)- pyrazine ( <b>3</b> ) in CDCl <sub>3</sub>                           | 223 |
| <b>Figure 4-14.</b> | Aromatic region of the gCOSY NMR spectrum of 2,5-bis(10-(4-<br>tert-butylphenyl)anthracen-9-yl)pyrazine ( <b>3</b> ) in CDCl <sub>3</sub>                | 223 |
| <b>Figure 4-15.</b> | Aromatic region of the HSQC NMR spectrum of 2,5-bis(10-(4-<br>tert-butylphenyl)anthracen-9-yl)pyrazine ( <b>3</b> ) in CDCl <sub>3</sub>                 | 224 |
| <b>Figure 4-16.</b> | MALDI-TOF mass spectrum of 2,5-bis(10-(4-tert-<br>butylphenyl)anthracen-9-yl)pyrazine ( <b>3</b> )   | 224 |
| <b>Figure 4-17.</b> | <sup>1</sup> H NMR spectrum of <b>4-Et</b> in CDCl <sub>3</sub>  | 225 |
| <b>Figure 4-18.</b> | <sup>13</sup> C NMR spectrum of <b>4-Et</b> in CDCl <sub>3</sub>   | 225 |
| <b>Figure 4-19.</b> | <sup>11</sup> B NMR spectrum of <b>4-Et</b> in CDCl <sub>3</sub>   | 226 |
| <b>Figure 4-20.</b> | MALDI-TOF mass spectrum of <b>4-Et</b>   | 226 |
| <b>Figure 4-21.</b> | <sup>1</sup> H NMR spectrum of <b>4-Pf</b> in CDCl <sub>3</sub>  | 227 |
| <b>Figure 4-22.</b> | <sup>13</sup> C NMR spectrum of <b>4-Pf</b> in CDCl <sub>3</sub>   | 227 |



|                     |  |     |
|---------------------|--|-----|
| <b>Figure 4-23.</b> | $^{11}\text{B}$ NMR spectrum of <b>4-Pf</b> in $\text{CDCl}_3$ | 228 |
| <b>Figure 4-24.</b> | $^{19}\text{F}$ NMR spectrum of <b>4-Pf</b> in $\text{CDCl}_3$ | 228 |
| <b>Figure 4-25.</b> | MALDI-TOF mass spectrum of <b>4-Pf</b>                         | 229 |

## List of Schemes

|                    |   |     |
|--------------------|---|-----|
| <b>Scheme 1-1.</b> | The first direct synthesis of pyridine-borane complexes by electrophilic borylation by Murakami | 10  |
| <b>Scheme 1-2.</b> | A method for less activated systems by Ingleson   | 12  |
| <b>Scheme 2-1.</b> | Synthesis of BN-fused 9,10-dipyridylanthracenes <b>3-R</b> (R = Ph, Et) and <b>4-Et</b>         | 52  |
| <b>Scheme 3-1.</b> | Synthesis of BN-Fused 9,10-Dipyridylanthracenes   | 127 |
| <b>Scheme 4-1.</b> | Synthesis of BN-fused dianthracenylpyrazines <b>4-Et</b> and <b>4-Pf</b>                        | 199 |

## List of Table

|                    |  |     |
|--------------------|--|-----|
| <b>Table 2-1.</b>  | Comparison of calculated orbital energy levels   | 59  |
| <b>Table 2-2.</b>  | Summary of electrochemical data of BN-functionalized anthracenes and comparison with data from DFT calculations  | 61  |
| <b>Table 2-3.</b>  | Summary of the calculated singlet and triplet energies of <b>3-Et</b> , <b>3-Ph</b> and <b>4-Et</b>              | 64  |
| <b>Table 2-4.</b>  | Summary of results from VT NMR spectroscopy studies  | 85  |
| <b>Table 2-5.</b>  | Comparison of geometric parameters obtained from X-ray structure analyses and DFT calculations                   | 88  |
| <b>Table 2-6.</b>  | Summary of photophysical data of BN-functionalized anthracenes in DCM solution                                   | 89  |
| <b>Table 2-7.</b>  | HOMO and LUMO orbital plots for BN-functionalized anthracenes  | 92  |
| <b>Table 2-8.</b>  | HOMO and LUMO orbital plots for 9,10-di(pyrid-4-yl)anthracene and related acyclic borane complexes.              | 93  |
| <b>Table 2-9.</b>  | TD-DFT data for precursors <b>2</b> and <b>2M</b>  | 95  |
| <b>Table 2-10.</b> | TD-DFT data for boranes <b>3-Ph</b> , <b>3-Et</b> and <b>4-Et</b>  | 96  |
| <b>Table 2-11.</b> | Comparison of structural parameter at S <sub>0</sub> , S <sub>1</sub> , and T <sub>1</sub> state                 | 97  |
| <b>Table 2-12.</b> | Comparison of geometric parameters for endoperoxides obtained from X-ray structure analysis and DFT calculations | 100 |
| <b>Table 2-13.</b> | Orbital plots for BN-functionalized anthracene endoperoxides   | 100 |
| <b>Table 3-1.</b>  | Comparison of computed geometric parameters of BDPA and its methyl-substituted derivatives                       | 126 |

|                    |  |     |
|--------------------|--|-----|
| <b>Table 3-2.</b>  | Summary of results from VT NMR spectroscopy studies  | 131 |
| <b>Table 3-3.</b>  | Comparison of photophysical data of BN-functionalized anthracenes and their ligand precursors  | 133 |
| <b>Table 3-4.</b>  | Electrochemical data of BN-functionalized anthracenes and comparison of HOMO-LUMO gaps with results from DFT calculations and UV-vis absorption spectroscopy | 136 |
| <b>Table 3-5.</b>  | Relative computed energies for isomeric BN-anthracenes and their endoperoxides   | 141 |
| <b>Table 3-6.</b>  | Comparison of computed total energies for cis- and trans-isomers.  | 163 |
| <b>Table 3-7.</b>  | Comparison of geometric parameters obtained from X-ray crystal structure analyses and DFT calculations   | 163 |
| <b>Table 3-8.</b>  | Electrochemical data of BN-functionalized anthracenes.   | 165 |
| <b>Table 3-9.</b>  | Comparison of calculated orbital energy levels for differently substituted B-N Lewis-pairs (cis-isomers)   | 165 |
| <b>Table 3-10.</b> | Kohn-Sham HOMO and LUMO orbital plots for differently substituted BN-functionalized anthracenes  | 165 |
| <b>Table 3-11.</b> | TD-DFT data for <b>BDPA-2Me</b> , <b>BDPA-3Me</b> , <b>BDPA-4Me</b> and <b>BDPA-5Me</b>  | 166 |
| <b>Table 3-12.</b> | Comparison of the calculated singlet state and triplet state energies for <b>BDPA-2Me</b> , <b>BDPA-3Me</b> , <b>BDPA-4Me</b> , and <b>BDPA-5Me</b>          | 167 |

|                    |  |     |
|--------------------|--|-----|
| <b>Table 3-13.</b> | Comparison of total energies for <b>BDPA-2Me</b> , <b>BDPA-3Me</b> , <b>BDPA-4Me</b> , <b>BDPA-5Me</b> and their endoperoxides   | 167 |
| <b>Table 3-14.</b> | Comparison of calculated geometric parameters for Singlet Ground State ( $S_0$ ), First Singlet Excited State ( $S_1$ ), and First Triplet Excited State ( $T_1$ ) for B-N anthracenes <b>BDPA-2Me</b> , <b>BDPA-3Me</b> , <b>BDPA-4Me</b> and <b>BDPA-5Me</b> | 168 |
| <b>Table 3-15.</b> | Comparison of calculated geometric parameters for endoperoxides obtained from DFT calculations   | 169 |
| <b>Table 4-1.</b>  | Summary of photophysical data in DCM solution  | 203 |
| <b>Table 4-2.</b>  | Electrochemical data of BN-fused dianthracenylpyrazine and comparison of HOMO-LUMO gaps with results from DFT calculations and UV-Vis absorption spectroscopy  | 205 |
| <b>Table 4-3.</b>  | Comparison of calculated orbital energy levels for differently substituted B-N Lewis-pairs   | 207 |
| <b>Table 4-4.</b>  | Summary of results from VT NMR spectroscopy studies  | 216 |
| <b>Table 4-5.</b>  | Comparison of UV-Vis spectra of boron complexes <b>4-Et</b> and <b>4-Pf</b> in different solvents  | 217 |
| <b>Table 4-6.</b>  | Electrochemical data of BN-fused dianthracenylpyrazines  | 217 |
| <b>Table 4-7.</b>  | Kohn-Sham HOMO and LUMO orbital plots for precursor <b>3</b>   | 218 |
| <b>Table 4-8.</b>  | Kohn-Sham HOMO and LUMO orbital plots for differently substituted BN-functionalized anthracenes  | 218 |

|                    |   |     |
|--------------------|---|-----|
| <b>Table 4-9.</b>  | Comparison of calculated geometric parameters for BN-fused<br>dianthracenylpyrazines <b>4-Et</b> and <b>4-Pf</b> and carbon analogs <b>4-<br/>Et-C</b> and <b>4-Pf-C</b> obtained from DFT calculations | 219 |
| <b>Table 4-10.</b> | TD-DFT data for precursors <b>3</b>   | 219 |
| <b>Table 4-11.</b> | TD-DFT data for <b>4-Et</b> and <b>4-Pf</b>   | 219 |
| <b>Table 4-12.</b> | Comparison of the calculated singlet and triplet state energies<br>for <b>4-Et</b> and <b>4-Pf</b>  | 220 |

## Chapter 1 General Introduction

### 1.1 $\pi$ -Conjugated Systems

A  $\pi$ -conjugated system consists of connected p-orbitals (in transition metals d-orbitals can be involved) with delocalized electrons, typically with alternating single and multiple bonds. A representative  $\pi$ -conjugated system can be divided into four constituting components: the conjugated core (backbone), heteroatoms, substituents (electron donating or withdrawing), and side chains (i.e., solubilizing groups). Such a structure can be a single molecule, a part of a conjugated oligomer or a repeat unit in a conjugated polymer.<sup>1</sup>  $\pi$ -conjugated systems are an important class of materials with a wide range of applications in organic field effect transistors (OFETs), organic light emitting diodes (OLEDs), solar cells and chemical sensors.<sup>1-6</sup> Compared to inorganic materials, conjugated materials have many advantages such as low-cost, high flexibility and good solubility.

#### 1.1.1 Polycyclic Aromatic Hydrocarbons (PAHs)

Among the wide array of different  $\pi$ -conjugated materials, polycyclic aromatic hydrocarbons define a class of unique compounds that consist of fused conjugated aromatic rings that do not contain heteroatoms or carry substituents.<sup>7</sup> PAHs have attracted enormous research interest for various organic electronic devices due to their unique electronic and optoelectronic properties. For instance, anthracene and pyrene derivatives are widely used as luminescent compounds, while the higher homologs are promising candidates in organic devices.<sup>8</sup> Additionally, graphene molecules with columnar superstructures exhibit the

highest local charge-carrier mobilities for discotics which are desirable for device processing.<sup>9</sup>

#### 1.1.1.1 Electronic Structure

Typically, PAHs exhibit two types of electronic states, i.e., closed-shell and open-shell states. The ground state of most  $\pi$ -conjugated molecules is a closed-shell singlet. Longer acenes consisting of linearly fused benzene rings can be characterized by an unusual open-shell electron configuration with the existence of one or more unpaired electrons, also known as radicals.<sup>5</sup> Early research on PAHs was mainly developed by Eric Clar and coworkers, who created the Sextet Theory, also called Clar's rule, to understand the behavior of PAHs.<sup>10</sup> According to Clar's rule, the stability and reactivity of PAHs can be assessed in a simplified manner by calculating the number of sextet rings. The most stable form is that with the most sextets. For example, anthracene and phenanthrene have the same molecular composition ( $C_{14}H_{10}$ ). However, phenanthrene is more stable than the isomeric linear acene, anthracene, based on the assignment of two sextet rings to phenanthrene and only one sextet ring to anthracene (Figure 1-1a). For linear acene molecules (Figure 1-1b), only one sextet ring exists and consequently, the longer the acene, the less stable the system. It is challenging to synthesize larger PAHs due to their poor solubility and low stability. To resolve these two problems, the prevailing strategy is to introduce different substituents, such as electron-withdrawing moieties to decrease the HOMO energy level and bulky groups at the periphery of the acene backbone for kinetic blocking of reactive sites.<sup>6</sup>



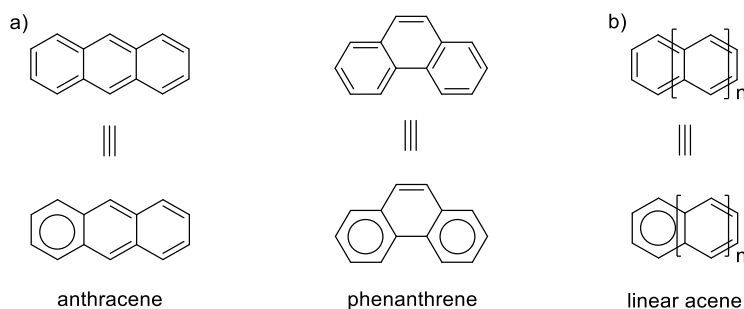


**Figure 1-1.** (a) Sextet rings in anthracene and phenanthrene; (b) Sextet rings in linear acenes

#### 1.1.1.2 Reactivity

As discussed above, with an increasing number of rings acenes becomes more reactive, especially at the central ring. The central rings in acenes are susceptible to oxidation, photodegeneration, and Diels-Alder reaction. On the one hand, acenes can be stabilized by the addition of different substituents for organic electronics device applications. On the other hand, acenes also benefit from the Diels-Alder reaction and cycloaddition with singlet oxygen to the central ring, which makes them suitable as “smart” materials with mechano-responsive properties and as singlet oxygen sensitizers and carriers for biomedical applications.<sup>11-16</sup> For example, Sumerlin and coworkers reported clean and efficient transformations of amphiphilic block copolymers and segmented hyperbranched polymers to hydrophobic block copolymers, comb copolymers or star polymers via Diels-Alder reaction (Figure 1-2).<sup>13</sup> The original furan-maleimide (Fur-Mal) Diels-Alder linkage (an amphiphilic block copolymer) was cleaved to release maleimide end groups that react with the different anthracene-based templates to form the more thermally stable anthracene-maleimide cycloadduct (hydrophobic block copolymer, comb copolymer or star polymer) through the application of a proper stimulus. These architectural transformations lead to a new generation of “smart” materials.

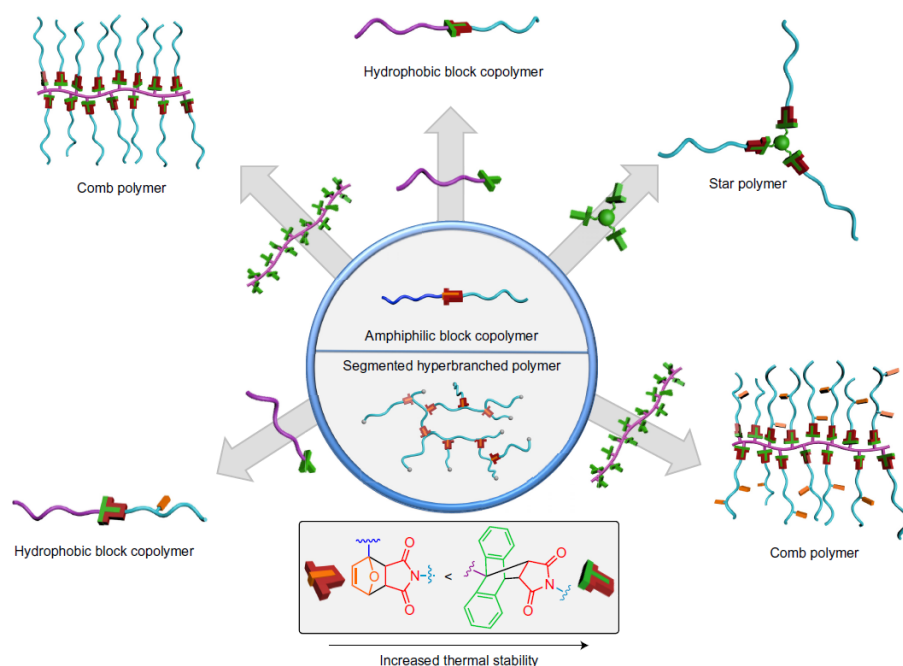


**Figure 1-2.** Example of Diels-Alder adducts in “smart” materials by Sumerlin.<sup>13</sup>  
 [Reproduced with permission from reference 13. Copyright © 2017, Springer Nature]

In another example, Ling’s group developed biocompatible nanoparticles (**PMT NPs**, Figure 1-3) containing diphenyl anthracene endoperoxides for near-infrared light-triggered controlled delivery of singlet oxygen for cancer treatment.<sup>14</sup> Under irradiation with an 808 nm laser the nanoparticles can release singlet oxygen to kill tumor cells both in vitro and in vivo in an oxygen deficient environment. The application of PAHs in photodynamic therapy is discussed in more detail in Section 1.3.3. The ability to reversibly form endoperoxides is not only important for biomedical applications, but has also been exploited in materials science, for instance, in photolithography<sup>17</sup>, fluorescent anti-counterfeiting<sup>18</sup>, and the development of molecular switches<sup>19-20</sup>.

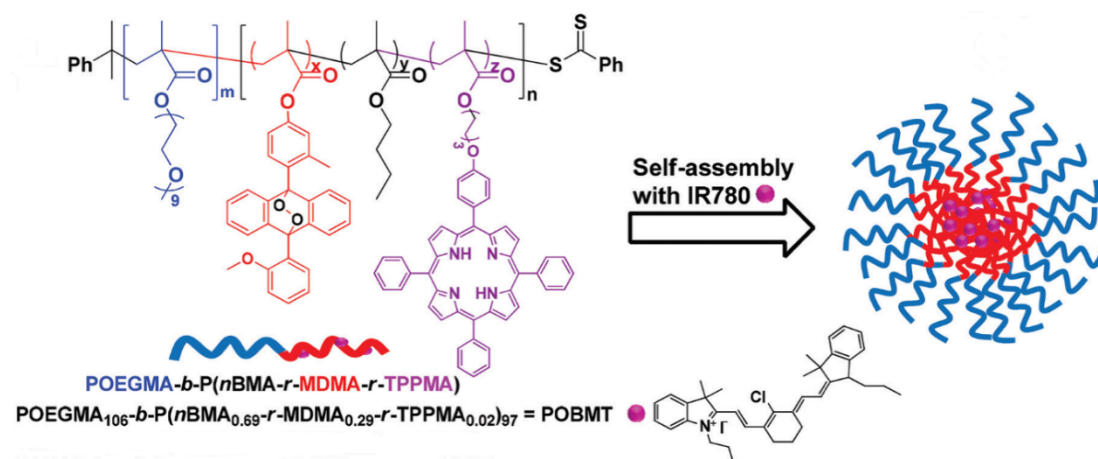


**Figure 1-3.** Preparation of oxygen self-carrying nanoparticles (**PMT NPs**) by Ling.<sup>14</sup>  
[Adapted with Ref. 14 with permission from The Royal Society of Chemistry.]

## 1.2 Boron doping of conjugated materials

The incorporation of main-group elements (i.e., B, Si, P, Se) into  $\pi$ -conjugated organic systems is an efficient strategy to create novel materials with remarkable optoelectronic properties e.g., by fine tuning frontier orbital energies. Recently, the embedding of boron atoms into fused structures has attracted increasing attention due to the intriguing properties that can be achieved, such as, low-lying LUMO orbitals, red shifted absorptions and emissions, and enhanced charge carrier mobility.<sup>21-22</sup> Boron, the third element in the second period, is an electron deficient atom with 3 valence electrons, and in tri-coordinated boranes the empty p orbital can interact with lone pair electrons and  $\pi$ -electrons of neighboring atoms or building blocks. Boron compounds can undergo Lewis acid-base interactions resulting in a coordination number change from three to four. Various tri- and tetra-coordinated organoboranes have been studied for applications in catalysis, organic electronic devices, sensory and biological imaging materials, and as photoresponsive materials.<sup>23-35</sup>

### 1.2.1 Conjugated systems with tri-coordinated boron

Tri-coordinated organoboron compounds, with the vacant  $p_z$  orbital on boron, are inherently electron deficient and serve as powerful  $\pi$ -electron acceptors when connected to a  $\pi$ -conjugated system. Figure 1-4 shows the general structure of tricoordinate organoboranes and illustrates how they interact through  $\pi$ -overlap with a  $\pi$ -conjugated substituent or form Lewis acid-Lewis base complexes.<sup>36</sup> The overlap between the empty  $p$  orbital on boron and substituents with extended  $\pi$  systems leads to interesting luminescent and nonlinear optical properties.<sup>23</sup> In addition, triarylboron compounds can act as Lewis acids to selectively react with nucleophiles and are thus very effective in the selective sensing of anions.<sup>37</sup> Moreover, Lewis acid-Lewis base interactions allow organoboron compounds to act as efficient catalysts and cocatalysts in organic synthesis.<sup>38</sup>

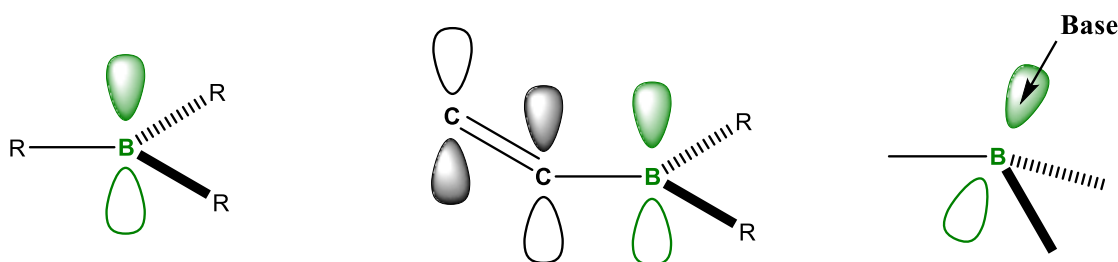


**Figure 1-4.** Schematic representation of common organoborane structures.

However, tri-coordinate organoboranes often lack chemical stability due to the high Lewis acidity of boron. An effective method to provide stability is to utilize bulky aromatic substituents, which significantly reduce the reactivity at boron by blocking the approach of nucleophiles. The common groups used for this purpose are 2,4,6-trimethylphenyl (Mes), 2,4,6-triisopropylphenyl (Tip) and 2,4,6-tritertbutylphenyl (Mes\*).<sup>24</sup> Enhanced stability is also typically seen for the Lewis acid-base complexes, especially in cases where the Lewis base is tethered to one of the substituents, resulting in chelate complexes.

### 1.2.2 Replacement of BN for CC units in conjugated materials

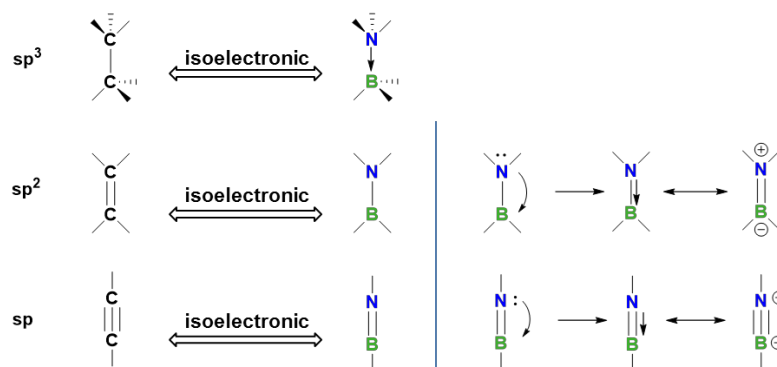


**Figure 1-5.** Isoelectronic relationship between CC and BN.<sup>39</sup> [Adapted with permission from reference 39. Copyright © 2012 WILEY - VCH Verlag GmbH & Co. KGaA, Weinheim]

An emerging strategy for incorporating boron into organic structures is the replacement of a CC unit with an isoelectronic BN unit. Figure 1-5 shows the three possible variants to replace a CC unit with a BN unit. The  $sp^2$ -type BN/CC isosterism has attracted the most attention among the three forms of replacing a CC unit with BN unit due to the broad utility of arene-containing compounds. Substitution of a CC unit with its isoelectronic BN unit in aromatics creates a new type of heteroarene that remains structurally similar to the all-carbon analogue. However, the dipolar nature of the BN bond can significantly alter both the molecular and the electronic properties of the system.<sup>39-40</sup> Indeed, compounds containing BN bonds in aromatic systems have been exploited for almost a century. In 1926, Alfred Stock successfully synthesized the first example of a BN/CC isoster of an arene-borazine ( $c\text{-B}_3\text{N}_3\text{H}_6$ ), the inorganic counterpart to benzene (Figure 1-6a).<sup>41</sup> In 1958, Dewar and co-workers reported the synthesis of the first BN-substituted aromatic compounds, 9,10-azaboraphenanthrenes (Figure 1-6b).<sup>42</sup> After decades of hibernation, the study of BN-substituted heterocycles has attracted great attention again in recent years owing to their

novel electronic properties and applications. Several BN-embedded acenes have been synthesized. For example, Liu and coworkers reported the synthesis of BN anthracenes<sup>43</sup> and a BN tetracene derivative<sup>44</sup> and demonstrated that BN/CC isosterism can lower HOMO energy levels of acene-type structures (Figure 1-6c). Pei and coworkers synthesized the first BN-embedded pentacene derivative with remarkable ambient stability (Figure 1-6d).<sup>45</sup> Recently, BN-doped graphene-like structures<sup>46-48</sup> and conjugated polymers<sup>49-52</sup> have been introduced.

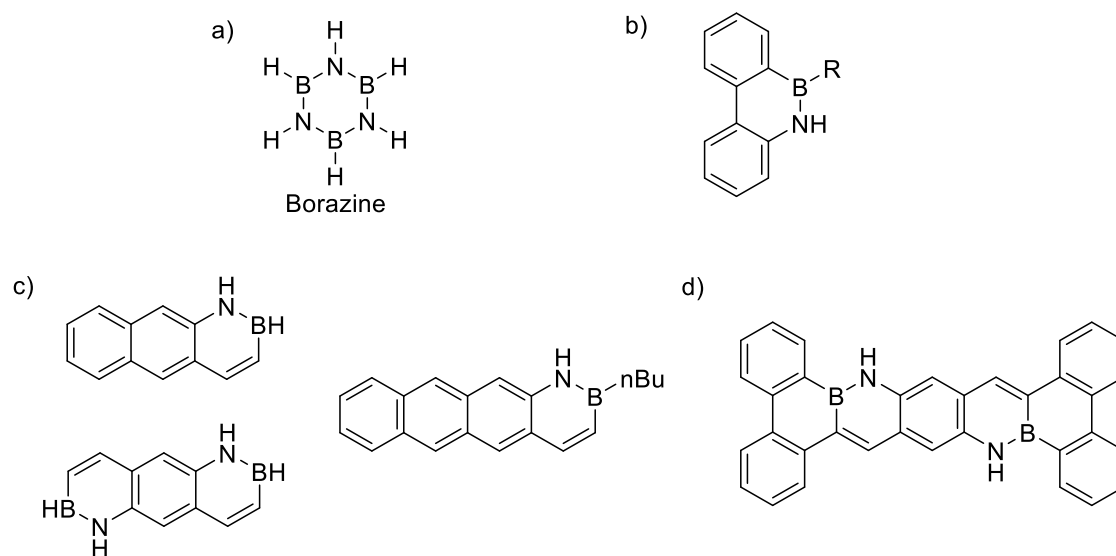


**Figure 1-6.** Examples of BN-substituted heterocycles by Stock<sup>41</sup> (a), Dewar<sup>42</sup> (b), Liu<sup>43-44</sup> (c), and Pei (d)<sup>45</sup>

### 1.2.3 Conjugated systems with tetra-coordinated boron via Lewis pair formation

Tetra-coordinated organoboron compounds with rigid  $\pi$ -conjugated structures have emerged recently as very attractive materials for various applications including emitters, organic light-emitting diodes (OLEDs), organic field-effect transistors, sensory and biological imaging materials, and photoresponsive materials.<sup>27, 32-33, 53-55</sup> In the construction of these tetra-coordinated boron compounds, chelate ligands with  $\pi$ -electrons are

coordinated to boron moieties which have vacant p-orbitals (Figure 1-7). The key role of the boron atom is to stabilize the ligand by coordination and to allow intramolecular electron delocalization, thereby enhancing the  $\pi$  conjugation. Such ring-fused structures also affect the electronic state by lowering the lowest unoccupied molecular orbital (LUMO) level to enhance the electron affinity, which enables use of the tetra-coordinated boron compounds as effective electron-transport materials. The type of the ligands and the nature of the R groups can have a great influence on the photophysical and electronic properties of the compounds due to the  $\pi$ - $\pi^*$  electronic transitions of the chelate or charge-transfer transition from the R group to the chelate. Recent research has also shown that tetra-coordinated boron compounds with an N, C-chelate backbone are capable of undergoing facile reversible photothermal isomerization, which opens exciting new opportunities to use this class of compounds as photo-responsive materials.<sup>26, 33, 56</sup> An emerging strategy that builds on this concept is to modulate the electronic structure of conjugated organic materials by B $\leftarrow$ N Lewis pair functionalization at their periphery. Several BN Lewis pair functionalized compounds exhibiting circularly polarized luminescence (CPL) have been synthesized.<sup>57-58</sup>

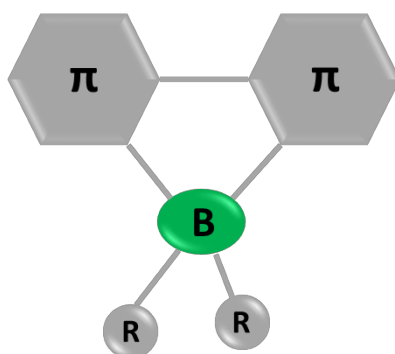
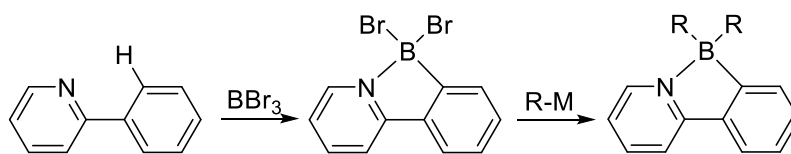


**Figure 1-7.** General structure of tetra-coordinated boron compounds with  $\pi$ -conjugated chelate ligands.

Methods for the synthesis of this type of  $\pi$ -conjugated materials having boron-nitrogen

coordination include lithiation-borylation reactions, metal-catalyzed borylation reactions and metal-free electrophilic borylations.<sup>59-61</sup> While all three methods have been widely utilized, we will focus here only on metal-free electrophilic borylation reactions. The synthesis of pyridine-borane complexes through metal-free electrophilic borylation has first been studied by Murakami and co-workers.<sup>60</sup> They investigated the electrophilic borylation of 2-arylpyridines with  $\text{BBr}_3$  (3 eq.) as the borylating agent and  $\text{Et}_2\text{NiPr}$  (1 eq.) as the base. The intermediate  $\text{BBr}_2$  complexes were stable enough to be handled in air, which made them easy to handle for further transformations by treatment with organoaluminum or organozinc reagents or reduction with  $\text{LiAlH}_4$  (Scheme 1-1). In 2012, Fu and co-workers used these reaction conditions for the functionalization of phenoxy pyridines (**1**, Figure 1-8a).<sup>62</sup> More recently, this methodology has been utilized for the preparation of new optical or electronic materials. For example, Tang and coworkers designed novel boron compounds containing the tetraphenylethene (TPE) moiety that can function as efficient solid-state emitters (**2** and **3**, Figure 1-8b).<sup>63</sup> Patil's group reported a series of highly emissive molecular solids prepared via aromatic borylation of quinolones (**4**, Figure 1-8c).<sup>64</sup> Fang et al. developed low band gap coplanar organic materials featuring intramolecular Lewis acid-base coordination (**5** and **6**, Figure 1-8d).<sup>65</sup>



**Scheme 1-1.** The first direct synthesis of pyridine-borane complexes by electrophilic borylation by Murakami<sup>60</sup> [Adapted with permission from reference 60. Copyright © 2010, American Chemical Society]



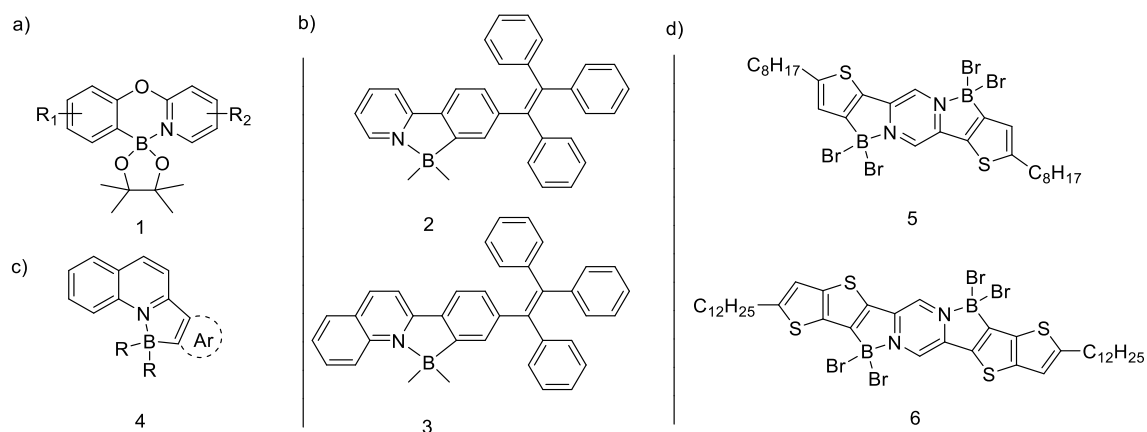
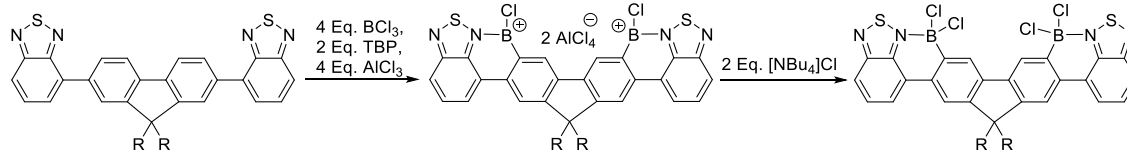


**Figure 1-8.** Examples of BN compounds obtained via electrophilic borylation with  $\text{BBr}_3$  by Fu<sup>62</sup> (a), Tang<sup>63</sup> (b), Patil<sup>64</sup> (c), and Fang<sup>65</sup> (d)

In 2015, Ingleson developed a simple strategy for less activated systems.<sup>66</sup> They pursued donor-acceptor materials containing benzo-thiadiazoles (BT), which are less nucleophilic relative to pyridyls. They described a facile synthetic method for the double borylation using excess  $\text{BCl}_3$  (4 eq.), a sterically hindered base (TBP, 2,4,6-tritbutyl-pyridine, 2 eq.) and  $\text{AlCl}_3$  (4 eq.).  $\text{AlCl}_3$  is essential to ensure clean conversion to a single product,  $[\text{5-(BCl}_2)_2]^{2+}$ , which is readily transformed to  $5\text{-(BCl}_2)_2$  by addition of  $[\text{NBu}_4]\text{Cl}$  (Scheme 1-2). Further functionalization of the  $\text{BCl}_2$  compounds gave stable fluorescent compounds with excellent solid-state quantum yields. The same group extended this approach to prepare (C-N-chelate) $\text{B(aryl)}$  species via catalytic (in  $\text{AlCl}_3$ ) borenium cation mediated arylation (7, Figure 1-9).<sup>67</sup> More recently, they utilized this methodology to form highly emissive far red/near-IR fluorophores based on borylated donor-acceptor materials that contain electron-rich aromatic units (fluorene-benzothiadiazole)<sup>68</sup> (8, Figure 1-9) and highly twisted borylated donor-acceptor compounds displaying donor-dependent delayed emission<sup>69</sup> (9, Figure 1-9).



**Scheme 1-2.** A method for less activated systems by Ingleson<sup>66</sup> [Adapted from Ref. 66 with permission from The Royal Society of Chemistry.]

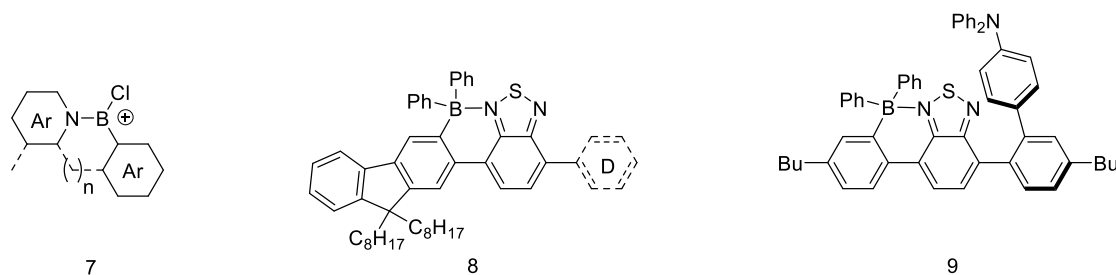


**Figure 1-9.** Examples of BN compounds obtained via electrophilic borylation with  $\text{BCl}_3$  by Ingleson<sup>67-69</sup>

### 1.3 Applications of BN Lewis pair functionalized conjugated materials

The use of electron-deficient boron atoms to form intramolecular B-N coordination compounds can enhance extension of  $\pi$ -conjugation and lower the LUMO level while reversibly forming the the Lewis pair. BN Lewis-pair functionalized conjugated materials generated based on this concept can be utilized as new luminescent materials for organic light emitting devices (OLEDs) and imaging applications, electron transporting and acceptor materials for organic photovoltaics (OPVs) and organic field-effect transistors (OFETs).<sup>27, 32, 70-71</sup> These BN compounds have also been widely used as NIR-emissive, molecular switching, photochromic and sensory materials.<sup>28, 33</sup> In addition, certain BN compounds can serve as singlet-oxygen carrier or sensitizer for applications in photodynamic therapy.<sup>72</sup>

### 1.3.1 Luminescent materials

One of the most important current issues in material science is the development of highly efficient luminescent materials for applications in organic light-emitting diodes (OLEDs), imaging materials, sensors and photoresponsive materials. Owing to their unique electron-deficient nature and tunable photophysical features, a variety of boron-containing luminescent compounds have been studied in the past few decades.

Organic light-emitting devices (OLEDs) have attracted interest due to their application in next-generation high quality flat-panel displays and lighting. The basic structure of OLEDs shown in Figure 1-10 consists of a stack of thin organic layers including the electron-transport layer (ETL), the emitting layer (EML), and the hole-transport layer (HTL)) sandwiched between the anode and cathode. To promote the development of OLEDs, more and more electroluminescent materials have been designed. Among them, B-N coordination complexes have attracted increasing attention because of their high fluorescence efficiency, high carrier mobility and good chemical and thermal stability. So far, blue, green and red EL emitters for full-color displays and lighting have all been realized based on four-coordinate boron compounds.<sup>27, 73-76</sup> Unfortunately, their electroluminescence performances are usually poor, unable to meet the requirements of commercial application.

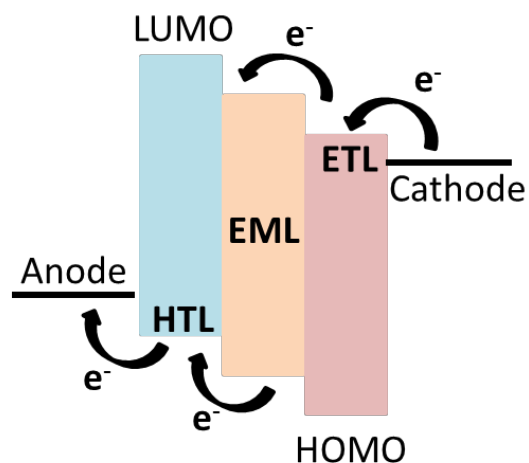


**Figure 1-10.** The basic structure of OLEDs<sup>34</sup> [Adapted with permission from reference 34. Copyright © 2019 Elsevier Inc.]

The key factor determining the efficiency of OLEDs is the ability to utilize triplets for light emission, which constitute 75% of the generated excitons. One approach is the development of phosphorescent emitters, which mainly rely on heavy-metal complexes to enhance the radiative transition from triplets. Another strategy relies on converting the long-lived triplets into emissive singlets through a process called thermally activated delayed fluorescence (TADF). TADF molecules are capable of achieving 100% internal quantum efficiency (IQE) via reverse intersystem crossing (RISC) from the first triplet excited state ( $T_1$ ) to the first singlet excited state ( $S_1$ ) even in the absence of heavy elements. In the design of efficient TADF emitters, a small energy gap ( $\Delta E_{ST}$ ) between the first excited singlet ( $S_1$ ) and triplet state ( $T_1$ ) is required to increase the RISC rate. Generally, a small  $\Delta E_{ST}$  can be achieved by spatially separating the frontier molecular orbitals (FMOs) as in aromatic compounds that show a twist between donor (D = donor) and acceptor (A = acceptor) units. In 2012, Adachi and coworkers reported the first efficient OLEDs TADF with purely organic small molecules as dopants.<sup>77</sup> Since then, great efforts have been

devoted to designing efficient TADF molecules for OLEDs. To date, many four-coordinate boron compounds with emission colors ranging from the blue to the near-infrared (NIR) region have been reported as TADF emitters for OLED applications.<sup>78-84</sup>

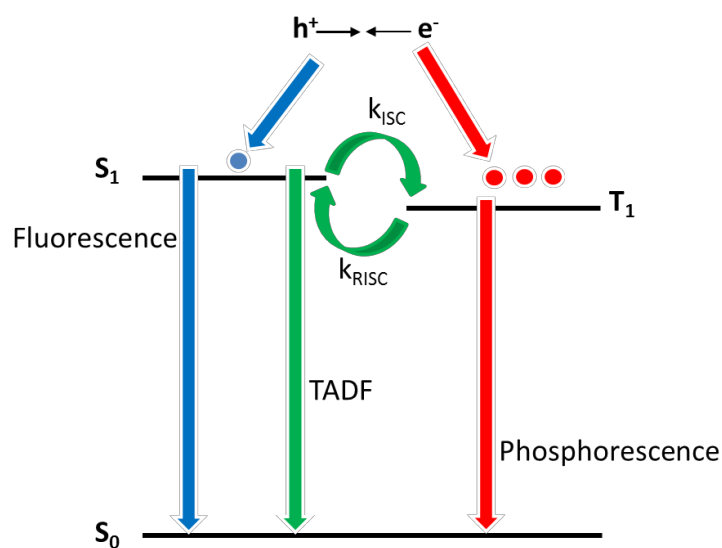


**Figure 1-11.** Jablonski diagram showing the various emission processes utilized in OLEDs<sup>34</sup> [Adapted with permission from reference 34. Copyright © 2019 Elsevier Inc.]

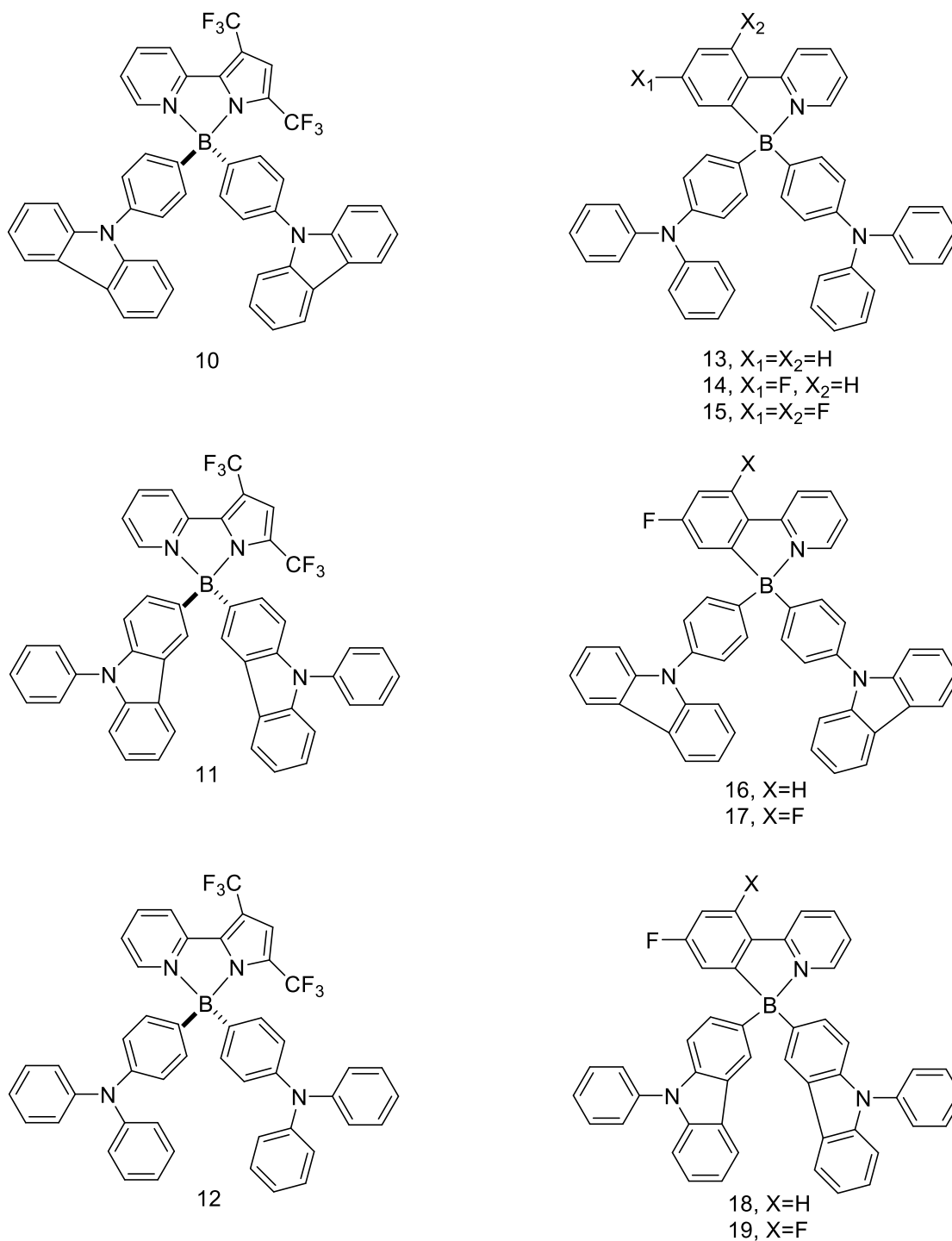


**Figure 1-12.** Four-coordinate boron TADF emitters by Chou<sup>78-79</sup>

The first examples of four-coordinate boron TADF emitters were reported by Chou and coworkers in 2016.<sup>78</sup> They developed a series of novel TADF molecules (**10-12**, Figure1-

12), in which the boron atom acts as a hub to anchor both the donor (phenylcarbazolyl or triphenylamine fragments) and acceptor (pyridyl pyrrolide) groups without affecting their electronic properties. Among all studied OLEDs, the device prepared using **12** gave the highest external quantum efficiency (EQE) of 13.5%. Later, the same group investigated a series of functional phenylpyridinato boron complexes in organic EL devices, including **14** and **15**, in which phenylpyridine as the electron acceptor (A) is linked to triphenylamine as the electron donor (D) via a core boron atom (**13-19**, Figure 1-12).<sup>79</sup> OLEDs based on **15** exhibited the highest performance with a nearly 27% EQE. Matsuo and Yasuda used a different strategy for the design of TADF molecules with the same phenylpyridine-borane building block.<sup>80</sup> In the above examples, the boron center served as the spiro center for separating the HOMOs and LUMOs. They reported a D-A TADF molecule using a phenylpyridine (PPy) scaffold bearing a coordinated boryl group as an acceptor (Figure 1-13). Intramolecular B-N coordination decreases the lowest singlet excited state energy, while the lowest triplet excited state energy remains unchanged. In addition, B-N coordination polarizes the orbital distribution, leading to minimal spatial overlap between the HOMO and the LUMO and a reduction in  $\Delta E_{ST}$  without changing the D-A conformation. An OLED device, based on compound **20**, emitted green light displaying high performance with EQE of 22.7%. Clark's group synthesized a series of four-coordinate boron complexes **22-29** as new color-tunable TADF-emitting materials for EL applications (Figure 1-14).<sup>81</sup> They emitted a wide range of color in organic EL devices, the colors of which were tuned by using a modular selection of donor and acceptor groups. Furthermore, device **26** had low efficiency roll-off (73% efficient at 18,000 cd/m<sup>2</sup>), which is promising for future OLED emitters.

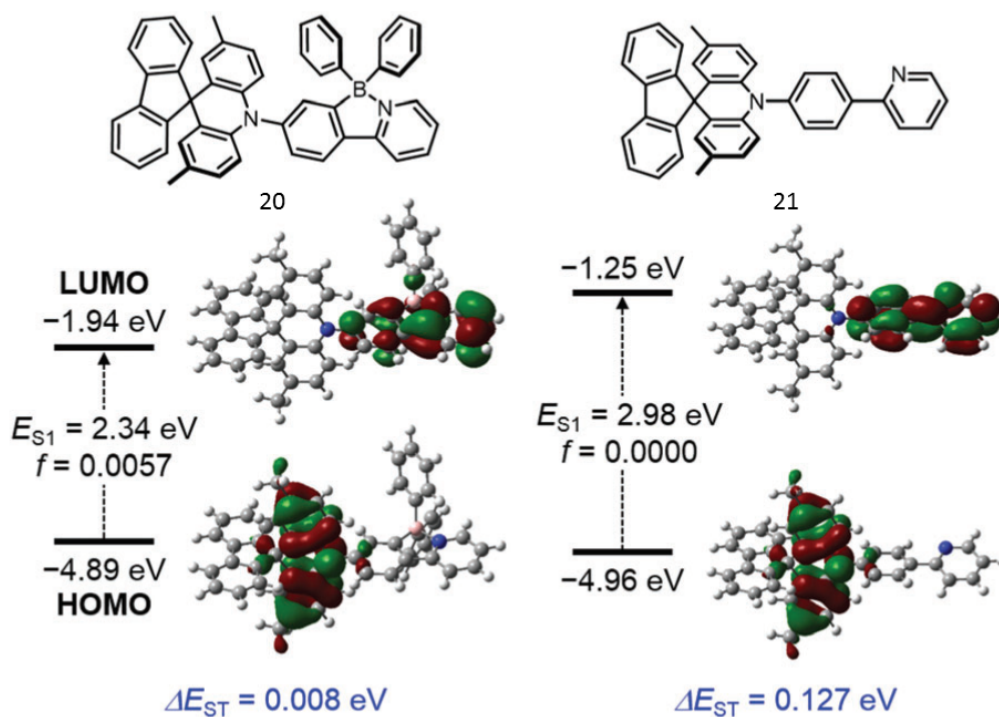


**Figure 1-13.** TADF molecule using a phenylpyridine coordinated boryl group as an acceptor by Matsuo<sup>80</sup>. [Reproduced from Ref. 80 with permission from The Royal Society of Chemistry.]

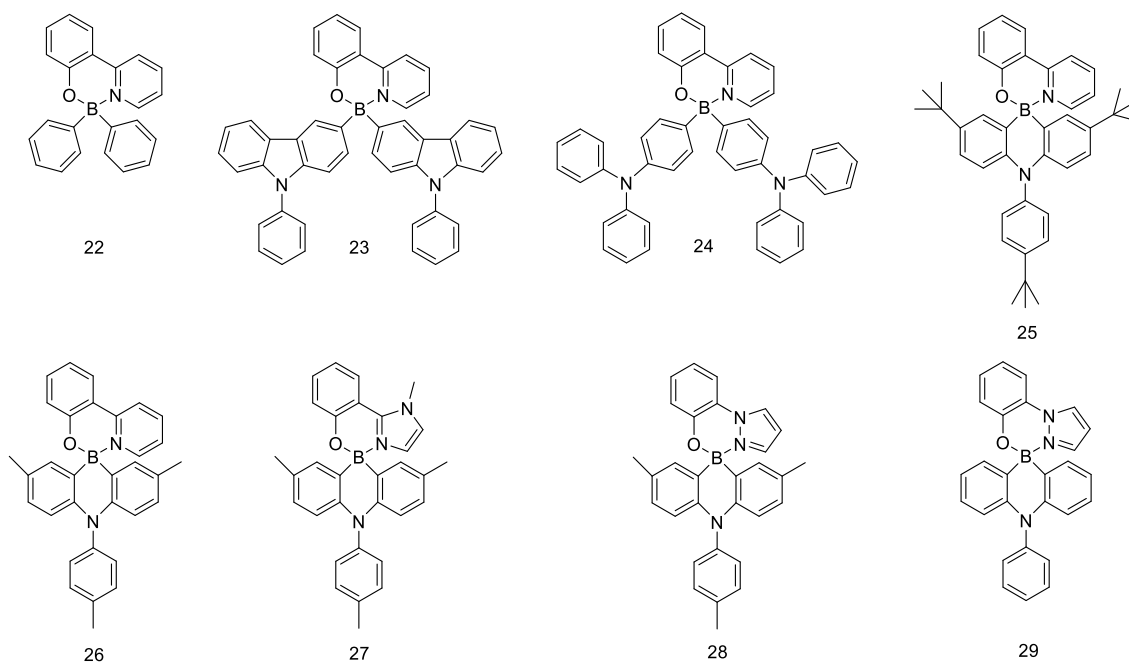


**Figure 1-14.** Four-coordinate boron complexes by Clark<sup>81</sup>



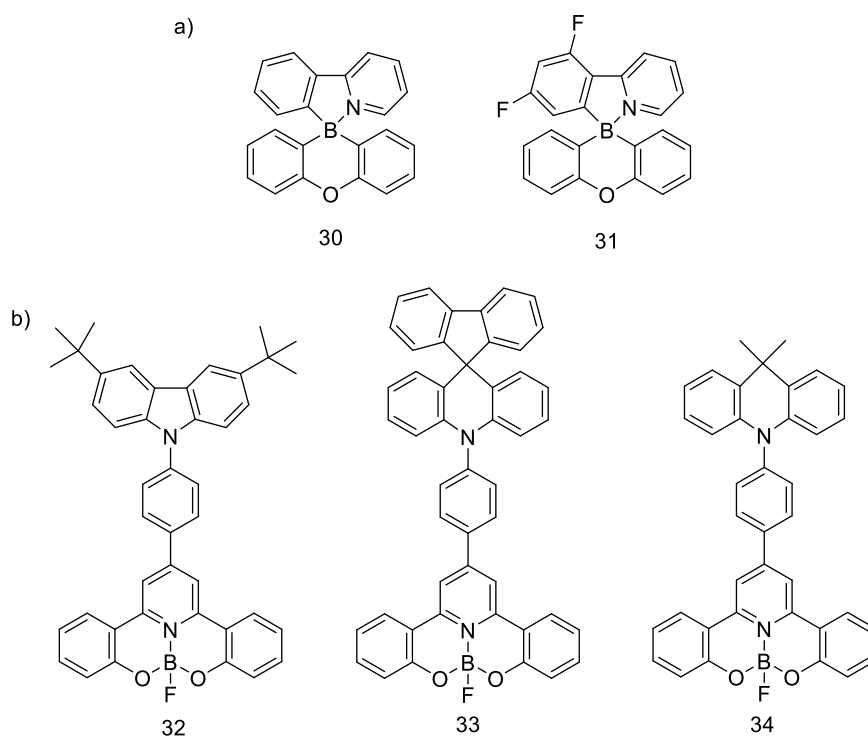


**Figure 1-15.** TADF molecules introduced by Adachi (a)<sup>82</sup> and Yam (b)<sup>84</sup>

Currently, most of the reported TADF molecules are based on an intramolecular donor-acceptor (D-A) system exhibiting a charge-transfer (CT) transition. Adachi designed intramolecular D-A systems which can form an exciplex based on spiro-type tetracoordinate boron derivatives (**30** and **31**, Figure 1-15a).<sup>82</sup> They demonstrated the importance of the triplet CT states ( $^3\text{CT}$ ) and the triplet local excited states ( $^3\text{LE}$ ) alignment as to allow  $^3\text{LE}$  to be involved in the RISC process for efficient TADF. Yam and coworkers designed and synthesized a class of donor-acceptor TADF materials with a four-coordinate boron center bearing a tridentate 2,2'-(pyridine-2,6-diyl)diphenolate (dppy) ligand as the acceptor and diarylamines as the donor (**32-34**, Figure 1-15b).<sup>84</sup> These compounds exhibited high EQEs of 18.0 % for green, 17.5 % for yellow and 8.8 % for blue emission. More importantly, TADF-based OLEDs exhibited long operational stabilities with half-lifetimes of ~2,354 hours for **32**, ~12,733 hours for **33** and ~9,495 hours for **34**, suggesting

four-coordinate fluoroboron compounds to be promising functional building blocks for stable and efficient TADF emitters. Another area of rapid development in highly efficient luminescent materials is that of boron-based imaging materials. Fluorophores containing tetra-coordinated boron centers, such as boron dipyrromethene (BODIPY), have been widely used in fluorescence imaging owing to their low cost, low toxicity, and tunable molecular structure. The development of fluorescent probes is key to advancing bioimaging applications. In the past few decades, many boron-based probes with tunable emission maxima throughout the visible spectral region have been developed and they have greatly accelerated the field of bioimaging for biological research and clinical needs.<sup>85-89</sup> For example, Li's group designed a simple and general strategy to synthesize meso-carboxyl-substituted BODIPY-based bioprobes with emission maxima ranging from green to far red (509, 585, and 660 nm) that contain a stimuli-responsive, self-immolative ester linkage (**35**, Figure 1-16a).<sup>85</sup> Their application as a mitochondria-targeting far-red probe for various biomolecules and enzymes was also validated in living cells. Cosa and coworkers constructed a lipophilic BODIPY-acrolein fluorogenic probe (**AcroB**, Figure 1-16b) that can be used for visualization of cellular response to a noncanonical lipophilic electrophile via a larger than 350-fold emission enhancement in live-cell imaging studies.<sup>86</sup> Kim reported a novel BODIPY probe (**36**, Figure 1-16c) that forms J-aggregates to provide a turn-on signal. This J-aggregating probe allowed for the selective detection, assaying, and imaging of EPO activity in live mice.<sup>88</sup> Zhang and coworkers synthesized a novel asymmetric boron-cored aggregation-induced emission (AIE) luminogen through the formation of oxygen-boron-nitrogen bonding (**37**, Figure 1-17).<sup>54</sup> Unlike BODIPY and its analogs, which often exhibit weak emission, this molecule with a sterically bulky

diphenylboron moiety exhibited AIE characteristics to achieve intriguing emission behavior in solid or aggregated states.

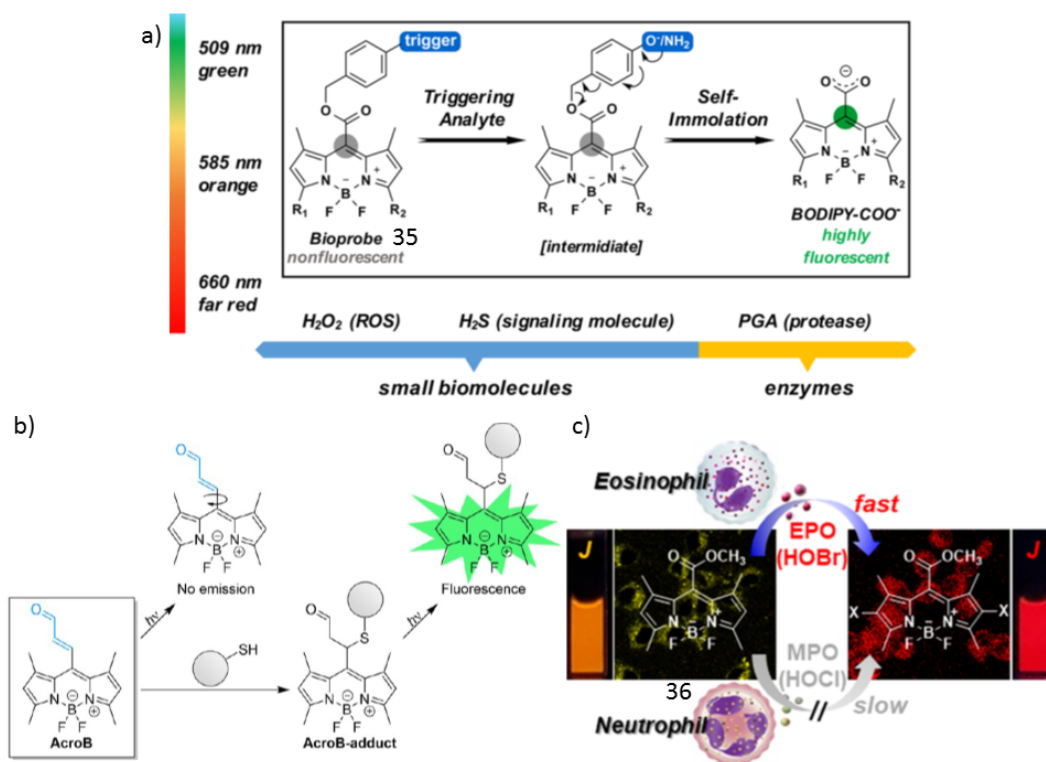


**Figure 1-16.** BODIPY-based bioprobes in visible wavelengths by Li<sup>85</sup> (a), Cosa<sup>86</sup> (b) and Kim<sup>88</sup> (c). [Reproduced with permission from references 85, 86 and 88. Copyright © 2017, American Chemical Society; Copyright © 2017, American Chemical Society; Copyright © 2018, American Chemical Society]

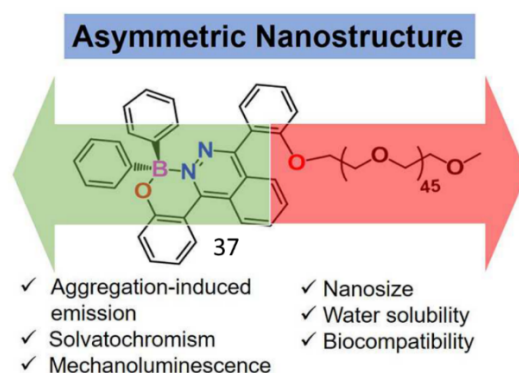


**Figure 1-17.** Asymmetric boron-cored AIE luminogen by Zhang<sup>54</sup>. [Reproduced with permission from references 54. Copyright © 2018, American Chemical Society.]

In recent times, the development of fluorescent probes with near-infrared (NIR) emission has received great attention in light of the potential applications in bioimaging. Fluorescent probes with near-infrared (NIR) emission can achieve great sample penetration depths, sensitive detection and less photo damage compared to fluorescent probes that operate at visible wavelengths. Recently, the fluorescence properties in the NIR region of tetra-coordinate boron-based probes have been studied.<sup>90-94</sup> For example, Cao and coworkers prepared aggregation-induced emission (AIE) active and NIR-emissive pyrrolopyrrole aza-BODIPY dyes (**38** and **39**, Figure 1-18a) from diketopyrrolopyrrole and heteroaromatic amines via a facile synthesis.<sup>90</sup> These aza-BODIPY luminogens solved the common problem of aggregation-caused quenching (ACQ) of fluorescent dyes in the solid state. Chan's group synthesized small-molecule NIR-photocontrolled nitric oxide (NO) donors that consist of an aza-BODIPY dye with an alkylated N-nitroso moiety (**40** and **41**, Figure 1-18b).<sup>92</sup> These molecules incorporate a direct photoacoustic (PA) readout to enable noninvasive monitoring of analyte release in live animals. Wang et al. presented stable BODIPY-based bis(arylamine) diradical dication (**42** and **43**, Figure 1-18c) that are generated by two-electron oxidation of the corresponding neutral molecules.<sup>93</sup> These BODIPY-bridged dication show near-infrared absorptions at 1274 nm and 1068 nm in CH<sub>2</sub>Cl<sub>2</sub> solution, respectively. This diradical dication strategy serves as a new approach to NIR dyes at longer wavelengths.

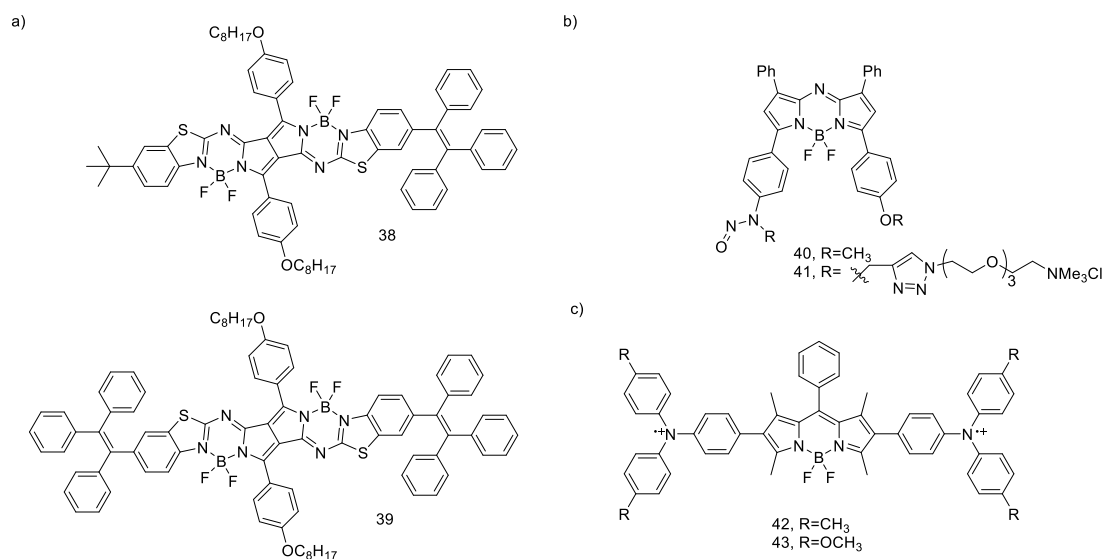


**Figure 1-18.** Fluorescent probes with NIR emission by Cao<sup>90</sup> (a), Chan<sup>92</sup> (b) and Wang<sup>93</sup> (c)

Another interesting research direction is to develop luminescent “smart” materials that respond to one or more environmental “triggers” such as light, heat, and force via several different mechanisms including structural isomerization, phase transitions in liquid crystals and changes in the intermolecular interactions. Boron-based stimuli-responsive materials have attracted much recent research interest, because they can form reversible coordination bonds between the Lewis-acidic boron center and the Lewis-basic nitrogen atom, which results in significant changes to their electronic, photophysical or mechanical properties. The group of Kawashima reported in 2005 the photoisomerization of azobenzene N,C-chelate boron compounds (**44**, Figure 1-19a).<sup>95</sup> A catecholborane bearing a 2-(phenylazo)phenyl group showed photoswitching with a change of the coordination number at boron from 3 to 4 upon irradiation at 360 nm. In 2008, Wang and coworkers reported another type of boron-containing compounds that undergo a reversible isomerization process through the formation/breaking of a C-C bond around a tetrahedral

boron center upon photoirradiation and heating (**45** and **46**, Figure 1-19b).<sup>96</sup> Upon irradiation by light (365 nm), the colorless four-coordinated N,C-chelate organoboron compounds rapidly changed color to dark olive green (**45**) or dark blue (**46**) and lost their fluorescence. The reaction is reversible as the dark-color species revert back to the colorless compounds upon heating in C<sub>6</sub>D<sub>6</sub> in the dark. This was the first example of organoboron compounds that exhibit reversible photo-thermal color switching. Subsequently, Wang's group made significant further contributions to the development of photochromic N,C-chelated organoboron compounds.<sup>26, 33, 55-56, 97-99</sup>

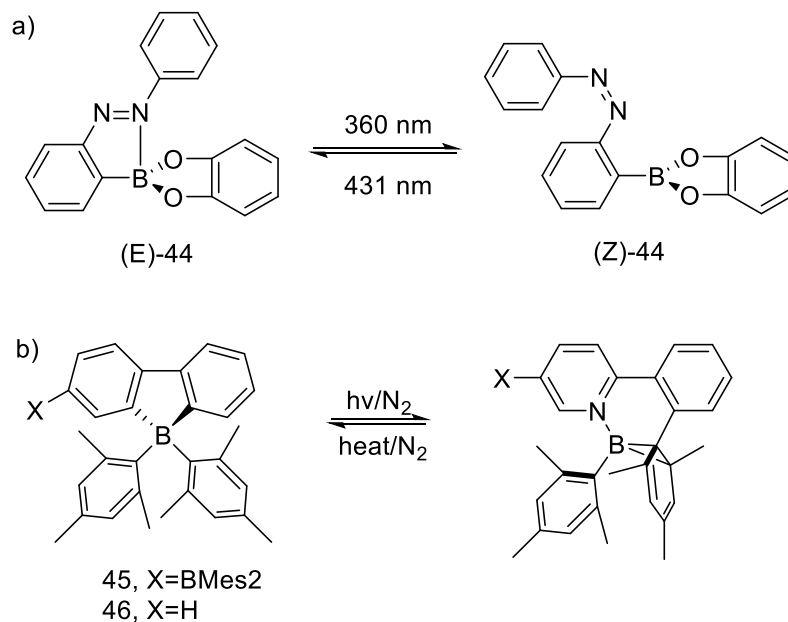


**Figure 1-19.** Photochromic N,C-chelated organoboron compounds by Kawashima<sup>95</sup> (a) and Wang<sup>96</sup> (b)

Recently, Murata and coworkers designed and synthesized the Mes<sub>2</sub>B-substituted benzothiadiazole derivative **47** (Figure 1-20a), which, triggered by changes in temperature, solvent polarity, and mechanical impact, experienced changes in the electronic structure and chromic behavior based on the reversible formation of an intramolecular B-N bond.<sup>100</sup>

Crystals of **47** were yellow in color ( $\lambda = 430$  nm) adopting an “open” form and dark blue ( $\lambda = 577$  nm) in the “mono-closed” form in  $\text{CHCl}_3$  solution. The color of solutions of **47** showed both temperature and solvent dependency. In toluene **47** is deep blue in color at 0 °C but turns brown at 80 °C. Grinding the bright yellow crystals of **47** leads to a color change to dark green. Another example of compounds with weak B-N bonds are the stimuli-responsive B/N Lewis pairs reported by Wang’s group (**48**, Figure 1-20b). The B-N bond strength can be tuned by varying the R group on the nitrogen atom and via external stimuli.<sup>98</sup> Very recently, the same group designed an effective fluorescence “turn-on” temperature probe (**49**, Figure 1-20c).<sup>99</sup> When increasing the temperature, the B-N bond of **49** opened and the fluorescence color changed from weakly green to bright sky-blue in  $\text{CH}_2\text{Cl}_2$ . The open structure proved to be very effective for  $\text{CO}_2$  sensing.

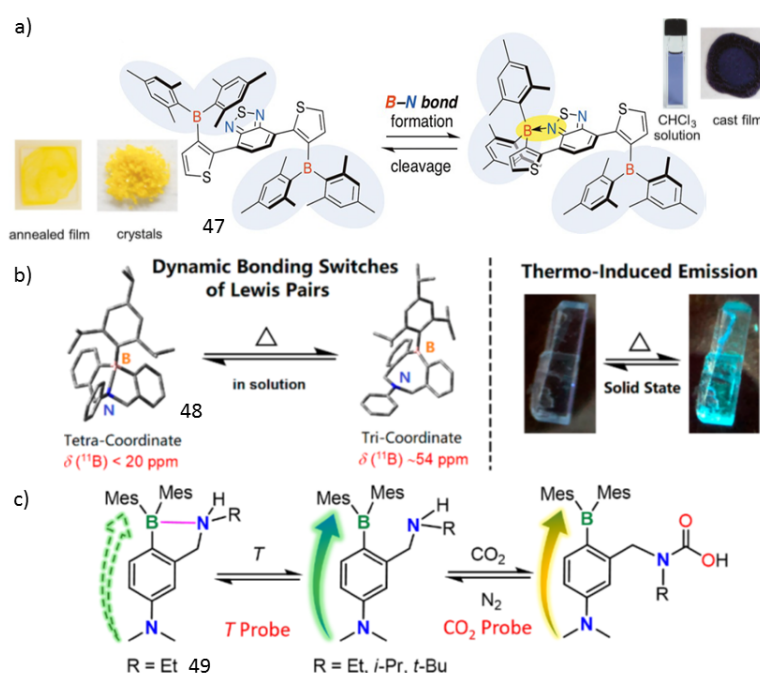


**Figure 1-20.** Photochromic N,C-chelated organoboron compounds by Murata<sup>100</sup> (a) and Wang<sup>98-99</sup> (b, c). [Reproduced with permission from references 100, 98 and 99. Copyright © 2017 Wiley - VCH Verlag GmbH & Co. KGaA, Weinheim; Copyright © 2018, American Chemical Society; Copyright © 2019, American Chemical Society.]

Compounds exhibiting circularly polarized luminescence (CPL) have received considerable attention owing to their great potential in chiroptical materials. Several BODIPY-based chiral architectures have been synthesized and found to show CPL effects.<sup>101-108</sup> Very recently, Ema and coworkers prepared chiral carbazole-based BODIPYs with a binaphthyl unit (**50** and **51**, Figure 1-21a), which showed strong CPL both in solution and in the solid state with  $g_{lum}$  values of up to  $7.0 \times 10^{-3}$ .<sup>109</sup> These compounds also represent the first BODIPY derivatives that exhibit CPL both in solution and in the solid state. In 2017, Crassous' group reported the first helical azaboroles which incorporate boron directly in the helical architecture (**52-55**, Figure 1-21b).<sup>57</sup> They synthesized a series of azaborahelicenes of different size ( $n=6, 8, 10$  ortho-fused cycles) bearing different numbers of boron atoms, which display chiroptical properties. In 2018, Ros et al. developed helicenes based on a borylated arylisoquinoline (BAI) skeleton that contain different aryl fragments at the 8-position of the naphthyl moiety (**56-58**, Figure 1-21c).<sup>58</sup> The helicenes **58** showed circularly polarized luminescence (CPL) emission with dissymmetry  $g$  factors of up to  $3.5 \times 10^{-3}$ .



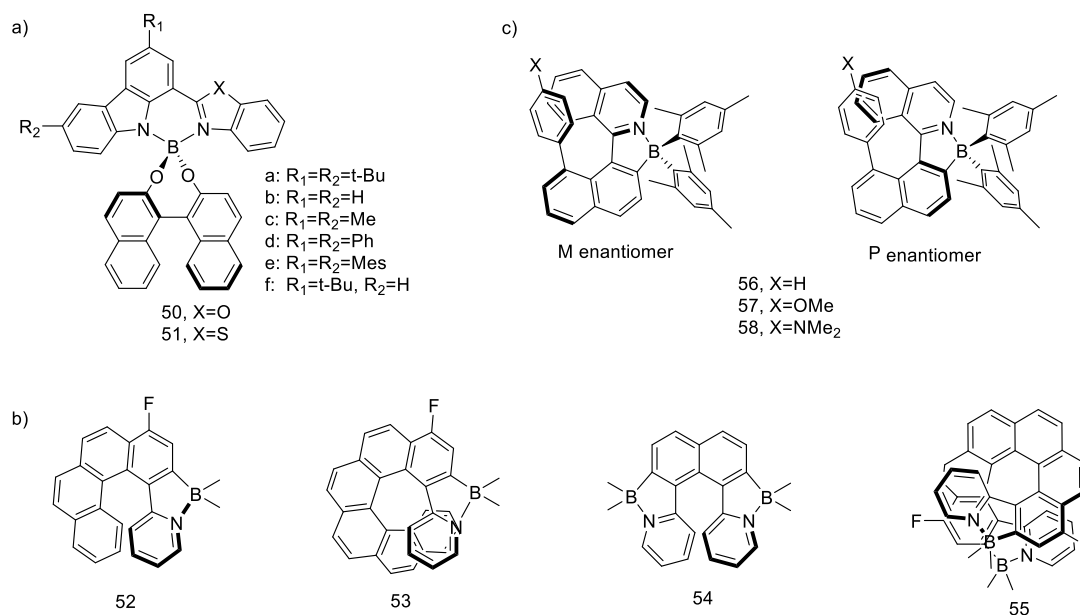


**Figure 1-21.** Organoboron compounds that exhibit circularly polarized luminescence (CPL) by Ema<sup>109</sup> (a), Crassous<sup>57</sup> (b) and Ros<sup>58</sup> (c)

### 1.3.2 Materials for singlet fission and triplet fusion upconversion

Singlet fission is an efficient multiple exciton generation (MEG) process in which some of the energy of a singlet excitation is transferred to a neighboring ground-state chromophore to convert to a pair of triplet excitons. A general description of singlet fission is illustrated in Figure 1-22. Singlet fission initiates with absorption of a photon to produce a singlet exciton,  $S_0S_1$  state (Step 1). The singlet excited state  $S_0S_1$  rapidly forms a correlated pair of triplets that are coupled to form an overall singlet,  $^1(T_1T_1)$  (Step 2). Step 3 involves spin decoherence of the  $^1(T_1T_1)$  state to two independent triplets  $T_1+T_1$ . Step 4 and 5 are decay to the ground state  $S_0S_0$ .<sup>110</sup> The process of generating two independent triplets from one excited singlet can potentially enhance the efficiency of solar cells.

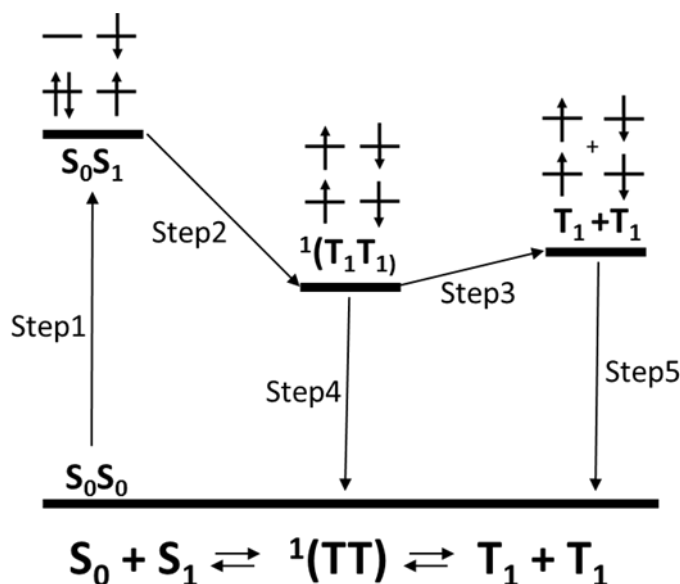


**Figure 1-22.** Schematic representation of the singlet fission process.<sup>111</sup> [Adapted with permission from Ref. 111. Copyright © 2016, American Chemical Society]

Singlet fission was first observed in 1965 to explain delayed fluorescence in crystalline anthracene, which was considered a rather inefficient process.<sup>112</sup> Singlet fission has attracted renewed interest in the last decade when Nozik pointed out that singlet fission could increase the efficiency limit of single junction solar cells to overcome the Shockley-Queisser limit of 33% to nearly 45%.<sup>113</sup> For singlet fission to occur, there are two energetic requirements: (1)  $E(S_1) \geq 2E(T_1)$ , the energy of the singlet exciton ( $S_1$ ) is greater than or equal to the energy of the lowest lying triplet exciton pair ( $T_1+T_1$ ) and (2)  $E(T_2) \geq 2E(T_1)$ , the energy of the second lowest lying triplet exciton ( $T_2$ ) is greater than or equal to the energy of the lowest lying triplet exciton pair ( $T_1+T_1$ ).<sup>114</sup> So far, the range of materials capable of SF is still quite limited, which are mainly restricted to tetracene, pentacene, diphenylisobenzofurans, carotenoids, perylenediimide, polyenes and their derivatives.

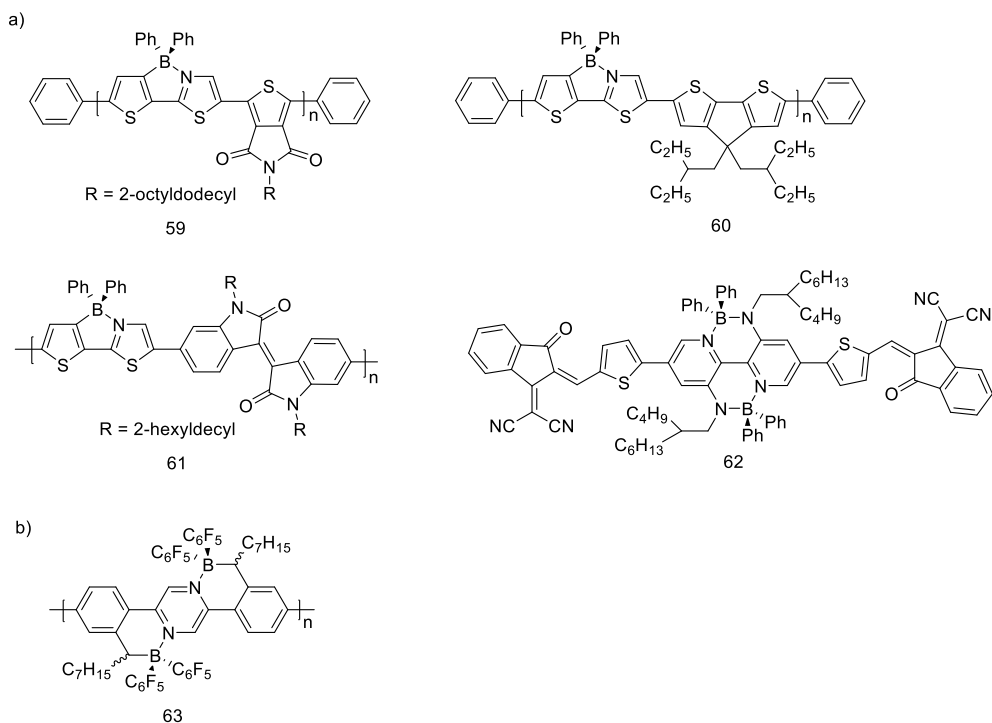


**Figure 1-23.** Examples of B-N substitution compounds in organic solar cells by Liu<sup>49, 115-117</sup> (a) and Pammer<sup>118</sup> (b)

BN Lewis-pair functionalized conjugated materials offer new approaches to adjust the optoelectronic properties of conjugated molecules, which are promising for organic solar cells (OSCs) applications. However, examples of B-N embedded  $\pi$ -units for OSCs applications are scarce. Recently, Liu's group reported the first example of B-N substitution polymers as acceptor materials for solar cells (**59**, Figure 1-23a).<sup>49</sup> They replaced a C-C unit to B-N unit in conjugated polymers to lower their HOMO and LUMO energy levels by about 0.6 eV, turning conjugated polymers from electron donor to electron acceptor materials. Their results indicate that B-N based copolymers have high electron affinity and can be used as electron acceptor in OSCs devices. Subsequently, the same group synthesized several compounds based on B-N units to improve photovoltaic performance for efficient solar cells (**60-62**, Figure 1-23a).<sup>115-117</sup> **62** exhibited the highest power

conversion efficiency (PCE) of 7.06% due to improved carrier mobility and a wide photoresponse from 350 nm to 880 nm. Very recently, Pammer and coworkers prepared B-N ladder polymers via postpolymerization modification of well-defined conjugated polymers (**63**, Figure 1-23b).<sup>118</sup> This postmodification strategy can modify the electronic and structural properties of conjugated polymers as organic electronic devices.

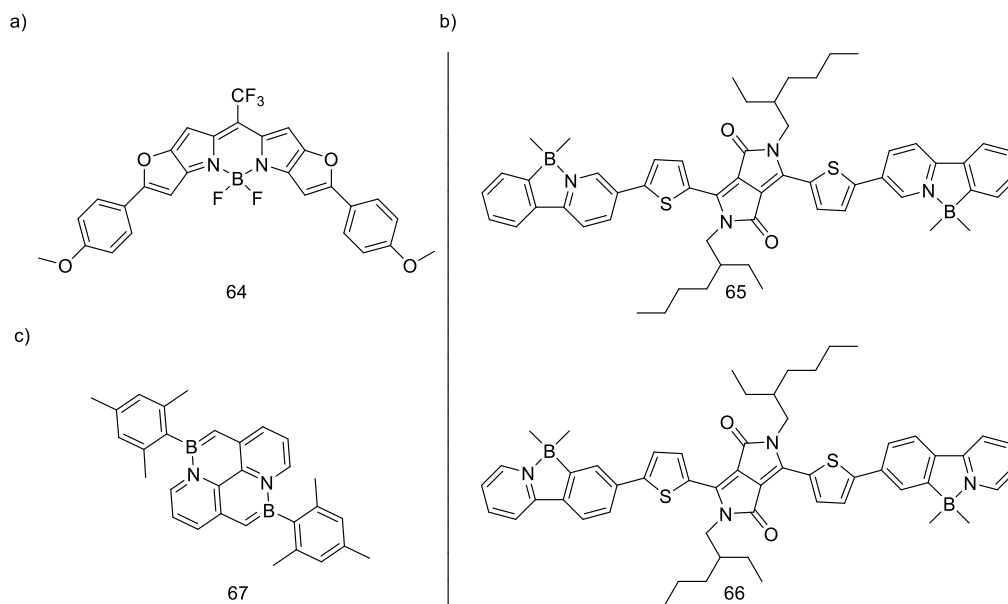


**Figure 1-24.** Examples of B-N substitution compounds in organic solar cells by Leo<sup>119</sup> (a), Huang<sup>120</sup> (b), and Wang<sup>121</sup> (c)

With respect to small molecule acceptors, Leo and coworkers synthesized furan-fused BODIPYs with a CF<sub>3</sub> group on the meso-carbon as near-infrared absorbing materials for organic solar cells (**64**, Figure 1-24a).<sup>119</sup> The best single junction device reached a PCE over 6%. They further combined **64** as the long wavelength absorber with the “green” absorbing donor DCV5T-Me in a vacuum-processed tandem solar cell, achieving a high PCE of 9.9%. Huang demonstrated that the aggregation modes, photophysical and solar cell performance of diketopyrrolopyrrole (DPP)-based molecules (**65** and **66**, Figure 1-24b)

can be tuned by introducing B-N units to replace C-C units and changing the orientation of the B-N bond.<sup>120</sup> So far, only one type of BN compound was confirmed to undergo singlet fission. Wang's group recently synthesized a diazadiborine-pyrene (**67**, Figure 1-24c) which may serve as a promising singlet fission chromophore according to density functional theory (DFT) calculations.<sup>121</sup>

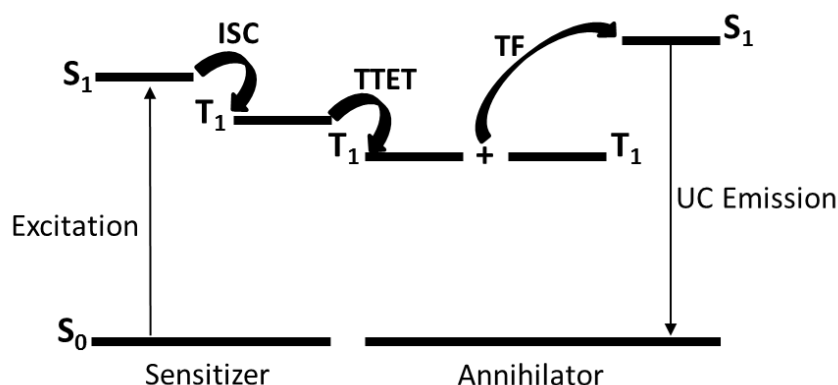


**Figure 1-25.** Simplified scheme of triplet fusion upconversion.<sup>122</sup> [Adapted with permission from Ref. 122. Copyright © 2017, American Chemical Society.]

The direct reverse process of singlet fission is called triplet fusion (TF), also known as triplet-triplet annihilation (TTA), a process in which two separate triplet excitons are converted to a higher energy singlet or triplet exciton. Triplet fusion upconversion, the conversion of two low-energy photons into one higher-energy photon, has recently attracted much attention for its wide variety of potential applications, ranging from solar cells to biological imaging, optogenetics and photochemistry.<sup>123-127</sup> This process requires two species, a sensitizer which absorbs low-energy photons and an annihilator which emits higher energy photons (Figure 1-25).<sup>122</sup> First, the sensitizer is excited to its singlet state  $S_1$  that undergoes intersystem crossing (ISC) to achieve the excited triplet state  $T_1$ . This triplet energy can then be transferred from the sensitizer to an organic annihilator via triplet-triplet

energy transfer (TTET). Two annihilators in the triplet state then come together and undergo triplet fusion (TF), yielding one annihilator in the singlet excited-state ( $S_1$ ) and another annihilator quenched to its ground state. The excited annihilator in its  $S_1$  state decays to the ground state via fluorescence at a higher energy than the incident light.

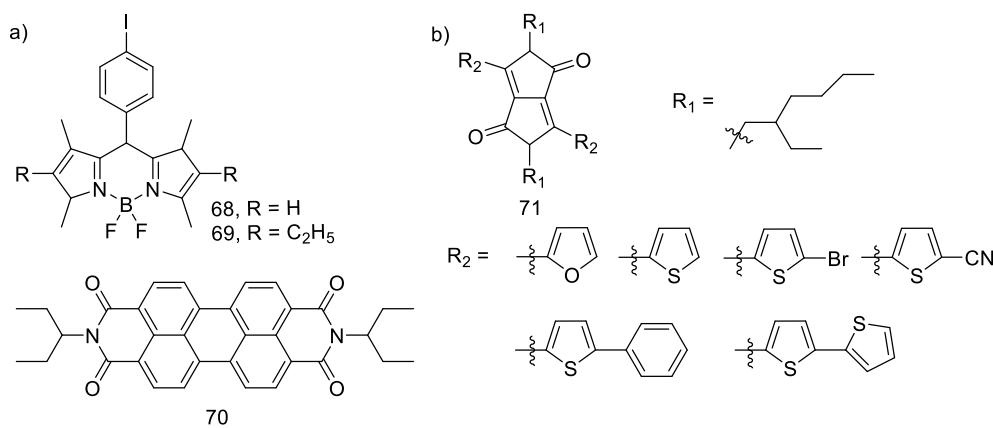


**Figure 1-26.** Heterocyclic Compounds As Annihilators by Castellano<sup>128-129</sup> (a) and Congreve (b)<sup>130</sup>

To date, most attention has been given to the development of novel sensitizers. The annihilator molecules have been largely based on aromatic hydrocarbons.<sup>131-134</sup> In 2008, Castellano et al. developed the first examples of BODIPY annihilators for upconversion (**68** and **69**, Figure 1-26a).<sup>129</sup> **68** and **69** exhibited green and yellow emission, respectively. Then the same group reported a perylenediimide (PDI) dye as a yellow emissive annihilator to provide NIR-to-vis upconversion (**70**, Figure 1-26a).<sup>128</sup> Very recently, Congreve and coworkers introduced diketopyrrolopyrroles (**71**, Figure 1-26b) as a new class of annihilators which can be modified to tune the output wavelength from upconversion.<sup>130</sup>

### 1.3.3 Photodynamic therapy

Photodynamic therapy (PDT) is an emerging photochemotherapeutic method which utilizes the photoexcitation of an external photosensitizer (PS) by appropriate light to generate cytotoxic singlet oxygen ( $^1\text{O}_2$ ) to kill the cancer cells without affecting the unexposed normal cells. Applications of PDT require visible light, a photosensitizer and oxygen, leading to the production of cytotoxic agent ( $^1\text{O}_2$ ) to inactivate tumor cells. The process of photodynamic cancer therapy is illustrated in the Jablonski diagram shown in Figure 1-27.<sup>135</sup> Following the absorption of light, the photosensitizer is excited from the ground state ( $S_0$ ) to the first excited single state ( $S_1$ ). The excited triplet state ( $T_1$ ) is achieved via intersystem crossing (ISC). Singlet oxygen is generated via an energy transfer process between the excited triplet state of the photosensitizer and the ground-state molecular oxygen. To date, a number of photosensitizers, such as quantum dots, upconversion nanoparticles and organic nanoparticles, have been investigated for potential application in PDT.<sup>72, 136-138</sup>

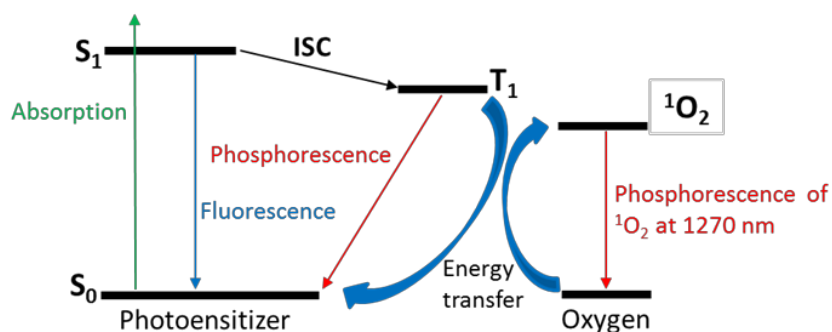


**Figure 1-27.** The process of photodynamic cancer therapy.<sup>135</sup> [Adapted with permission from reference 135. Copyright © 2002 Elsevier Science B.V.]

Boron-dipyrromethene (BODIPY) is a class of metal-free dyes, which has been used as a new class of photosensitizers for PDT over the past decade. BODIPYs have many ideal

photosensitizer properties such as high absorption coefficient, high photostability, anti-photobleaching property, etc.<sup>72</sup> So far, there have been a number of reports on the attributes of BODIPY dyes for PDT.<sup>72, 139-150</sup> The first BODIPY photosensitizer was developed by O'Shea's group for singlet oxygen generation in PDT (**72**, Figure 1-28a).<sup>139</sup> They attached two bromine atoms directly onto BODIPY to enhance the intersystem crossing efficiency by the internal heavy-atom effect. Measurements of QY for  $^1\text{O}_2$ -generation revealed that compound **72** has a high efficiency of  $^1\text{O}_2$  generation of 74%.<sup>140</sup> A disadvantage of the halogenation of BODIPY is the low dark cytotoxicity ratio. This problem can be overcome by using the heavy-atom-free BODIPY. In 2012, Zhao and coworkers prepared styryl BODIPY-C60 dyads (**73**, Figure 1-28b) as efficient heavy atom-free organic triplet photosensitizers.<sup>141</sup> The photosensitizing efficiency of the dyads is much higher (ca. 20-fold) than for the conventional  $^1\text{O}_2$  photosensitizers. Recently, Senge et al. reported heavy atom-free BODIPY-anthracene dyads (**74** and **75**, Figure 1-28c) that can efficiently generate triplet excited states via photoinduced electron transfer and can be used as  $^1\text{O}_2$  sensitizers.<sup>143</sup> Photoinduced electron transfer (PeT) as a new strategy to enhance ISC has attracted lots of attention owing to the advantages over the conventional heavy atom insertion method. In addition, this donor-acceptor dyad becomes fluorescent in response to the generated  $^1\text{O}_2$  in biological media. Very recently, the same group demonstrated that dyads combining BODIPY as an electron acceptor and pyrene or perylene as electron donor subunits can act as heavy atom-free singlet oxygen sensitizers.<sup>147</sup> The most efficient  $^1\text{O}_2$  sensitization was observed for **76** (Figure 1-28c), which showed quantum yields of singlet oxygen of up to 0.75 in polar media (ethanol).



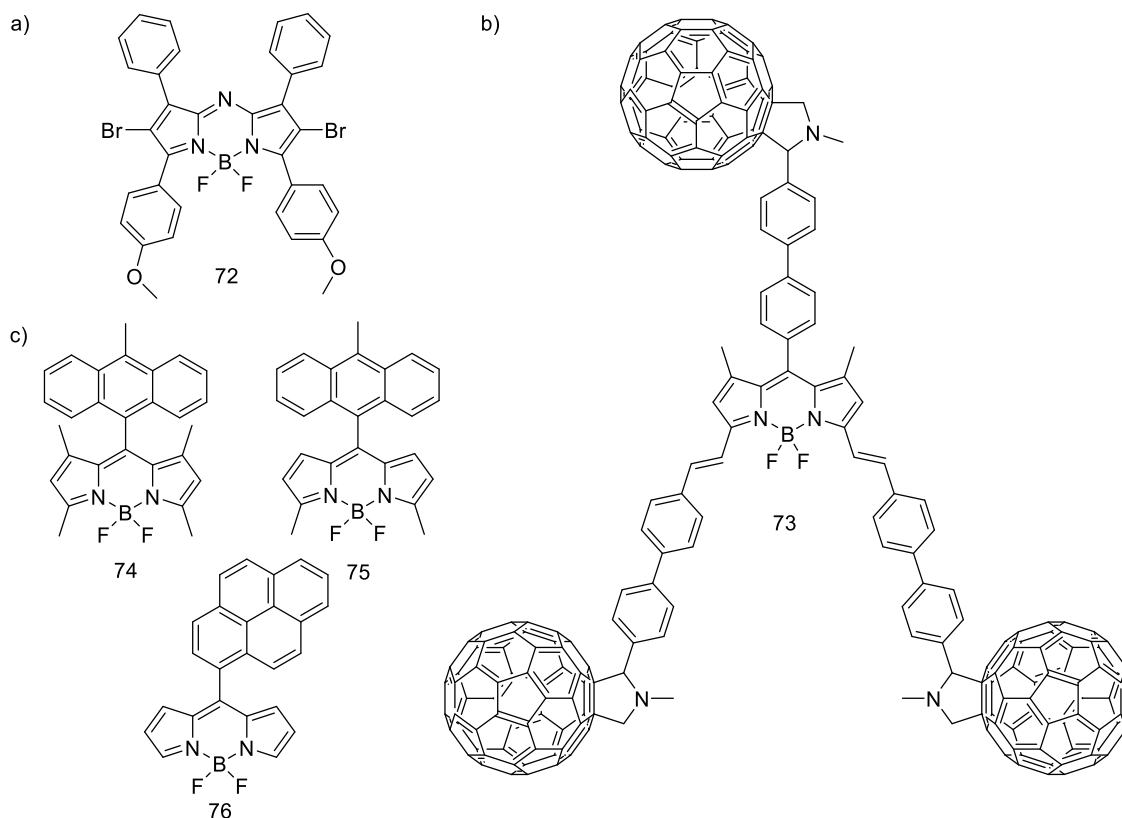


**Figure 1-28.** Examples of BODIPY dyads as photosensitizers for PDT by O'Shea<sup>139</sup> (a), Zhao<sup>141</sup> (b), and Senge<sup>143, 147</sup> (c)

Beyond BODIPY, similar properties as singlet oxygen sensitizers were recently observed for N,C-chelate organoboron dyes. Pischel and coworkers introduced four-coordinate N,C-chelate organoboron dyes, based on arylisoquinoline ligands (**77**, Figure 1-29a).<sup>151</sup> Compound **77** underwent efficient ISC with triplet state formation, and showed quantum yields of singlet oxygen larger than 0.3. Our group developed a new class of BN functionalized PAHs (**78**, Figure 1-29b) by electrophilic aromatic borylation of pyridylanthracenes in 2017.<sup>152</sup> These contorted BN-fused PAHs can react with O<sub>2</sub> in the presence of light without the need for an external photosensitizer, which opens the possibility for applications in photodynamic therapy (PDT). This work is described in Chapter 2. In continuation of this work, we investigated the effect of structural

modifications on the pyridyl moiety. We found that placement of a methyl group in different positions can alter dramatically the reactivity of the BN-anthracenes. Hence, they can be exploited for applications as singlet oxygen sensitizers or for the on-demand delivery of singlet oxygen as described in Chapter 3.<sup>153</sup>

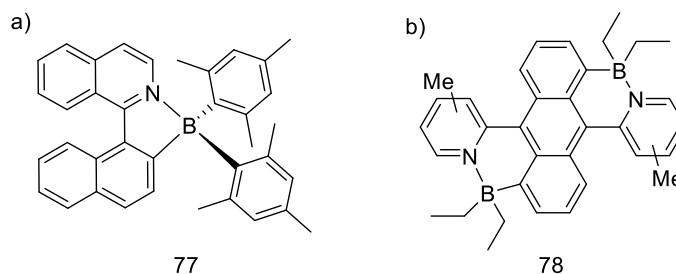


**Figure 1-29.** Examples of N,C-chelate organoboron compounds as photosensitizers for PDT by Pischel<sup>151</sup> (a) and Jäkle (b)<sup>152-153</sup>

## 1.4 References

1. Mei, J.; Diao, Y.; Appleton, A. L.; Fang, L.; Bao, Z., Integrated materials design of organic semiconductors for field-effect transistors. *J. Am. Chem. Soc.* **2013**, *135* (18), 6724-6746.
2. Anthony, J. E., Functionalized Acenes and Heteroacenes for Organic Electronics. *Chem. Rev.* **2006**, *106* (12), 5028-5048.
3. Beaujuge, P. M.; Frechet, J. M., Molecular design and ordering effects in pi-functional materials for transistor and solar cell applications. *J. Am. Chem. Soc.* **2011**, *133* (50), 20009-20029.
4. Wang, C.; Dong, H.; Hu, W.; Liu, Y.; Zhu, D., Semiconducting pi-conjugated systems in field-effect transistors: a material odyssey of organic electronics. *Chem. Rev.* **2012**, *112* (4), 2208-2267.
5. Sun, Z.; Ye, Q.; Chi, C.; Wu, J., Low band gap polycyclic hydrocarbons: from closed-shell near infrared dyes and semiconductors to open-shell radicals. *Chem. Soc. Rev.* **2012**, *41* (23), 7857-7889.
6. Ye, Q.; Chi, C., Recent Highlights and Perspectives on Acene Based Molecules and Materials. *Chem. Mater.* **2014**, *26* (14), 4046-4056.
7. Feng, X.; Pisula, W.; Müllen, K., Large polycyclic aromatic hydrocarbons:

Synthesis and discotic organization. *Pure Appl. Chem.* **2009**, *81* (12), 2203-2224.

8. Watson, M. D.; tter, A. F.; Mu"llen, K., Big Is Beautiful—"Aromaticity" Revisited from the Viewpoint of Macromolecular and Supramolecular Benzene Chemistry. *Chem. Rev.* **2001**, *101* (5), 1267-1300.
9. Feng, X.; Liu, M.; Pisula, W.; Takase, M.; Li, J.; Mullen, K., Supramolecular Organization and Photovoltaics of Triangle-shaped Discotic Graphenes with Swallow-tailed Alkyl Substituents. *Adv. Mater.* **2008**, *20* (14), 2684-2689.
10. Clar, E., E. Clar : Vorschlage zur Nomenklatur kondensierter Ringsysteme (Aromatische Kohlenwasserstoffe, XXVI. Mitteil.). *Chem. Ber.* **1939**, *72*, 2137-2139.
11. VanVeller, B.; Schipper, D. J.; Swager, T. M., Polycyclic aromatic triptycenes: oxygen substitution cyclization strategies. *J. Am. Chem. Soc.* **2012**, *134* (17), 7282-7285.
12. Martins, S.; Farinha, J. P.; Baleizao, C.; Berberan-Santos, M. N., Controlled release of singlet oxygen using diphenylanthracene functionalized polymer nanoparticles. *Chem. Commun.* **2014**, *50* (25), 3317-3320.
13. Sun, H.; Kabb, C. P.; Dai, Y.; Hill, M. R.; Ghiviriga, I.; Bapat, A. P.; Sumerlin, B. S., Macromolecular metamorphosis via stimulus-induced transformations of polymer architecture. *Nat. Chem.* **2017**, *9* (8), 817-823.
14. Yuan, Z.; Yu, S.; Cao, F.; Mao, Z.; Gao, C.; Ling, J., Near-infrared light triggered photothermal and photodynamic therapy with an oxygen-shuttle endoperoxide of anthracene against tumor hypoxia. *Polym. Chem.* **2018**, *9* (16), 2124-2133.
15. Fudickar, W.; Linker, T., Release of Singlet Oxygen from Organic Peroxides under Mild Conditions. *Chem. Photo Chem.* **2018**, *2* (7), 548-558.
16. Pibiri, I.; Buscemi, S.; Palumbo Piccionello, A.; Pace, A., Photochemically Produced Singlet Oxygen: Applications and Perspectives. *Chem. Photo Chem.* **2018**, *2* (7), 535-547.
17. Fudickar, W.; Fery, A.; Linker, T., Reversible Light and Air-Driven Lithography by Singlet Oxygen. *J. Am. Chem. Soc.* **2005**, *127* (26), 9386-9387.
18. Gao, Z.; Han, Y.; Wang, F., Cooperative supramolecular polymers with anthraceneendoperoxide photo-switching for fluorescent anti-counterfeiting. *Nat. Commun.* **2018**, *9* (1), 3977.
19. Zehm, D.; Fudickar, W.; Linker, T., Molecular switches flipped by oxygen. *Angew. Chem., Int. Ed.* **2007**, *46* (40), 7689-7692.
20. Zehm, D.; Fudickar, W.; Hans, M.; Schilde, U.; Kelling, A.; Linker, T., 9,10-diarylanthracenes as molecular switches: syntheses, properties, isomerisations and their reactions with singlet oxygen. *Chem. - Eur. J.* **2008**, *14* (36), 11429-11441.

21. Escande, A.; Ingleson, M. J., Fused polycyclic aromatics incorporating boron in the core: fundamentals and applications. *Chem. Commun.* **2015**, 51 (29), 6257-6274.
22. Wakamiya, A.; Yamaguchi, S., Designs of Functional  $\pi$ -Electron Materials based on the Characteristic Features of Boron. *Bull. Chem. Soc. Jpn.* **2015**, 88 (10), 1357-1377.
23. D.Entwistle, C.; B.Marder, T., Boron Chemistry Lights the Way: Optical Properties of Molecular and Polymeric Systems. *Angew. Chem., Int. Ed.* **2002**, 41 (16), 2927-2931.
24. Entwistle, C. D.; Marder, T. B., Applications of Three-Coordinate Organoboron Compounds and Polymers in Optoelectronics. *Chem. Mater.* **2004**, 16 (23), 4574-4585.
25. Jäkle, F., Advances in the Synthesis of Organoborane Polymers for Optical, Electronic, and Sensory Applications. *Chem. Rev.* **2010**, 110 (7), 3985-4022.
26. Rao, Y.-L.; Amarne, H.; Wang, S., Photochromic four-coordinate N,C-chelate boron compounds. *Coord. Chem. Rev.* **2012**, 256 (5-8), 759-770.
27. Li, D.; Zhang, H.; Wang, Y., Four-coordinate organoboron compounds for organic light-emitting diodes (OLEDs). *Chem. Soc. Rev.* **2013**, 42 (21), 8416-8433.
28. Mukherjee, S.; Thilagar, P., Stimuli and shape responsive 'boron-containing' luminescent organic materials. *J. Mater. Chem. C* **2016**, 4 (14), 2647-2662.
29. Stepien, M.; Gonka, E.; Zyla, M.; Sprutta, N., Heterocyclic Nanographenes and Other Polycyclic Heteroaromatic Compounds: Synthetic Routes, Properties, and Applications. *Chem. Rev.* **2017**, 117 (4), 3479-3716.
30. Yang, Z.; Mao, Z.; Xie, Z.; Zhang, Y.; Liu, S.; Zhao, J.; Xu, J.; Chi, Z.; Aldred, M. P., Recent advances in organic thermally activated delayed fluorescence materials. *Chem. Soc. Rev.* **2017**, 46 (3), 915-1016.
31. von Grotthuss, E.; John, A.; Kaese, T.; Wagner, M., Doping Polycyclic Aromatics with Boron for Superior Performance in Materials Science and Catalysis. *Asian J. Org. Chem.* **2018**, 7 (1), 37-53.
32. Huang, J.; Li, Y., BN Embedded Polycyclic  $\pi$ -Conjugated Systems: Synthesis, Optoelectronic Properties, and Photovoltaic Applications. *Front. Chem.* **2018**, 6, 341.
33. Mellerup, S. K.; Wang, S., Boron-based stimuli responsive materials. *Chem. Soc. Rev.* **2019**, 48 (13), 3537-3549.
34. Mellerup, S. K.; Wang, S., Boron-Doped Molecules for Optoelectronics. *Trends in Chemistry* **2019**, 1 (1), 77-89.
35. Namirembe, S.; Morken, J. P., Reactions of organoboron compounds enabled by catalyst-promoted metalate shifts. *Chem. Soc. Rev.* **2019**, 48 (13), 3464-3474.

36. Jäkle, F., Lewis acidic organoboron polymers. *Coord. Chem. Rev.* **2006**, *250* (9-10), 1107-1121.
37. Wade, C. R.; Broomsgrove, A. E. J.; Aldridge, S.; Gabbai, F. P., Fluoride Ion Complexation and Sensing Using Organoboron Compounds. *Chem. Rev.* **2010**, *110* (7), 3958-3984.
38. Piers, W. E.; Irvine, G. J.; Williams, V. C., Highly Lewis Acidic Bifunctional Organoboranes. *Eur. J. Inorg. Chem.* **2000**, *2000* (10), 2131-2142.
39. Campbell, P. G.; Marwitz, A. J.; Liu, S. Y., Recent advances in azaborine chemistry. *Angew. Chem., Int. Ed.* **2012**, *51* (25), 6074-6092.
40. Wang, X. Y.; Wang, J. Y.; Pei, J., BN heterosuperbenzenes: synthesis and properties. *Chem. - Eur. J.* **2015**, *21* (9), 3528-3539.
41. Stock, A.; Pohland, E.; Dtsch, B., Borwasserstoffe, IX.: B<sub>3</sub>N<sub>3</sub>H<sub>6</sub>. *Chem. Ges.* **1926**, *59*, 2215-2223.
42. Dewar, M. J. S.; Kubba, V. P.; Pettit, R., New Heteroaromatic Compounds. Part I. 9-Axa-10-boraphenanthrene. *J. Chem. Soc.* **1958**, 3073-3076.
43. Ishibashi, J. S.; Marshall, J. L.; Maziere, A.; Lovinger, G. J.; Li, B.; Zakharov, L. N.; Dargelos, A.; Graciaa, A.; Chrostowska, A.; Liu, S. Y., Two BN isosteres of anthracene: synthesis and characterization. *J. Am. Chem. Soc.* **2014**, *136* (43), 15414-15421.
44. Ishibashi, J. S. A.; Dargelos, A.; Darrigan, C.; Chrostowska, A.; Liu, S.-Y., BN Tetracene: Extending the Reach of BN/CC Isosterism in Acenes. *Organometallics* **2017**, *36* (14), 2494-2497.
45. Zhuang, F. D.; Sun, Z. H.; Yao, Z. F.; Chen, Q. R.; Huang, Z.; Yang, J. H.; Wang, J. Y.; Pei, J., BN-Embedded Tetrabenzopentacene: A Pentacene Derivative with Improved Stability. *Angew. Chem., Int. Ed.* **2019**, *58* (31), 10708-10712.
46. Ci, L.; Song, L.; Jin, C.; Jariwala, D.; Wu, D.; Li, Y.; Srivastava, A.; Wang, Z. F.; Storr, K.; Balicas, L.; Liu, F.; Ajayan, P. M., Atomic layers of hybridized boron nitride and graphene domains. *Nat. Mater.* **2010**, *9* (5), 430-435.
47. Wang, X. Y.; Zhuang, F. D.; Wang, R. B.; Wang, X. C.; Cao, X. Y.; Wang, J. Y.; Pei, J., A straightforward strategy toward large BN-embedded pi-systems: synthesis, structure, and optoelectronic properties of extended BN heterosuperbenzenes. *J. Am. Chem. Soc.* **2014**, *136* (10), 3764-3767.
48. Zhong, Z.; Wang, X.-Y.; Zhuang, F.-D.; Ai, N.; Wang, J.; Wang, J.-Y.; Pei, J.; Peng, J.; Cao, Y., Curved BN-embedded nanographene for application in organic solar cells. *J. Mater. Chem. A* **2016**, *4* (40), 15420-15425.
49. Dou, C.; Ding, Z.; Zhang, Z.; Xie, Z.; Liu, J.; Wang, L., Developing conjugated

polymers with high electron affinity by replacing a C-C unit with a B<-N unit. *Angew. Chem., Int. Ed.* **2015**, *54* (12), 3648-3652.

50. Ayhan, O.; Eckert, T.; Plamper, F. A.; Helten, H., Poly(iminoborane)s: An Elusive Class of Main-Group Polymers? *Angew. Chem., Int. Ed.* **2016**, *55* (42), 13321-13325.

51. Baggett, A. W.; Guo, F.; Li, B.; Liu, S. Y.; Jäkle, F., Regioregular synthesis of azaborine oligomers and a polymer with a syn conformation stabilized by N-Hpi interactions. *Angew. Chem., Int. Ed.* **2015**, *54* (38), 11191-11195.

52. Lin, H.; McConnell, C. R.; Jilus, B.; Liu, S.-Y.; Jäkle, F., Changing up BN-Polystyrene: Effect of Substitution Pattern on the Free-Radical Polymerization and Polymer Properties. *Macromolecules* **2019**, *52* (12), 4500-4509.

53. Frath, D.; Massue, J.; Ulrich, G.; Ziessel, R., Luminescent materials: locking pi-conjugated and heterocyclic ligands with boron(III). *Angew. Chem., Int. Ed.* **2014**, *53* (9), 2290-2310.

54. Qiu, F.; Zhang, N.; Tang, R.; Zhou, M.; Wang, Y.; Wei, W.; Bi, S.; Han, S.; Zhang, F., Asymmetric Boron-Cored Aggregation-Induced Emission Luminogen with Multiple Functions Synthesized through Stepwise Conversion from a Symmetric Ligand. *J. Org. Chem.* **2018**, *83* (21), 12977-12984.

55. Rao, Y. L.; Wang, S., Four-coordinate organoboron compounds with a pi-conjugated chelate ligand for optoelectronic applications. *Inorg. Chem.* **2011**, *50* (24), 12263-12274.

56. Møllerup, S. K.; Wang, S., Isomerization and rearrangement of boriranes: from chemical rarities to functional materials. *Sci. China Mater.* **2018**, *61* (10), 1249-1256.

57. Shen, C.; Srebro-Hooper, M.; Jean, M.; Vanthuyne, N.; Toupet, L.; Williams, J. A.; Torres, A. R.; Riives, A. J.; Müller, G.; Autschbach, J.; Crassous, J., Synthesis and Chiroptical Properties of Hexa-, Octa-, and Deca-azaborahelicenes: Influence of Helicene Size and of the Number of Boron Atoms. *Chem. - Eur. J.* **2017**, *23* (2), 407-418.

58. Dominguez, Z.; Lopez-Rodriguez, R.; Alvarez, E.; Abbate, S.; Longhi, G.; Pischel, U.; Ros, A., Azabora[5]helicene Charge-Transfer Dyes Show Efficient and Spectrally Variable Circularly Polarized Luminescence. *Chem. - Eur. J.* **2018**, *24* (48), 12660-12668.

59. Wakamiya, A.; Taniguchi, T.; Yamaguchi, S., Intramolecular B-N coordination as a scaffold for electron-transporting materials: synthesis and properties of boryl-substituted thienylthiazoles. *Angew. Chem., Int. Ed.* **2006**, *45* (19), 3170-3173.

60. Ishida, N.; Moriya, T.; Goya, T.; Murakami, M., Synthesis of pyridine-borane complexes via electrophilic aromatic borylation. *J. Org. Chem.* **2010**, *75* (24), 8709-8712.

61. Ros, A.; Fernandez, R.; Lassaletta, J. M., Functional group directed C-H borylation. *Chem. Soc. Rev.* **2014**, *43* (10), 3229-3243.

62. Niu, L.; Yang, H.; Wang, R.; Fu, H., Metal-Free Ortho C-H Borylation of 2-Phenoxy pyridines under Mild Conditions. *Org. Lett.* **2012**, *14* (10), 2618-2621.
63. Zhao, Z.; Chang, Z.; He, B.; Chen, B.; Deng, C.; Lu, P.; Qiu, H.; Tang, B. Z., Aggregation-induced emission and efficient solid-state fluorescence from tetraphenylethene-based N,C-chelate four-coordinate organoborons. *Chem. - Eur. J.* **2013**, *19* (35), 11512-11517.
64. Shaikh, A. C.; Ranade, D. S.; Thorat, S.; Maity, A.; Kulkarni, P. P.; Gonnade, R. G.; Munshi, P.; Patil, N. T., Highly emissive organic solids with remarkably broad color tunability based on N,C-chelate, four-coordinate organoborons. *Chem. Commun.* **2015**, *51* (89), 16115-16118.
65. Zhu, C.; Guo, Z. H.; Mu, A. U.; Liu, Y.; Wheeler, S. E.; Fang, L., Low Band Gap Coplanar Conjugated Molecules Featuring Dynamic Intramolecular Lewis Acid-Base Coordination. *J. Org. Chem.* **2016**, *81* (10), 4347-4352.
66. Crossley, D. L.; Cade, I. A.; Clark, E. R.; Escande, A.; Humphries, M. J.; King, S. M.; Vitorica-Yrezabal, I.; Ingleson, M. J.; Turner, M. L., Enhancing electron affinity and tuning band gap in donor-acceptor organic semiconductors by benzothiadiazole directed C-H borylation. *Chem. Sci.* **2015**, *6* (9), 5144-5151.
67. Crossley, D. L.; Cid, J.; Curless, L. D.; Turner, M. L.; Ingleson, M. J., Facile Arylation of Four-Coordinate Boron Halides by Boremium Cation Mediated Boro-desilylation and -destannylation. *Organometallics* **2015**, *34* (24), 5767-5774.
68. Crossley, D. L.; Vitorica-Yrezabal, I.; Humphries, M. J.; Turner, M. L.; Ingleson, M. J., Highly Emissive Far Red/Near-IR Fluorophores Based on Borylated Fluorene-Benzothiadiazole Donor-Acceptor Materials. *Chem. - Eur. J.* **2016**, *22* (35), 12439-12448.
69. Crossley, D. L.; Kulapichitr, P.; Radcliffe, J. E.; Dunsford, J. J.; Vitorica-Yrezabal, I.; Kahan, R. J.; Woodward, A. W.; Turner, M. L.; McDouall, J. J. W.; Ingleson, M. J., C-H Borylation/Cross-Coupling Forms Twisted Donor-Acceptor Compounds Exhibiting Donor-Dependent Delayed Emission. *Chem. - Eur. J.* **2018**, *24* (41), 10521-10530.
70. Min, Y.; Dou, C.; Tian, H.; Geng, Y.; Liu, J.; Wang, L., n-Type Azaacenes Containing B←N Units. *Angew. Chem., Int. Ed.* **2018**, *57* (7), 2000-2004.
71. Min, Y.; Dou, C.; Tian, H.; Liu, J.; Wang, L., A disk-type polyarene containing four B←N units. *Chem. Commun.* **2019**, *55* (25), 3638-3641.
72. Kamkaew, A.; Lim, S. H.; Lee, H. B.; Kiew, L. V.; Chung, L. Y.; Burgess, K., BODIPY dyes in photodynamic therapy. *Chem. Soc. Rev.* **2013**, *42* (1), 77-88.
73. Durka, K.; Głowacki, I.; Luliński, S.; Łuszczynska, B.; Smętek, J.; Szczepanik, P.; Serwatowski, J.; Wawrzyniak, U. E.; Wesela-Bauman, G.; Witkowska, E.; Wiosna-Sałyga, G.; Woźniak, K., Efficient 8-oxyquinolino emitters based on a 9,10-dihydro-9,10-diboraanthracene scaffold for applications in optoelectronic devices. *J. Mater. Chem. C*

**2015**, 3 (6), 1354-1364.

74. Zhang, Z.; Zhang, Z.; Ye, K.; Zhang, J.; Zhang, H.; Wang, Y., Diboron complexes with bis-spiro structures as high-performance blue emitters for OLEDs. *Dalton Trans.* **2015**, 44 (32), 14436-14443.

75. Zhang, Z.; Zhang, Z.; Zhang, H.; Wang, Y., 2-(2-Hydroxyphenyl)imidazole-based four-coordinate organoboron compounds with efficient deep blue photoluminescence and electroluminescence. *Dalton Trans.* **2017**, 47 (1), 127-134.

76. Ishimatsu, R.; Shintaku, H.; Kage, Y.; Kamioka, M.; Shimizu, S.; Nakano, K.; Furuta, H.; Imato, T., Efficient Electrogenenerated Chemiluminescence of Pyrrolopyrrole Aza-BODIPYs in the Near-Infrared Region with Tripropylamine: Involving Formation of S2 and T2 States. *J. Am. Chem. Soc.* **2019**, 141 (30), 11791-11795.

77. Uoyama, H.; Goushi, K.; Shizu, K.; Nomura, H.; Adachi, C., Highly efficient organic light-emitting diodes from delayed fluorescence. *Nature* **2012**, 492 (7428), 234-238.

78. Shiu, Y. J.; Cheng, Y. C.; Tsai, W. L.; Wu, C. C.; Chao, C. T.; Lu, C. W.; Chi, Y.; Chen, Y. T.; Liu, S. H.; Chou, P. T., Pyridyl Pyrrolide Boron Complexes: The Facile Generation of Thermally Activated Delayed Fluorescence and Preparation of Organic Light-Emitting Diodes. *Angew. Chem., Int. Ed.* **2016**, 55 (9), 3017-3021.

79. Shiu, Y.-J.; Chen, Y.-T.; Lee, W.-K.; Wu, C.-C.; Lin, T.-C.; Liu, S.-H.; Chou, P.-T.; Lu, C.-W.; Cheng, I. C.; Lien, Y.-J.; Chi, Y., Efficient thermally activated delayed fluorescence of functional phenylpyridinato boron complexes and high performance organic light-emitting diodes. *J. Mater. Chem. C* **2017**, 5 (6), 1452-1462.

80. Matsuo, K.; Yasuda, T., Enhancing thermally activated delayed fluorescence characteristics by intramolecular B-N coordination in a phenylpyridine-containing donor-acceptor pi-system. *Chem. Commun.* **2017**, 53 (62), 8723-8726.

81. Bell, B. M.; Clark, T. P.; De Vries, T. S.; Lai, Y.; Laitar, D. S.; Gallagher, T. J.; Jeon, J.-H.; Kearns, K. L.; McIntire, T.; Mukhopadhyay, S.; Na, H.-Y.; Paine, T. D.; Rachford, A. A., Boron-based TADF emitters with improved OLED device efficiency roll-off and long lifetime. *Dyes Pigments* **2017**, 141, 83-92.

82. Mamada, M.; Tian, G.; Nakanotani, H.; Su, J.; Adachi, C., The Importance of Excited-State Energy Alignment for Efficient Exciplex Systems Based on a Study of Phenylpyridinato Boron Derivatives. *Angew. Chem., Int. Ed.* **2018**, 57 (38), 12380-12384.

83. Stanoppi, M.; Lorbach, A., Boron-based donor-spiro-acceptor compounds exhibiting thermally activated delayed fluorescence (TADF). *Dalton Trans.* **2018**, 47 (31), 10394-10398.

84. Li, P.; Chan, H.; Lai, S. L.; Ng, M.; Chan, M. Y.; Yam, V. W., Four-Coordinate Boron Emitters with Tridentate Chelating Ligand for Efficient and Stable Thermally



Activated Delayed Fluorescence Organic Light-Emitting Devices. *Angew. Chem., Int. Ed.* **2019**, *58* (27), 9088-9094.

85. Chen, H.; He, X.; Su, M.; Zhai, W.; Zhang, H.; Li, C., A General Strategy Toward Highly Fluorogenic Bioprobes Emitting across the Visible Spectrum. *J. Am. Chem. Soc.* **2017**, *139* (29), 10157-10163.

86. Lincoln, R.; Greene, L. E.; Zhang, W.; Louisia, S.; Cosa, G., Mitochondria Alkylation and Cellular Trafficking Mapped with a Lipophilic BODIPY-Acrolein Fluorogenic Probe. *J. Am. Chem. Soc.* **2017**, *139*, 16273-16281.

87. Santos, F. M. F.; Domínguez, Z.; Alcaide, M. M.; Matos, A. I.; Florindo, H. F.; Candeias, N. R.; Gois, P. M. P.; Pischel, U., Highly Efficient Energy Transfer Cassettes by Assembly of Boronic Acid Derived Salicylidenehydrazone Complexes. *Chem. Photo Chem.* **2018**, *2* (12), 1038-1045.

88. Kim, T. I.; Hwang, B.; Lee, B.; Bae, J.; Kim, Y., Selective Monitoring and Imaging of Eosinophil Peroxidase Activity with a J-Aggregating Probe. *J. Am. Chem. Soc.* **2018**, *140* (37), 11771-11776.

89. Hu, D.; Zhang, T.; Li, S.; Yu, T.; Zhang, X.; Hu, R.; Feng, J.; Wang, S.; Liang, T.; Chen, J.; Sobenina, L. N.; Trofimov, B. A.; Li, Y.; Ma, J.; Yang, G., Ultrasensitive reversible chromophore reaction of BODIPY functions as high ratio double turn on probe. *Nat. Commun.* **2018**, *9* (1), 362.

90. Li, L.; Wang, L.; Tang, H.; Cao, D., A facile synthesis of novel near-infrared pyrrolopyrrole aza-BODIPY luminogens with aggregation-enhanced emission characteristics. *Chem. Commun.* **2017**, *53* (59), 8352-8355.

91. Sansalone, L.; Tang, S.; Garcia-Amoros, J.; Zhang, Y.; Nonell, S.; Baker, J. D.; Captain, B.; Raymo, F. M., A Photoactivatable Far-Red/Near-Infrared BODIPY To Monitor Cellular Dynamics in Vivo. *ACS Sens.* **2018**, *3* (7), 1347-1353.

92. Zhou, E. Y.; Knox, H. J.; Reinhardt, C. J.; Partipilo, G.; Nilges, M. J.; Chan, J., Near-Infrared Photoactivatable Nitric Oxide Donors with Integrated Photoacoustic Monitoring. *J. Am. Chem. Soc.* **2018**, *140* (37), 11686-11697.

93. Wei, H.; Feng, R.; Fang, Y.; Wang, L.; Chen, C.; Zhang, L.; Cui, H.; Wang, X., The Diradical-Dication Strategy for BODIPY- and Porphyrin-Based Dyes with Near-Infrared Absorption Maxima from 1070 to 2040 nm. *Chem. - Eur. J.* **2018**, *24* (72), 19341-19347.

94. Ren, C.; Deng, X.; Hu, W.; Li, J.; Miao, X.; Xiao, S.; Liu, H.; Fan, Q.; Wang, K.; He, T., A near-infrared I emissive dye: toward the application of saturable absorber and multiphoton fluorescence microscopy in the deep-tissue imaging window. *Chem. Commun.* **2019**, *55* (35), 5111-5114.

95. Kano, N.; Yoshino, J.; Kawashima, T., Photoswitching of the Lewis Acidity of a Catecholborane Bearing an Azo Group Based on the Change in Coordination Number of

Boron. *Org. Lett.* **2005**, 7 (18), 3909-3911.

96. Rao, Y.-L.; Amarne, H.; Zhao, S.-B.; McCormick, T. M.; Martić, S.; Sun, Y.; Wang, R.-Y.; Wang, S., Reversible Intramolecular C-C Bond Formation/Breaking and Color Switching Mediated by a N,C-Chelate in (2-ph-py)BMes2 and (5-BMes2-2-ph-py)BMes2. *J. Am. Chem. Soc.* **2008**, 130, 12898-12900.

97. Møllerup, S. K.; Li, C.; Peng, T.; Wang, S., Regioselective Photoisomerization/C-C Bond Formation of Asymmetric B(ppy)(Mes)(Ar): The Role of the Aryl Groups on Boron. *Angew. Chem., Int. Ed.* **2017**, 56 (22), 6093-6097.

98. Hou, Q.; Liu, L.; Møllerup, S. K.; Wang, N.; Peng, T.; Chen, P.; Wang, S., Stimuli-Responsive B/N Lewis Pairs Based on the Modulation of B-N Bond Strength. *Org. Lett.* **2018**, 20 (20), 6467-6470.

99. Li, H. J.; Møllerup, S. K.; Wang, X.; Wang, S., D-π-A Triarylboranes as Reversible Fluorescent Probes for CO2 and Temperature. *Org. Lett.* **2019**, 21 (8), 2838-2842.

100. Shimogawa, H.; Yoshikawa, O.; Aramaki, Y.; Murata, M.; Wakamiya, A.; Murata, Y., 4,7-Bis[3-(dimesitylboryl)thien-2-yl]benzothiadiazole: Solvato-, Thermo-, and Mechanochromism Based on the Reversible Formation of an Intramolecular B-N Bond. *Chem. - Eur. J.* **2017**, 23 (15), 3784-3791.

101. Ray, C.; Sánchez-Carnerero, E. M.; Moreno, F.; Maroto, B. L.; Agarrabeitia, A. R.; Ortiz, M. J.; Lopez-Arbeloa, I.; Banuelos, J.; Cohovi, K. D.; Lunkley, J. L.; Müller, G.; de la Moya, S., Bis(haloBODIPYs) with Labile Helicity: Valuable Simple Organic Molecules That Enable Circularly Polarized Luminescence. *Chem. - Eur. J.* **2016**, 22 (26), 8805-8808.

102. Alnoman, R. B.; Rihn, S.; O'Connor, D. C.; Black, F. A.; Costello, B.; Waddell, P. G.; Clegg, W.; Peacock, R. D.; Herrebout, W.; Knight, J. G.; Hall, M. J., Circularly Polarized Luminescence from Helically Chiral N,N,O,O-Boron-Chelated Dipyrrromethenes. *Chem. - Eur. J.* **2016**, 22 (1), 93-96.

103. Saikawa, M.; Nakamura, T.; Uchida, J.; Yamamura, M.; Nabeshima, T., Synthesis of figure-of-eight helical bisBODIPY macrocycles and their chiroptical properties. *Chem. Commun.* **2016**, 52 (71), 10727-10730.

104. FrancescoZinna; Bruhn, T.; Bari, L. D.; Guido, C. A.; Pescitelli, G., Circularly Polarized Luminescence from Axially Chiral BODIPY DYEsters: An Experimental and Computational Study. *Chem. - Eur. J.* **2016**, 22 (45), 16089-16098.

105. Toyoda, M.; Imai, Y.; Mori, T., Propeller Chirality of Boron Heptaaryldipyrrromethene: Unprecedented Supramolecular Dimerization and Chiroptical Properties. *J. Phys. Chem. Lett.* **2017**, 8 (1), 42-48.

106. Jimenez, J.; Cerdan, L.; Moreno, F.; Maroto, B. L.; Garcia-Moreno, I.; Lunkley, J. L.; Müller, G.; de la Moya, S., Chiral Organic Dyes Endowed with Circularly Polarized Laser Emission. *J. Phys. Chem. C* **2017**, 121 (9), 5287-5292.

107. Clarke, R.; Ho, K. L.; Alsimaree, A. A.; Woodford, O. J.; Waddell, P. G.; Bogaerts, J.; Herrebout, W.; Knight, J. G.; Pal, R.; Penfold, T. J.; Hall, M. J., Circularly Polarised Luminescence from Helically Chiral “Confused” N, N, O ,C-Boron-Chelated Dipyrromethenes (BODIPYs). *Chem. Photo Chem.* **2017**, *1* (11), 513-517.
108. Ikai, T.; Yoshida, T.; Awata, S.; Wada, Y.; Maeda, K.; Mizuno, M.; Swager, T. M., Circularly Polarized Luminescent Triptycene-Based Polymers. *ACS Macro Lett.* **2018**, *7* (3), 364-369.
109. Maeda, C.; Nagahata, K.; Takaishi, K.; Ema, T., Synthesis of chiral carbazole-based BODIPYs showing circularly polarized luminescence. *Chem. Commun.* **2019**, *55* (21), 3136-3139.
110. Hetzer, C.; Guldi, D. M.; Tykwinski, R. R., Pentacene Dimers as a Critical Tool for the Investigation of Intramolecular Singlet Fission. *Chem. - Eur. J.* **2018**, *24* (33), 8245-8257.
111. Korovina, N. V.; Das, S.; Nett, Z.; Feng, X.; Joy, J.; Haiges, R.; Krylov, A. I.; Bradforth, S. E.; Thompson, M. E., Singlet Fission in a Covalently Linked Cofacial Alkynyltetracene Dimer. *J. Am. Chem. Soc.* **2016**, *138* (2), 617-627.
112. S. Singh, W. J. J., W. Siebrand, B. P. Stoicheff, W. G. Schneider, Laser Generation of Excitons and Fluorescence in Anthracene Crystals. *J. Chem. Phys.* **1965**, *42*, 330.
113. M. C. Hanna, A. J. N., Solar conversion efficiency of photovoltaic and photoelectrolysis cells with carrier multiplication absorbers. *J. Appl. Phys.* **2006**, *100*, 074510.
114. Smith, M. B.; Michl, J., Recent advances in singlet fission. *Annu. Rev. Phys. Chem.* **2013**, *64*, 361-386.
115. Zhang, Z.; Ding, Z.; Dou, C.; Liu, J.; Wang, L., Development of a donor polymer using a B  $\leftarrow$  N unit for suitable LUMO/HOMO energy levels and improved photovoltaic performance. *Polym. Chem.* **2015**, *6* (46), 8029-8035.
116. Zhao, R.; Dou, C.; Xie, Z.; Liu, J.; Wang, L., Polymer Acceptor Based on B $\leftarrow$ N Units with Enhanced Electron Mobility for Efficient All-Polymer Solar Cells. *Angew. Chem., Int. Ed.* **2016**, *55* (17), 5313-5317.
117. Liu, F.; Ding, Z.; Liu, J.; Wang, L., An organoboron compound with a wide absorption spectrum for solar cell applications. *Chem. Commun.* **2017**, *53* (90), 12213-12216.
118. Grandl, M.; Schepper, J.; Maity, S.; Peukert, A.; von Hauff, E.; Pammer, F., N  $\rightarrow$  B Ladder Polymers Prepared by Postfunctionalization: Tuning of Electron Affinity and Evaluation as Acceptors in All-Polymer Solar Cells. *Macromolecules* **2019**, *52* (3), 1013-1024.

119. Li, T. Y.; Meyer, T.; Ma, Z.; Benduhn, J.; Korner, C.; Zeika, O.; Vandewal, K.; Leo, K., Small Molecule Near-Infrared Boron Dipyrromethene Donors for Organic Tandem Solar Cells. *J. Am. Chem. Soc.* **2017**, *139* (39), 13636-13639.
120. Pang, S.; Mas-Montoya, M.; Xiao, M.; Duan, C.; Wang, Z.; Liu, X.; Janssen, R. A. J.; Yu, G.; Huang, F.; Cao, Y., Adjusting Aggregation Modes and Photophysical and Photovoltaic Properties of Diketopyrrolopyrrole-Based Small Molecules by Introducing B←N Bonds. *Chem. - Eur. J.* **2019**, *25* (2), 564-572.
121. Zeng, T.; Møllerup, S. K.; Yang, D.; Wang, X.; Wang, S.; Stampelcoskie, K., Identifying (BN)2-pyrenes as a New Class of Singlet Fission Chromophores: Significance of Azaborine Substitution. *J. Phys. Chem. Lett.* **2018**, *9* (11), 2919-2927.
122. Yanai, N.; Kimizuka, N., New Triplet Sensitization Routes for Photon Upconversion: Thermally Activated Delayed Fluorescence Molecules, Inorganic Nanocrystals, and Singlet-to-Triplet Absorption. *Acc. Chem. Res.* **2017**, *50* (10), 2487-2495.
123. Schulze, T. F.; Schmidt, T. W., Photochemical upconversion: present status and prospects for its application to solar energy conversion. *Energy Environ. Sci.* **2015**, *8* (1), 103-125.
124. Gray, V.; Dzebo, D.; Abrahamsson, M.; Albinsson, B.; Møth-Poulsen, K., Triplet-triplet annihilation photon-upconversion: towards solar energy applications. *Phys. Chem. Chem. Phys.* **2014**, *16* (22), 10345-10352.
125. Liu, S. W.; Lee, C. C.; Yuan, C. H.; Su, W. C.; Lin, S. Y.; Chang, W. C.; Huang, B. Y.; Lin, C. F.; Lee, Y. Z.; Su, T. H.; Chen, K. T., Transparent organic upconversion devices for near-infrared sensing. *Adv. Mater.* **2015**, *27* (7), 1217-1222.
126. Kwon, O. S.; Song, H. S.; Conde, J.; Kim, H. I.; Artzi, N.; Kim, J. H., Dual-Color Emissive Upconversion Nanocapsules for Differential Cancer Bioimaging In Vivo. *ACS Nano* **2016**, *10* (1), 1512-1521.
127. Ravetz, B. D.; Pun, A. B.; Churchill, E. M.; Congreve, D. N.; Rovis, T.; Campos, L. M., Photoredox catalysis using infrared light via triplet fusion upconversion. *Nature* **2019**, *565* (7739), 343-346.
128. Tanya N. Singh-Rachford, A. N., Maria L. Muro-Small, Sébastien Goeb, Michael J. Therien, and Felix N. Castellano, Supermolecular-Chromophore-Sensitized Near-Infrared-to-Visible Photon Upconversion. *J. Am. Chem. Soc.* **2010**, *132* (40), 14203-14211.
129. Tanya N. Singh-Rachford, A. H., Raymond Ziessel, and Felix N. Castellano, Boron Dipyrromethene Chromophores: Next Generation Triplet Acceptors/ Annihilators for Low Power Upconversion Schemes. *J. Am. Chem. Soc.* **2008**, *130* (48), 16164-16165.
130. Pun, A. B.; Campos, L. M.; Congreve, D. N., Tunable Emission from Triplet Fusion Upconversion in Diketopyrrolopyrroles. *J. Am. Chem. Soc.* **2019**, *141* (9), 3777-3781.

131. Balushev, S.; Yakutkin, V.; Miteva, T.; Avlasevich, Y.; Chernov, S.; Aleshchenkov, S.; Nelles, G.; Cheprakov, A.; Yasuda, A.; Mullen, K.; Wegner, G., Blue-green up-conversion: noncoherent excitation by NIR light. *Angew. Chem., Int. Ed.* **2007**, *46* (40), 7693-7696.
132. Sugunan, S. K.; Greenwald, C.; Paige, M. F.; Steer, R. P., Efficiency of noncoherent photon upconversion by triplet-triplet annihilation: the C60 plus anthanthrene system and the importance of tuning the triplet energies. *J. Phys. Chem. A* **2013**, *117* (26), 5419-5427.
133. Yu, X.; Cao, X.; Chen, X.; Ayres, N.; Zhang, P., Triplet-triplet annihilation upconversion from rationally designed polymeric emitters with tunable inter-chromophore distances. *Chem. Commun.* **2015**, *51* (3), 588-591.
134. Dzebo, D.; Börjesson, K.; Gray, V.; Moth-Poulsen, K.; Albinsson, B., Intramolecular Triplet–Triplet Annihilation Upconversion in 9,10-Diphenylanthracene Oligomers and Dendrimers. *J. Phys. Chem. C* **2016**, *120* (41), 23397-23406.
135. DeRosa, M. C.; Crutchley, R. J., Photosensitized singlet oxygen and its applications. *Coord. Chem. Rev.* **2002**, *223-224*, 351-371.
136. Huang, P.; Lin, J.; Wang, S.; Zhou, Z.; Li, Z.; Wang, Z.; Zhang, C.; Yue, X.; Niu, G.; Yang, M.; Cui, D.; Chen, X., Photosensitizer-conjugated silica-coated gold nanoclusters for fluorescence imaging-guided photodynamic therapy. *Biomaterials* **2013**, *34* (19), 4643-4654.
137. Lucky, S. S.; Soo, K. C.; Zhang, Y., Nanoparticles in photodynamic therapy. *Chem. Rev.* **2015**, *115* (4), 1990-2042.
138. Zou, J.; Yin, Z.; Wang, P.; Chen, D.; Shao, J.; Zhang, Q.; Sun, L.; Huang, W.; Dong, X., Photosensitizer synergistic effects: D-A-D structured organic molecule with enhanced fluorescence and singlet oxygen quantum yield for photodynamic therapy. *Chem. Sci.* **2018**, *9* (8), 2188-2194.
139. Killoran, J.; Allen, L.; Gallagher, J. F.; Gallagher, W. M.; O'Shea, D. F., Synthesis of BF<sub>2</sub>chelates of tetraarylazadipyrrromethenes and evidence for their photodynamic therapeutic behaviour. *Chem. Commun.* **2002**, (17), 1862-1863.
140. Batat, P.; Cantuel, M.; Jonusauskas, G.; Scarpantonio, L.; Palma, A.; O'Shea, D. F.; McClenaghan, N. D., BF<sub>2</sub>-azadipyrrromethenes: probing the excited-state dynamics of a NIR fluorophore and photodynamic therapy agent. *J. Phys. Chem. A* **2011**, *115* (48), 14034-14039.
141. Huang, L.; Yu, X.; Wu, W.; Zhao, J., Styryl Bodipy-C60 Dyads as Efficient Heavy-Atom-Free Organic Triplet Photosensitizers. *Org. Lett.* **2012**, *14* (10), 2594-2597.
142. Palao, E.; Sola-Llano, R.; Tabero, A.; Manzano, H.; Agarrabeitia, A. R.; Villanueva, A.; Lopez-Arbeloa, I.; Martinez-Martinez, V.; Ortiz, M. J., AcetylacetonateBODIPY-Biscyclometalated Iridium(III) Complexes: Effective Strategy towards Smarter

Fluorescent Photosensitizer Agents. *Chem. - Eur. J.* **2017**, *23* (42), 10139-10147.

143. Filatov, M. A.; Karuthedath, S.; Polestshuk, P. M.; Savoie, H.; Flanagan, K. J.; Sy, C.; Sitte, E.; Telitchko, M.; Laquai, F.; Boyle, R. W.; Senge, M. O., Generation of Triplet Excited States via Photoinduced Electron Transfer in meso-anthra-BODIPY: Fluorogenic Response toward Singlet Oxygen in Solution and in Vitro. *J. Am. Chem. Soc.* **2017**, *139* (18), 6282-6285.

144. Ramu, V.; Gautam, S.; Garai, A.; Kondaiah, P.; Chakravarty, A. R., Glucose-Appended Platinum(II)-BODIPY Conjugates for Targeted Photodynamic Therapy in Red Light. *Inorg. Chem.* **2018**, *57* (4), 1717-1726.

145. Kim, S.; Zhou, Y.; Tohnai, N.; Nakatsuji, H.; Matsusaki, M.; Fujitsuka, M.; Miyata, M.; Majima, T., Aggregation-Induced Singlet Oxygen Generation: Functional Fluorophore and Anthrylphenylene Dyad Self-Assemblies. *Chem. - Eur. J.* **2018**, *24* (3), 636-645.

146. Guo, X.; Li, X.; Liu, X. C.; Li, P.; Yao, Z.; Li, J.; Zhang, W.; Zhang, J. P.; Xue, D.; Cao, R., Selective visible-light-driven oxygen reduction to hydrogen peroxide using BODIPY photosensitizers. *Chem. Commun.* **2018**, *54* (7), 845-848.

147. Filatov, M. A.; Karuthedath, S.; Polestshuk, P. M.; Callaghan, S.; Flanagan, K. J.; Wiesner, T.; Laquai, F.; Senge, M. O., BODIPY-Pyrene and Perylene Dyads as Heavy-Atom-Free Singlet Oxygen Sensitizers. *Chem. Photo Chem.* **2018**, *2* (7), 606-615.

148. Zou, J.; Wang, P.; Wang, Y.; Liu, G.; Zhang, Y.; Zhang, Q.; Shao, J.; Si, W.; Huang, W.; Dong, X., Penetration depth tunable BODIPY derivatives for pH triggered enhanced photothermal/photodynamic synergistic therapy. *Chem. Sci.* **2019**, *10* (1), 268-276.

149. Miao, X.; Hu, W.; He, T.; Tao, H.; Wang, Q.; Chen, R.; Jin, L.; Zhao, H.; Lu, X.; Fan, Q.; Huang, W., Deciphering the intersystem crossing in near-infrared BODIPY photosensitizers for highly efficient photodynamic therapy. *Chem. Sci.* **2019**, *10* (10), 3096-3102.

150. Ucar, E.; Seven, O.; Lee, D.; Kim, G.; Yoon, J.; Akkaya, E. U., Selectivity in Photodynamic Action: Higher Activity of Mitochondria Targeting Photosensitizers in Cancer Cells. *Chem. Photo Chem.* **2019**, *3* (3), 129-132.

151. Boscá, F.; Cuquerella, M. C.; Pais, V. F.; Ros, A.; Pischel, U., Excited-State Pathways of Four-Coordinate N,C-Chelate Organoboron Dyes. *Chem. Photo Chem.* **2018**, *2* (1), 34-41.

152. Liu, K.; Lalancette, R. A.; Jakle, F., B-N Lewis Pair Functionalization of Anthracene: Structural Dynamics, Optoelectronic Properties, and O<sub>2</sub> Sensitization. *J. Am. Chem. Soc.* **2017**, *139* (50), 18170-18173.

153. Liu, K.; Lalancette, R. A.; Jakle, F., Tuning the Structure and Electronic Properties of B-N Fused Dipyridylanthracene and Implications on the Self-Sensitized Reactivity with Singlet Oxygen. *J. Am. Chem. Soc.* **2019**, *141* (18), 7453-7462.

154. Vadrucci, R.; Weder, C.; Simon, Y. C., Organogels for low-power light upconversion. *Mater. Horiz.* **2015**, 2 (1), 120-124.
155. Aubry, J. M.; Pierlot, C.; Rigaudy, J.; Schmidt, R., Reversible binding of oxygen to aromatic compounds. *Acc. Chem. Res.* **2003**, 36 (9), 668-675.
156. Zehm, D.; Fudickar, W.; Linker, T., Molecular switches flipped by oxygen. *Angew. Chem., Int. Ed.* **2007**, 46 (40), 7689-7692.
157. Klaper, M.; Linker, T., Intramolecular Transfer of Singlet Oxygen. *J. Am. Chem. Soc.* **2015**, 137 (43), 13744-13747.
158. Altinok, E.; Smith, Z. C.; Thomas, S. W., Two-Dimensional, Acene-Containing Conjugated Polymers That Show Ratiometric Fluorescent Response to Singlet Oxygen. *Macromolecules* **2015**, 48 (19), 6825-6831.
159. Filatov, M. A.; Karuthedath, S.; Polestshuk, P. M.; Savoie, H.; Flanagan, K. J.; Sy, C.; Sitte, E.; Telitchko, M.; Laquai, F.; Boyle, R. W.; Senge, M. O., Generation of Triplet Excited States via Photoinduced Electron Transfer in meso-anthra-BODIPY: Fluorogenic Response toward Singlet Oxygen in Solution and in Vitro. *J. Am. Chem. Soc.* **2017**, 139 (18), 6282-6285.
160. VanVeller, B.; Schipper, D. J.; Swager, T. M., Polycyclic Aromatic Triptycenes: Oxygen Substitution Cyclization Strategies. *J. Am. Chem. Soc.* **2012**, 134 (17), 7282-7285.
161. Telitel, S.; Blasco, E.; Bangert, L. D.; Schacher, F. H.; Goldmann, A. S.; Barner-Kowollik, C., Photo-reversible bonding and cleavage of block copolymers. *Polym. Chem.* **2017**, 8 (27), 4038-4042.
162. Sun, H.; Kabb, C. P.; Dai, Y. Q.; Hill, M. R.; Ghiviriga, I.; Bapat, A. P.; Sumerlin, B. S., Macromolecular metamorphosis via stimulus-induced transformations of polymer architecture. *Nature Chem.* **2017**, 9 (8), 817-823.
163. Ball, M.; Zhong, Y.; Wu, Y.; Schenck, C.; Ng, F.; Steigerwald, M.; Xiao, S. X.; Nuckolls, C., Contorted Polycyclic Aromatics. *Acc. Chem. Res.* **2015**, 48 (2), 267-276.
164. Katayama, T.; Nakatsuka, S.; Hirai, H.; Yasuda, N.; Kumar, J.; Kawai, T.; Hatakeyama, T., Two-Step Synthesis of Boron-Fused Double Helicenes. *J. Am. Chem. Soc.* **2016**, 138 (16), 5210-5213.
165. Baumgartner, T.; Reau, R., Organophosphorus pi-conjugated materials. *Chem. Rev.* **2006**, 106 (11), 4681-4727.
166. Hissler, M.; Lescop, C.; Reau, R., Functional phosphorus-based  $\pi$ -conjugated systems: Structural diversity without multistep synthesis. *Pure Appl. Chem.* **2007**, 79 (2), 201-212.
167. Miao, Q., *Polycyclic Arenes and Heteroarenes: Synthesis, Properties, and*

*Applications*. Wiley-VCH Verlag GmbH & Co. KGaA: Weinheim, 2016.

168. Stępień, M.; Gońka, E.; Żyła, M.; Sprutta, N., Heterocyclic Nanographenes and Other Polycyclic Heteroaromatic Compounds: Synthetic Routes, Properties, and Applications. *Chem. Rev.* **2017**, 117(4), 3479-3716.

169. Christensen, P. R.; Patrick, B. O.; Caron, E.; Wolf, M. O., Oxidation-State-Dependent Photochemistry of Sulfur-Bridged Anthracenes. *Angew. Chem., Int. Ed.* **2013**, 52 (49), 12946-12950.

170. Narita, A.; Wang, X. Y.; Feng, X. L.; Mullen, K., New advances in nanographene chemistry. *Chem. Soc. Rev.* **2015**, 44 (18), 6616-6643.

171. Escande, A.; Ingleson, M. J., Fused polycyclic aromatics incorporating boron in the core: fundamentals and applications. *Chem. Commun.* **2015**, 51 (29), 6257-6274.

172. Park, Y. S.; Dibble, D. J.; Kim, J.; Lopez, R. C.; Vargas, E.; Gorodetsky, A. A., Synthesis of Nitrogen-Containing Rubicene and Tetrabenzopentacene Derivatives. *Angew. Chem., Int. Ed.* **2016**, 55 (10), 3352-3355.

173. Romero-Nieto, C.; Baumgartner, T., Dithieno[3,2-b:2',3'-d]phospholes: A Look Back at the First Decade. *Synlett* **2013**, 24 (8), 920-937.

174. Endres, A. H.; Schaffroth, M.; Paulus, F.; Reiss, H.; Wadepohl, H.; Rominger, F.; Kramer, R.; Bunz, U. H. F., Coronene-Containing N-Heteroarenes: 13 Rings in a Row. *J. Am. Chem. Soc.* **2016**, 138 (6), 1792-1795.

175. Hindenberg, P.; pez-Andarias, A. L.; Rominger, F.; zar, A. d. C.; Romero-Nieto, C., A Guide for the Design of Functional Polyaromatic Organophosphorus Materials. *Chem. - Eur. J.* **2017**, 23, 13919-13928.



## Chapter 2 BN Lewis Pair Functionalization of Anthracene <sup>[a]</sup>

### 2.1 Introduction

Polycyclic aromatic hydrocarbons (PAHs) continue to attract immense interest for applications in organic electronics and as luminescent materials.<sup>1</sup> They are also of key importance as sensitizers and in the selective release of singlet oxygen for biomedical applications.<sup>2</sup> Upon incorporation into polymers, the reversible formation of Diels-Alder adducts can be exploited in “smart” materials with self-healing or mechano-responsive properties.<sup>3</sup> In another twist, deliberate distortions to the conjugated framework in contorted PAHs alters the reactivity, photophysical and optoelectronic properties, while also offering structural complementary and thus enhanced interactions with fullerenes and related nanomaterials.<sup>4</sup>

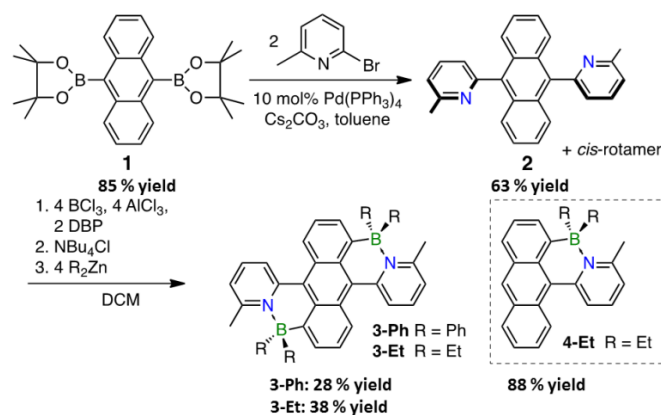
A powerful approach to modifying PAHs is to introduce heteroatoms such as B, Si, N, P, S, etc; the intrinsically different features of these main group elements can dramatically change the electronic structure and reactivity of PAHs.<sup>5</sup> For example, replacement of carbons with tricoordinate borons yields materials that display strong fluorescence, phosphorescence or even thermally activated delayed fluorescence (TADF).<sup>6</sup> Similarly, the replacement of CC units for isoelectronic and isosteric BN units modifies the aromatic character and charge transport properties.<sup>7</sup> On the other hand, B←N Lewis pair functionalization (tetracoordinate boron) of conjugated materials can lead to materials with NIR-emissive, enhanced acceptor, and photoswitchable characteristics.<sup>8</sup> However, B←N Lewis pair functionalization approaches have not been explored as a design motif to

---

[a] This chapter is adapted from a journal publication (ref. 24).

contorted PAHs, potentially offering unprecedented electronic structure modulation and reactivity patterns.

## 2.2 Results and Discussion



**Scheme 2-1.** Synthesis of BN-fused 9,10-dipyridylanthracenes **3-R** (**R** = **Ph**, **Et**) and **4-Et**

Suzuki-Miyaura coupling of **1** with 2-bromo-6-methylpyridine gives 9,10-di(pyrid-2-yl)anthracene (**2**) (Scheme 2-1), which was isolated as a light yellow crystalline solid that shows a strong blue-purple luminescence in solution, typical of 9,10-diarylanthracenes.<sup>9</sup> The <sup>1</sup>H NMR spectrum of **2** in CDCl<sub>3</sub> at RT reveals two sets of peaks with a relative intensity of 1:3.4, which are attributed to rotamers based on H,H-EXSY 2D NMR measurements (Figure. 2-1). The barrier to inter-conversion between the *cis* and *trans*-isomer is  $\Delta G_{318}^{\ddagger} = 69.7 \pm 1.1$  kJ mol<sup>-1</sup> based on VT NMR experiments in d8-toluene (Figure 2-2). According to an X-ray analysis, compound **2** preferably crystallizes in its *trans* configuration with the pyridyl rings oriented perpendicular to the anthracene moiety ( $\angle 87.2^\circ$ ; Figure 2-3).

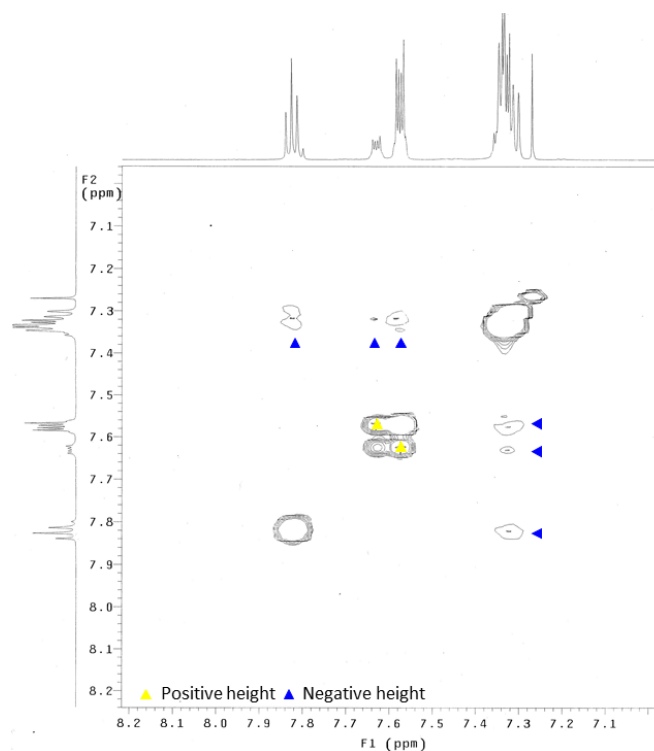


**Figure 2-1.** H,H-EXSY NMR spectrum (aromatic region,  $\text{CDCl}_3$ , 25 °C, mixing time: 0.6 s) of 9,10-bis(6-methylpyrid-2-yl)anthracene (**2**); cross-peaks labeled yellow are due to exchange, those labeled blue are due to NOEs.

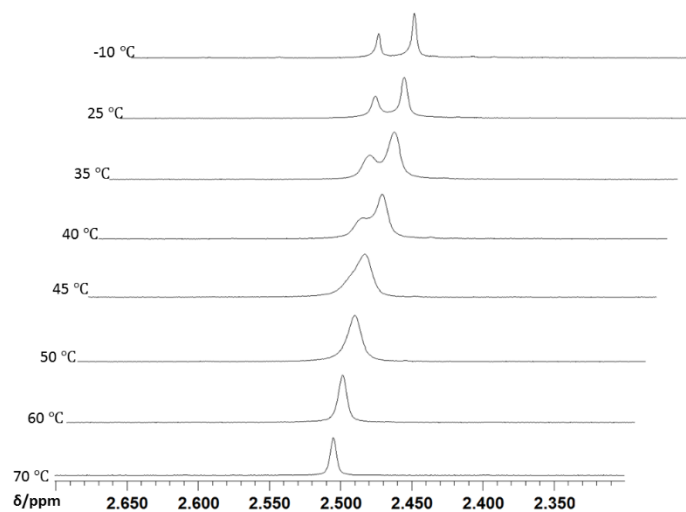


**Figure 2-2.** VT  $^1\text{H}$  NMR spectra of **2** (N-Me region,  $\text{d}_8$ -toluene, 599.7 MHz); only one N-Me signal is observed in  $\text{CDCl}_3$  at RT.

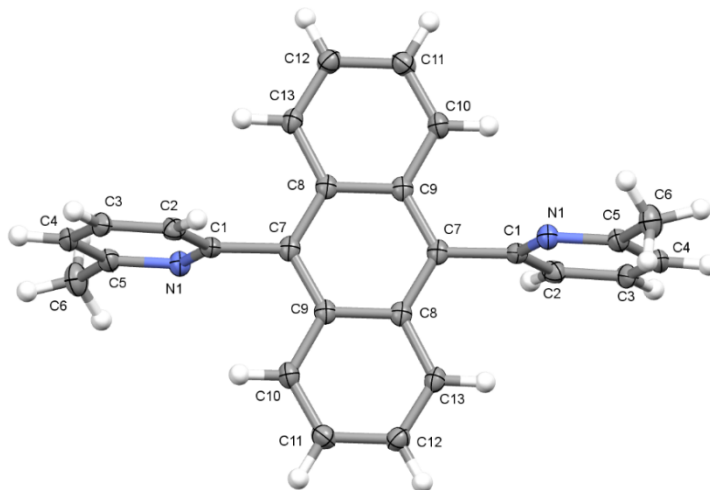


**Figure 2-3.** X-ray crystal structure plot of **2** (50% thermal ellipsoids). Selected bond distances (Å) and interplanar angles (°): C1-C7 1.4997(17), Ph<sub>An,outer</sub> // Ph<sub>An,outer</sub> 0.0, Ph<sub>An,inner</sub> // Py 87.2.

Compound **2** was then subjected to a Lewis base-directed electrophilic aromatic borylation<sup>8c, 10</sup> with BCl<sub>3</sub> and AlCl<sub>3</sub> in the presence of 2,6-di-*tert*-butylpyridine (DBP) as a sterically hindered base, resulting in annulation by concurrent formation of two new BN heterocycles (Scheme 2-1). Subsequent treatment with organozinc reagents (R<sub>2</sub>Zn, R = Ph, Et) gave the targeted BN-fused PAHs **3-Ph** (28%) and **3-Et** (38%) in moderate yields. Using similar methods, a mono-functional derivative (**4-Et**, 88%) was prepared for comparison. The products were isolated by recrystallization from CH<sub>2</sub>Cl<sub>2</sub>/hexanes and fully characterized by multinuclear NMR and high-resolution MALDI-TOF MS. Signals at 0.8 (**3-Ph**), 2.8 (**3-Et**), and 3.5 ppm (**4-Et**) in the <sup>11</sup>B NMR spectra confirm the presence of tetracoordinate boron centers. The <sup>1</sup>H NMR spectra are complex, but all the protons for **3-Ph** and **3-Et** could be assigned by H,H-COSY and NOESY 2D NMR (appendix). Importantly, for both the mono- and bifunctional derivatives, two separate sets of signals are detected for the Ph and Et substituents, but only one set for the anthracene moiety. This

suggests that the  $\text{BR}_2$  moieties do not lie within the anthracene plane and thus the overall structure is non-planar.

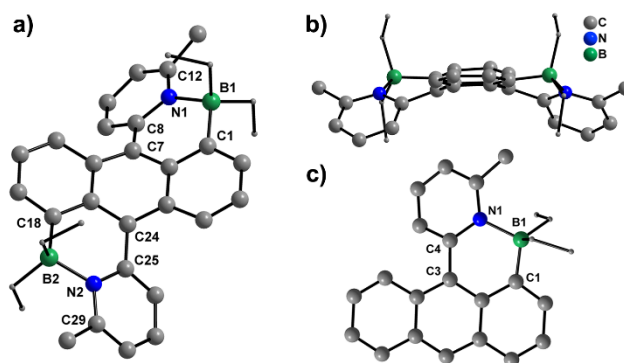


**Figure 2-4.** X-ray structure plots of a,b) **3-Et** and c) **4-Et**.

The X-ray structures of **3-Et** and **4-Et** are depicted in Figure 2-4 and they confirm the formation of contorted PAHs. The anthracene backbone of **3-Et** is strongly distorted as deduced from an inter-planar angle between the terminal benzene rings of anthracene of  $21.5^\circ$ , whereas a value of only  $4.4^\circ$  in **4-Et** indicates a more planar environment for the mono-functional system. Strain is also evident from the displacement of the boron atoms relative to the anthracene backbone; this type of distortion is more pronounced for **4-Et** than for **3-Et** as indicated by a much larger deviation of the centroid<sub>Ph</sub>-C<sub>ipso</sub>-B angle from the ideal value of  $180^\circ$  (**3-Et**:  $173.6, 174.8^\circ$ ; **4-Et**:  $167.9^\circ$ ). We conclude that steric strain results either in large tilting of the boryl moiety with respect to anthracene (dominant for **4-Et**) or a distortion of the anthracene backbone itself (dominant for **3-Et**). The steric strain is induced in part by interference of protons on anthracene with the *meta*-pyridyl protons that are in close proximity, but the incorporation of tetrahedral boron centers into the 6-membered B-N heterocycles likely also plays a role. The B-N distances ( $1.671(4)$  to  $1.685(3)$  Å) are on the longer side of typical B-N donor-acceptor bonding,<sup>11</sup> whereas the

C-C bonds that connect the anthracene to the pyridyl moieties (1.479(3) Å for **3-Et**, 1.482(3) Å for **4-Et**) are slightly shorter than that of **2** (1.500(2) Å), which may suggest enhanced  $\pi$ -delocalization.

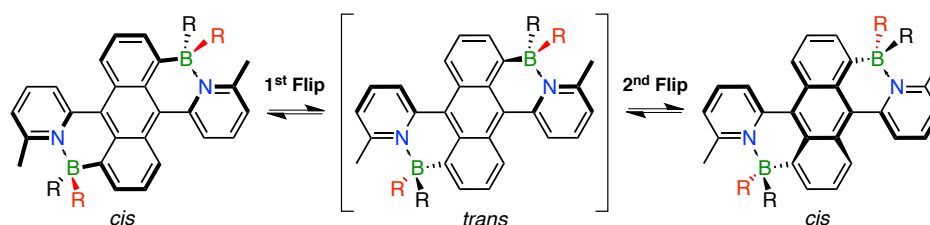


**Figure 2-5.** Proposed structural inversion of compounds **3-R** (R = Et, Ph) via a planarized *trans*-isomer as an intermediate.

Structure optimization of **3-Et**, **3-Ph**, and **4-Et** using DFT methods (rb3lyp/6-31g(d)) reproduced the distortions to the anthracene backbone in all cases very well (Table 2-5). Interestingly, when optimizing the structure of the experimentally undetected *trans*-isomer of **3-Et** (Figure 2-5) in which the pyridyl groups are oriented on opposite sides, a more planar anthracene backbone is predicted (angle of 3.2° between the outer benzene rings). However, the B-N heterocycles are highly distorted and the boron atoms strongly displaced from the anthracene backbone. The predicted B-N and B-C distances are further elongated and the endocyclic C-B-N angles more acute. This suggests that the B-N Lewis pair interactions are further weakened and the heterocycles should open up easily as in so-called “flexible” Lewis pairs.<sup>12, 13</sup>

In the case of **3-Et**, the calculated Gibbs free energy is 19.8 kJ mol<sup>-1</sup> higher for the *trans*- than the *cis*-isomer, which corresponds to  $K_{298} = 3.4 \times 10^{-4}$ ; these values are consistent with the fact that we cannot experimentally detect the *trans*-isomer.<sup>13</sup> Nevertheless, a *trans*-

isomer is likely involved as an intermediate in the inversion of the *cis*-isomer (flip of the bent anthracene, Figure 2-5). First evidence for such a process was gathered from H,H-EXSY NMR data, which show exchange peaks between the non-equivalent exocyclic R groups (Figures 2-12 to 2-14). Furthermore, VT  $^1\text{H}$  NMR experiments reveal two distinct sets of signals of equal intensity for the  $\text{BR}_2$  groups at low temperature, which gradually merge into one set of peaks as the temperature is raised (Figures 2-15 to 2-17). From the coalescence temperatures we estimate the free energy barrier to be  $68 \pm 1 \text{ kJ mol}^{-1}$  (**3-Ph**),  $68 \pm 1 \text{ kJ mol}^{-1}$  (**3-Et**), and  $64 \pm 1 \text{ kJ mol}^{-1}$  (**4-Et**). This inversion requires a “buckling” with simultaneous change in the orientation of the pyridyl moieties (Figure 2-5). The unusually long B-N distances<sup>11a</sup> and the similarity of the energy barrier for **3-Et** and **3-Ph** to that determined for inversion of the pyridyl groups in precursor **2** (*vide supra*) suggest a mechanism that involves two successive sequences of B-N dissociation/pyridyl rotation/B-N association events.

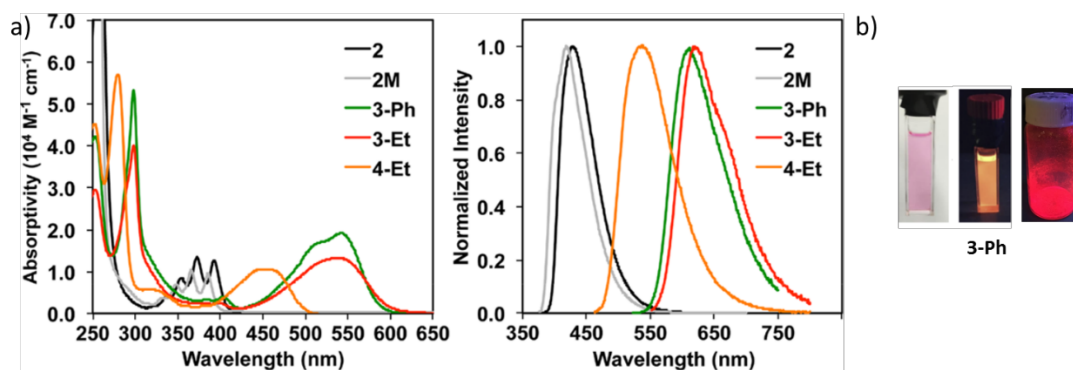


**Figure 2-6.** a) UV-Vis absorption (left) and fluorescence (right) spectra in DCM; b) Photographs of **3-Ph** in DCM solutions under daylight (left) and under UV irradiation ( $\lambda_{\text{ex}}=365 \text{ nm}$ ) (middle); solid-state fluorescence under UV irradiation ( $\lambda_{\text{ex}}=365 \text{ nm}$ ) (right).

The bis-borane complexes **3-R** (**R** = **Ph**, **Et**) are obtained as red crystalline solids that display a very bright orange-red emission in solution and red emission in solid state. A comparison of the absorption and emission spectra of **3-R** and **4-Et** with those of the respective precursors **2** and **2M** is displayed in Figure 2-6 and further details are provided in Table 2-6. **2** and **2M** show spectral features typical of 9,10-diarylanthracenes with a structured absorption and a blue-violet fluorescence. In stark contrast, formation of the BN heterocycles results in strongly red-shifted and broadened absorptions and long wavelength emissions. The bis-borane species **3-R** give rise to maximum absorptions and emissions ( $\lambda_{\text{Abs}} = 538, 542 \text{ nm}$ ;  $\lambda_{\text{Fl}} = 611, 620 \text{ nm}$ ) at far longer wavelengths than the mono-borane **4-Et** ( $\lambda_{\text{Abs}} = 453$ ;  $\lambda_{\text{Fl}} = 538 \text{ nm}$ ). According to TD-DFT calculations, the dominant absorption band of **3-R** and **4-Et** is due to a high intensity  $S_0 \rightarrow S_1$  (HOMO  $\rightarrow$  LUMO) transition with intramolecular charge transfer (ICT) character. The ICT character is likely responsible for the fact that the absorptions are broad and featureless. The quantum yield of the bis-boranes remains very high (**3-Ph**: 56%, **3-Et**: 53%), despite the dramatic decrease in the transition energy. That of the mono-borane **4-Et** (22%) is relatively lower. The bis-boranes also exhibit longer fluorescence lifetimes (**3-Ph**: 10.9 ns, **3-Et**: 11.1 ns) than the corresponding mono-functional species (**4-Et**: 4.1 ns).



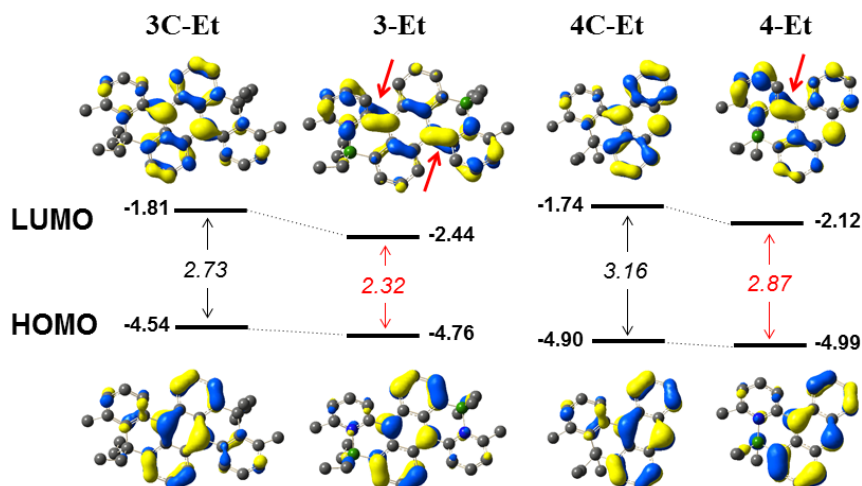


**Figure 2-7.** Calculated orbital energy levels and HOMO/LUMO orbital plots of **3-Et** and **4-Et** in comparison to their all-carbon analogs **3C-Et** and **4C-Et**. Red arrows show cross-conjugation.

**Table 2-1.** Comparison of calculated orbital energy levels (rb3lyp/6-31g(d)) for ligand precursors (orange), B-N Lewis-pairs (black), and all-carbon analogs (green)

| Compound            | LUMO (eV) | HOMO (eV) | $E_{\text{gap}}$ (eV) |
|---------------------|-----------|-----------|-----------------------|
| <b>2 (trans)</b>    | -1.57     | -5.03     | 3.46                  |
| <b>2M</b>           | -1.58     | -5.13     | 3.55                  |
| <b>3-Et (cis)</b>   | -2.44     | -4.76     | 2.32                  |
| <b>3-Et (trans)</b> | -2.47     | -4.86     | 2.39                  |
| <b>3-Ph (cis)</b>   | -2.64     | -4.93     | 2.29                  |
| <b>3C-Et (cis)</b>  | -1.81     | -4.54     | 2.73                  |
| <b>4-Et</b>         | -2.12     | -4.99     | 2.87                  |
| <b>4C-Et</b>        | -1.74     | -4.90     | 3.16                  |

DFT calculations offer further insights into the electronic structure of the BN-functionalized anthracenes. The results are compared to those of the corresponding all-carbon analogs **3C-Et**<sup>14</sup> and **4C-Et** in Figure 2-7 and Table 2-1 (see also Table 2-7). The HOMO orbital is in all cases localized primarily on the anthracene moiety and only a slight decrease in energy is observed as the carbon atoms are replaced with the B-N units.

However, dramatic differences are apparent for the LUMO orbitals. They are localized on anthracene for **3C-Et** and **4C-Et**, but extensively delocalized into the pyridyl groups for the BN-substituted compounds **3-Et** and **4-Et**. The ensuing “quinoid”-like cross-conjugation leads to much lower LUMO energy levels. As a consequence, the HOMO-LUMO gaps decrease by 0.41 eV upon BN-substitution of the bifunctional and by 0.29 eV upon BN-substitution of the mono-functional system. Replacement of Et with Ph groups in **3-Ph** lowers both the HOMO and LUMO to a similar extent, leading to a small further decrease in the energy gap. Calculations on isomer 9,10-di(pyrid-4-yl)anthracene and the respective acyclic borane complexes (Table 2-8) confirm that the observed effects are not only due to electronic substituent effects, but the result of distortions to the anthracene backbone and a more coplanar orientation of the pyridyl groups in **3-R**.

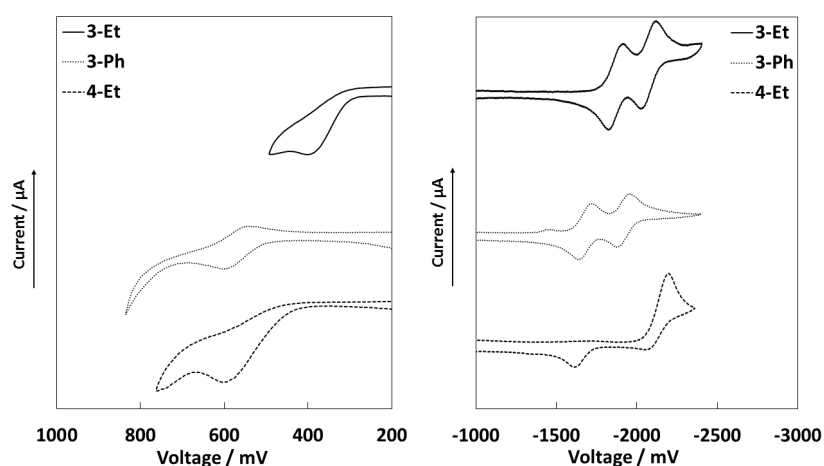


**Figure 2-8.** Cyclic voltammetry (CV) data for the oxidation (0.1M Bu<sub>4</sub>N[PF<sub>6</sub>] in DCM) and reduction (0.1M Bu<sub>4</sub>N[PF<sub>6</sub>] in THF) of BN-functionalized anthracenes (vs Fc<sup>+0</sup>,  $\nu = 100 \text{ mV s}^{-1}$ ).

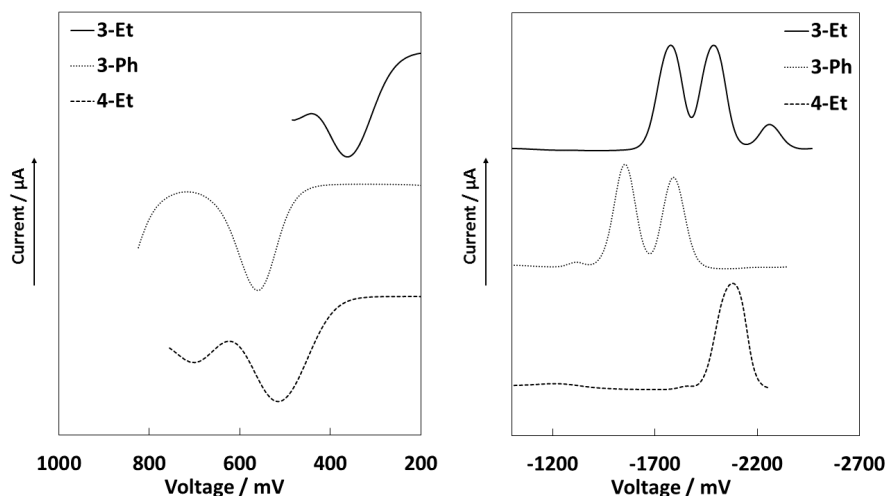


**Figure 2-9.** Square wave voltammetry (SWV) data for the oxidation (0.1M Bu<sub>4</sub>N[PF<sub>6</sub>] in DCM) and reduction (0.1M Bu<sub>4</sub>N[PF<sub>6</sub>] in THF) of BN-functionalized anthracenes (vs Fc<sup>+/0</sup>).

**Table 2-2.** Summary of electrochemical data of BN-functionalized anthracenes and comparison with data from DFT calculations

| Compound    | $E_{\text{red}}$                           | $E_{\text{red}}$<br>(SWV) | $E_{\text{ox}}$   | $E_{\text{ox}}$<br>(SWV) | LUMO <sup>a</sup><br>[eV] | LUMO <sup>b</sup><br>[eV] | HOMO <sup>a</sup><br>[eV] | HOMO <sup>b</sup><br>[eV] |
|-------------|--|---------------------------|-------------------|--------------------------|---------------------------|---------------------------|---------------------------|---------------------------|
| <b>3-Et</b> | -1.87 <sup>c</sup> ,<br>-2.07 <sup>c</sup> | -1.78,<br>-1.99           | 0.40 <sup>d</sup> | 0.36                     | -2.93                     | -2.44                     | -5.20                     | -4.76                     |
| <b>3-Ph</b> | -1.68 <sup>c</sup> ,<br>-1.92 <sup>c</sup> | -1.55,<br>-1.79           | 0.57 <sup>c</sup> | 0.56                     | -3.12                     | -2.64                     | -5.37                     | -4.93                     |
| <b>4-Et</b> | -2.20 <sup>d</sup>                         | -2.08                     | 0.61 <sup>d</sup> | 0.52                     | -2.60                     | -2.12                     | -5.41                     | -4.99                     |

[a] Determined from CV data using the equation  $E_{\text{LUMO}} = -(4.8 + E_{\text{red},1/2})$  and  $E_{\text{HOMO}} = -(4.8 + E_{\text{ox}})$ ; [b] from DFT calculations at rb3lyp/6-31g(d) level of theory; [c] quasi-reversible or reversible ( $E_{\text{red}}$  or  $E_{\text{ox}} = 0.5 (E_{\text{pc}} + E_{\text{pa}})$ ); [d] Irreversible ( $E_{\text{ox}} = E_{\text{pa}}$ ;  $E_{\text{red}} = E_{\text{pc}}$ ).

Lowering of the LUMO upon BN functionalization also translates into an enhanced electron acceptor character as further verified by electrochemical methods. The bis-boranes undergo two consecutive reversible reduction processes (Table 2-2) and, in good agreement with our DFT results, the first occurs more readily for **3-Ph** ( $E_{\text{red}} = -1.68$  V) than for **3-Et** ( $E_{\text{red}} = -1.87$  V). For the mono-borane **4-Et**, only one irreversible reduction is observed, suggesting that the unsymmetrical compound is not stable at the much more negative

potential for reduction or that it is deposited on the electrode. The reduction potential ( $E_{pc} = -2.20$  V) is more cathodic for **4-Et** as expected if the LUMO level is successively lowered upon introduction of each BN moiety. Only **3-Ph** ( $E_{ox} = 0.57$  V) undergoes a reversible oxidation, whereas **3-Et** and **4-Et** show irreversible processes at  $E_{pa} = 0.40$  and  $0.61$  V vs.  $Fc^{+/0}$  (Figure 2-8 and Figure 2-9). Cyclic voltammetry data at different scan rates ( $100\text{ mV s}^{-1}$ ,  $250\text{ mV s}^{-1}$  and  $500\text{ mV s}^{-1}$ ) show similar features.

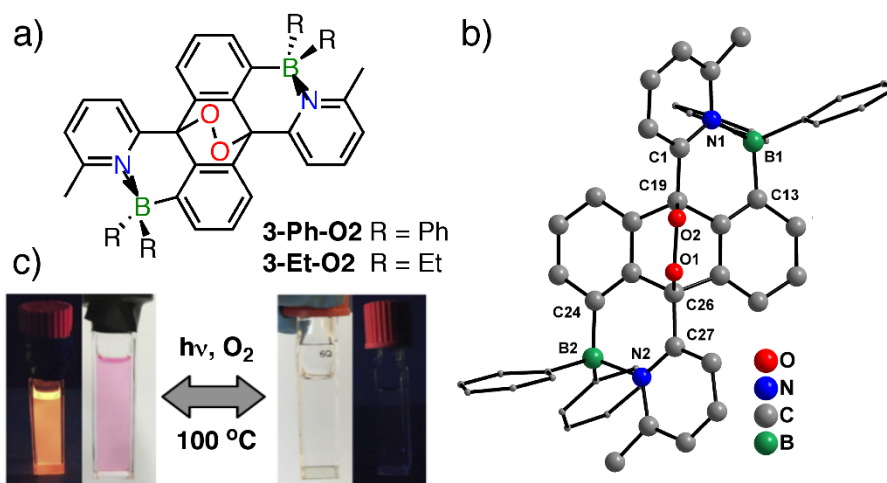


**Figure 2-10.** a) Endoperoxides **3-R-O2**; b) X-ray crystal structure of **3-Ph-O2**; c) absorption and emission color changes upon uptake and release of  $O_2$ .

We further discovered that the intensely red colored BN-functionalized anthracenes **3-R** rapidly react with  $O_2$  in the presence of light to form the respective colorless endoperoxides **3-R-O2** (EPOs, Figure 2-10a). An X-ray structure analysis of **3-Ph-O2** confirms the presence of a peroxo bridge and the ensuing change in geometry of the anthracene backbone, which releases the steric strain inherent to complexes **3-R** (Figure 2-10b). The latter is evident from  $\text{Cent}_{An}\text{-C-B}$  angles that are much closer to  $180^\circ$ , whereas the B-N distances remain in a similar range as those of the oxygen-free species. Remarkably, this

EPO formation occurs in the absence of a photosensitizer typically required to promote singlet  $O_2$  generation for typical diarylanthracenes, suggesting self-sensitizing properties of the boranes (Figure 2-11a).<sup>2a</sup> We hypothesize that the high reactivity of **3-R** toward  $O_2$  is a result of the strong absorption of visible light, the small singlet-triplet gaps (Figure 2-11b and Table 2-3) relative to other diarylanthracenes,<sup>15</sup> and the release of steric strain upon peroxide formation. While the B-N distances in the triplet  $T_1$  state are similar to those in the ground state, the anthracene backbone is even more severely distorted (Table 2-11) and the spin density on the 9,10-carbons is high (Figure 2-11). The photooxidation is reversible as the EPOs revert back to the parent acenes upon heating in toluene. This process can be monitored by naked eye based on the reappearance of the characteristic red color of compounds **3-R** (Figure 2-10c).

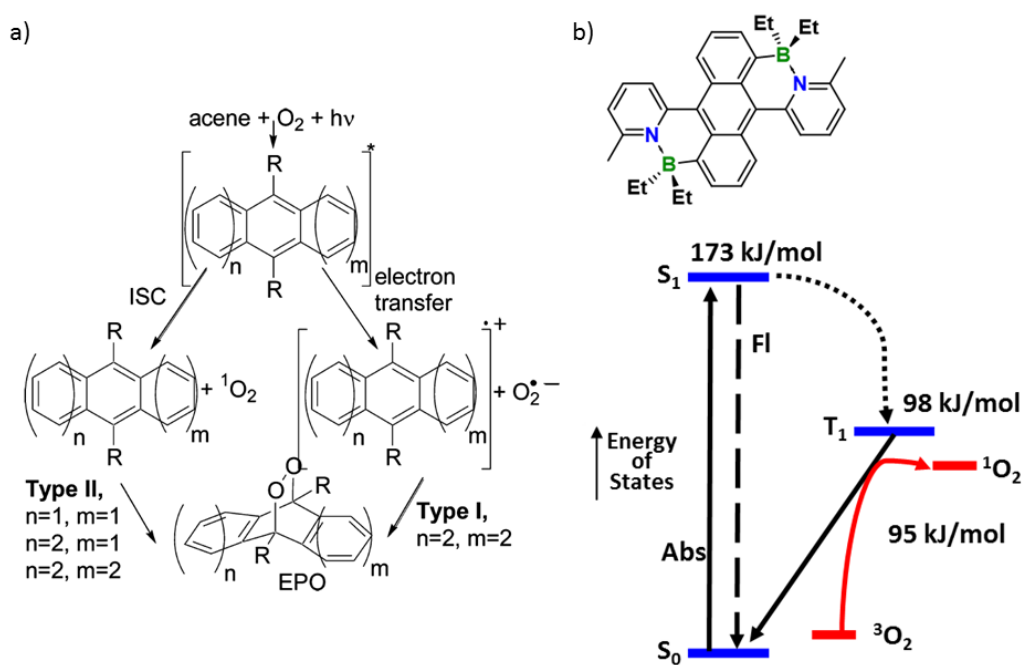


**Figure 2-11.** a) Formation of EPOs from oligoacenes by type I and type II mechanisms [Adapted with permission from reference 16. Copyright © 2012, American Chemical Society]; b) The energy for the ground singlet and triplet states of **3-Et**

**Table 2-3.** Summary of the calculated singlet and triplet energies of **3-Et**, **3-Ph** and **4-Et**

|             | $S_0$ <sup>[a]</sup> | $T_1$ <sup>[a]</sup> | $S_1$ <sup>[b]</sup> | $\Delta E_{ad}(S_0-T_1)$     | $\Delta E_{ad}(S_0-S_1)$     | $\Delta E_{ad}(S_1-T_1)$     |
|-------------|----------------------|----------------------|----------------------|------------------------------|------------------------------|------------------------------|
|             | (Hartree)            | (Hartree)            | (Hartree)            | (eV / kJ mol <sup>-1</sup> ) | (eV / kJ mol <sup>-1</sup> ) | (eV / kJ mol <sup>-1</sup> ) |
| <b>3-Et</b> | -1477.791            | -1477.753            | -1477.725            | 1.016 / 98.1                 | 1.793 / 173.0                | 0.777 / 75.0                 |
| <b>3-Ph</b> | -2087.506            | -2087.471            | -2087.441            | 0.946 / 91.2                 | 1.750 / 168.8                | 0.804 / 77.6                 |
| <b>4-Et</b> | -1008.663            | -1008.611            | -1008.581            | 1.407 / 135.8                | 2.246 / 216.7                | 0.839 / 81.0                 |

[a]  $S_0$  optimized with rb3lyp/6-31g(d),  $T_1$  optimized with ub3lyp/6-31g(d). [b] From TD-DFT optimization of  $S_1$  state with rb3lyp/6-31g(d).

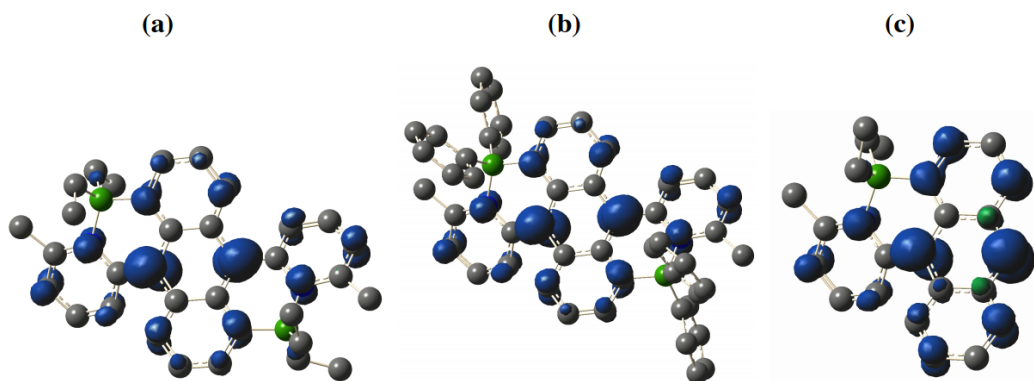


**Figure 2-11.** Illustration of spin densities in the  $T_1$  state for (a) **3-Et**, (b) **3-Ph**, and (c) **4-Et**.

## 2.3 Experimental

**Materials and General Methods.** All reactions were carried out under an atmosphere of pre-purified nitrogen using either Schlenk techniques or an inert-atmosphere glovebox. THF was distilled from Na/benzophenone prior to use. Dimethylformamide (DMF) was distilled from  $\text{CaH}_2$  and degassed via several freeze-pump-thaw cycles. Hydrocarbon and chlorinated solvents were purified using a solvent purification system (alumina/copper columns for hydrocarbon solvents), and the chlorinated solvents were subsequently distilled from  $\text{CaH}_2$  and degassed via several freeze-pump-thaw cycles. All chemicals were

purchased from commercial sources and directly used without further purification unless noted otherwise.

NMR data were acquired at ambient temperature unless noted otherwise. 499.9 MHz  $^1\text{H}$  and 160.4 MHz  $^{11}\text{B}$  NMR data were recorded on a 500 MHz Bruker AVANCE spectrometer; 500.2 MHz  $^1\text{H}$  and 125.8 MHz  $^{13}\text{C}$  NMR data were recorded on a 500 MHz Bruker Auto AVANCE spectrometer; 599.7 MHz  $^1\text{H}$ , 150.8 MHz  $^{13}\text{C}$  and 192.4 MHz  $^{11}\text{B}$  NMR data were recorded on a Varian INOVA 600 spectrometer.  $^{11}\text{B}$  NMR spectra were acquired with boron-free quartz NMR tubes either on the Varian INOVA 600 with a boron-free 5 mm dual broadband gradient probe (Nalorac, Varian Inc., Martinez, CA) or the 500 MHz Bruker Auto Avance with a 5mm PH SEX 500S1 11B-H/F-D probe.  $^1\text{H}$  and  $^{13}\text{C}$  NMR spectra were referenced internally to solvent signals ( $\text{CDCl}_3$ : 7.27 ppm for  $^1\text{H}$  NMR, 77.23 ppm for  $^{13}\text{C}$  NMR; d8-toluene: 2.08 ppm for  $^1\text{H}$  NMR) and all other NMR spectra externally to  $\text{SiMe}_4$  (0 ppm). Abbreviations used for signal assignments: An = anthracene, Ph = phenyl, Py = pyridyl, Me = methyl, s = singlet, d = doublet, t = triplet, q = quartet, td = triplet of doublets, dq = doublet of quartets, m = multiplet, br = broad.

MALDI-TOF MS measurements were performed on a Bruker Ultraflextreme in reflectron mode with delayed extraction. Anthracene (10 mg/mL) was used as the matrix for the MALDI-TOF MS analyses and mixed with the samples (10 mg/mL in DCM) in a 1:1 ratio, and then spotted on the wells of a target plate. Red phosphorus was used for calibration.

UV-visible absorption data were acquired on a Varian Cary 5000 UV-Vis/NIR spectrophotometer. The fluorescence data and lifetimes were measured using a Horiba Fluorolog-3 spectrofluorometer equipped with a 349, 388 or 450 nm nanoLED and a FluoroHub R-928 detector. Absolute quantum yields ( $\Phi_F$ ) were measured on the HORIBA

Fluorolog-3 using a pre-calibrated Quanta- $\phi$  integrating sphere. Light from the sample compartment is directed into the sphere via a fiber-optic cable and an F-3000 Fiber-Optic Adapter, and then returned to the sample compartment (and to the emission monochromator) via a second fiber-optic cable and an F-3000 Fiber-Optic Adapter.

Cyclic voltammetry (CV) and square wave voltammetry (SWV) experiments were carried out on a CV-50W analyzer from BASi. The three-electrode system consisted of an Au disk as working electrode, a Pt wire as counter electrode and an Ag wire as the pseudo-reference electrode. The voltammograms were recorded with ca.  $10^{-3}$  to  $10^{-4}$  M solutions in THF (reduction scans) or DCM (oxidation scans) containing  $\text{Bu}_4\text{N}[\text{PF}_6]$  (0.1 M) as the supporting electrolyte. The scans were referenced after the addition of a small amount of ferrocene as internal standard. The potentials are reported relative to the ferrocene/ferrocenium couple.

DFT calculations were performed with the Gaussian09 suite of programs.<sup>17</sup> The input files were generated from single crystal structures when available or otherwise generated in Chem3D and pre-optimized in Spartan '08 V 1.2.0. Ground and first triplet excited state geometries were then optimized in Gaussian09 using the hybrid density functional rb3lyp with a 6-31g(d) basis set. Frequency calculations were performed to confirm the presence of local minima (only positive frequencies). Vertical excitations were calculated by TD-DFT methods at the rcam-b3lyp/6-31g(d) level. The first singlet excited state geometry was also optimized by TD-DFT methods.

Single crystals of **2** suitable for X-ray analysis were grown by slow evaporation of a solution in  $\text{CH}_2\text{Cl}_2$ /toluene, single crystals of **3-Et** by slow evaporation of a solution in toluene/decane, single crystals of **4-Et** from  $\text{CH}_2\text{Cl}_2$ /hexanes mixture at  $-20^\circ\text{C}$ , and single



crystals of **3-Ph-O2** by slow evaporation of a solution in CH<sub>2</sub>Cl<sub>2</sub>/hexanes. X-ray diffraction intensities on **2**, **3-Et**, **4-Et**, and **3-Ph-O2** were collected on a Bruker SMART APEX II CCD Diffractometer using CuK $\alpha$  (1.54178 Å) radiation at 100(2) K. The structures were refined by full-matrix least squares based on *F*<sup>2</sup> with all reflections (SHELXTL V5.10; G. Sheldrick, Siemens XRD, Madison, WI).<sup>18</sup> Non-hydrogen atoms were refined with anisotropic displacement coefficients, and hydrogen atoms were treated as idealized contribution. SADABS (Sheldrick, 12 G.M. SADABS (2.01), Bruker/Siemens Area Detector Absorption Correction Program; Bruker AXS: Madison, WI, 1998) absorption correction was applied.<sup>19</sup> Crystallographic data for the structure of **2**, **3-Et**, **4-Et**, and **3-Ph-O2** have been deposited with the Cambridge Crystallographic Data Center as supplementary publications CCDC-1573498-1573501. Copies of the data can be obtained free of charge on application to CCDC, 12 Union Road, Cambridge CB2 1EZ, UK (fax: (+44) 1223-336-033; email: [deposit@ccdc.cam.ac.uk](mailto:deposit@ccdc.cam.ac.uk)).

**Synthesis of 9,10-bis(pinacolboryl)anthracene (1)<sup>20a</sup>:** In a glovebox, 9,10-dibromoanthracene (5.40 g, 16.1 mmol) and bis(pinacolato)diboron (9.80 g, 38.6 mmol, 2.4 equiv) were dissolved in DMF, followed by the addition of palladium acetate (0.22 g, 0.97 mmol, 6 mol%) and potassium acetate (9.48 g, 96.6 mmol, 6 equiv). The reaction mixture was then stirred at 80 °C overnight under nitrogen atmosphere. After that, the mixture was cooled to room temperature and poured into water with stirring. The mixture was extracted with DCM. The organic layer was washed with brine and dried over anhydrous sodium sulfate. After rotary evaporation the residue was recrystallized from ethanol to give the product as yellow crystals in a yield of 85 %. <sup>1</sup>H NMR (500.2 MHz, CDCl<sub>3</sub>, 25 °C):  $\delta$  (ppm) = 8.35 (m, 4H; An), 7.46 (m, 4H; An), 1.59 (s, 24H; Me). The

NMR data are consistent with those reported in the literature.<sup>20a</sup>

**Synthesis of 9,10-bis(6-methylpyrid-2-yl)anthracene (2):** The compound was prepared in analogy to a procedure for 9,10-bis(pyrid-2-yl)anthracene<sup>20d</sup>. In a glovebox, 9,10-bis(pinacolboryl)anthracene (**1**) (2.00 g, 4.65 mmol) and 2-bromo-6-methylpyridine (1.20 mL, 10.2 mmol, 2.2 equiv) were dissolved in toluene, followed by the addition of tetrakis(triphenylphosphine)palladium(0) (0.538 g, 0.465 mmol, 10 mol%) and cesium carbonate (9.10 g, 27.9 mmol, 6 equiv). The reaction mixture was stirred at 100 °C for 2 days under nitrogen atmosphere, allowed to cool to room temperature, and then poured into water with stirring. The mixture was extracted with DCM, the organic layer was washed with brine and dried over anhydrous sodium sulfate. After rotary evaporation the crude product was dissolved in a minimum amount of DCM and carefully layered with toluene (v/v = 1:1) at room temperature. Solvent diffusion and slow partial evaporation of the solvent resulted in light yellow crystals (1.05 g, 62.7%). <sup>1</sup>H NMR (500.2 MHz, CDCl<sub>3</sub>, 25 °C) for major isomer (77%): δ (ppm) = 7.83 (t, J = 7.5 Hz, 2H; Py), 7.57 (m, 4H; An), 7.36-7.30 (overlapped, 8H; An, Py), 2.73 (s, 6H; Me); minor isomer (23%): δ (ppm) = 7.81 (t, J = 7.0 Hz, 2H; Py), 7.63 (m, 4H; An), 7.36-7.30 (overlapped, 8H; An, Py), 2.73 (s, 6H; Me). <sup>13</sup>C NMR (125.8 MHz, CDCl<sub>3</sub>, 25 °C) for major isomer: δ (ppm) = 158.9, 158.0, 136.7, 136.4, 130.1, 126.6, 125.5, 124.0, 122.0, 25.0. High-resolution MALDI-TOF mass spectrum (pos. mode, neat): m/z = 360.1597 ([M]<sup>+</sup>, 100 %, calcd for <sup>12</sup>C<sub>26</sub><sup>1</sup>H<sub>20</sub><sup>14</sup>N<sub>2</sub> 360.1621).

**Synthesis of Bis-Borane Complex 3-Ph:** In a glovebox, BCl<sub>3</sub> (6.7 mL, 1M solution in hexane, 6.7 mmol, 4 equiv) was added to a bright yellow solution of **2** (0.60 g, 1.66 mmol) in DCM. The solution instantly changed color to orange red. 2,6-Di-*tert*-butylpyridine (0.64 g, 3.33 mmol, 2 equiv) and AlCl<sub>3</sub> (0.67 g, 4.99 mmol, 3 equiv) were added to the

reaction mixture. After stirring for 16 hours, an additional portion of  $\text{AlCl}_3$  (0.22 g, 1.66 mmol, 1 equiv) was added and the mixture was stirred for a further 16 hours whereupon it turned dark green. Addition of  $\text{Bu}_4\text{NCl}$  (0.92 g, 3.33 mmol, 2 equiv) resulted in a dark purple suspension to which  $\text{ZnPh}_2$  (1.50 g, 6.82 mmol, 4.1 equiv) was added as a solution. The reaction mixture was stirred for 16 hours at room temperature after which the solvent was removed under reduced pressure. The dark red residue was redissolved in toluene and insoluble components were removed by filtration through a fritted funnel. The solution was concentrated under reduced pressure. Recrystallization in dichloromethane/hexanes at  $-20\text{ }^\circ\text{C}$  gave the product as red crystals. Yield: 318 mg (28 %).  $^1\text{H}$  NMR (599.7 MHz,  $\text{CDCl}_3$ ,  $25\text{ }^\circ\text{C}$ ):  $\delta$  (ppm) = 8.19 (d,  $J = 7.8\text{ Hz}$ , 2H; Py), 7.94 (d,  $J = 8.4\text{ Hz}$ , 2H; An), 7.91 (t,  $J = 8.1\text{ Hz}$ , 2H; Py), 7.37-7.33 (overlapped, 6H; An, o- $\text{Ph}_\text{B}$ ), 7.27-7.26 (overlapped, 2H; Py), 7.23-7.17 (overlapped, 12H; An, o- $\text{Ph}_\text{A}$ , m- $\text{Ph}_\text{B}$ , p- $\text{Ph}_\text{B}$ ), 7.04 (t,  $J = 7.2\text{ Hz}$ , 4H; m- $\text{Ph}_\text{A}$ ), 6.94 (t,  $J = 7.2\text{ Hz}$ , 2H; p- $\text{Ph}_\text{A}$ ), 2.17 (s, 6H; Me).  $^{13}\text{C}$  NMR (150.8 MHz,  $\text{CDCl}_3$ ,  $25\text{ }^\circ\text{C}$ ):  $\delta$  (ppm) = 160.6, 156.9 (br), 155.3, 151.9 (br), 149.5 (br), 138.4, 134.5, 132.4, 131.2, 131.1, 129.2, 128.5, 128.2, 127.8, 127.3, 127.1, 126.4, 125.1, 125.0, 121.1, 26.6.  $^{11}\text{B}$  NMR (160.4 MHz,  $\text{CDCl}_3$ ,  $25\text{ }^\circ\text{C}$ ):  $\delta$  (ppm) = 0.8 ( $w_{1/2} = 570\text{ Hz}$ ). High-resolution MALDI-TOF mass spectrum (neg. mode, neat):  $m/z = 688.3258$  ( $[\text{M}]^-$ , 100 %, calcd for  $^{12}\text{C}_{50}^{11}\text{H}_{38}^{11}\text{B}_2^{14}\text{N}_2$  688.3231), 643.2726 ( $[\text{M}+\text{O}_2-\text{Ph}]^-$ , 16 %, calcd for  $^{12}\text{C}_{44}^{11}\text{H}_{33}^{11}\text{B}_2^{14}\text{N}_2^{16}\text{O}_2$  643.2737), 611.2870 ( $[\text{M}-\text{Ph}]^-$ , 48 %, calcd for  $^{12}\text{C}_{44}^{11}\text{H}_{33}^{11}\text{B}_2^{14}\text{N}_2$  611.2839).

**Synthesis of Bis-Borane Complex 3-Et:** In a glovebox,  $\text{BCl}_3$  (2.77 mL, 1M solution in hexane, 2.77 mmol, 4 equiv) was added to a bright yellow solution of **2** (250 mg, 0.694 mmol) in DCM. The solution instantly changed color to orange red. 2,6-Di-*tert*-butylpyridine (265 mg, 1.39 mmol, 2 equiv) and  $\text{AlCl}_3$  (278 mg, 2.08 mmol, 3 equiv) were

added to the reaction mixture. After stirring for 16 hours, an additional portion of  $\text{AlCl}_3$  (93.0 mg, 0.694 mmol, 1 equiv) was added and the mixture was stirred for a further 16 hours whereupon it turned dark green. Addition of  $\text{Bu}_4\text{NCl}$  (386 mg, 1.39 mmol, 2 equiv) resulted in a dark purple suspension to which  $\text{ZnEt}_2$  (0.30 mL, 2.8 mmol, 4.1 equiv) was added dropwise. The reaction mixture was then stirred for 16 hours at room temperature after which the solvent was removed under reduced pressure. The dark red residue was redissolved in toluene and insoluble components were removed by filtration through a fritted funnel. The solution was concentrated under reduced pressure. Recrystallization in dichloromethane/hexanes at  $-20\text{ }^\circ\text{C}$  gave the product as red crystals. Yield: 130 mg (38 %).

$^1\text{H}$  NMR (599.7 MHz,  $\text{CDCl}_3$ ,  $25\text{ }^\circ\text{C}$ ):  $\delta$  (ppm) = 8.03 (d,  $J$  = 7.8 Hz, 2H; Py), 7.87 (d,  $J$  = 8.4 Hz, 2H; An), 7.79 (t,  $J$  = 8.4 Hz, 2H; Py), 7.62 (d,  $J$  = 6.6 Hz, 2H; An), 7.45 (t,  $J$  = 7.5 Hz, 2H; An), 7.32 (dd,  $J$  = 7.2 Hz,  $J$  = 1.2 Hz, 2H; Py), 3.13 (s, 6H; Me), 1.25 (m, 2H; Et), 1.16 (m, 2H; Et), 0.91 (m, 2H; Et), 0.56 (m, 2H; Et), 0.39 (t,  $J$  = 7.8 Hz, 6H; Et), 0.32 (t,  $J$  = 7.8 Hz, 6H; Et).  $^{13}\text{C}$  NMR (150.8 MHz,  $\text{CDCl}_3$ ,  $25\text{ }^\circ\text{C}$ ):  $\delta$  (ppm) = 159.2, 156.3, 152.9 (br), 137.3, 133.4, 129.5, 128.7, 128.5, 127.4, 127.2, 125.7, 120.2, 24.5, 21.3 (br), 17.5 (br), 10.7, 10.2.  $^{11}\text{B}$  NMR (160.4 MHz,  $\text{CDCl}_3$ ,  $25\text{ }^\circ\text{C}$ ):  $\delta$  (ppm) = 2.8 ( $w_{1/2}$  = 400 Hz). High-resolution MALDI-TOF mass spectrum (neg. mode, neat):  $m/z$  = 467.2836 ( $[\text{M-Et}]^-$ , 100 %, calcd for  $^{12}\text{C}_{32}^{11}\text{H}_{33}^{11}\text{B}_2^{14}\text{N}_2$  467.2835).

**Synthesis of Endoperoxide 3-Ph-O2:** **3-Ph** (30 mg, 0.044 mmol) was dissolved in DCM (10 mL) in a vial that was capped with a rubber septum. A needle was stitched through the septum and connected with an air balloon. The solution was irradiated at room temperature with sunlight for one day. The solution was then concentrated under reduced pressure. Recrystallization in dichloromethane/hexanes gave the product as light pink crystals. Yield:

23 mg (74 %).  $^1\text{H}$  NMR (599.7 MHz,  $\text{CDCl}_3$ , 25 °C):  $\delta$  (ppm) = 8.31 (dd,  $J$  = 7.8 Hz,  $J$  = 1.2 Hz, 2H; Py), 8.11 (t,  $J$  = 7.8 Hz, 2H; Py), 7.49 (overlapped, 6H; Py, o-Ph<sub>B</sub>), 7.27 (overlapped, 4H; o-Ph<sub>A</sub>), 7.22 (t,  $J$  = 7.2 Hz, 4H; m-Ph<sub>B</sub>), 7.11 (overlapped, na; An, m-Ph<sub>A</sub>, p-Ph<sub>B</sub>), 7.00 (t,  $J$  = 7.2 Hz, 2H; p-Ph<sub>A</sub>), 6.91 (t,  $J$  = 7.2 Hz, 2H; An), 6.46 (dd,  $J$  = 7.2 Hz,  $J$  = 0.6 Hz, 2H; An), 2.36 (s, 6H; Me).  $^{13}\text{C}$  NMR (150.8 MHz,  $\text{CDCl}_3$ , 25 °C):  $\delta$  (ppm) = 161.2, 153.1 (br), 151.8, 151.1 (br), 148.0 (br), 139.9, 138.0, 133.6, 132.4, 131.8, 131.6, 130.9, 128.5, 127.6, 127.5, 127.0, 125.1, 125.0, 118.7, 83.6, 27.0.  $^{11}\text{B}$  NMR (192.4 MHz,  $\text{CDCl}_3$ , 25 °C):  $\delta$  (ppm) = 0.9 ( $w_{1/2}$  = 650 Hz). High-resolution MALDI-TOF mass spectrum (neg. mode, neat):  $m/z$  = 643.2721 ( $[\text{M-Ph}]^-$ , 100 %, calcd for  $^{12}\text{C}_{44}^{1}\text{H}_{33}^{11}\text{B}_2^{14}\text{N}_2^{16}\text{O}_2$  643.2737).

**Synthesis of Endoperoxide 3-Et-O2:** In a glovebox,  $\text{BCl}_3$  (2.77 mL, 1M solution in hexane, 2.77 mmol, 4 equiv) was added to a bright yellow solution of **2** (250 mg, 0.694 mmol) in DCM. The solution instantly changed color to orange red. 2,6-Di-*tert*-butylpyridine (265 mg, 1.39 mmol, 2 equiv) and  $\text{AlCl}_3$  (278 mg, 2.08 mmol, 3 equiv) were added to the reaction mixture. After stirring for 16 hours, an additional portion of  $\text{AlCl}_3$  (93.0 mg, 0.694 mmol, 1 equiv) was added and the mixture was stirred for a further 16 hours whereupon it turned dark green. Addition of  $\text{Bu}_4\text{NCl}$  (386 mg, 1.387 mmol, 2 equiv) resulted in a dark purple suspension to which  $\text{ZnEt}_2$  (0.30 mL, 2.8 mmol, 4.1 equiv) was added dropwise. The reaction mixture was then stirred for 16 hours at room temperature after which the solvent was removed under reduced pressure. The dark red residue was redissolved in toluene and insoluble components were removed by filtration through a fritted funnel. The solution was concentrated under reduced pressure. The residue was redissolved in a minimum amount of DCM in the air and carefully layered with hexanes

(v/v = 1:1) at room temperature. Solvent diffusion and slow partial evaporation of the solvent resulted in white crystals. Yield: 260 mg (71 %).  $^1\text{H}$  NMR (500.2 MHz,  $\text{CDCl}_3$ , 25 °C):  $\delta$  (ppm) = 8.16 (dd,  $J$  = 8.0 Hz,  $J$  = 1.0 Hz, 2H; Py), 8.01 (t,  $J$  = 7.8 Hz, 2H; Py), 7.57 (dd,  $J$  = 8.0 Hz,  $J$  = 1.3 Hz, 2H; Py), 7.30 (d,  $J$  = 7.5 Hz, 2H; An), 7.06 (t,  $J$  = 7.5 Hz, 2H; An), 6.30 (dd,  $J$  = 7.3 Hz,  $J$  = 0.8 Hz, 2H; An), 3.18 (s, 6H; Me), 1.13 (m, 4H; Et), 0.85 (dq,  $^2J$  = 15 Hz,  $^3J$  = 7.8 Hz, 2H; Et), 0.65 (dq,  $^2J$  = 14.5 Hz,  $^3J$  = 7.5 Hz, 2H; Et), 0.35 (t,  $J$  = 7.8 Hz, 6H; Et), 0.22 (t,  $J$  = 7.8 Hz, 6H; Et).  $^{13}\text{C}$  NMR (150.8 MHz,  $\text{CDCl}_3$ , 25 °C):  $\delta$  (ppm) = 159.6, 153.0, 150.0 (br), 138.8, 138.7, 134.6, 130.0, 129.6, 128.3, 126.2, 118.4, 83.7, 24.8, 19.6 (br), 18.4 (br), 10.7, 10.2.  $^{11}\text{B}$  NMR (192.4 MHz,  $\text{CDCl}_3$ , 25 °C):  $\delta$  (ppm) = 4.1 ( $w_{1/2}$  = 510 Hz). High-resolution MALDI-TOF mass spectrum (neg. mode, neat):  $m/z$  = 499.2779 ( $[\text{M-Et}]^-$ , 100 %, calcd for  $^{12}\text{C}_{32}^{1}\text{H}_{33}^{11}\text{B}_2^{14}\text{N}_2^{16}\text{O}_2$  499.2733).

**Synthesis of 9-(pinacolboryl)anthracene (1M)<sup>21</sup>:** In a glovebox, 9-bromoanthracene (25.0 g, 97.2 mmol) and bis(pinacolato)diboron (29.6 g, 117 mmol, 1.2 equiv) were dissolved in DMF, followed by the addition of palladium acetate (0.655 g, 2.92 mmol, 3 mol%) and potassium acetate (28.6 g, 292 mmol, 3 equiv). The reaction mixture was then stirred at 80 °C for 2 days under nitrogen atmosphere. After that, the mixture was cooled to room temperature and poured into water with stirring. The mixture was extracted with DCM, the organic layer was washed with brine and dried over anhydrous sodium sulfate. After rotary evaporation the crude product was purified by column chromatography (silica gel) with hexanes/ dichloromethane (v/v = 3:2) as eluent and then concentrated on a rotary evaporator. The residue was dissolved in a minimum amount of DCM and carefully layered with ethanol (v/v = 1:1) and the solution was left in a -20 °C freezer. A small amount of insoluble byproducts was separated by filtration. The volatile components were then

removed under high vacuum to give the product as a light yellow solid (28.2 g, 95% yield). The product was used in the next step without further purification. <sup>1</sup>H NMR (499.9 MHz, CDCl<sub>3</sub>, 25 °C): δ (ppm) = 8.49 (s, 1H, An), 8.46 (d, J = 8.0 Hz, 2H, An), 8.00 (d, J = 8.5 Hz, 2H, An), 7.51-7.44 (m, 4H, An), 1.59 (s, 12H, Me). The NMR data are consistent with those reported in the literature.<sup>21</sup>

**Synthesis of 9-(6-methylpyrid-2-yl)anthracene (2M):** The compound was prepared in analogy to a procedure for 9-(pyrid-2-yl)anthracene<sup>20d</sup>. In a glovebox, 9-(pinacolboranyl)anthracene (**1M**) (2.30 g, 7.56 mmol) and 2-bromo-6-methylpyridine (0.98 mL, 8.32 mmol, 1.1 equiv) were dissolved in toluene, followed by the addition of tetrakis(triphenylphosphine)palladium(0) (0.437 g, 0.378 mmol, 5 mol%) and cesium carbonate (7.39 g, 22.7 mmol, 3 equiv). The reaction mixture was then stirred at 100 °C for 2 days under nitrogen atmosphere, allowed to cool to room temperature, and then poured into water with stirring. The mixture was extracted with DCM, the organic layer was washed with brine and dried over anhydrous sodium sulfate. After rotary evaporation the crude product was purified by column chromatography (silica gel) with hexanes/triethylamine (v/v = 10:1) as eluent. The crude product was dissolved in a minimum amount of DCM and carefully layered with toluene (v/v = 1:1) at room temperature. Solvent diffusion and slow partial evaporation of the solvent resulted in yellow crystals (1.38 g, 68% yield). <sup>1</sup>H NMR (499.9 MHz, CDCl<sub>3</sub>, 25 °C): δ (ppm) = 8.53 (s, 1H, An), 8.05 (d, J = 8.5 Hz, 2H, An), 7.82 (t, J = 7.5 Hz, 1H, Py), 7.59 (d, J = 9.0 Hz, 2H, An), 7.46 (t, J = 7.3 Hz, 2H, An), 7.37 (t, J = 7.8 Hz, 2H, An), 7.33 (d, J = 7.5 Hz, 2H, Py), 2.72 (s, 3H, Me). <sup>13</sup>C NMR (150.8 MHz, CDCl<sub>3</sub>, 25 °C): δ (ppm) = 158.9, 157.8, 136.7, 135.6, 131.7, 130.3, 128.6, 127.6, 126.4, 125.9, 125.3, 123.9, 122.0, 25.0. High-resolution

MALDI-TOF mass spectrum (pos. mode, anthracene):  $m/z = 269.1142$  ( $[M]^+$ , 100 %, calcd for  $^{12}\text{C}_{20}^{1}\text{H}_{15}^{14}\text{N}_1$  269.1199).

**Synthesis of Mono-Borane Complex 4-Et:** In a glovebox,  $\text{BCl}_3$  (5.35 mL, 1M solution in hexane, 5.35 mmol, 2 equiv) was added to a bright yellow solution of **2M** (0.72 g, 2.673 mmol) in DCM. The solution instantly changed color to orange. 2,6-Di-*tert*-butylpyridine (0.511 g, 2.67 mmol, 1 equiv) and  $\text{AlCl}_3$  (0.535 g, 4.01 mmol, 1.5 equiv) were added to the reaction mixture. After stirring for 16 hours, an additional portion of  $\text{AlCl}_3$  (0.178 g, 1.34 mmol, 0.5 equiv) was added and the mixture was stirred for a further 16 hours whereupon it turned dark purple. Addition of  $\text{Bu}_4\text{NCl}$  (0.743 g, 2.67 mmol, 1 equiv) resulted in a dark orange suspension to which  $\text{ZnEt}_2$  (0.58 mL, 5.5 mmol, 2.05 equiv) was added dropwise. The reaction mixture was then stirred for 16 hours at room temperature after which the solvent was removed under reduced pressure. The yellow residue was redissolved in toluene and insoluble components were removed by filtration through a fritted funnel. The solution was concentrated under reduced pressure. Recrystallization in dichloromethane/hexanes at  $-20\text{ }^\circ\text{C}$  gave the product as yellow crystals that were suitable for X-ray analysis. Yield: 0.796 g (88 %).  $^1\text{H}$  NMR (599.7 MHz,  $\text{CDCl}_3$ ,  $-5\text{ }^\circ\text{C}$ ):  $\delta$  (ppm) = 8.54 (s, 1H; An), 8.20 (d,  $J = 9.0\text{ Hz}$ , 1H; An), 8.06 (d,  $J = 8.4\text{ Hz}$ , 1H; An), 7.90 (dd,  $J = 7.8\text{ Hz}$ ,  $J = 1.2\text{ Hz}$ , 1H; Py), 7.82-7.79 (overlapped, 2H; Py, An), 7.66 (dd,  $J = 6.6\text{ Hz}$ ,  $J = 1.2\text{ Hz}$ , 1H; An), 7.59 (dd,  $J = 8.1\text{ Hz}$ ,  $J = 6.9\text{ Hz}$ , 1H; An), 7.44 (td,  $^2J = 7.5\text{ Hz}$ ,  $^3J = 1.2\text{ Hz}$ , 1H; An), 7.40 (td,  $^2J = 7.5\text{ Hz}$ ,  $^3J = 1.2\text{ Hz}$ , 1H; An), 7.32 (dd,  $J = 7.5\text{ Hz}$ ,  $J = 1.5\text{ Hz}$ , 1H; Py), 3.11 (s, 3H; Me), 1.20-1.12 (m, 2H; Et), 0.84 (dq,  $^2J = 13.8\text{ Hz}$ ,  $^3J = 7.8\text{ Hz}$ , 1H; Et), 0.49 (dq,  $^2J = 13.8\text{ Hz}$ ,  $^3J = 7.8\text{ Hz}$ , 1H; Et), 0.31 (t,  $J = 7.8\text{ Hz}$ , 3H; Et), 0.25 (t,  $J = 7.8\text{ Hz}$ , 3H; Et).  $^{13}\text{C}$  NMR (150.8 MHz,  $\text{CDCl}_3$ ,  $25\text{ }^\circ\text{C}$ ):  $\delta$  (ppm) = 159.8, 156.6, 152.7 (br),



137.3, 133.4, 132.2, 130.6, 130.4, 129.9, 129.5, 128.3, 127.9, 127.2, 126.5, 125.9, 125.5, 125.3, 124.6, 123.3, 24.5, 21.4 (br), 17.1 (br), 10.6, 10.0.  $^{11}\text{B}$  NMR (160.4 MHz,  $\text{CDCl}_3$ , 25 °C):  $\delta$  (ppm) = 3.5 ( $w_{1/2}$  = 240 Hz). High-resolution MALDI-TOF mass spectrum (neg. mode, neat):  $m/z$  = 673.1566 ( $[\text{2M-H}]^-$ , 5 %, calcd for  $^{12}\text{C}_{48}^{11}\text{H}_{47}^{11}\text{B}_2^{14}\text{N}_2$  673.3935), 337.2021 ( $[\text{M}]^-$ , 100 %, calcd for  $^{12}\text{C}_{24}^{11}\text{H}_{24}^{11}\text{B}_1^{14}\text{N}_1$  337.2001).

## 2.4 Conclusions

In conclusion, we introduce a new class of BN-substituted PAHs with unique structural features and electronic properties. The formation of B-N Lewis pairs at the periphery of anthracene leads to severe distortions due to steric strain. Photophysical studies and DFT calculations reveal a dramatic effect of borane functionalization on the electronic structure, as a low lying quinoid LUMO is established, giving rise to strong low-energy emissions. These intriguing properties are promising for optoelectronic materials development, while the facile reactivity with  $\text{O}_2$  suggests potential in  $\text{O}_2$  capture/release applications and possibly the broader field of small molecule activation.<sup>22</sup>

## 2.5 References

(1) a) Bendikov, M.; Wudl, F.; Perepichka, D. F. *Chem. Rev.* **2004**, *104*, 4891; b) Anthony, J. E. *Chem. Rev.* **2006**, *106*, 5028; c) J. Wu, W. Pisula and K. Müllen, *Chem. Rev.* **2007**, *107*, 718.

(2) a) Aubry, J. M.; Pierlot, C.; Rigaudy, J.; Schmidt, R. *Acc. Chem. Res.* **2003**, *36*, 668; b) Klaper, M.; Linker, T. *J. Am. Chem. Soc.* **2015**, *137*, 13744; c) Altinok, E.; Smith, Z. C.; Thomas, S. W. *Macromolecules* **2015**, *48*, 6825; d) Filatov, M. A.; Karuthedath, S.; Polestshuk, P. M.; Savoie, H.; Flanagan, K. J.; Sy, C.; Sitte, E.; Telitchko, M.; Laquai, F.; Boyle, R. W.; Senge, M. O. *J. Am. Chem. Soc.* **2017**, *139*, 6282.

(3) a) VanVeller, B.; Schipper, D. J.; Swager, T. M. *J. Am. Chem. Soc.* **2012**, *134*, 7282; b) Sun, H.; Kabb, C. P.; Dai, Y. Q.; Hill, M. R.; Ghiviriga, I.; Bapat, A. P.; Sumerlin, B. S. *Nature Chem.* **2017**, *9*, 817.

(4) a) Ball, M.; Zhong, Y.; Wu, Y.; Schenck, C.; Ng, F.; Steigerwald, M.; Xiao, S. X.; Nuckolls, C. *Acc. Chem. Res.* **2015**, *48*, 267; b) Katayama, T.; Nakatsuka, S.; Hirai, H.; Yasuda, N.; Kumar, J.; Kawai, T.; Hatakeyama, T. *J. Am. Chem. Soc.* **2016**, *138*, 5210.

(5) a) Narita, A.; Wang, X. Y.; Feng, X. L.; Müllen, K. *Chem. Soc. Rev.* **2015**, *44*, 6616; b) Stępień, M.; Gońka, E.; Żyła, M.; Sprutta, N. *Chem. Rev.* **2017**, *117*, 3479.

(6) a) Hashimoto, S.; Ikuta, T.; Shiren, K.; Nakatsuka, S.; Ni, J. P.; Nakamura, M.; Hatakeyama, T. *Chem. Mater.* **2014**, *26*, 6265; b) Numata, M.; Yasuda, T.; Adachi, C. *Chem. Commun.* **2015**, *51*, 9443; c) Kushida, T.; Shuto, A.; Yoshio, M.; Kato, T.; Yamaguchi, S. *Angew. Chem., Int. Ed.* **2015**, *54*, 6922; d) Escande, A.; Ingleson, M. J. *Chem. Commun.* **2015**, *51*, 6257; e) John, A.; Bolte, M.; Lerner, H. W.; Wagner, M. *Angew. Chem., Int. Ed.* **2017**, *56*, 5588; f) Farrell, J. M.; Schmidt, D.; Grande, V.; Würthner, F. *Angew. Chem., Int. Ed.* **2017**, *56*, 11846; g) Ji, L.; Griesbeck, S.; Marder, T. B. *Chem. Sci.* **2017**, *8*, 846. h) Shiotari, A.; Nakae, T.; Iwata, K.; Mori, S.; Okujima, T.; Uno, H.; Sakaguchi, H.; Sugimoto, Y. *Nature Commun.* **2017**, *8*, 16089.

(7) a) Liu, Z. Q.; Marder, T. B. *Angew. Chem. Int. Ed.* **2008**, *47*, 242; b) Bosdet, M. J. D.; Piers, W. E. *Can. J. Chem.* **2009**, *87*, 8; c) Campbell, P. G.; Marwitz, A. J. V.; Liu, S. Y. *Angew. Chem. Int. Ed.* **2012**, *51*, 6074; d) Wang, X. Y.; Wang, J. Y.; Pei, J. *Chem. Eur. J.* **2015**, *21*, 3528; e) Baggett, A. W.; Guo, F.; Li, B.; Liu, S.-Y.; Jäkle, F. *Angew. Chem. Int. Ed.* **2015**, *54*, 11191; f) Wang, X. Y.; Zhang, F.; Schellharnmer, K. S.; Machata, P.; Ortmann, F.; Cuniberti, G.; Fu, Y. B.; Hunger, J.; Tang, R. Z.; Popov, A. A.; Berger, R.; Müllen, K.; Feng, X. L. *J. Am. Chem. Soc.* **2016**, *138*, 11606.

(8) a) Shaikh, A. C.; Ranade, D. S.; Thorat, S.; Maity, A.; Kulkarni, P. P.; Gonnade, R. G.; Munshi, P.; Patil, N. T. *Chem. Commun.* **2015**, *51*, 16115; b) Crossley, D. L.; Cade, I. A.; Clark, E. R.; Escande, A.; Humphries, M. J.; King, S. M.; Vitorica-Yrezabal, I.; Ingleson,

M. J.; Turner, M. L. *Chem. Sci.* **2015**, *6*, 5144; c) Zhao, R. Y.; Dou, C. D.; Xie, Z. Y.; Liu, J.; Wang, L. X. *Angew. Chem. Int. Ed.* **2016**, *55*, 5313; d) Yusuf, M.; Liu, K. L.; Guo, F.; Lalancette, R. A.; Jäkle, F. *Dalton Trans.* **2016**, *45*, 4580; e) Yang, D. T.; Mellerup, S. K.; Peng, J.; Wang, X.; Li, Q.; Wang, S. *J. Am. Chem. Soc.* **2016**, *138*, 11513; f) Wong, B. Y. W.; Wong, H. L.; Wong, Y. C.; Chan, M. Y.; Yam, V. W. W. *Chem. - Eur. J.* **2016**, *22*, 15095; g) Shen, C.; Srebro-Hooper, M.; Jean, M.; Vanthuyne, N.; Toupet, N.; Williams, J. A. G.; Torres, A. R.; Riives, A. J.; Muller, G.; Autschbach, J.; Crassous, J. *Chem. Eur. J.* **2017**, *23*, 407.

(9) Serevicius, T.; Komskis, R.; Adomenas, P.; Adomeniene, O.; Jankauskas, V.; Gruodis, A.; Kazlauskas, K.; Jursenas, S. *Phys. Chem. Chem. Phys.* **2014**, *16*, 7089.

(10) Ingleson, M. J. *Synlett* **2012**, *23*, 1411.

(11) a) For a closely related system with shorter B-N distance and proven B-N dissociation, see: Chen, J. W.; Lalancette, R. A.; Jäkle, F. *Chem. - Eur. J.* **2014**, *20*, 9120; b) Matsuo, K.; Saito, S.; Yamaguchi, S. *J. Am. Chem. Soc.* **2014**, *136*, 12580.

(12) a) D. W. Stephan *J. Am. Chem. Soc.* **2015**, *137*, 10018; b) Cao, Y.; Nagle, J. K.; Wolf, M. O.; Patrick, B. O. *J. Am. Chem. Soc.* **2015**, *137*, 4888; c) Shimogawa, H.; Yoshikawa, O.; Aramaki, Y.; Murata, M.; Wakamiya, A.; Murata, Y. *Chem. Eur. J.* **2017**, *23*, 3784; d) Schraff, S.; Sun, Y.; Pammer, F. *J. Mater. Chem. C* **2017**, *5*, 1730.

(13) For **3C-Et<sub>th,cis</sub>** and **3C-Et<sub>th,trans</sub>** the endocyclic C-C bonds are shorter than the B-N and N-C bonds of **3-Et<sub>th</sub>**, but similar distortions to the anthracene backbone and dislocations of phenyl *ipso*-carbons are observed (Table S2). As in the case of the B-N structures, the *cis*-isomer is energetically favored by 19.2 kJ/mol.

(14) Yang, C.; Jacob, J.; Müllen, K. *Macromolecules* **2006**, *39*, 5696.

(15) *Handbook of Photochemistry*, 3<sup>rd</sup> Ed., Montalti, M.; Credi, A.; Prodi, L.; Gandolfi, M. T., Eds., CRC Press, Boca Raton, FL, 2006.

(16) Fudickar, W.; Linker, T. *J. Am. Chem. Soc.* **2012**, *134*, 15071.

(17) Gaussian 09, Revision B.01, M. J. Frisch, G. W. Trucks, H. B. Schlegel, G. E. Scuseria, M. A. Robb, J. R. Cheeseman, G. Scalmani, V. Barone, B. Mennucci, G. A. Petersson, H. Nakatsuji, M. Caricato, X. Li, H. P. Hratchian, A. F. Izmaylov, J. Bloino, G. Zheng, J. L. Sonnenberg, M. Hada, M. Ehara, K. Toyota, R. Fukuda, J. Hasegawa, M. Ishida, T. Nakajima, Y. Honda, O. Kitao, H. Nakai, T. Vreven, J. A. Montgomery, Jr., J. E. Peralta, F. Ogliaro, M. Bearpark, J. J. Heyd, E. Brothers, K. N. Kudin, V. N. Staroverov, T. Keith, R. Kobayashi, J. Normand, K. Raghavachari, A. Rendell, J. C. Burant, S. S. Iyengar, J. Tomasi, M. Cossi, N. Rega, J. M. Millam, M. Klene, J. E. Knox, J. B. Cross, V. Bakken,

C. Adamo, J. Jaramillo, R. Gomperts, R. E. Stratmann, O. Yazyev, A. J. Austin, R. Cammi, C. Pomelli, J. W. Ochterski, R. L. Martin, K. Morokuma, V. G. Zakrzewski, G. A. Voth, P. Salvador, J. J. Dannenberg, S. Dapprich, A. D. Daniels, O. Farkas, J. B. Foresman, J. V. Ortiz, J. Cioslowski, and D. J. Fox, Gaussian, Inc., Wallingford CT, 2010.

(18) Bruker (2005). *SAINT* Version 7.23a. Bruker AXS Inc., Madison, Wisconsin, USA. Bruker (2006). *APEX 2* Version 2.0-2. Bruker AXS Inc., Madison, Wisconsin, USA.

(19) G. M. Sheldrick (2008). SADABS. University of Göttingen, Germany. G. M. Sheldrick, *Acta Cryst.* **2008**, A64, 112-122. G. M. Sheldrick, SHELXL, *Acta Cryst.* **2015**, C71, 3-8.

(20) a) Y. Zhu, A. R. Rabindranath, T. Beyerlein and B. Tiede, *Macromolecules* **2007**, 40, 6981; b) P. Patel, S. Chang, *Org. Lett.* **2014**, 16, 3328-3331; d) T. Chatterjee, M. G. Choi, J. Kim, S.-K. Chang, E. J. Cho, *Chem. Comm.* **2016**, 52, 4203; c) X. Li, A. Fast, Z. Huang, D. A. Fishman and M. L. Tang *Angew. Chem. Int. Ed.* **2017**, 56, 5598.

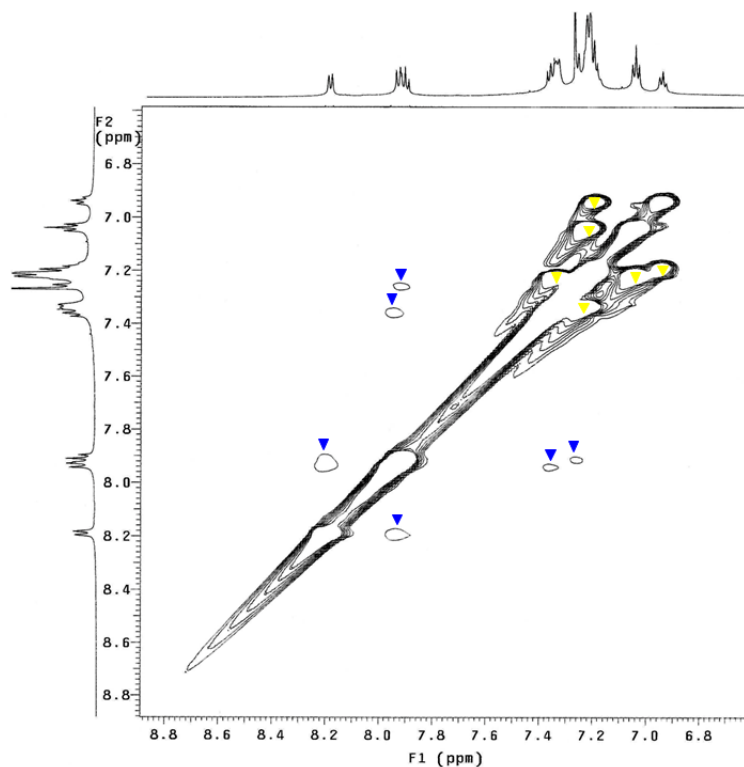
(21) S. Ye, J. Chen, C. Di, Y. Liu, K. Lu, W. Wu, C. Du, Y. Liu, Z. Shuai and G. Yu, *J. Mater. Chem.* **2010**, 20, 3186.

(22) a) Velian, A.; Cummins, C. C. *J. Am. Chem. Soc.* **2012**, 134, 13978; b) Taylor, J. W.; McSkimming, A.; Guzman, C. F.; Harman, W. H. *J. Am. Chem. Soc.* **2017**, 139, 11032.

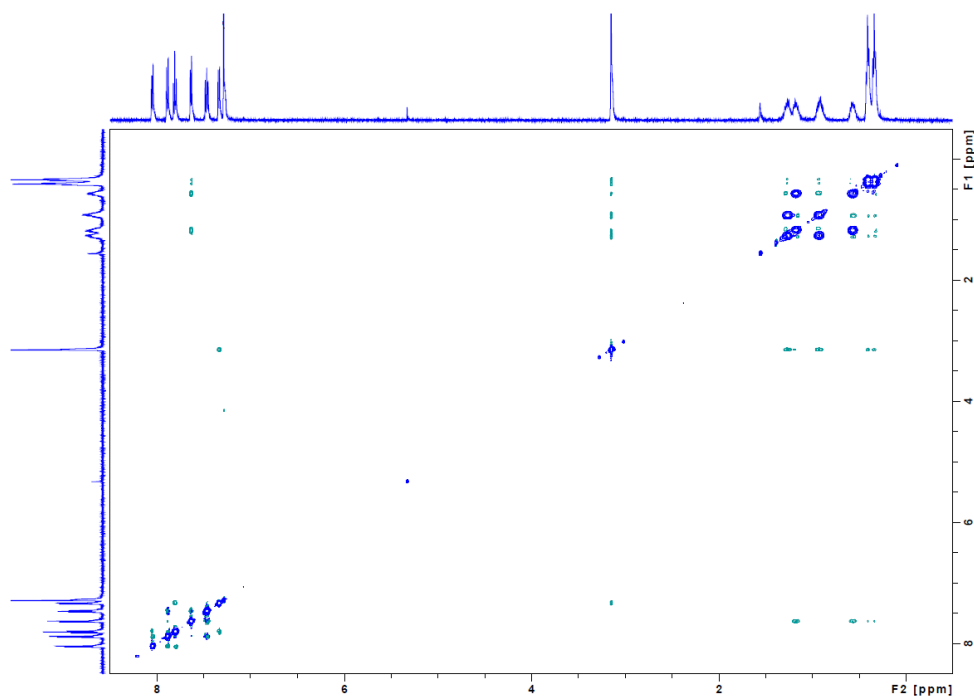
(23) Sandström, *Dynamic NMR Spectroscopy*, Academic Press, London, **1982**.

(24) Liu, K. L.; Lalancette, R. A.; Jakle, F. *J. Am. Chem. Soc.* **2017**, 139, 18170.

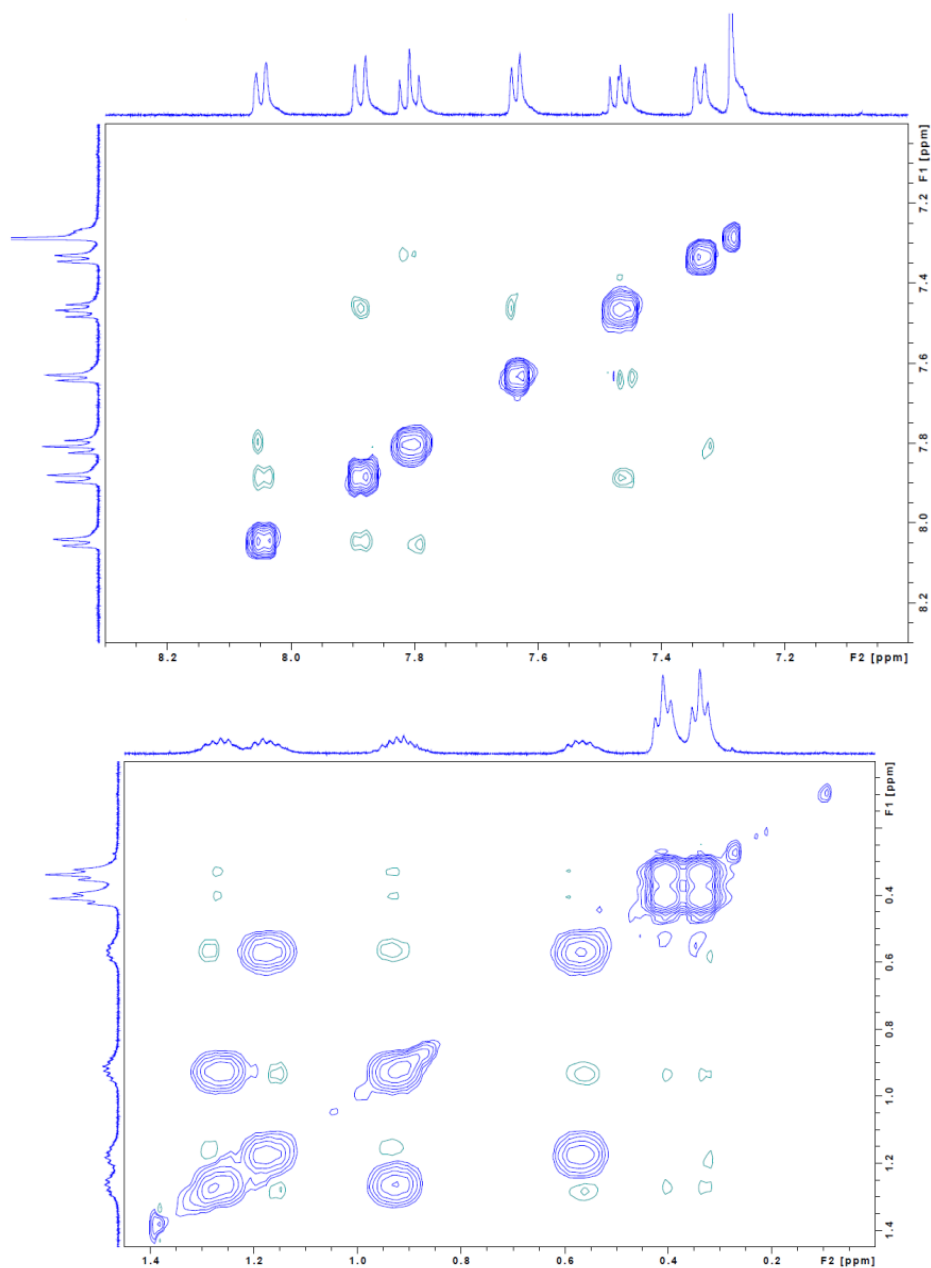
## Appendix

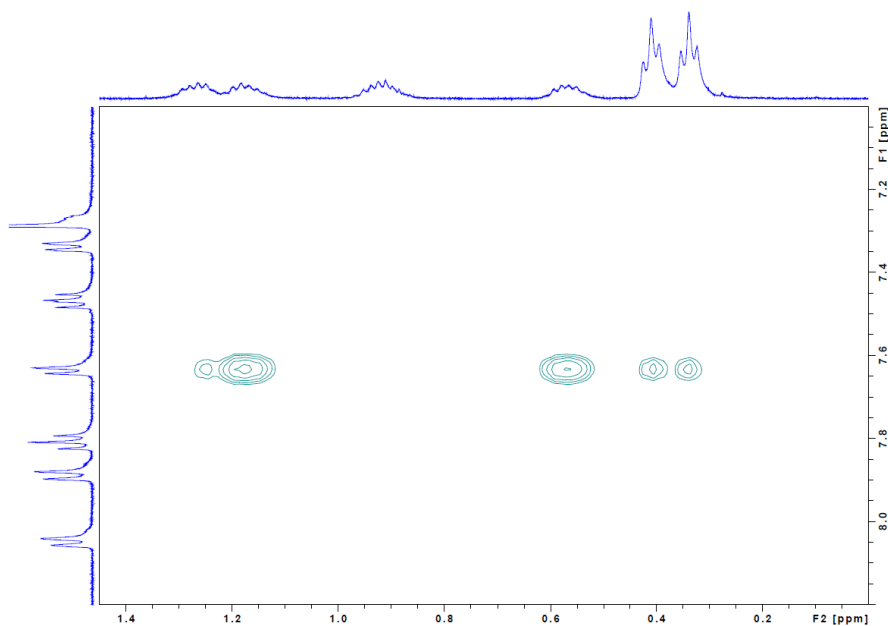


**Figure 2-13.** H,H-EXSY (NOESY) NMR spectrum of **3-Ph** (aromatic region, CDCl<sub>3</sub>, 25 °C, mixing time: 0.6 s); cross-peaks labeled yellow are due to exchange, those labeled blue are due to NOEs.

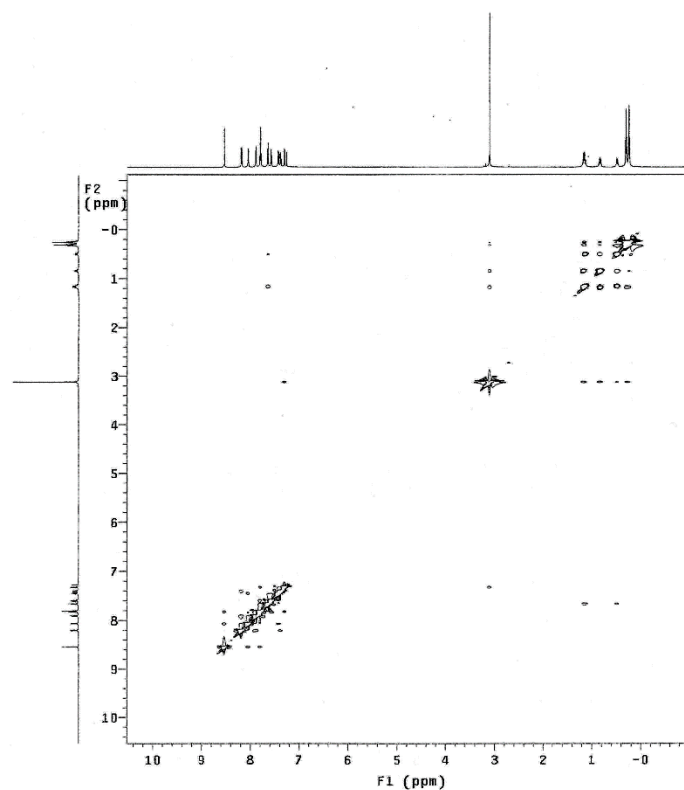


**Figure 2-14a.** Full H,H-EXSY (NOESY) NMR spectrum of **3-Et** (CDCl<sub>3</sub>, 25 °C, mixing time: 0.5 s); cross-peaks in dark blue are due to exchange, those in blue-green are due to NOEs.

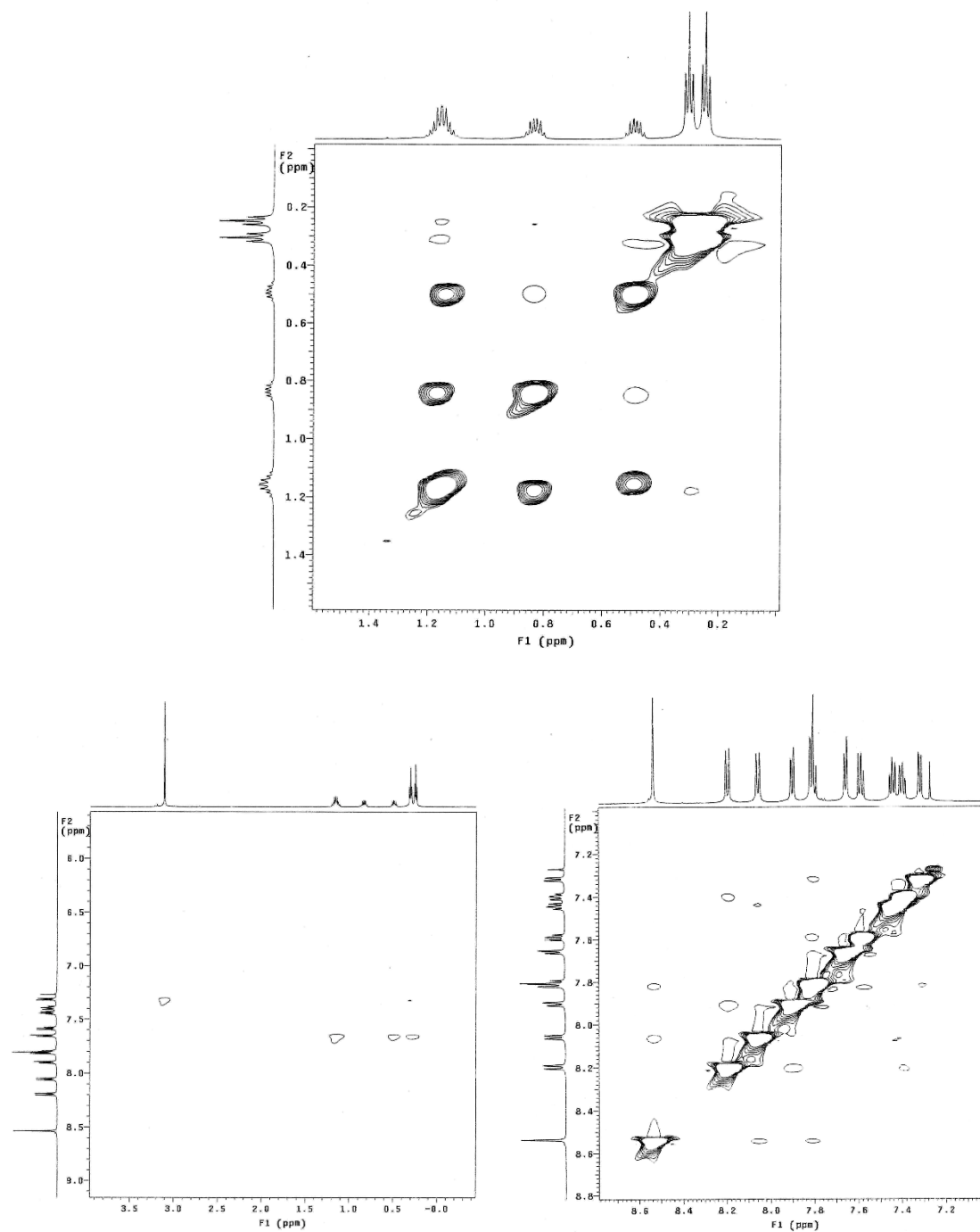




**Figure 2-14b.** Expansions of H,H-EXSY (NOESY) NMR spectrum of **3-Et** ( $\text{CDCl}_3$ , 25  $^\circ\text{C}$ , mixing time: 0.5 s); cross-peaks in dark blue are due to exchange, those in blue-green are due to NOEs.

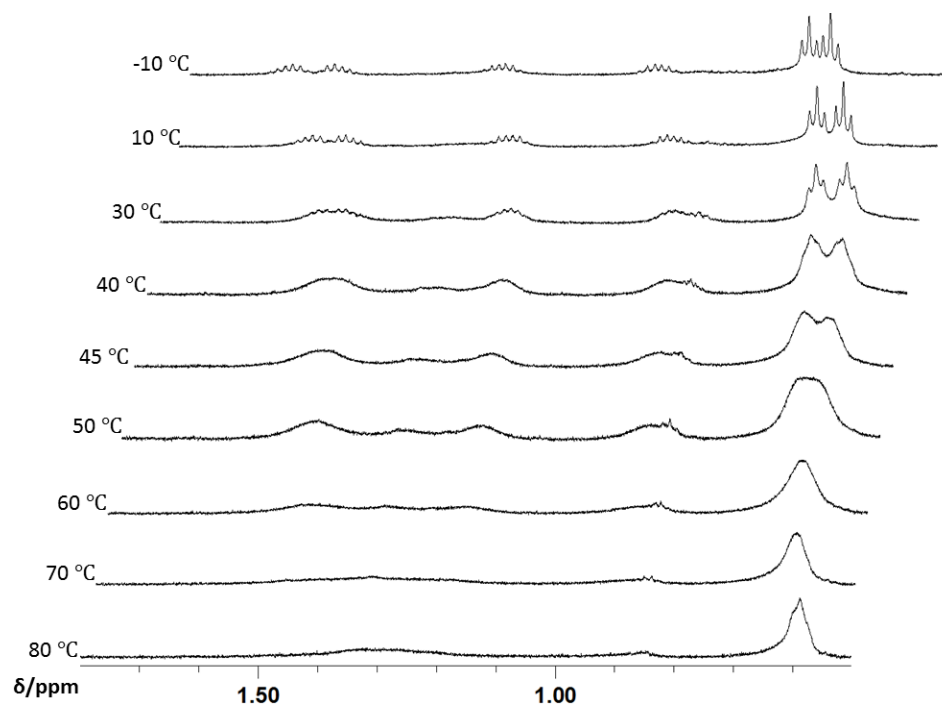


**Figure 2-15a.** Full H,H-EXSY (NOESY) NMR spectrum of **4-Et** ( $\text{CDCl}_3$ , 25  $^\circ\text{C}$ , mixing time: 0.6 s); minor cross-peaks are due to NOEs, major cross-peaks are due to exchange.

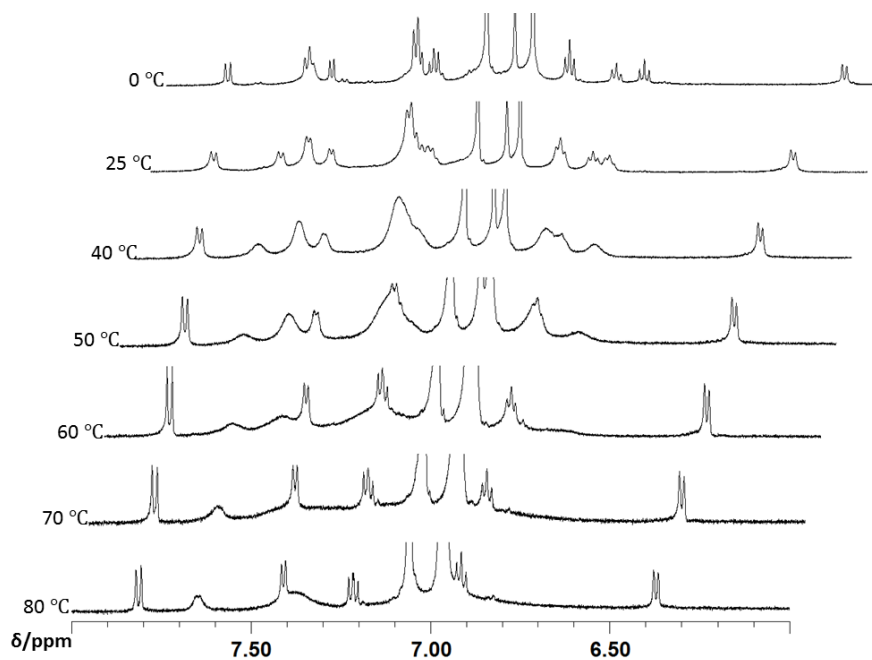


**Figure 2-15b.** Expansions of the H,H-EXSY (NOESY) NMR spectrum of **4-Et** ( $\text{CDCl}_3$ , 25 °C, mixing time: 0.6 s); minor cross-peaks are due to NOEs, major cross-peaks are due to exchange.

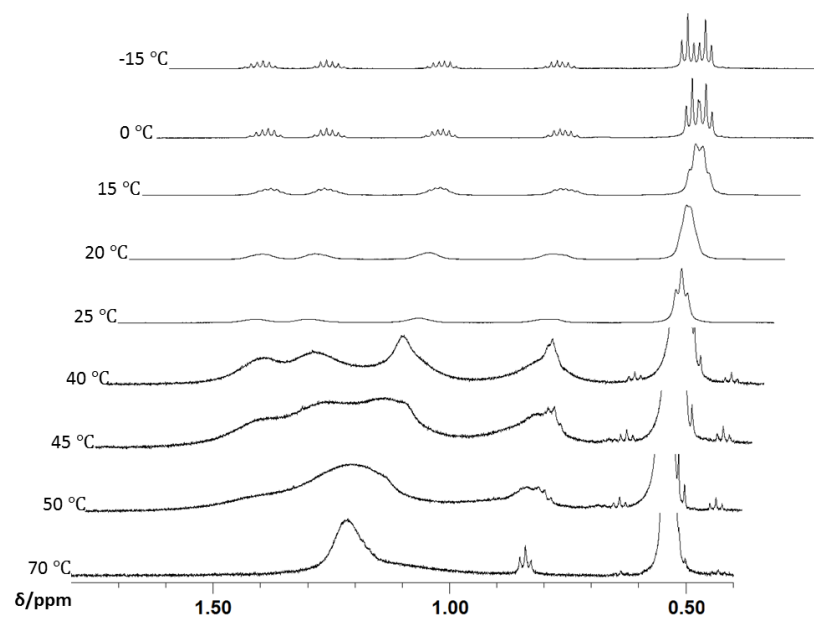




**Figure 2-16.** VT <sup>1</sup>H NMR spectra of **3-Et** (Et region, d<sub>8</sub>-toluene, 599.7 MHz)



**Figure 2-17.** VT <sup>1</sup>H NMR spectra of **3-Ph** (aromatic region, d<sub>8</sub>-toluene, 599.7 MHz)

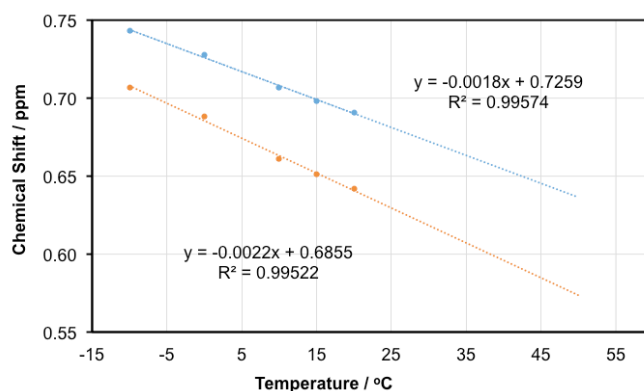
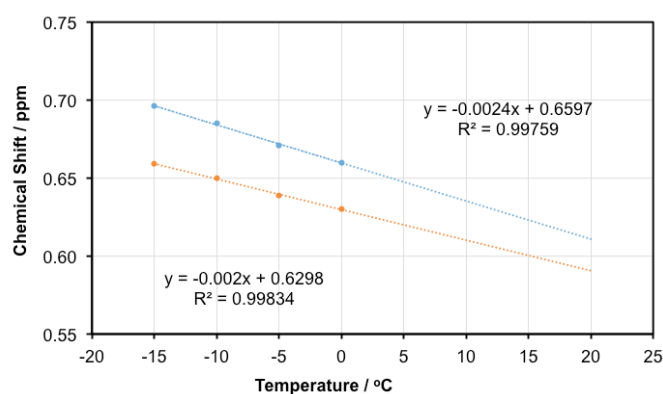


**Figure 2-18.** VT  $^1\text{H}$  NMR spectra of **4-Et** (Et region,  $\text{d8-toluene}$ , 599.7 MHz)

**Table 2-4.** Summary of results from VT NMR spectroscopy studies

| Compound    | Probe                | $T_c$ [a] [K] | $\Delta\nu$ [Hz] [b] | $\Delta G^\ddagger_{T_c}$ [a] [kJ mol <sup>-1</sup> ] |
|-------------|----------------------|---------------|----------------------|---|
| <b>2</b>    | CH <sub>3</sub> (Py) | 318 ± 5       | 15.0                 | 69.7 ± 1.1  |
| <b>3-Et</b> | CH <sub>3</sub> (Et) | 323 ± 3       | 36.2 [c]             | 68.4 ± 0.7  |
| <b>3-Ph</b> | <i>o</i> -Ph         | 343 ± 5       | 181                  | 68.2 ± 1.0  |
| <b>4-Et</b> | CH <sub>3</sub> (Et) | 293 ± 3       | 13.1 [c]             | 64.4 ± 0.7  |
|             | CH <sub>2</sub> (Et) | 321 ± 3       | 150                  | 64.2 ± 0.6  |

[a] Data from coalescence temperature method by using the approximation  $\Delta G^\ddagger = 0.0194T_c [9.972 + \lg(T_c \Delta\nu^{-1})]$  for estimation of  $\Delta G^\ddagger$  at  $T_c$ ;<sup>23</sup> [b] an error of 5% in the line width determination is assumed; [c] values for  $\Delta\nu$  at  $T_c$  were estimated by linear extrapolation of chemical shift trends at low temperature (where exchange is negligible) to  $T_c$ .

**Figure 2-19.** Projection of <sup>1</sup>H NMR chemical shifts for CH<sub>3</sub> groups of compound **3-Et** by extrapolation of low temperature data to 50 °C for determination of  $\Delta\nu$  at  $T_c$ .**Figure 2-20.** Projection of <sup>1</sup>H NMR chemical shifts for CH<sub>3</sub> groups of compound **4-Et** by extrapolation of low temperature data to 20 °C for determination of  $\Delta\nu$  at  $T_c$ .

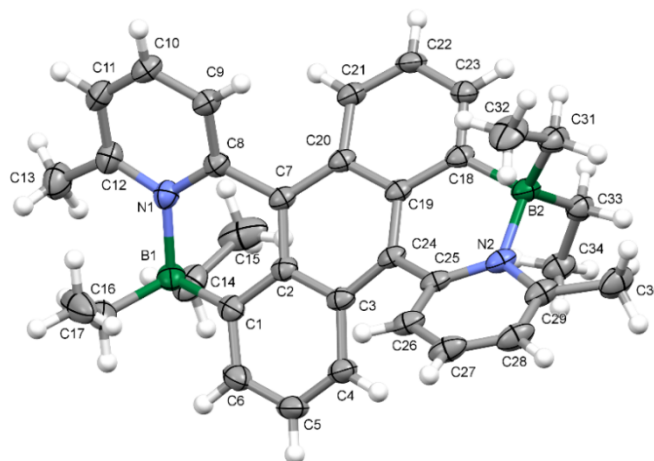


**Figure 2-21a.** X-ray crystal structure of **3-Et** (50% thermal ellipsoids). Selected bond distances (Å) and interplanar angles (°): B1-N1 1.685(3), B2-N2 1.671(4), B1-C1 1.616(4), B2-C18 1.626(4), N1-C8 1.362(3), N1-C12 1.371(3), N2-C25 1.362(3), N2-C29 1.374(3), C7-C8 1.479(3), C24-C25 1.479(3), N1-B1-C1 106.52(19), N2-B2-C18 107.6(2), B1-N1-C8 120.36(19), B2-N2-C25 120.36(19), B1-C1-C2 123.1(2), B2-C18-C19 123.9(2), C2-C7-C8 119.3(2), C19-C24-C25 120.2(2), C8-N1-C12 117.9(2), C25-N2-C29 117.7(2),  $\text{Ph}_{\text{An,outer}} // \text{Ph}_{\text{An,outer}}$  21.5,  $\text{Ph}_{\text{An,inner}} // \text{Py}$  39.0, 38.8.

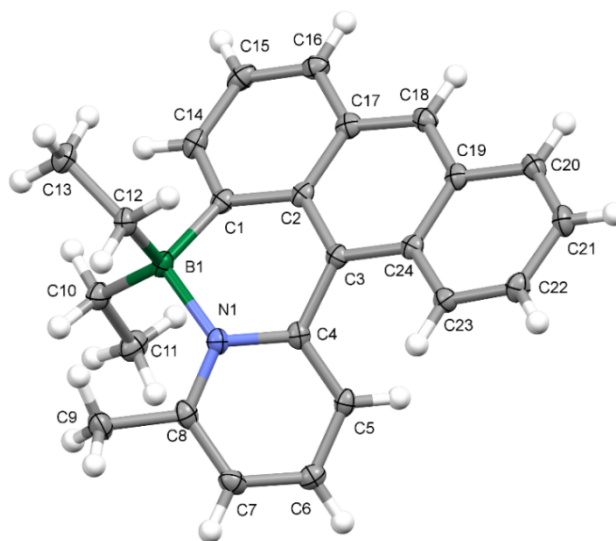


**Figure 2-21b.** X-ray crystal structure plot of **4-Et** (50% thermal ellipsoids). Selected bond distances (Å) and angles (°): B1-N1 1.685(3), B1-C1 1.626(3), N1-C4 1.373(3), N1-C8 1.363(3), C3-C4 1.482(3), N1-B1-C1 106.66(17), B1-N1-C4 119.07(17), B1-C1-C2 120.97(18), C2-C3-C4 119.00(19), C4-N1-C8 117.71(18),  $\text{Ph}_{\text{An,outer}} // \text{Ph}_{\text{An,outer}}$  4.4,  $\text{Ph}_{\text{An,inner}} // \text{Py}$  39.3.

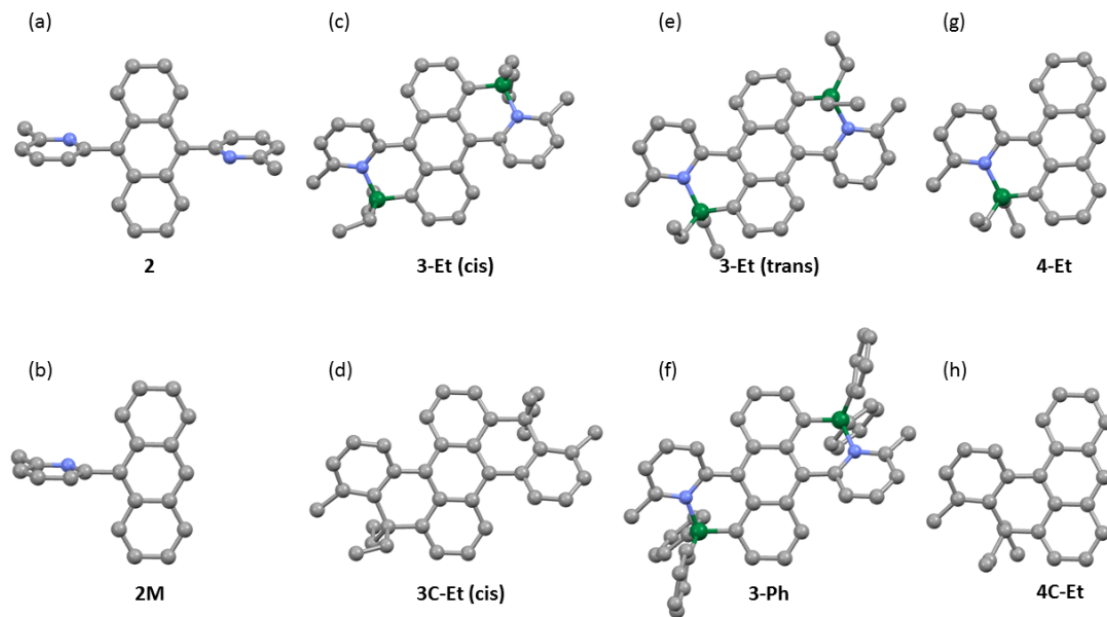


**Figure 2-22.** Optimized structures of (a) **2** (trans), (b) **2M**, (c) **3-Et** (cis), (d) **3C-Et** (cis), (e) **3-Et** (trans), (f) **3-Ph** (cis), (g) **4-Et**, (h) **4C-Et** (Gaussian 09; rb3lyp/6-31g(d)). C grey, B green, N blue.

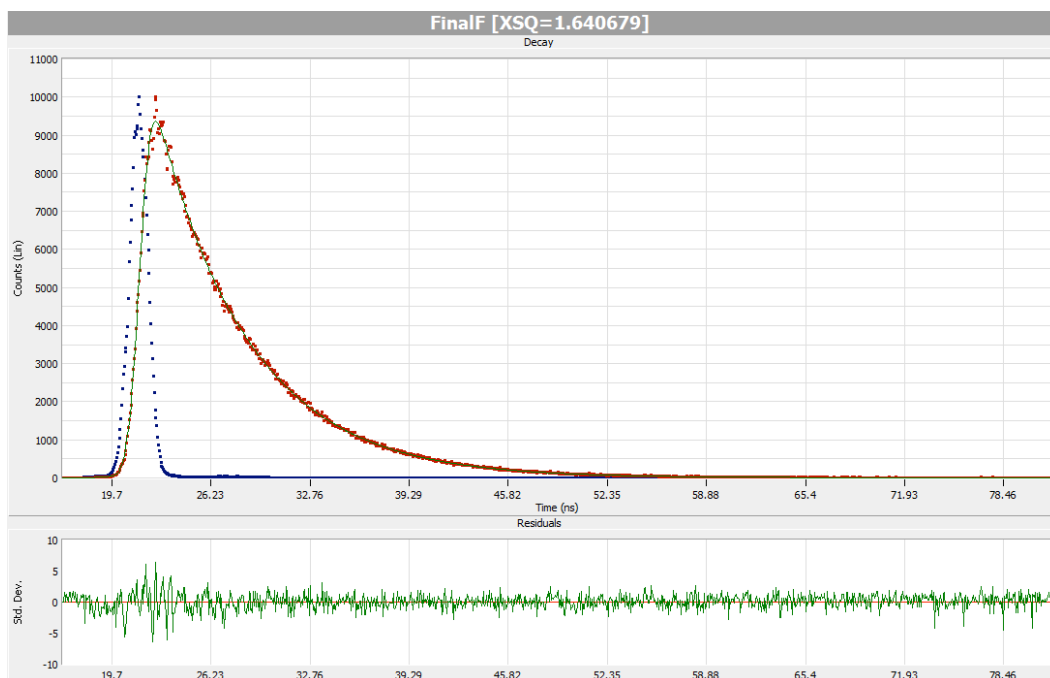
**Table 2-5.** Comparison of geometric parameters (distances in Å, angles in °) obtained from X-ray structure analyses and DFT calculations (Gaussian 09; rb3lyp/6-31g(d))

|                                 | B-N                               | B-C <sub>An</sub>                | C <sub>An</sub> -C <sub>Py</sub> | C <sub>An</sub> -B-N                                   | Cent <sub>An</sub> -<br>C-B                | Cent <sub>An</sub> -<br>C-C <sub>Py</sub> | Ph <sub>An,outer</sub> //<br>Ph <sub>An,outer</sub> | Ph <sub>An,inner</sub> //<br>Py |
|---------------------------------|-----------------------------------|----------------------------------|----------------------------------|--|--|---|---|---------------------------------|
| <b>3-Et<sub>X-ray</sub></b>     | 1.685(3),<br>1.671(4)             | 1.616(4),<br>1.626(4)            | 1.479(3),<br>1.479(3)            | 106.5(2),<br>107.6(2)                                  | 173.6,<br>174.8                            | 164.7,<br>166.4                           | 21.5  | 39.0,<br>38.8                   |
| <b>3-Et<sub>th,cis</sub></b>    | 1.688,<br>1.700                   | 1.622,<br>1.625                  | 1.475,<br>1.474                  | 108.0,<br>107.9  | 174.8,<br>176.7                            | 168.9,<br>170.3                           | 20.3  | 35.9,<br>35.7                   |
| <b>3-Et<sub>th,trans</sub></b>  | 1.687,<br>1.718                   | 1.629,<br>1.631                  | 1.478,<br>1.483                  | 106.3,<br>101.2  | 167.5,<br>167.5                            | 169.5,<br>163.9                           | 3.2   | 35.4,<br>40.9                   |
| <b>3-Ph<sub>th,cis</sub></b>    | 1.680                             | 1.627                            | 1.474                            | 107.8  | 173.7                                      | 167.8                                     | 21.3  | 35.6                            |
| <b>4-Et<sub>X-ray</sub></b>     | 1.685(3)                          | 1.626(3)                         | 1.482(3)                         | 106.7(2)   | 167.9                                      | 168.3                                     | 4.4   | 39.3                            |
| <b>4-Et<sub>th</sub></b>        | 1.699                             | 1.627                            | 1.476                            | 106.1  | 168.9                                      | 167.8                                     | 9.7   | 37.9                            |
|                                 | C <sub>Et2</sub> -C <sub>Ph</sub> | C <sub>Ph</sub> -C <sub>An</sub> | C <sub>An</sub> -C <sub>Ph</sub> | C <sub>An</sub> -C <sub>Et2</sub> -<br>C <sub>Ph</sub> | Cent <sub>An</sub> -<br>C-C <sub>Et2</sub> | Cent <sub>An</sub> -<br>C-C <sub>Ph</sub> | Ph <sub>An,outer</sub> //<br>Ph <sub>An,outer</sub> | Ph <sub>An,inner</sub> //<br>Ph |
| <b>3C-Et<sub>th,cis</sub></b>   | 1.551,<br>1.547                   | 1.550,<br>1.545                  | 1.473,<br>1.475                  | 113.6,<br>113.7  | 177.4,<br>177.1                            | 172.4,<br>170.8                           | 26.3  | 27.6,<br>29.1                   |
| <b>3C-Et<sub>th,trans</sub></b> | 1.550,<br>1.550                   | 1.542,<br>1.547                  | 1.478,<br>1.480                  | 111.3,<br>110.6  | 171.0,<br>169.6                            | 171.7,<br>170.8                           | 1.9   | 29.4,<br>32.8                   |
| <b>4C-Et<sub>th</sub></b>       | 1.554                             | 1.546                            | 1.478                            | 111.1  | 170.4                                      | 169.3                                     | 10.3  | 33.3                            |

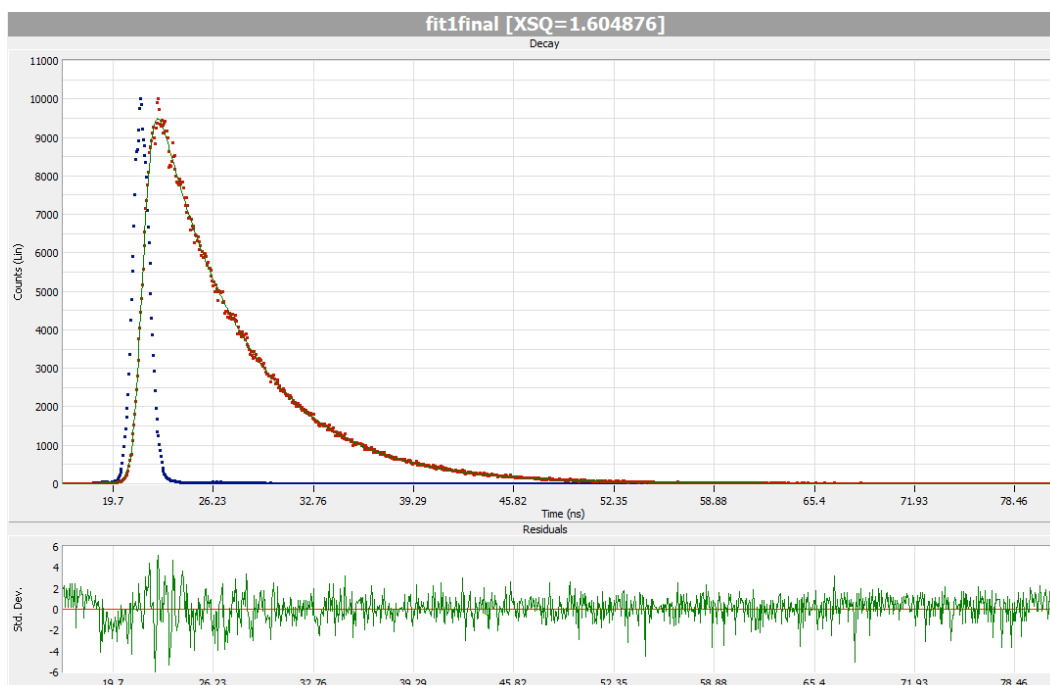
**Table 2-6.** Summary of photophysical data of BN-functionalized anthracenes in DCM solution

| Compound    | $\lambda_{\text{abs}}$ / nm | $\epsilon_{\text{abs}}$ /<br>$10^4 \text{ M}^{-1}\text{cm}^{-1}$ | $\lambda_{\text{abs}}$ / nm(TDDFT) | $\lambda_{\text{Fl}}$ / nm<br>[a] | $\tau_{\text{Fl}}$ / ns [b]    | $\Phi_{\text{Fl}}$ / %<br>[c] |
|-------------|-----------------------------|--|------------------------------------|-----------------------------------|--------------------------------|-------------------------------|
| <b>2</b>    | 393                         | 1.27   | 359                                | 428                               | 6.0<br>( $\chi^2 = 1.64$ )     | 77                            |
|             | 372                         | 1.35   |                                    |                                   |                                |                               |
|             | 354                         | 0.86   |                                    |                                   |                                |                               |
|             | 259                         | 9.38   |                                    |                                   |                                |                               |
| <b>2M</b>   | 385                         | 0.96   | 347                                | 418                               | 5.7<br>( $\chi^2 = 1.60$ )     | 48                            |
|             | 366                         | 1.04   |                                    |                                   |                                |                               |
|             | 348                         | 0.69   |                                    |                                   |                                |                               |
|             | 257                         | 12.38  |                                    |                                   |                                |                               |
| <b>3-Ph</b> | 542                         | 1.92   | 536                                | 611                               | 10.9<br>( $\chi^2 = 1.41$ )    | 56                            |
|             | 513 (sh)                    | 1.67   |                                    |                                   |                                |                               |
|             | 298                         | 5.33   |                                    |                                   |                                |                               |
|             | 253                         | 4.22   |                                    |                                   |                                |                               |
| <b>3-Et</b> | 538                         | 1.33   | 528                                | 620                               | 11.1<br>( $\chi^2 = 1.54$ )    | 53                            |
|             | 298                         | 4.01   |                                    |                                   |                                |                               |
|             | 293                         | 2.95   |                                    |                                   |                                |                               |
| <b>4-Et</b> | 453                         | 1.06   | 428                                | 538                               | 4.1<br>( $\chi^2 = 1.99$ ) [d] | 22                            |
|             | 280                         | 5.69   |                                    |                                   |                                |                               |

[a] Excited at 372 nm (**2**), 366 nm (**2M**), 513 nm (**3-Ph**), 538 nm (**3-Et**) and 453 nm (**4-Et**); [b] excited with a nanoLED at 388 nm (**2**), 349 nm (**2M**), or 450 nm (complexes **3** and **4**); [c] absolute quantum yield determined using an integrating sphere; [d] for double-exponential fit:  $\tau_{\text{Fl}} = 4.1 \text{ ns}$  (99%), 50.2 ns (1%) ( $\chi^2 = 1.73$ )

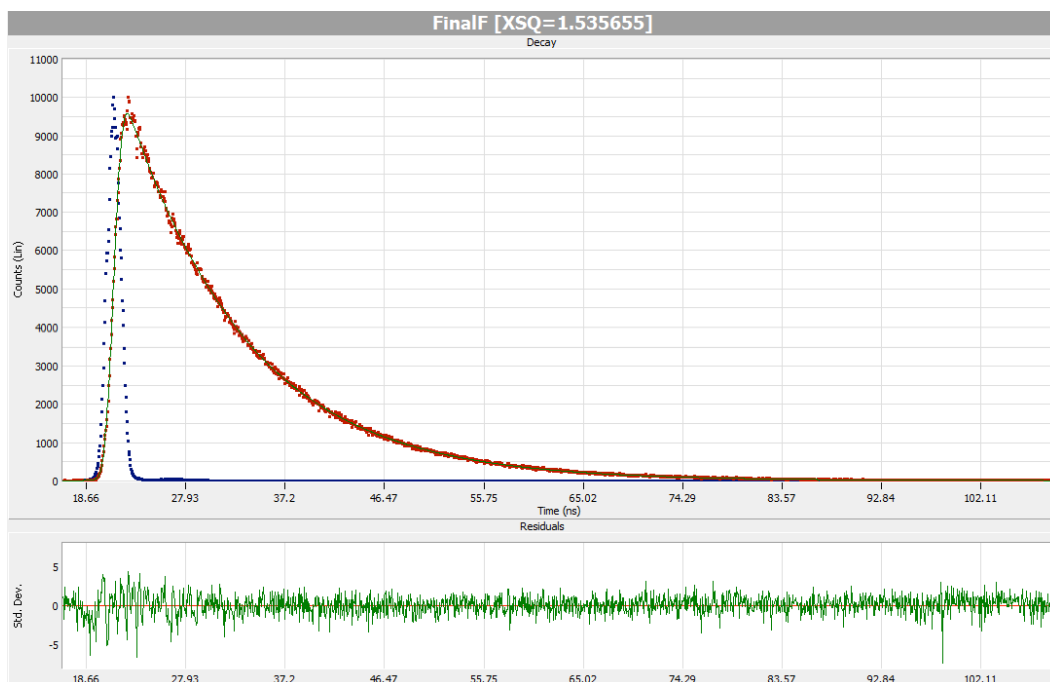


**Figure 2-23a.** Single-exponential fit of fluorescence decay of **2** in degassed DCM excited with a 388 nm nanoLED.

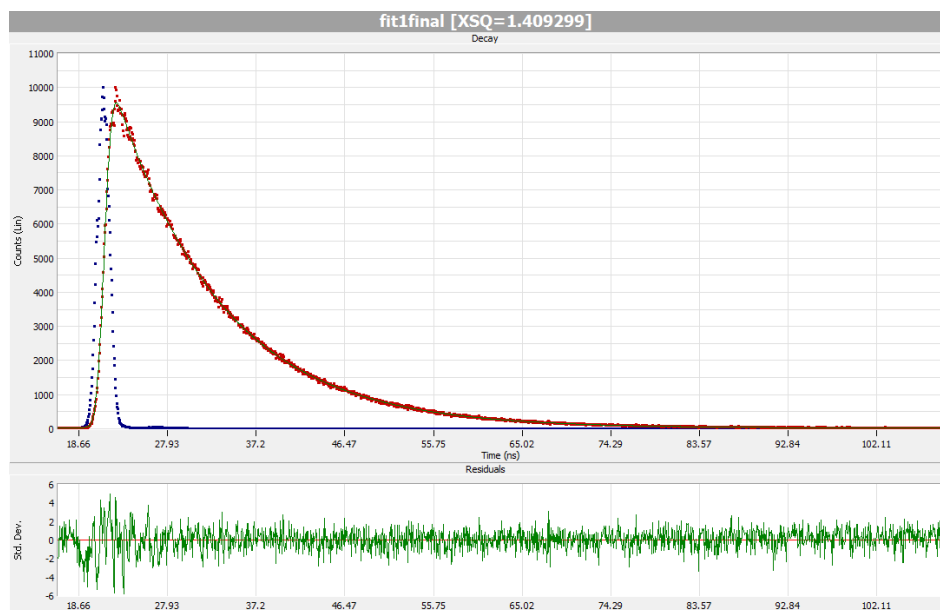


**Figure 2-23b.** Single-exponential fit of fluorescence decay of **2M** in degassed DCM excited with a 349 nm nanoLED.

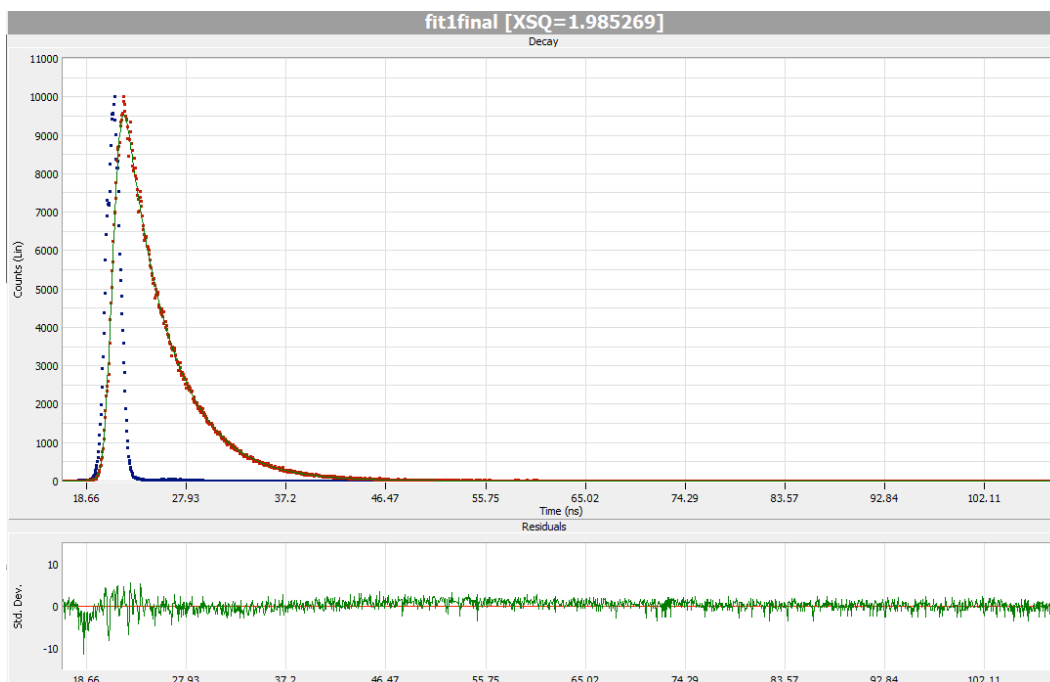




**Figure 2-23c.** Single-exponential fit of fluorescence decay of **3-Et** in degassed DCM excited with a 450 nm nanoLED.

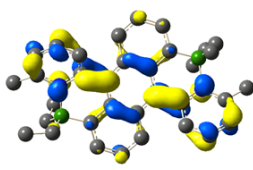
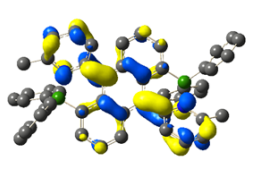
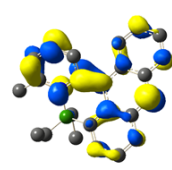
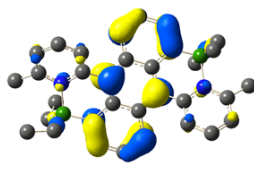
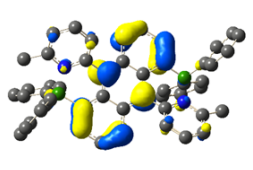
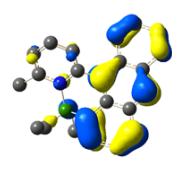


**Figure 2-23d.** Single-exponential fit of fluorescence decay of **3-Ph** in degassed DCM excited with a 450 nm nanoLED.

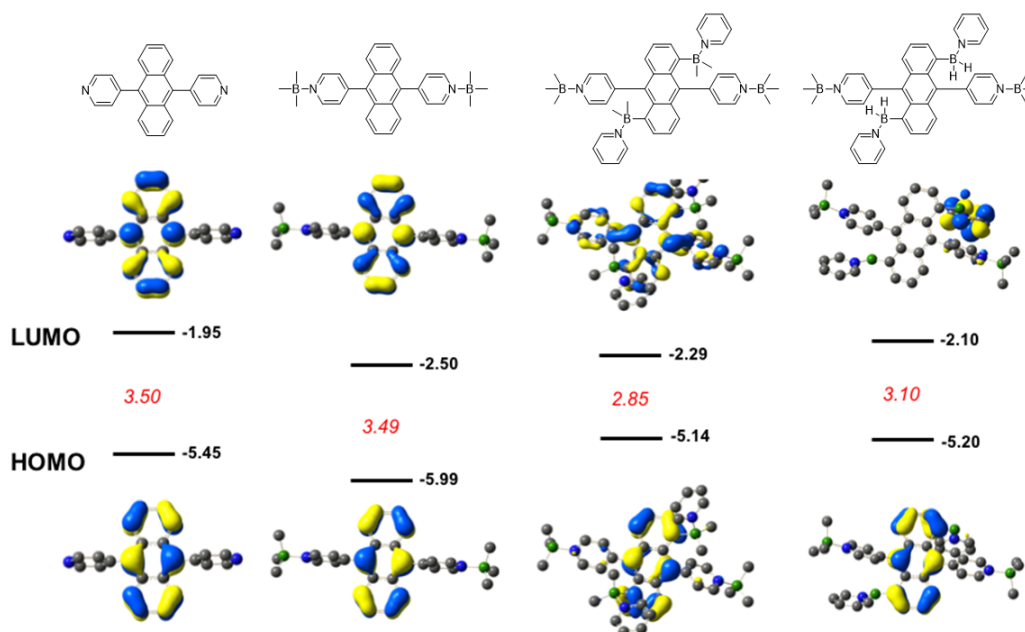


**Figure 2-23e.** Single-exponential fit of fluorescence decay of **4-Et** in degassed DCM excited with a 450 nm nanoLED.

**Table 2-7.** HOMO and LUMO orbital plots for BN-functionalized anthracenes (rb3lyp/6-31g(d), scaling radii of 75%, isovalue = 0.04)

|      | 3-Et   | 3-Ph  | 4-Et   |
|------|--|---|--|
| LUMO | <br>- 2.44 eV | <br>- 2.64 eV | <br>- 2.12 eV |
| HOMO | <br>- 4.76 eV | <br>- 4.93 eV | <br>- 4.99 eV |

**Table 2-8.** HOMO and LUMO orbital plots for 9,10-di(pyrid-4-yl)anthracene and related acyclic borane complexes (rb3lyp/6-31g(d), scaling radii of 75%, isovalue = 0.04). From left to right: 9,10-di(pyrid-4-yl)anthracene, 9,10-di(pyrid-4-yl)anthracene – BMe<sub>3</sub> complex, 9,10-di(pyrid-4-yl)-4,8-bis(pyridine-dimethylboryl)anthracene – BMe<sub>3</sub> complex, 9,10-di(pyrid-4-yl)-4,8-bis(pyridine-dihydroboryl)anthracene – BMe<sub>3</sub> complex.



Borane complexation of the pyridyl moieties in 9,10-di(pyrid-4-yl)anthracene results in the expected decrease in both the HOMO and LUMO energy levels, but the HOMO/LUMO orbitals remain localized on the anthracene backbone and the HOMO-LUMO gap is almost unchanged. This clearly demonstrates that the observed electronic effects for **3-R** are not only a result of borane complexation to the pyridyl moieties and the enhanced acceptor character of the pyridyl groups.

Calculations on the corresponding species with dimethylboryl-pyridine groups in 4,8-position that are complexed with pyridine reveal that the HOMO-LUMO gap decreases significantly and partial delocalization of the LUMO onto the 9,10-pyridyl moieties is detected. However, inspection of the optimized geometry reveals that the placement of the boryl moieties in 4,8-positions right next to the pyridyl groups in 9,10-positions results in severe distortions to the anthracene backbone. While the HOMO-LUMO gap is lowered to 2.85 eV, it remains much larger than that of the title compounds **3-R** (due to the unfavorable orthogonal orientation of the pyridyl moieties in 9,10-positions). To further examine this aspect, we also performed a calculation on a sterically less demanding model system with BH<sub>2</sub>-pyridine substituents in 4,8-positions. The distortions are less pronounced, but the HOMO-LUMO gap for this molecule becomes even larger (3.10 eV) and the LUMO localized on the BH<sub>2</sub>-pyridyl groups, again due to the unfavorable orientation of the pyridyl groups relative to the anthracene backbone.

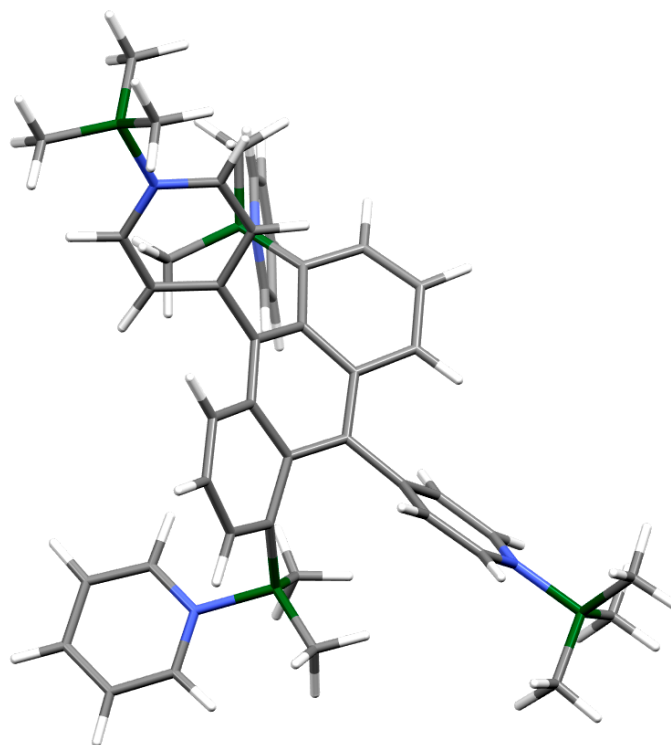


Illustration of severe steric distortions in 9,10-di(pyrid-4-yl)-4,8-bis(pyridine-dimethylboryl)anthracene-BMe<sub>3</sub> complex.

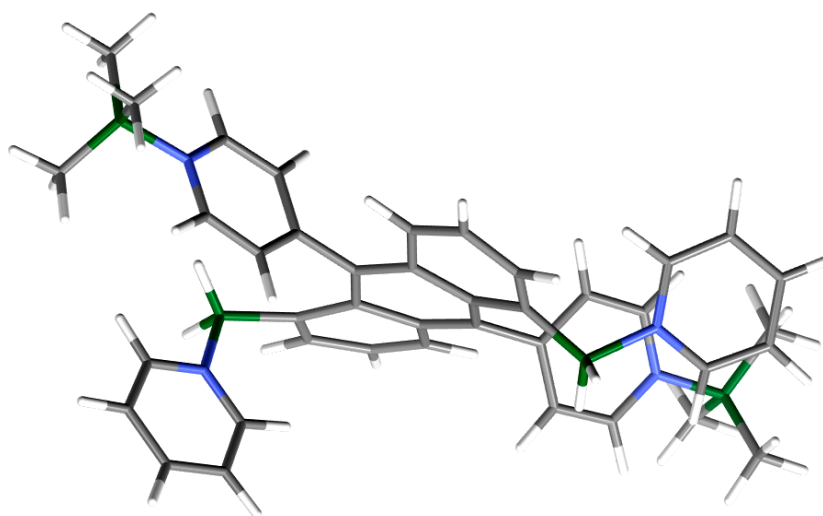


Illustration of less pronounced steric distortions, but orthogonal positioning of pyridyl groups relative to anthracene backbone in 9,10-di(pyrid-4-yl)-4,8-bis(pyridine-dihydroboryl)anthracene-BMe<sub>3</sub> complex.

**Table 2-9.** TD-DFT data for precursors **2** and **2M** (rcam-b3lyp/6-31g(d))

| Compound  | Transition <sup>[a]</sup> | $E_{\text{ex}}$ (eV) | $\lambda$ (nm) | Oscillator strength $f$ | Assignment                                 |
|-----------|---------------------------|----------------------|----------------|-------------------------|--|
| <b>2</b>  | $S_0 \rightarrow S_1$     | <b>3.45</b>          | <b>358.98</b>  | <b>0.2489</b>           | <b>H <math>\rightarrow</math> L (0.70)</b> |
|           |                           |                      |                |                         | H-1 $\rightarrow$ L (-0.14)                |
|           | $S_0 \rightarrow S_9$     | 5.16                 | 240.26         | 0.1194                  | H $\rightarrow$ L+1 (-0.28)                |
|           |                           |                      |                |                         | H $\rightarrow$ L+3 (-0.37)                |
|           |                           |                      |                |                         | H $\rightarrow$ L+5 (0.47)                 |
|           |                           |                      |                |                         | H-5 $\rightarrow$ L (-0.17)                |
|           |                           |                      |                |                         | H-4 $\rightarrow$ L+2 (0.16)               |
|           |                           |                      |                |                         | H-3 $\rightarrow$ L (0.38)                 |
|           |                           |                      |                |                         | H-3 $\rightarrow$ L+1 (0.15)               |
|           | $S_0 \rightarrow S_{10}$  | 5.33                 | 232.42         | 0.6058                  | H-2 $\rightarrow$ L+2 (-0.11)              |
|           |                           |                      |                |                         | H-1 $\rightarrow$ L (-0.33)                |
|           |                           |                      |                |                         | H $\rightarrow$ L+1 (-0.15)                |
|           |                           |                      |                |                         | H $\rightarrow$ L+3 (-0.20)                |
|           |                           |                      |                |                         | H $\rightarrow$ L+5 (-0.20)                |
|           |                           |                      |                |                         |  |
| <b>2M</b> | $S_0 \rightarrow S_1$     | <b>3.57</b>          | <b>346.97</b>  | <b>0.1406</b>           | <b>H <math>\rightarrow</math> L (0.70)</b> |
|           |                           |                      |                |                         | H-4 $\rightarrow$ L+2 (-0.12)              |
|           |                           |                      |                |                         | H-3 $\rightarrow$ L (0.19)                 |
|           |                           |                      |                |                         | H-1 $\rightarrow$ L (0.39)                 |
|           | $S_0 \rightarrow S_8$     | 5.49                 | 225.69         | 1.2157                  | H $\rightarrow$ L+1 (0.16)                 |
|           |                           |                      |                |                         | H $\rightarrow$ L+2 (0.24)                 |
|           |                           |                      |                |                         | H $\rightarrow$ L+3 (0.33)                 |
|           |                           |                      |                |                         | H $\rightarrow$ L+4 (-0.30)                |

[a] Only transitions with oscillator strengths >0.1 are presented.

**Table 2-10.** TD-DFT data for boranes **3-Ph**, **3-Et** and **4-Et** (rcam-b3lyp/6-31g(d))

| Compound    | Transition <sup>[a]</sup> | $E_{\text{ex}}$ (eV) | $\lambda$ (nm) | Oscillator strength $f$ | Assignment (%)  |
|-------------|---------------------------|----------------------|----------------|-------------------------|---|
| <b>3-Ph</b> | $S_0 \rightarrow S_1$     | <b>2.31</b>          | <b>536.42</b>  | <b>0.3880</b>           | <b>H <math>\rightarrow</math> L (0.70)</b>  |
|             | $S_0 \rightarrow S_{16}$  | 4.61                 | 269.04         | 0.1540                  | H-12 $\rightarrow$ L+1 (-0.11)  |
|             |                           |                      |                |                         | H-11 $\rightarrow$ L (0.53)   |
|             |                           |                      |                |                         | H-9 $\rightarrow$ L (0.28)  |
|             |                           |                      |                |                         | H-4 $\rightarrow$ L (-0.19)   |
|             |                           |                      |                |                         | H $\rightarrow$ L+2 (-0.10)   |
|             |                           |                      |                |                         | H $\rightarrow$ L+5 (-0.16)   |
|             | $S_0 \rightarrow S_{17}$  | 4.64                 | 266.99         | 0.5727                  | H-11 $\rightarrow$ L (0.14)<br>H-9 $\rightarrow$ L (0.16)<br>H-7 $\rightarrow$ L (-0.26)<br>H-7 $\rightarrow$ L+3 (-0.13)<br>H $\rightarrow$ L+5 (0.56) |
| <b>3-Et</b> | $S_0 \rightarrow S_1$     | <b>2.35</b>          | <b>528.04</b>  | <b>0.3555</b>           | <b>H <math>\rightarrow</math> L (0.70)</b>  |
|             | $S_0 \rightarrow S_8$     | 4.37                 | 283.86         | 0.1739                  | H-8 $\rightarrow$ L+1 (-0.14)   |
|             |                           |                      |                |                         | H-7 $\rightarrow$ L (0.13)  |
|             |                           |                      |                |                         | H-3 $\rightarrow$ L (0.59)  |
|             |                           |                      |                |                         | H-1 $\rightarrow$ L+1 (-0.22)   |
|             | $S_0 \rightarrow S_{10}$  | 4.63                 | 267.81         | 0.2553                  | H $\rightarrow$ L+4 (0.16)  |
|             |                           |                      |                |                         | H-7 $\rightarrow$ L (-0.23)   |
|             |                           |                      |                |                         | H-6 $\rightarrow$ L (-0.13)   |
|             |                           |                      |                |                         | H-5 $\rightarrow$ L (0.24)  |
|             |                           |                      |                |                         | H-2 $\rightarrow$ L (0.27)  |
|             | $S_0 \rightarrow S_{11}$  | 4.67                 | 265.25         | 0.1132                  | H-2 $\rightarrow$ L+3 (0.11)  |
|             |                           |                      |                |                         | H-1 $\rightarrow$ L+1 (-0.12)   |
|             |                           |                      |                |                         | H $\rightarrow$ L+5 (0.47)  |
|             |                           |                      |                |                         | H-6 $\rightarrow$ L (-0.35)   |
|             |                           |                      |                |                         | H-5 $\rightarrow$ L (0.48)  |
| <b>4-Et</b> | $S_0 \rightarrow S_{14}$  | 4.79                 | 258.62         | 0.1709                  | H-4 $\rightarrow$ L+1 (-0.11)   |
|             |                           |                      |                |                         | H-2 $\rightarrow$ L (-0.15)   |
|             |                           |                      |                |                         | H $\rightarrow$ L+5 (-0.22)   |
|             |                           |                      |                |                         | H-7 $\rightarrow$ L (0.49)  |
|             |                           |                      |                |                         | H-6 $\rightarrow$ L (0.17)  |
|             |                           |                      |                |                         | H-5 $\rightarrow$ L (0.19)  |
|             | $S_0 \rightarrow S_1$     | <b>2.89</b>          | <b>428.37</b>  | <b>0.2064</b>           | <b>H <math>\rightarrow</math> L (0.70)</b>  |

|                       |      |        |        |                               |
|-----------------------|------|--------|--------|-------------------------------|
| $S_0 \rightarrow S_8$ | 4.91 | 252.55 | 0.4576 | H-5 $\rightarrow$ L (0.24)    |
|                       |      |        |        | H-4 $\rightarrow$ L (-0.23)   |
|                       |      |        |        | H-2 $\rightarrow$ L+1 (0.19)  |
|                       |      |        |        | H-1 $\rightarrow$ L (-0.35)   |
|                       |      |        |        | H-1 $\rightarrow$ L+1 (0.15)  |
|                       |      |        |        | H-1 $\rightarrow$ L+2 (-0.12) |
|                       |      |        |        | H $\rightarrow$ L+3 (0.39)    |
| $S_0 \rightarrow S_9$ | 5.11 | 242.74 | 0.2714 | H-5 $\rightarrow$ L (0.56)    |
|                       |      |        |        | H-4 $\rightarrow$ L (0.19)    |
|                       |      |        |        | H-1 $\rightarrow$ L (0.13)    |
|                       |      |        |        | H $\rightarrow$ L+3 (-0.21)   |

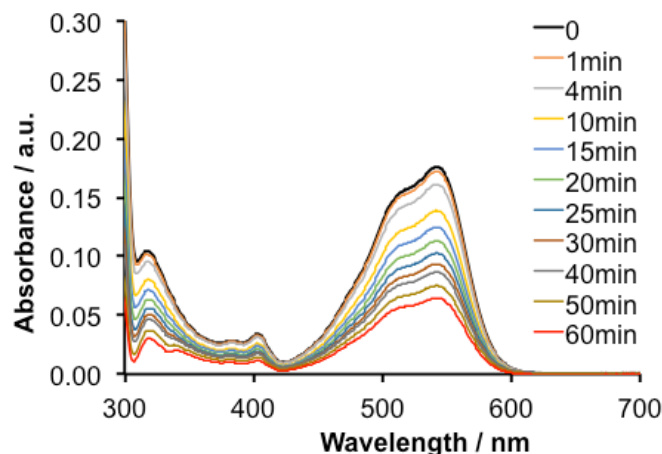
[a] Only transitions with oscillator strengths >0.1 are presented.

**Table 2-11.** Comparison of structural parameter at  $S_0$ ,  $S_1$ , and  $T_1$  state.

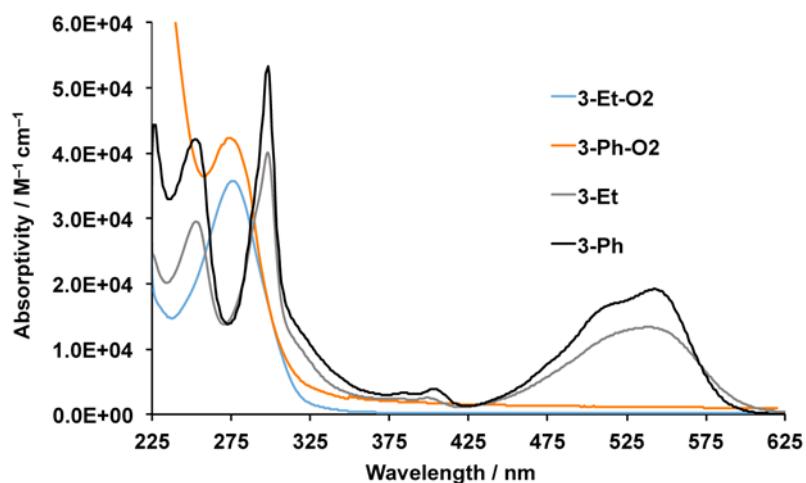
|                              | B-N    | B-C <sub>An</sub> | C <sub>An</sub> -C <sub>Py</sub> | C <sub>An</sub> -B-N | Cent <sub>An</sub> -<br>C-B | Cent <sub>An</sub> -C-<br>C <sub>Py</sub> | Ph <sub>An,outer</sub> //<br>Ph <sub>An,outer</sub> | Ph <sub>An,inner</sub> //<br>Py |
|------------------------------|--------|-------------------|----------------------------------|----------------------|-----------------------------|---|---|---------------------------------|
| <b>3-Et<sub>S0,cis</sub></b> | 1.688, | 1.622,            | 1.475,                           | 108.0,               | 174.8,                      | 168.9,                                    | 20.3  | 35.9,                           |
|                              | 1.700  | 1.625             | 1.474                            | 107.9                | 176.7                       | 170.3                                     |   | 35.7                            |
| <b>3-Et<sub>S1,cis</sub></b> | 1.649, | 1.611,            | 1.449,                           | 109.2,               | 176.8,                      | 168.9,                                    | 26.4  | 31.7,                           |
|                              | 1.659  | 1.616             | 1.450                            | 109.0                | 176.3                       | 169.9                                     |   | 31.0                            |
| <b>3-Et<sub>T1,cis</sub></b> | 1.669, | 1.617,            | 1.442,                           | 108.6,               | 177.0,                      | 167.8,                                    | 30.2  | 31.2,                           |
|                              | 1.677  | 1.621             | 1.441                            | 108.6                | 175.2                       | 169.0                                     |   | 29.8                            |
| <b>3-Ph<sub>S0,cis</sub></b> | 1.680  | 1.627             | 1.474                            | 107.8                | 173.7                       | 167.8                                     | 21.3  | 35.6                            |
| <b>3-Ph<sub>S1,cis</sub></b> | 1.639, | 1.618,            | 1.447,                           | 109.4                | 177.6                       | 168.3                                     | 32.1  | 29.3                            |
|                              | 1.640  | 1.617             | 1.448                            |                      |                             |   |   |                                 |
| <b>3-Ph<sub>T1,cis</sub></b> | 1.660, | 1.621             | 1.441                            | 108.8                | 177.7                       | 167.2,                                    | 34.3  | 30.1                            |
|                              | 1.661  |                   |                                  |                      |                             | 167.3                                     |   |                                 |
| <b>4-Et<sub>S0</sub></b>     | 1.699  | 1.627             | 1.476                            | 106.1                | 168.9                       | 167.8                                     | 9.7   | 37.9                            |
| <b>4-Et<sub>S1</sub></b>     | 1.612  | 1.596             | 1.461                            | 109.8                | 172.0                       | 169.0                                     | 12.7  | 34.2                            |
| <b>4-Et<sub>T1</sub></b>     | 1.675  | 1.621             | 1.439                            | 107.2                | 175.5                       | 165.2                                     | 16.4  | 33.6                            |

## Formation of Endoperoxides

Kinetic experiments were performed using a commercially available blue LED light with an emission maximum at 464 nm. The respective borane compound was dissolved in oxygen-saturated DCM at a concentration of ca. 0.01 mM and the sample placed in a quartz cuvette at a distance of 10 cm from the LED light source. The photooxygenation was monitored by UV-vis spectroscopy, following the decrease of the absorption maximum of the oxygen-free compound.

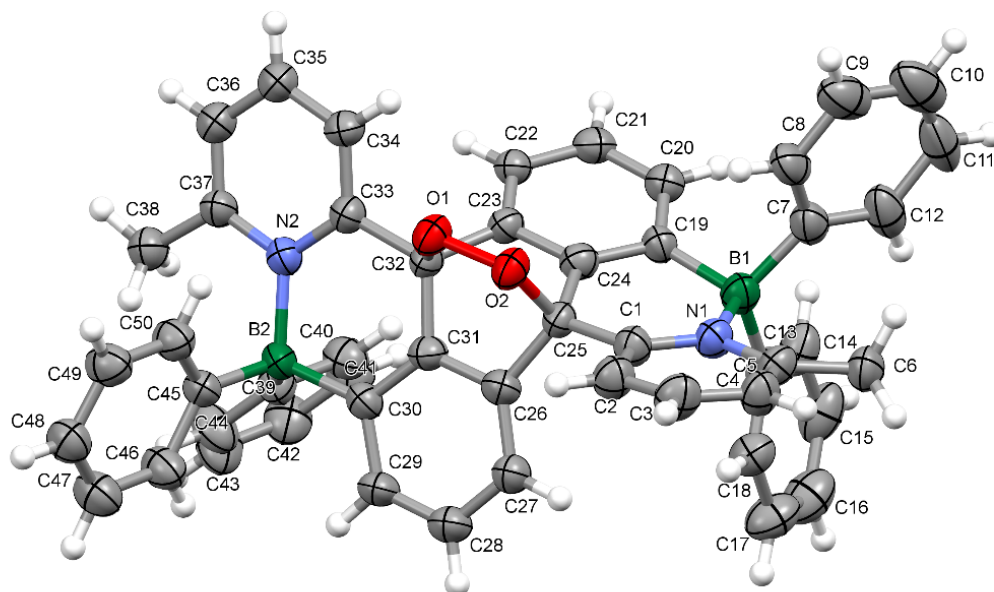


**Figure 2-24.** Illustration of changes in the absorption for an oxygen-saturated solution of compound **3-Ph** in DCM upon irradiation with a blue LED.

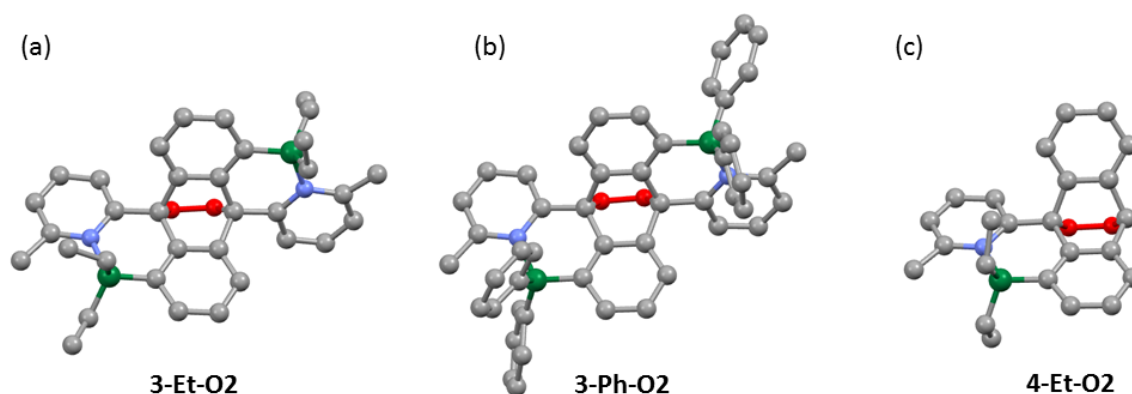


**Figure 2-25.** Normalized UV-Vis absorption spectra in DCM of endoperoxides **3-R-O2** in comparison to the O<sub>2</sub>-free species **3-R** (R = Ph, Et). For **3-Ph-O2**:  $\epsilon_{\text{abs}} = 4.24 \times 10^4 \text{ M}^{-1}\text{cm}^{-1}$ ; for **3-Et-O2**:  $\epsilon_{\text{abs}} = 3.58 \times 10^4 \text{ M}^{-1}\text{cm}^{-1}$ .





**Figure 2-26.** X-ray crystal structure of one of three independent molecules of **3-Ph-O2** (50% thermal ellipsoids). Selected bond distances (Å) and interplanar angles (°): B1-N1 1.641(6), B2-N2 1.665(5), B1-C19 1.615(6), B2-C30 1.618(6), N1-C1 1.366(5), N1-C5 1.383(5), N2-C33 1.368(5), N2-C37 1.377(5), C1-C25 1.505(5), C32-C33 1.519(5), O1-O2 1.486(3), N1-B1-C19 108.5(3), N2-B2-C30 109.1(3), B1-N1-C1 123.7(3), B2-N2-C33 123.8(3), B1-C19-C24 121.8(4), B2-C30-C31 123.0(4), C1-C25-C24 116.1(3), C31-C32-C33 118.7(3), C1-N1-C5 117.9(4), C33-N2-C37 116.8(3),  $\text{Ph}_{\text{An,outer}} // \text{Ph}_{\text{An,outer}}$  57.5,  $\text{Ph}_{\text{An,inner}} // \text{Py}$  46.3, 36.7.

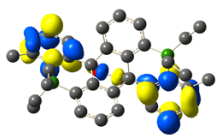
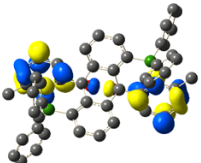
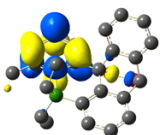
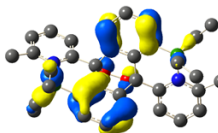
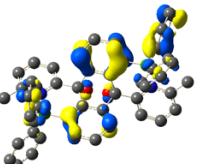
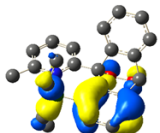


**Figure 2-27.** Optimized structures of (a) **3-Et-O2**, (b) **3-Ph-O2**, (c) **4-Et-O2** (Gaussian 09; rb3lyp/6-31g(d)). C grey, B green, N blue, O red.

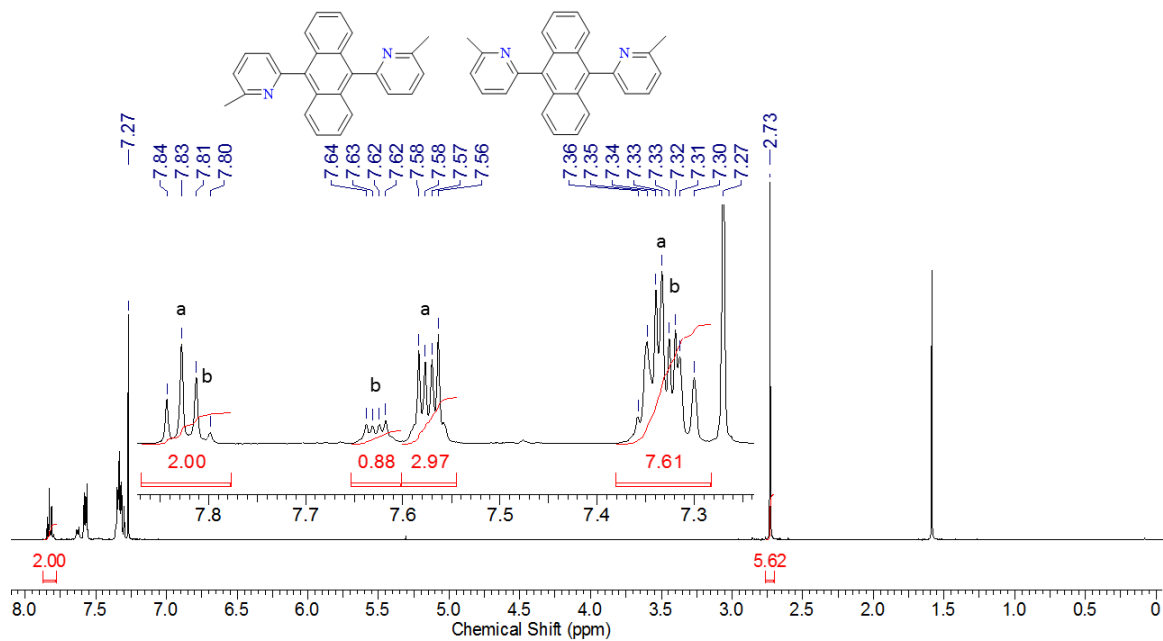
**Table 2-12.** Comparison of geometric parameters for endoperoxides (distances in Å, angles in °) obtained from X-ray structure analysis and DFT calculations

|  | B-N                   | B-C <sub>An</sub>     | C <sub>An</sub> -C <sub>Py</sub> | O-O      | C <sub>An</sub> -B-N  | Cent <sub>An</sub> -<br>C-B | Cent <sub>An</sub> -<br>C-C <sub>Py</sub> | Ph <sub>An,outer</sub> //<br>Ph <sub>An,outer</sub> | Ph <sub>An,inner</sub> //<br>Py |
|--|-----------------------|-----------------------|----------------------------------|----------|-----------------------|-----------------------------|---|---|---------------------------------|
| <b>3-Ph-O2<sub>X-ray</sub></b><br><b>(1)</b> | 1.641(6),<br>1.665(5) | 1.615(6),<br>1.618(6) | 1.505(5),<br>1.519(5)            | 1.486(3) | 108.5(3),<br>109.1(3) | 176.6,<br>178.4             | 171.5,<br>168.4                           | 57.5  | 46.3,<br>36.7                   |
| <b>3-Ph-O2<sub>X-ray</sub></b><br><b>(2)</b> | 1.649(6),<br>1.666(6) | 1.613(6),<br>1.609(6) | 1.506(6),<br>1.519(6)            | 1.489(4) | 108.0(3),<br>108.4(3) | 177.4,<br>177.8             | 170.6,<br>169.7                           | 46.9  | 38.6,<br>35.7                   |
| <b>3-Ph-O2<sub>X-ray</sub></b><br><b>(3)</b> | 1.681(6),<br>1.641(7) | 1.602(6),<br>1.611(7) | 1.504(5),<br>1.506(6)            | 1.483(4) | 108.3(4),<br>108.7(4) | 173.0,<br>175.1             | 168.1,<br>170.3                           | 64.9  | 28.1,<br>37.7                   |
| <b>3-Et-O2<sub>th</sub></b>                  | 1.727,<br>1.745       | 1.617,<br>1.619       | 1.517,<br>1.515                  | 1.465    | 107.5,<br>107.7       | 175.1,<br>176.0             | 170.3,<br>169.8                           | 58.4  | 40.0,<br>41.9                   |
| <b>3-Ph-O2<sub>th</sub></b>                  | 1.706,<br>1.700       | 1.618                 | 1.515                            | 1.468    | 108.7,<br>108.7       | 179.0,<br>178.0             | 169.4,<br>170.1                           | 57.9  | 37.3,<br>38.7                   |
| <b>4-Et-O2<sub>th</sub></b>                  | 1.740                 | 1.614                 | 1.517                            | 1.473    | 107.5                 | 177.9                       | 170.3                                     | 57.1  | 38.6                            |

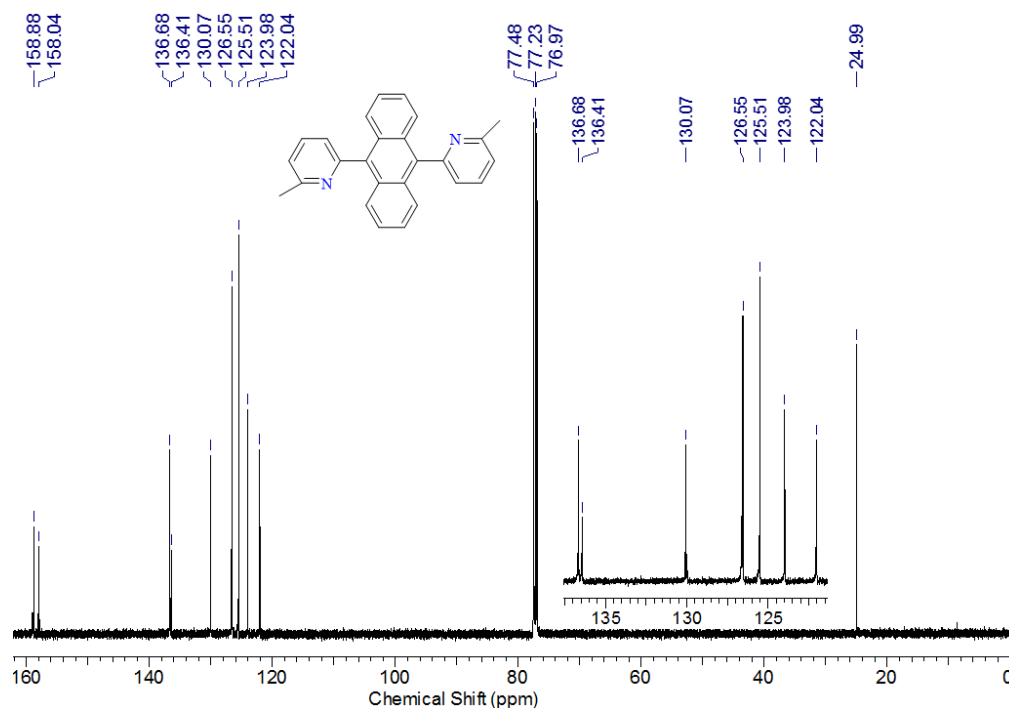
**Table 2-13.** Orbital plots for BN-functionalized anthracene endoperoxides ((rb3lyp/6-31g(d), scaling radii of 75%, isovalue = 0.04)

|      | 3-Et-O2  | 3-Ph-O2   | 4-Et-O2  |
|------|--|---|--|
| LUMO | <br>- 1.89 eV | <br>- 2.07 eV | <br>- 1.91 eV |
| HOMO | <br>- 5.84 eV | <br>- 5.81 eV | <br>- 5.91 eV |

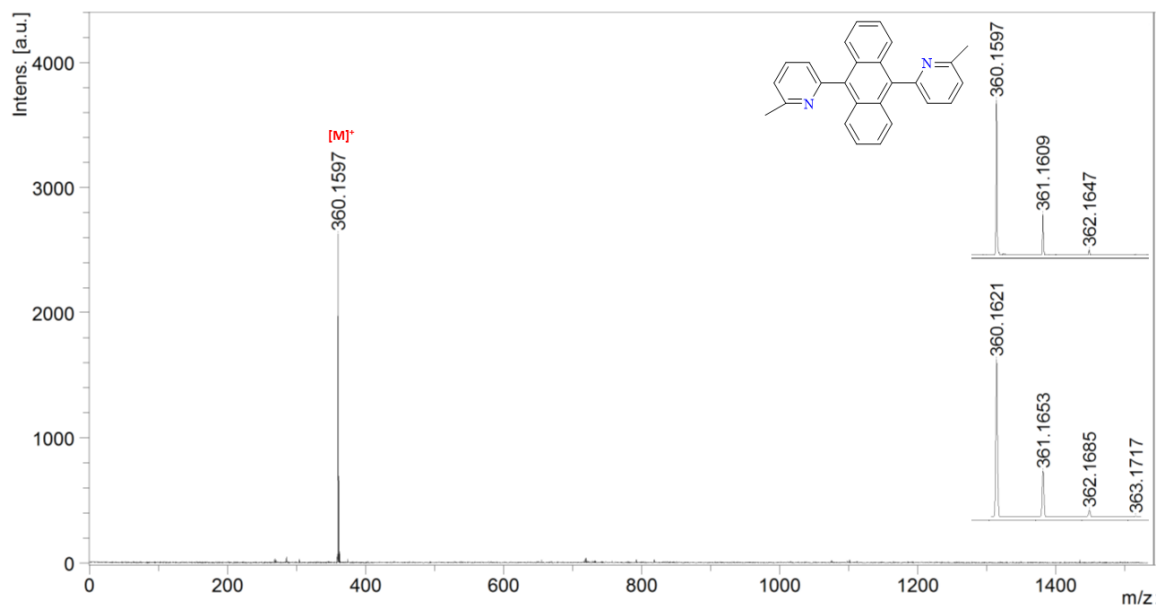
### Spectral Data for Isolated Compounds



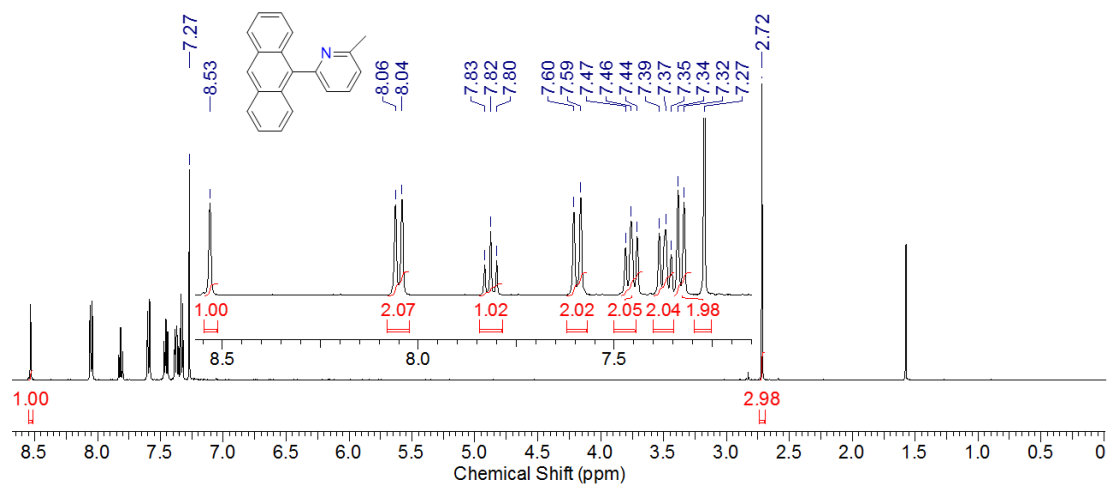
**Figure 2-28.**  $^1\text{H}$  NMR spectrum of 9,10-bis(6-methylpyrid-2-yl)anthracene (**2**) in  $\text{CDCl}_3$ ; the two isomers are assigned as a and b



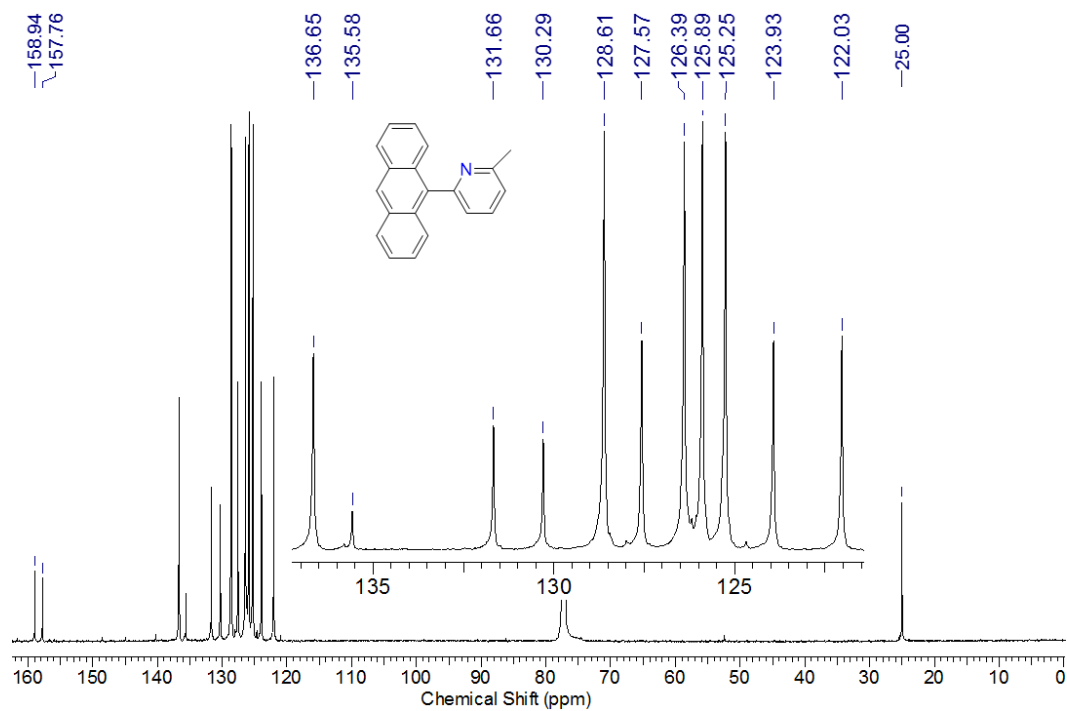
**Figure 2-29.**  $^{13}\text{C}$  NMR spectrum of 9,10-bis(6-methylpyrid-2-yl)anthracene (**2**) in  $\text{CDCl}_3$



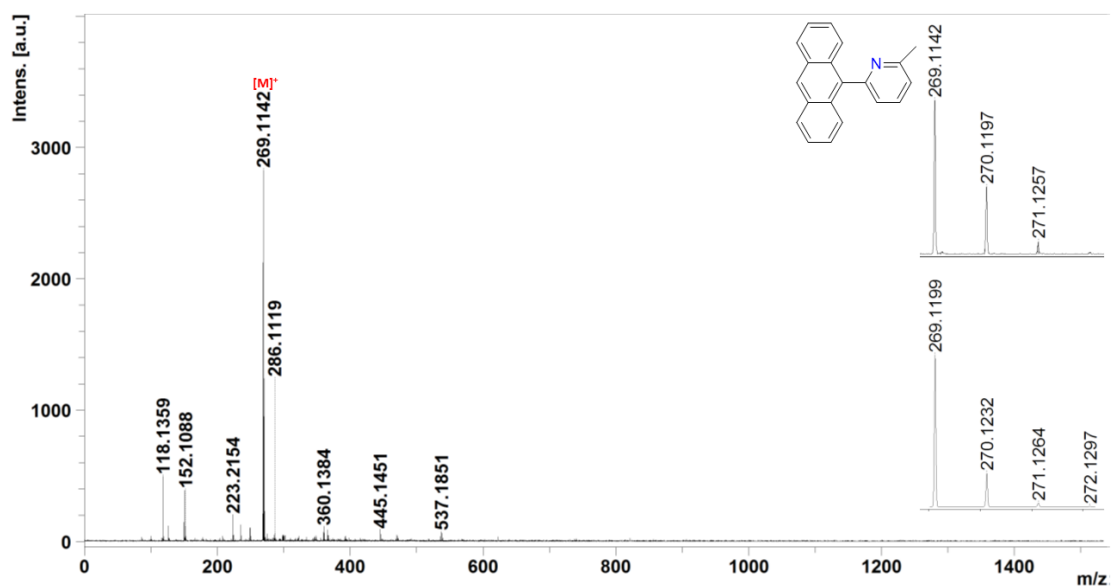
**Figure 2-30.** MALDI-TOF mass spectrum (pos. mode) of 9,10-bis(6-methylpyrid-2-yl)anthracene (**2**)



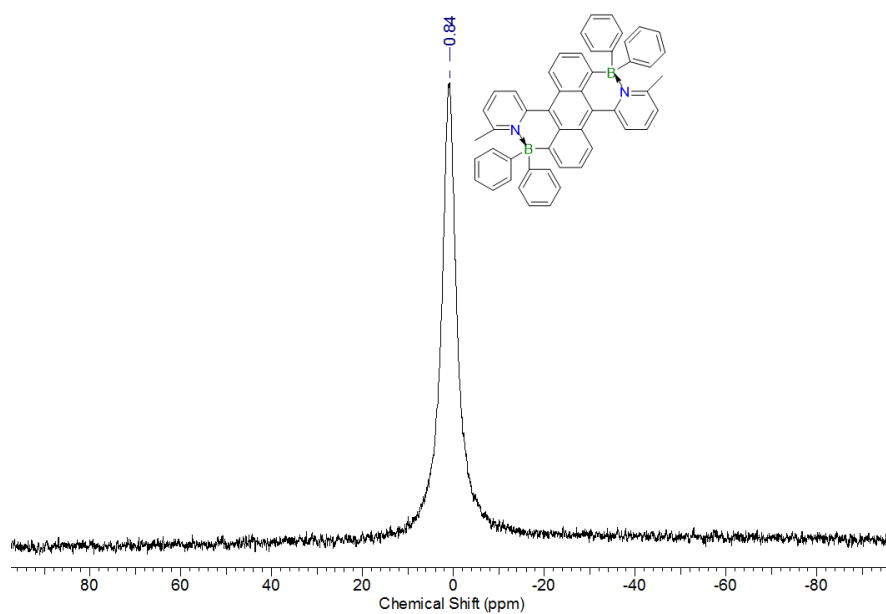
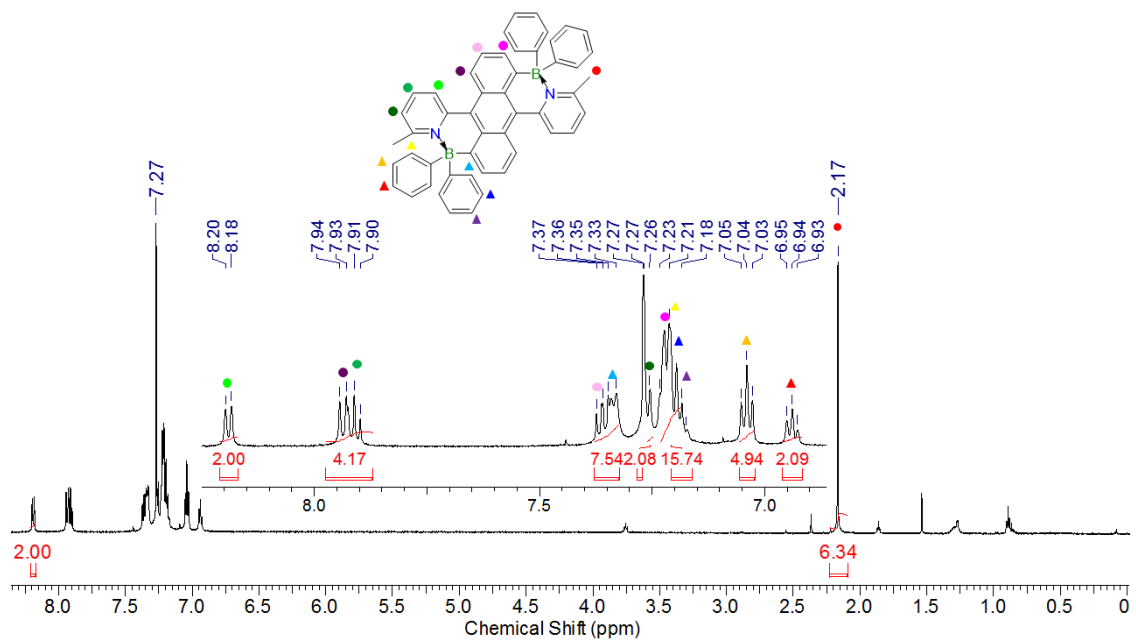
**Figure 2-31.**  $^1\text{H}$  NMR spectrum of 9-(6-methylpyrid-2-yl)anthracene (**2M**) in  $\text{CDCl}_3$



**Figure 2-32.** <sup>13</sup>C NMR spectrum of 9-(6-methylpyrid-2-yl)anthracene (**2M**) in CDCl<sub>3</sub>



**Figure 2-33.** MALDI-TOF mass spectrum (pos. mode) of 9-(6-methylpyrid-2-yl)anthracene (**2M**)



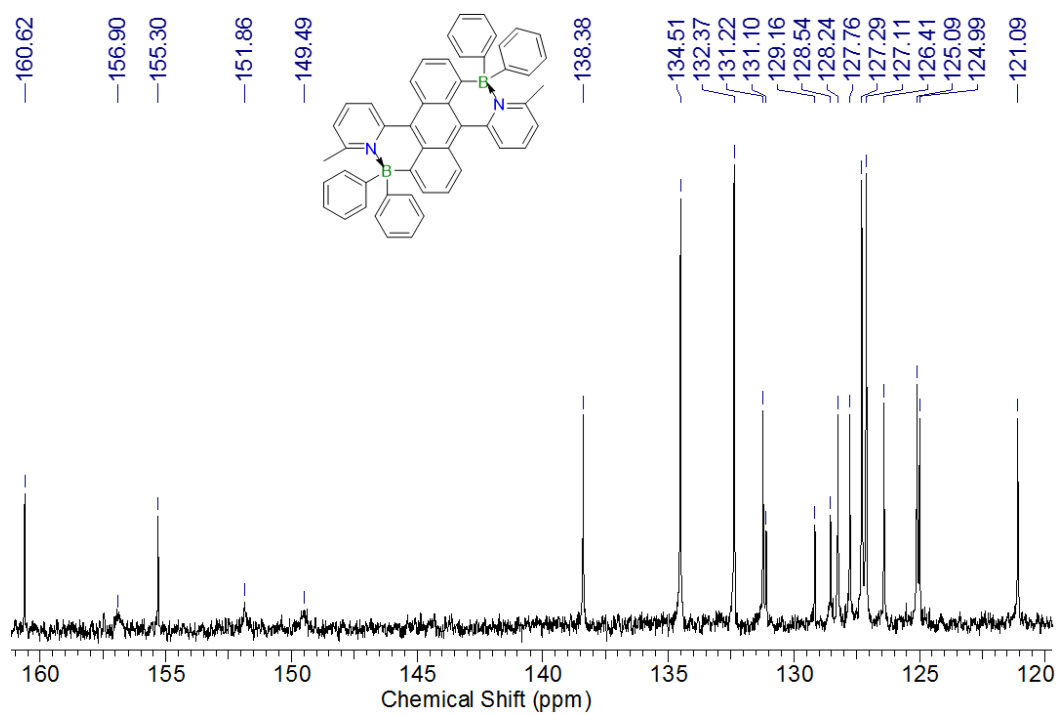
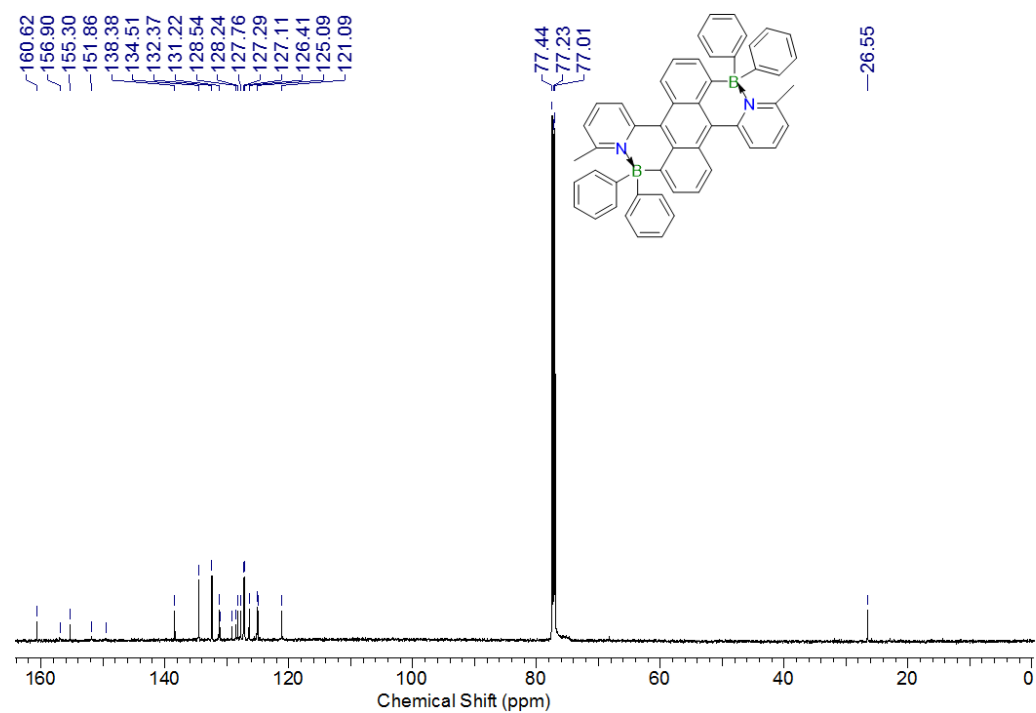


**Figure 2-36.** <sup>13</sup>C NMR spectrum of **3-Ph** in CDCl<sub>3</sub>

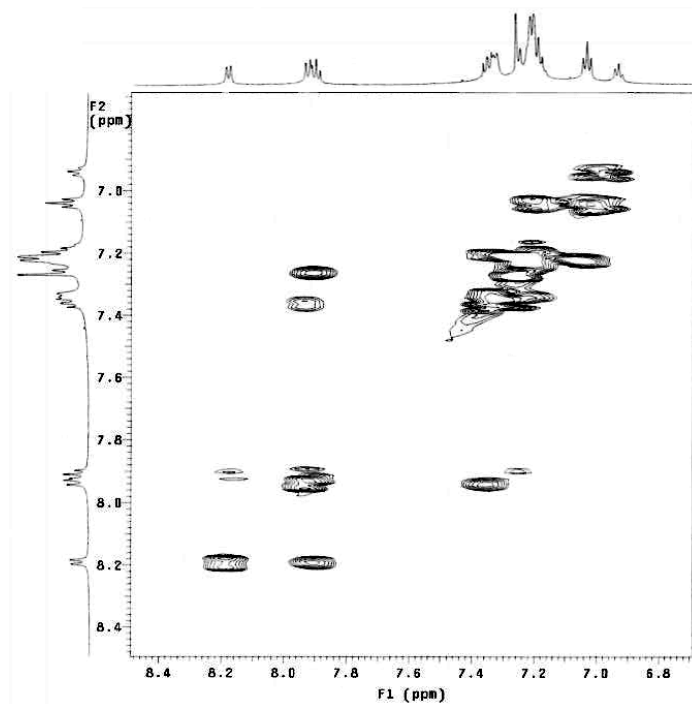


**Figure 2-37.** gCOSY NMR spectrum of **3-Ph** (aromatic region, CDCl<sub>3</sub>, 25 °C)

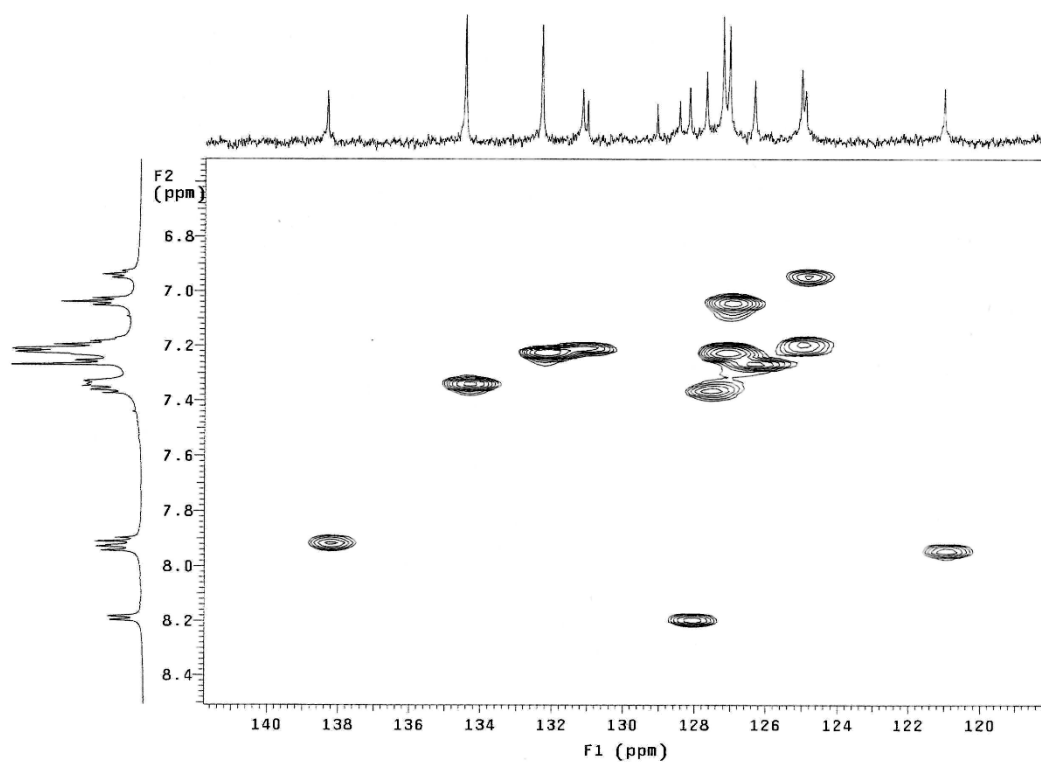


**Figure 2-38.** HMQC NMR spectrum of **3-Et** (aromatic region, CDCl<sub>3</sub>, 25 °C)



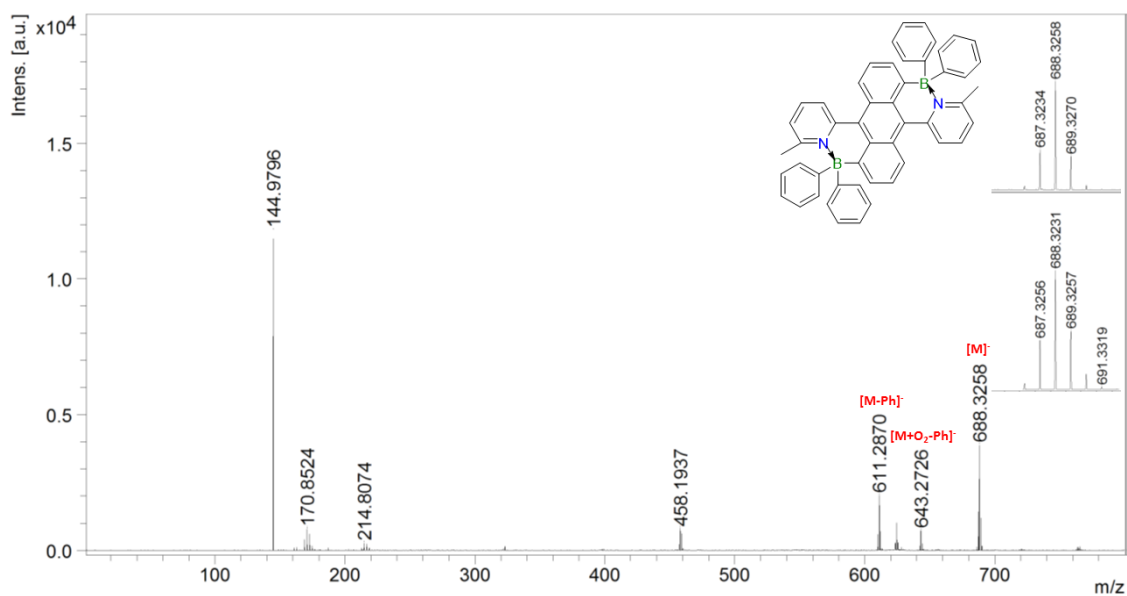


**Figure 2-39.** MALDI-TOF mass spectrum (neg. mode) of **3-Ph**

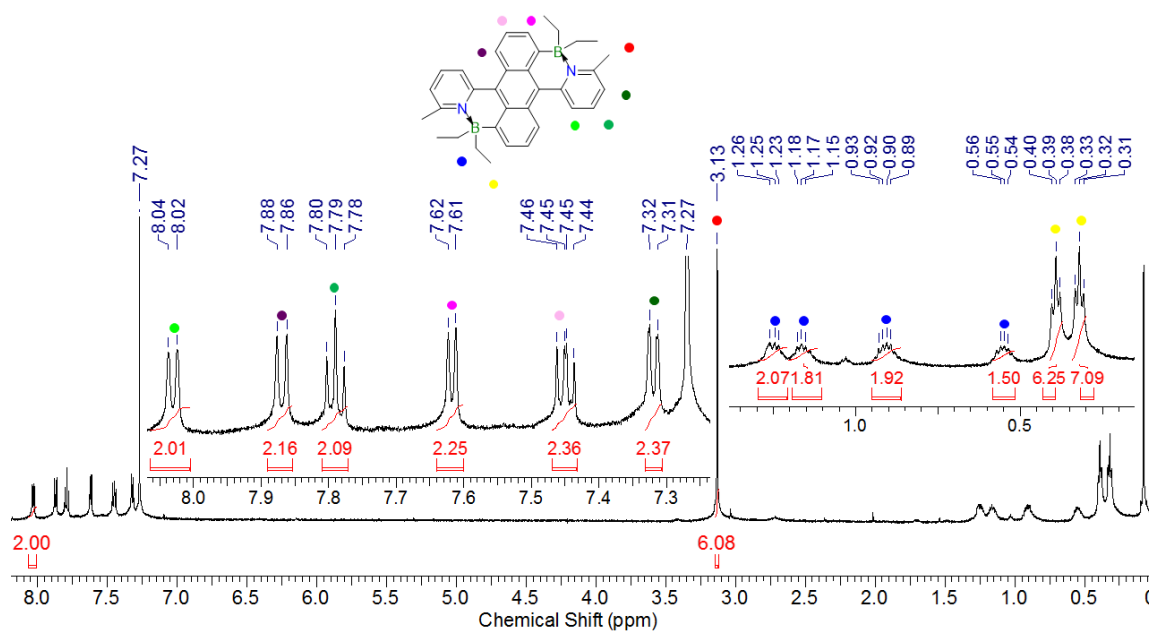


**Figure 2-40.** <sup>1</sup>H NMR spectrum of **3-Et** in CDCl<sub>3</sub>

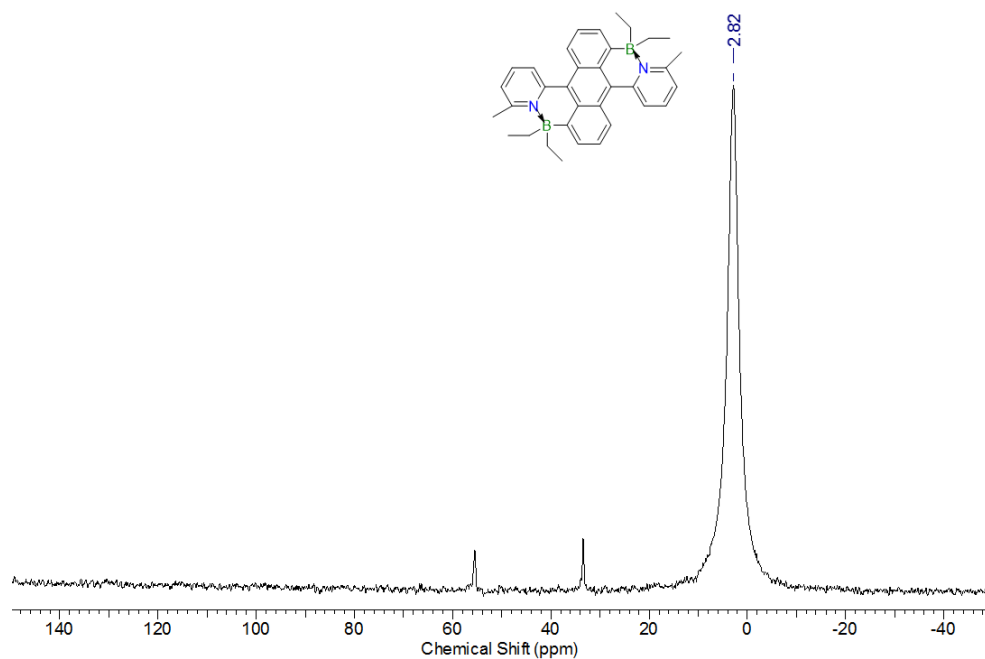


**Figure 2-41.**  $^{11}\text{B}$  NMR spectrum of **3-Et** in  $\text{CDCl}_3$

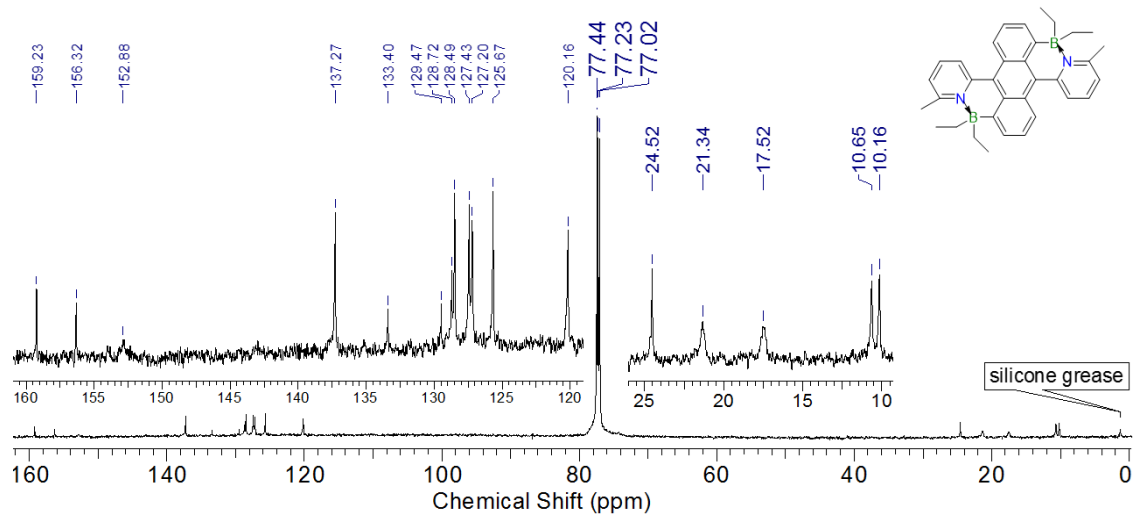


**Figure 2-42.**  $^{13}\text{C}$  NMR spectrum of **3-Et** in  $\text{CDCl}_3$

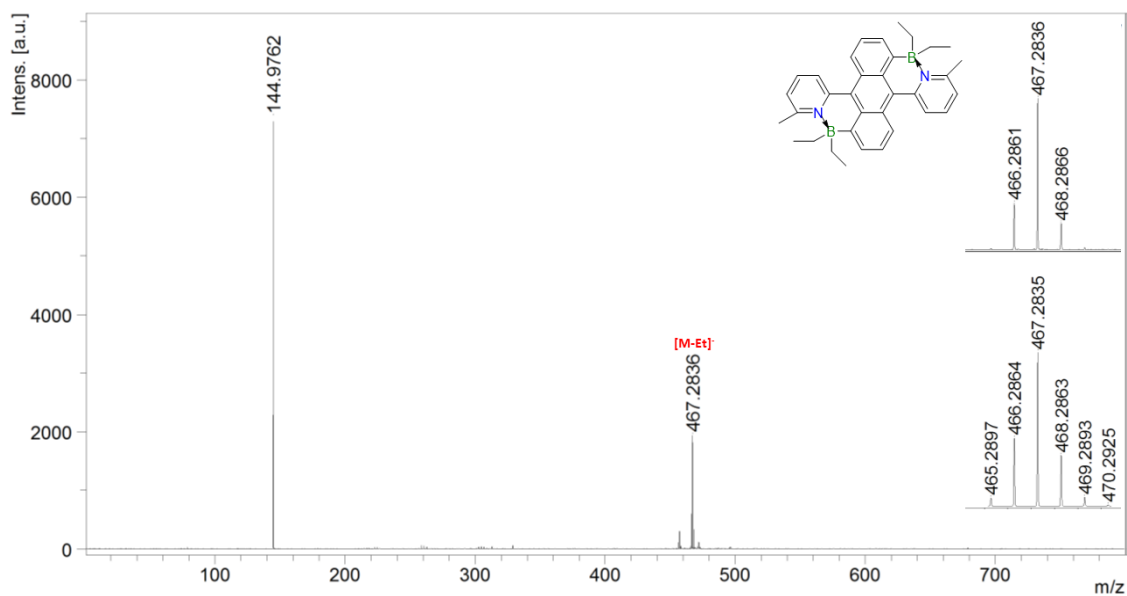


**Figure 2-43.** MALDI-TOF mass spectrum (neg. mode) of **3-Et**

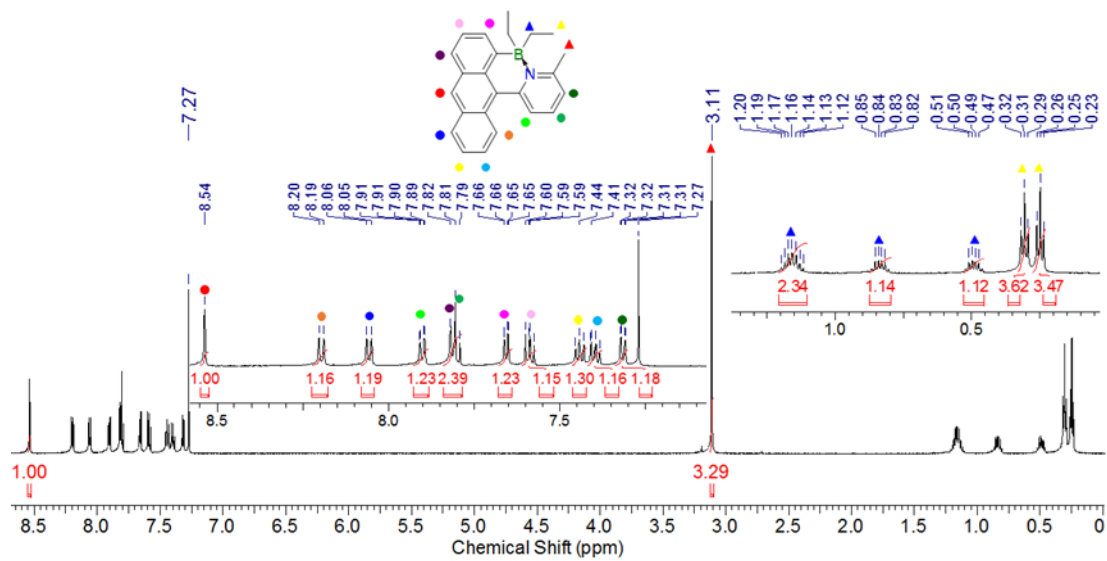


**Figure 2-44.**  $^1\text{H}$  NMR spectrum of **4-Et** in  $\text{CDCl}_3$  ( $-5^\circ\text{C}$ )

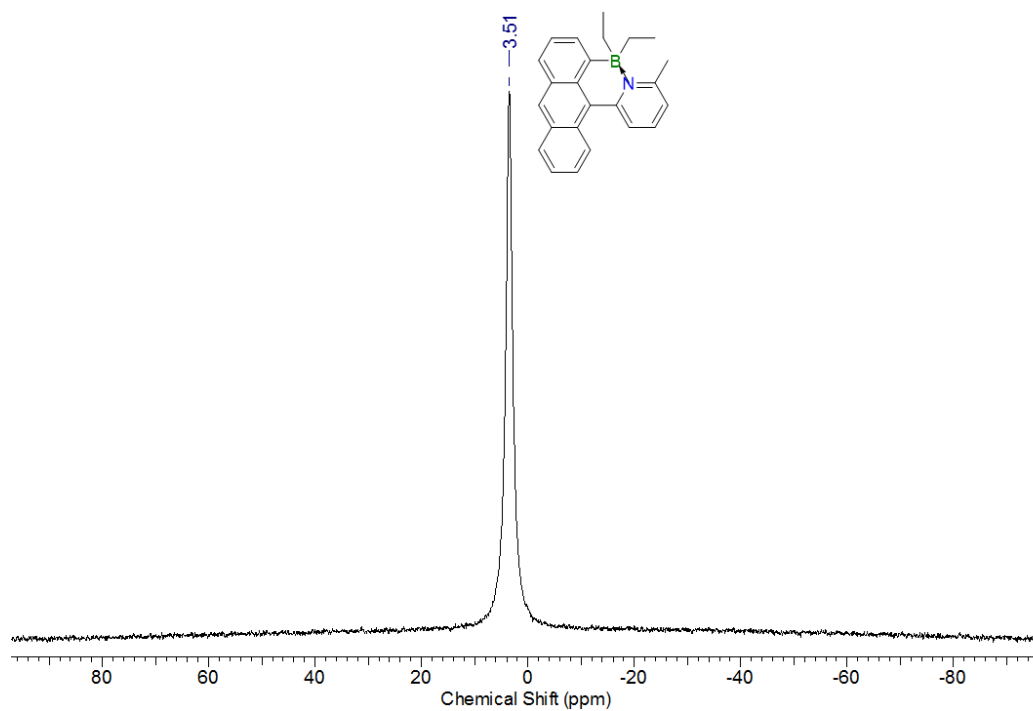


**Figure 2-45.**  $^{11}\text{B}$  NMR spectrum of 4-Et in  $\text{CDCl}_3$

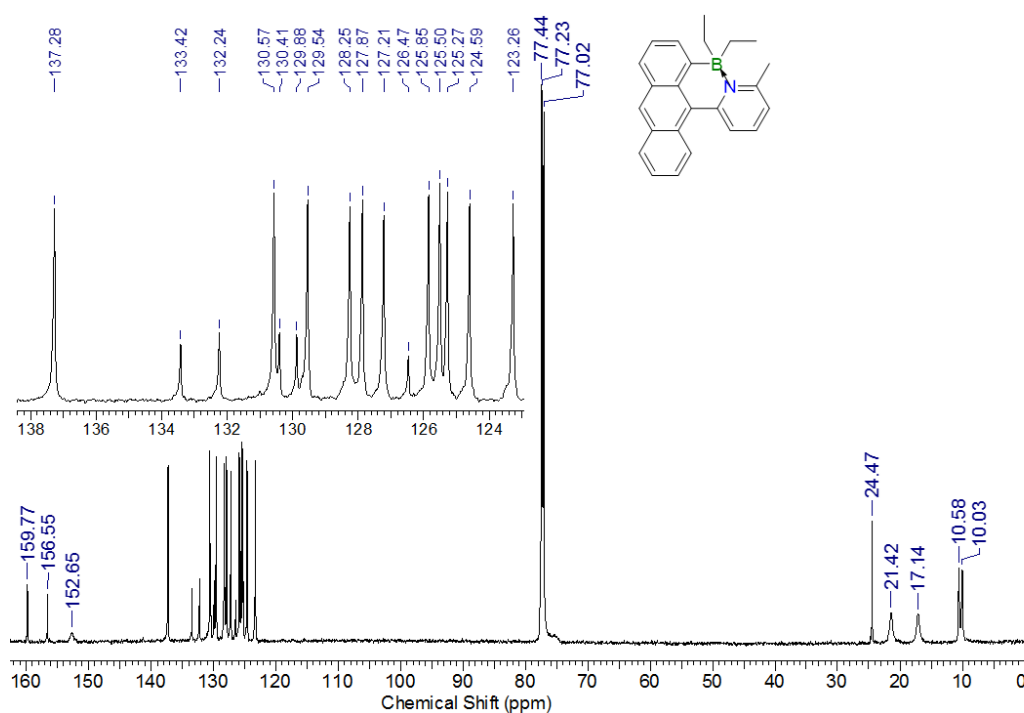


**Figure 2-46.**  $^{13}\text{C}$  NMR spectrum of 4-Et in  $\text{CDCl}_3$

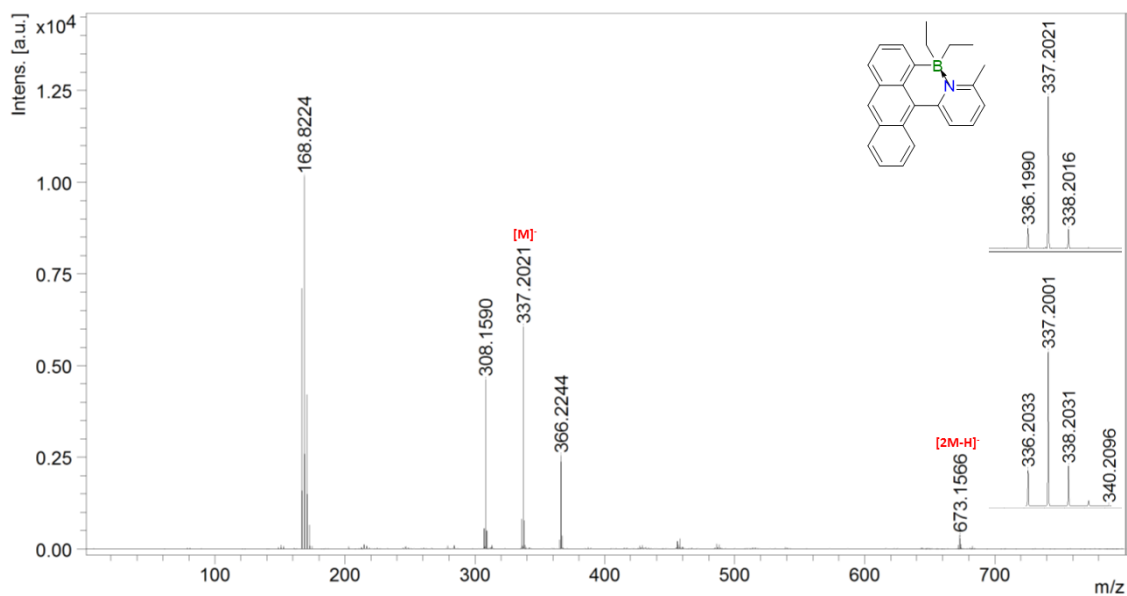


**Figure 2-47.** MALDI-TOF mass spectrum (neg. mode) of 4-Et

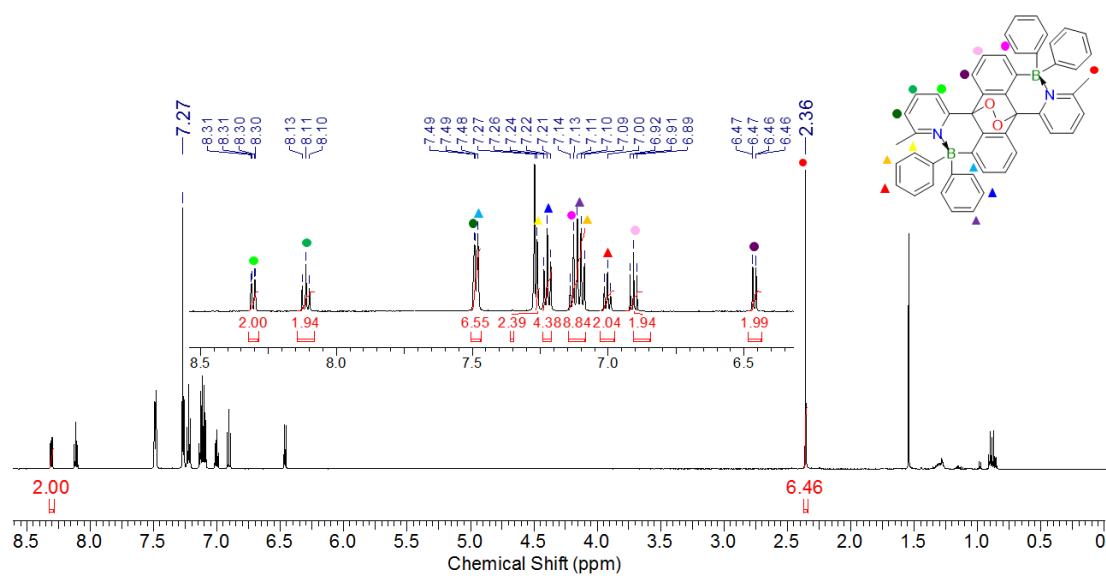


**Figure 2-48.**  $^1\text{H}$  NMR spectrum of 3-Ph-O2 in  $\text{CDCl}_3$

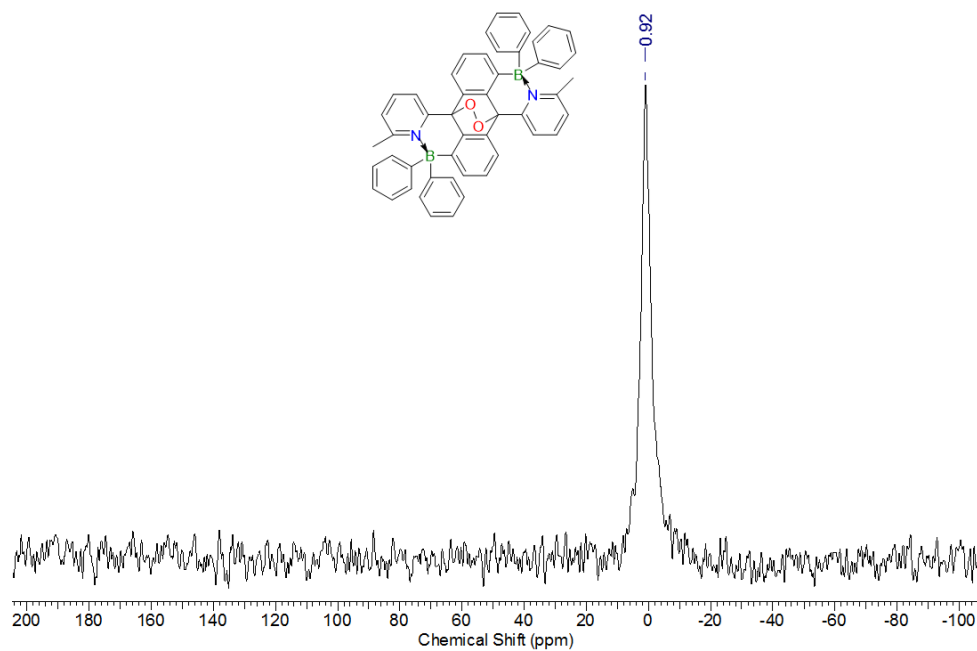


**Figure 2-49.**  $^{11}\text{B}$  NMR spectrum of **3-Ph-O2** in  $\text{CDCl}_3$

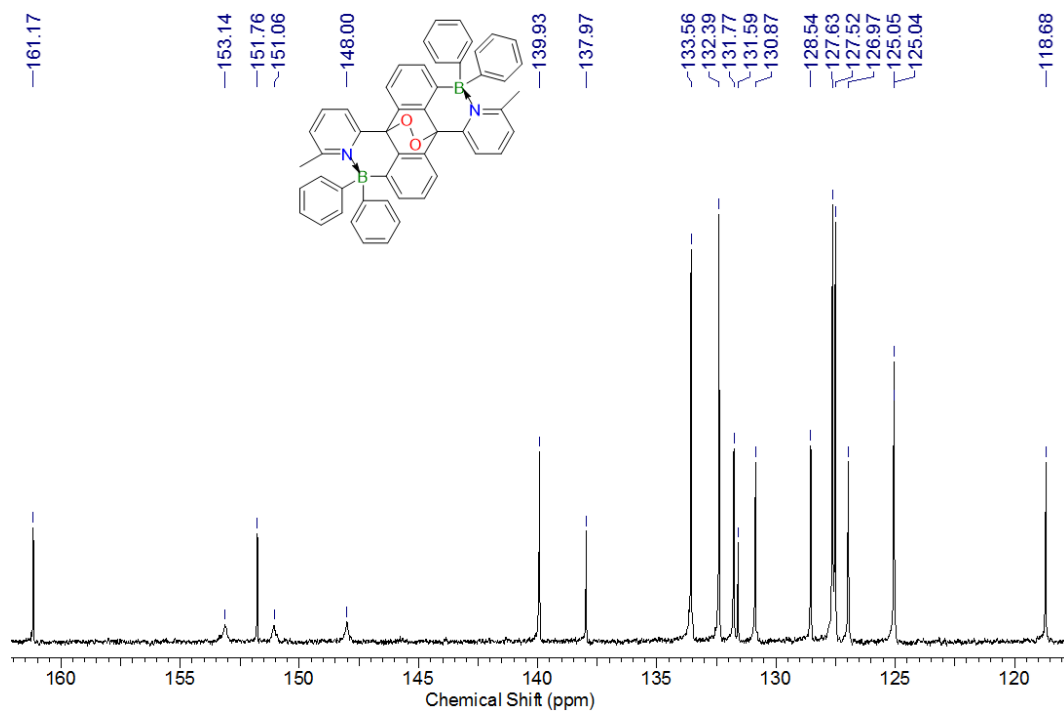
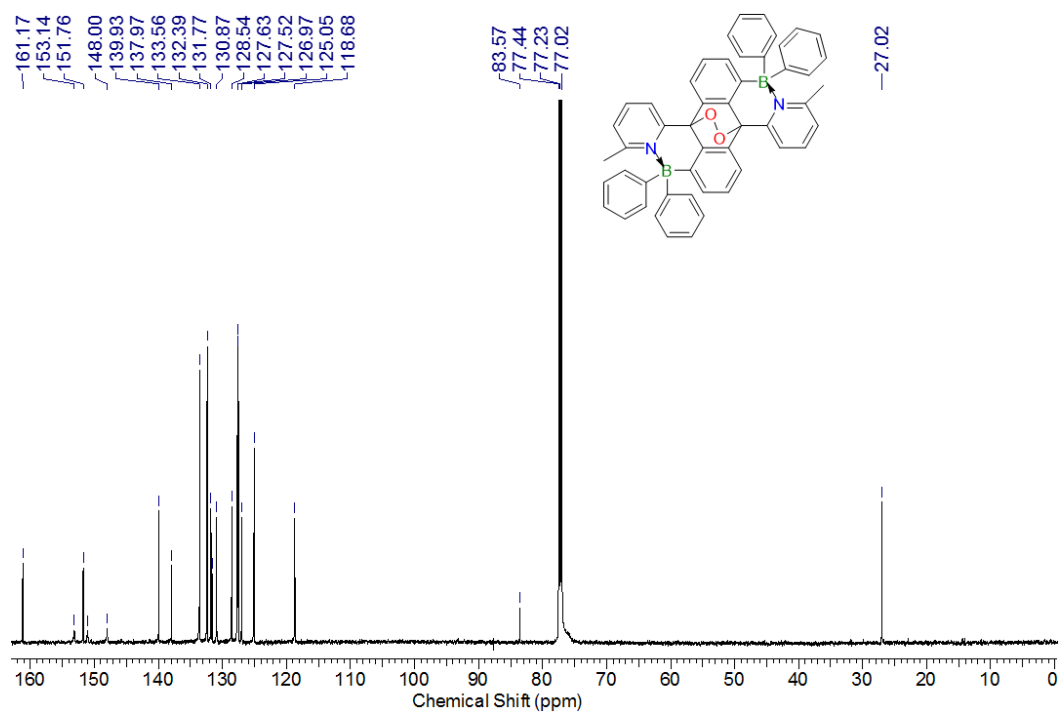


**Figure 2-50.**  $^{13}\text{C}$  NMR spectrum of **3-Ph-O2** in  $\text{CDCl}_3$

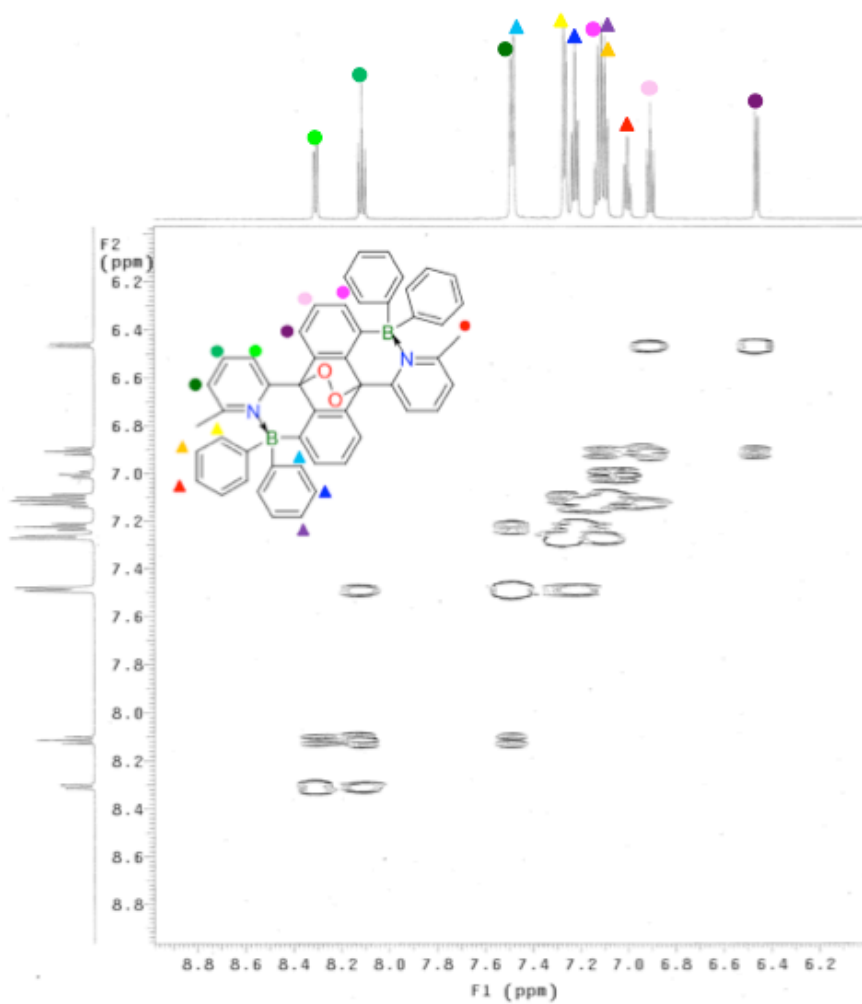


**Figure 2-51.** gCOSY NMR spectrum of **3-Ph-O2** (aromatic region, CDCl<sub>3</sub>, RT)



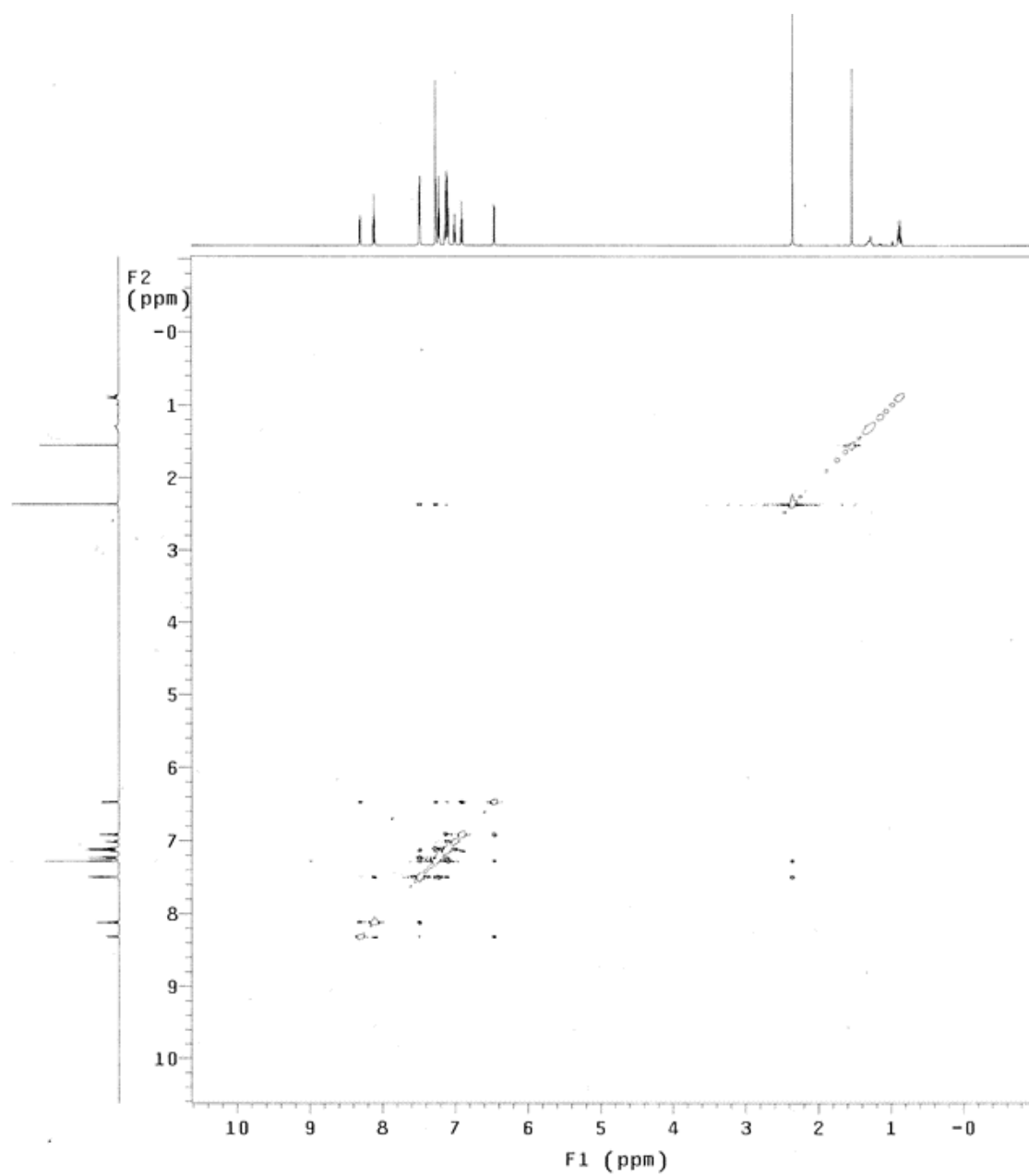


**Figure 2-52a.** Full  $^1\text{H}$ , $^1\text{H}$ -NOESY NMR spectrum of **3-Ph-O2** ( $\text{CDCl}_3$ , RT, mixing time: 0.6 s).

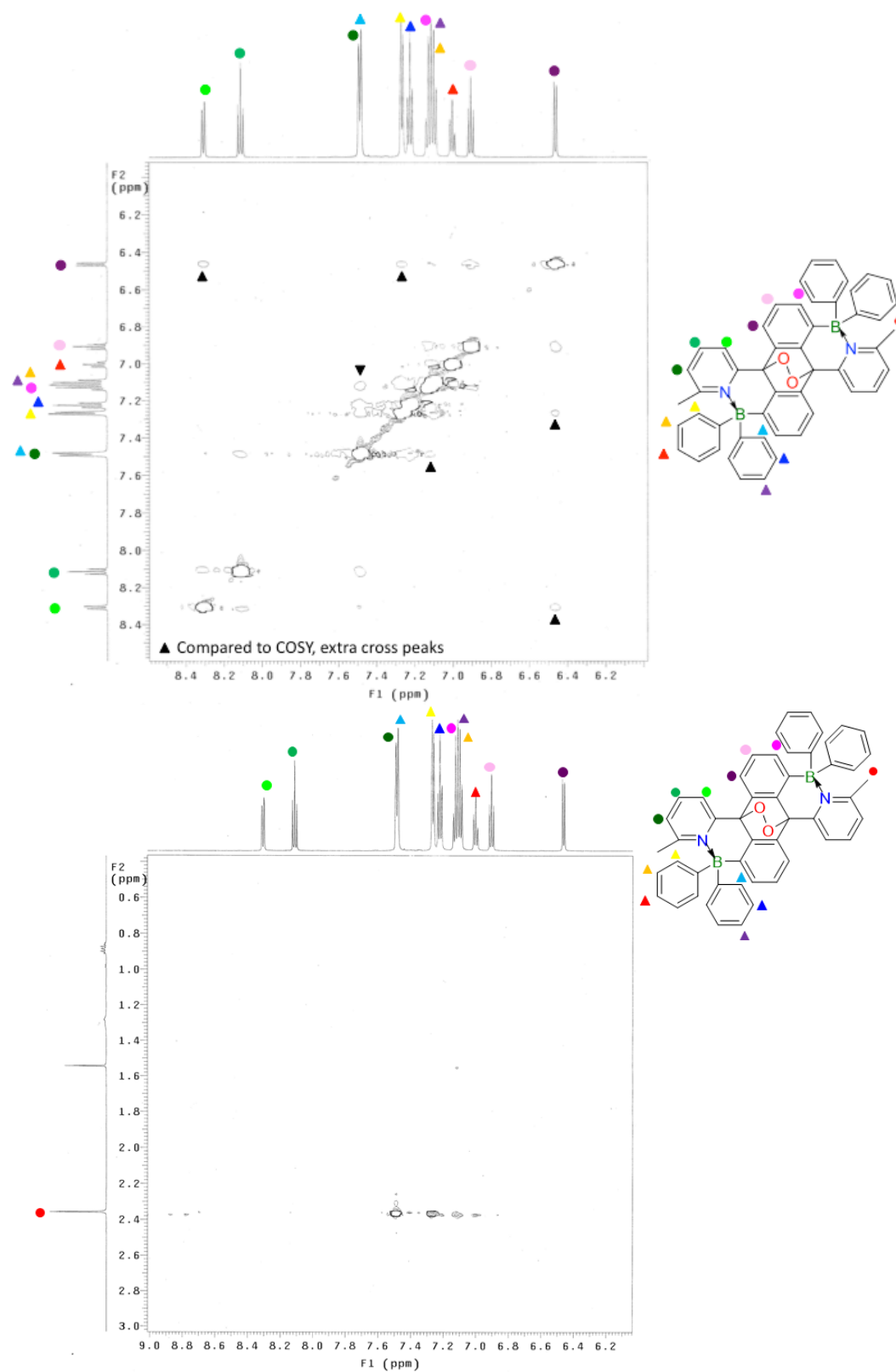


**Figure 2-52b.** Expansions of  $^1\text{H}$ - $^1\text{H}$  NOESY NMR spectrum of **3-Ph-O2** ( $\text{CDCl}_3$ , RT, mixing time: 0.6 s).

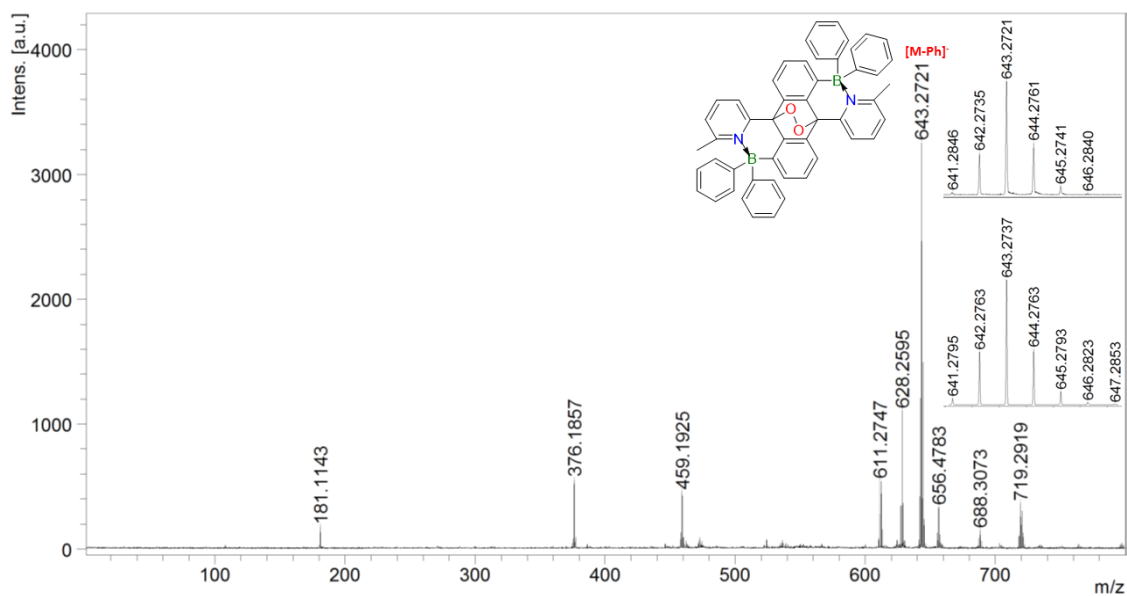


**Figure 2-53.** MALDI-TOF mass spectrum (neg. mode) of **3-Ph-O2**

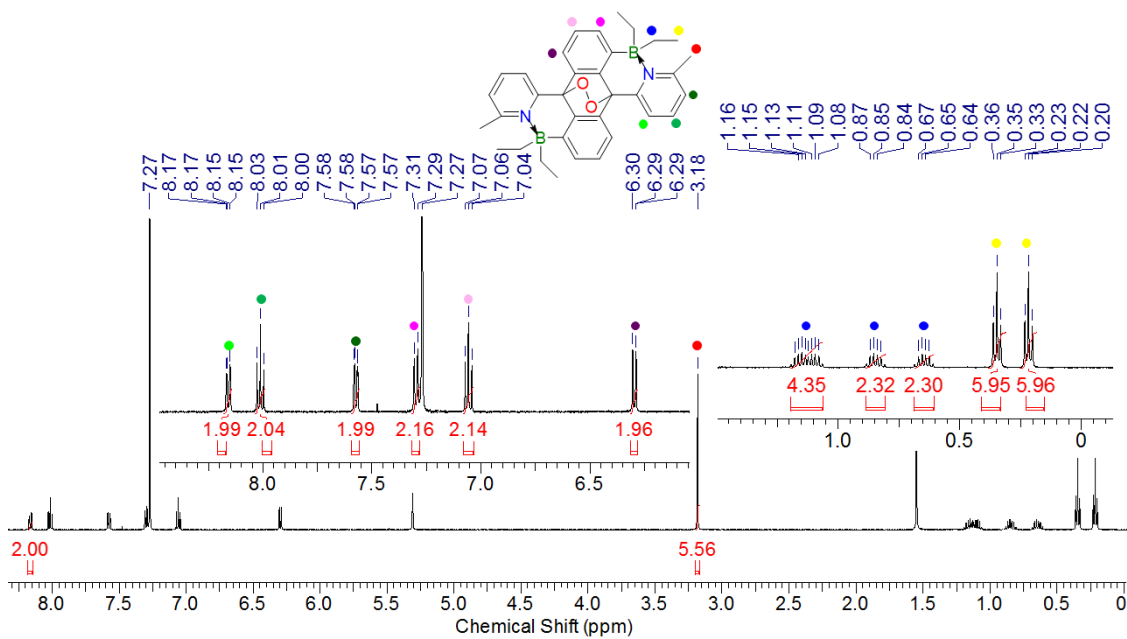


**Figure 2-54.**  $^1\text{H}$  NMR spectrum of **3-Et-O2** in  $\text{CDCl}_3$

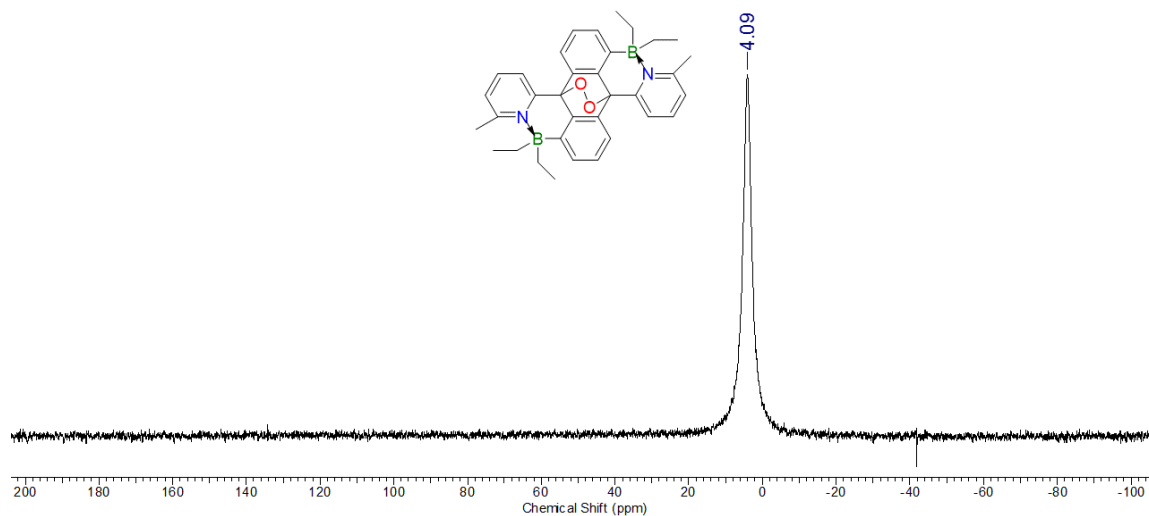


**Figure 2-55.**  $^{11}\text{B}$  NMR spectrum of **3-Et-O2** in  $\text{CDCl}_3$

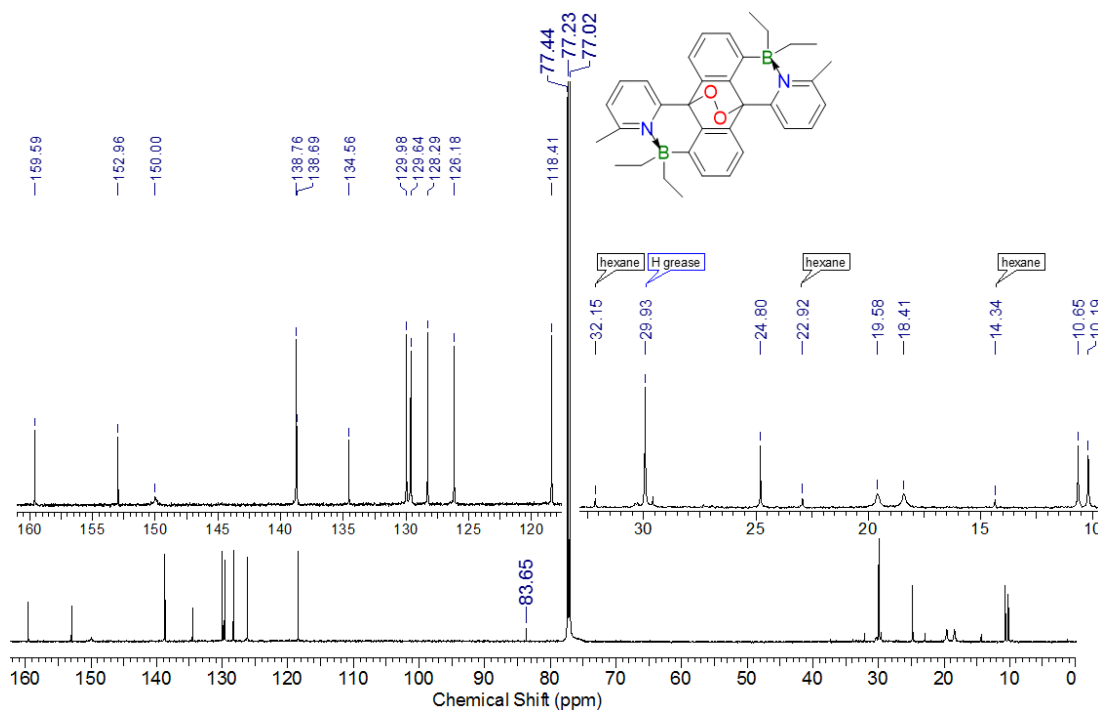


**Figure 2-56.**  $^{13}\text{C}$  NMR spectrum of **3-Et-O2** in  $\text{CDCl}_3$

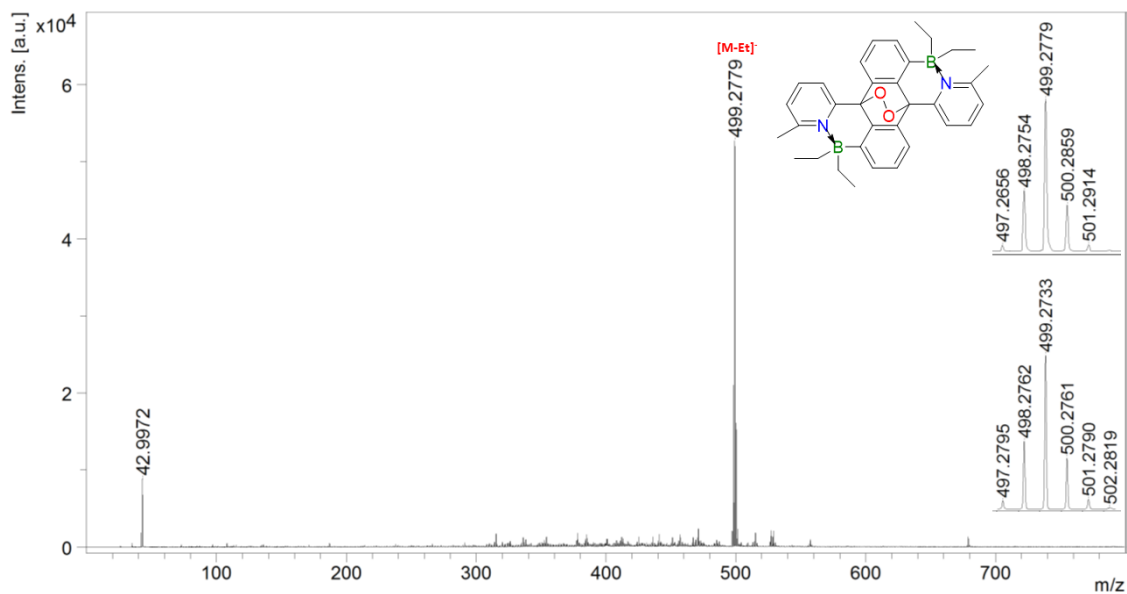


**Figure 2-57.** MALDI-TOF mass spectrum (neg. mode) of **3-Et-O2**

## Chapter 3 Steric and Electronic Effects of Pyridyl Substituents and Implications on the Self-Sensitized Reactivity with Singlet Oxygen

[a]

### 3.1 Introduction

The incorporation of heteroatoms presents a promising approach to judiciously alter the optical and electronic properties of organic  $\pi$ -conjugated materials.<sup>1</sup> By embedding electron-deficient boron atoms or replacing C-C for isoelectronic B-N units in particular, desirable properties such as acceptor character due to lower lying LUMO orbitals, red-shifted absorptions and emissions reaching into the near-IR, thermally activated delayed fluorescence (TADF), and enhanced charge carrier mobilities can be realized.<sup>2</sup> In a conceptually different approach the electronic structure of conjugated organic materials can also be modulated by B $\leftarrow$ N Lewis pair functionalization at their periphery. In this case, Lewis acid-base interactions result in the formation of tetra- rather than tricoordinate borane groups. Such an approach offers intriguing opportunities due to (i) the ensuing planarization of the molecular skeleton that results in enhanced extension of  $\pi$ -conjugation and improved rigidity favoring radiative over non-radiative decay; (ii) the increased electron-deficient character due to lower LUMO levels upon attachment of the borane Lewis acid groups; (iii) the potential for stimuli-responsive “smart” materials and molecular switches enabled by the reversibility of the Lewis pair formation.<sup>3</sup>

---

[a] This chapter is adapted from a journal publication (ref. 33).

Several methods are available for the attachment of B←N Lewis pairs including lithiation-borylation sequences, transition metal-catalyzed C-H borylation,<sup>4</sup> hydroboration of vinyl-functionalized derivatives,<sup>5</sup> or Lewis base-directed electrophilic borylation<sup>6</sup>. Taking advantage of these diverse synthetic routes, researchers have functionalized various N-heterocyclic-substituted conjugated organic materials with boron in an effort at developing new luminescent materials for OLEDs and imaging applications, electron transporting and acceptor materials for transistors and organic solar cells (OSCs), as well as photochromic and pH-switchable materials.<sup>3d, 3e, 6b, 7</sup>

We have recently embarked on an effort to explore the effects of the Lewis pair functionalization on larger  $\pi$ -conjugated scaffolds based on polycyclic aromatic hydrocarbons (PAHs). PAHs are attracting enormous research interest because of their desirable optical and electronic properties with applications ranging from organic electronics (OLEDs, OPVs, OFETs, singlet fission) to chemical sensors, catalysis and bioimaging.<sup>8</sup> They also serve important roles as models and building blocks for the bottom-up synthesis of larger conjugated carbon materials<sup>1c, 9</sup> and as components of supramolecular materials via Diels-Alder and photocyclization chemistries.<sup>10</sup> In addition, the ability of certain PAHs to reversibly form endoperoxides<sup>11</sup> can be exploited to deliver singlet oxygen for applications in photodynamic therapy,<sup>12</sup> in sensing,<sup>13</sup> lithography,<sup>14</sup> fluorescent anti-counterfeiting<sup>15</sup>, and switches<sup>16</sup>.

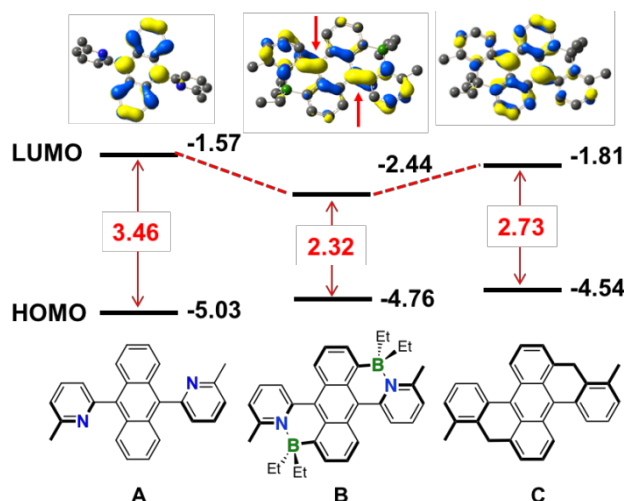


**Figure 3-1.** Structure, orbital energies, and LUMO plot of borylated BN-anthracene (**B**) in comparison to the all-carbon analog (**C**) and the boron-free ligand (**A**).

Efforts at the B←N Lewis pair functionalization of larger PAHs are only just emerging. Unique reactivity patterns have been uncovered,<sup>17</sup> intriguing molecular switching properties have been reported,<sup>7e, 7f, 18</sup> and circularly polarized luminescence (CPL) has been realized in the case of borylated helicenes.<sup>19</sup> We are pursuing the functionalization of PAHs by utilizing Lewis basic pyridyl<sup>20</sup> anchoring groups. In a first foray, we have recently demonstrated that the directed electrophilic borylation of dipyrrolylanthracene (**A**) results in selective borylation in the 1,5-positions<sup>11c, 21</sup> to give novel BN-fused polycyclic aromatic hydrocarbons (**B**, Figure 3-1).<sup>22</sup> The formation of the B←N Lewis pairs at the periphery of anthracene leads on one hand to planarization as the pyridyl groups adopt a more coplanar conformation with the anthracene core, but on the other hand induces significant steric strain that results in deformation (buckling) of the anthracene backbone. In addition, the BN units result in a polarization relative to the respective planarized all-carbon congener,<sup>23</sup> hence the LUMO is dramatically lowered and displays an enhanced quinoidal character relative to the all-carbon congener (**C**). Collectively, the planarization and polarization



leads to an unusual change in color to deep red with a strong orange emission, as well as self-sensitized reactivity with O<sub>2</sub> to reversibly produce the corresponding endoperoxides. As part of our continuing efforts to better understand the effects of borane functionalization on the structural features and electronic properties, in this work we have investigated four isomeric derivatives of BN-fused dipyridylanthracene with Me groups in different positions of the pyridyl ring. We find that the steric and electronic effects have a significant influence on the B←N bond strength, the extent of distortion, and the structural dynamics in this system. In addition, we demonstrate that different substituents dramatically affect the photophysical and electrochemical properties, as well as the self-sensitized reactivity of the acenes toward oxygen and the subsequent thermal release of singlet oxygen from the respective endoperoxides.

### 3.2 Results and Discussion

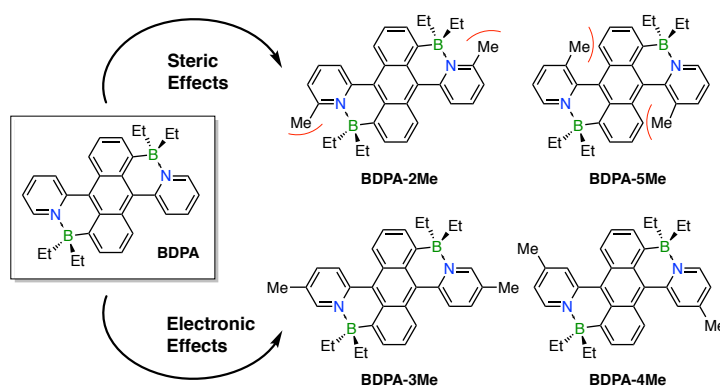


**Figure 3-2.** Structures of BN-anthracenes investigated by DFT methods.

To examine the effects of different substituents on the B-N bond lengths, structural distortions and electronic properties of BN-fused dipyridylanthracene we first conducted DFT calculations on four isomeric derivatives with Me groups in different positions of the pyridyl rings, as well as the parent non-methylated species **BDPA** (Figure 3-2). We

anticipated the methyl groups in derivatives **BDPA-3Me** and **BDPA-4Me** to have no significant steric influence, but to differ in terms of the electronic effects as 4-methylpyridine is expected to be a relatively stronger Lewis base. In contrast, the methyl groups in **BDPA-2Me** are expected to exert front strain that disfavors B←N Lewis pair formation, whereas steric strain in **BDPA-5Me** would be derived from interference of the methyl groups with the adjacent anthracene backbone protons in the 4 and 8-positions. We determined previously that the *cis*-isomer of **BDPA-2Me**, in which the pyridyl nitrogens point in the same direction and the boron atoms are dislocated from the anthracene backbone toward the same side, is significantly lower in energy than its *trans*-isomer.<sup>22</sup> Indeed, the same is true for all the other compounds (Table 3-6) and the results of the calculations on the thermodynamically favored *cis*-isomers for **BDPA-3Me**, **BDPA-4Me** and **BDPA-5Me** are presented in the following.

Geometry optimization predicts the longest B-N distance for the previously reported derivative **BDPA-2Me** (1.690 Å) and the shortest for **BDPA-4Me** (1.640 Å) (Table 3-1). The relatively longer B-N distance for **BDPA-2Me** is consistent with steric interference between the Py-Me and BEt<sub>2</sub> groups, whereas the shorter B-N distance for **BDPA-4Me** highlights the enhanced Lewis basicity of 4-methylpyridine, though the differences between **BDPA-3Me**, **BDPA-4Me** and the non-methylated parent molecule are modest. An important observation is that the B-N distance for **BDPA-5Me** (1.655 Å) is significantly larger than that for **BDPA-3Me** (1.643 Å) (both have the Me group in *meta*-position), which suggests that remote steric effects also influence the strength of the B←N interactions. Indeed, by far the largest distortions to the anthracene backbone are found for **BDPA-5Me** with an interplanar angle between the terminal benzene rings of  $\epsilon = 25.6^\circ$

(Figure 3-3). Another criterion to assess the steric strain is the dislocation of the boron atoms from the plane of the benzene rings that they are attached to. Again, the largest distortions are found for **BDPA-5Me** with Cent1-C<sub>1,5</sub>-B angles of  $\beta = 168.8^\circ$  that significantly deviate from the ideal angle of  $180^\circ$ . Our results suggest that in the case of **BDPA-5Me**, the close proximity of the Me substituents to the anthracene backbone results not only in strong “buckling” of the anthracene backbone, but also greater dislocation of the boron substituents and weaker B←N interactions. While the Me substituents in 2-position lead primarily to a lengthening of the B←N bonds, the molecule appears to be otherwise less distorted than **BDPA-3Me**, **BDPA-4Me**, or even the non-methylated derivative. This indicates that a lengthening of the B-N distance leads to a relaxation of the overall steric strain of the molecule. We also note that the internal bending of the central benzene ring ( $\delta$ ) is in all cases less than the interplanar angle between the terminal benzene rings ( $\epsilon$ ), which indicates that the terminal benzene rings of anthracene also contribute to the distortions.

**Table 3-1.** Comparison of computed geometric parameters of **BDPA** and its methyl-substituted derivatives (DFT, rb3lyp/6-31g(d))

| Compound        | B-N   | B-C <sub>1,5</sub> | C <sub>9,10</sub> -C <sub>Py</sub> | $\alpha$ [a] | $\beta$ [b] | $\gamma$ [c] | $\delta$ [d] | $\varepsilon$ [e] | $\phi$ [f] |
|-----------------|-------|--------------------|------------------------------------|--------------|-------------|--------------|--------------|-------------------|------------|
| <b>BDPA</b>     | 1.642 | 1.619              | 1.471                              | 105.3        | 171.2       | 165.4        | 18.4         | 21.3              | 36.2       |
| <b>BDPA-2Me</b> | 1.690 | 1.626              | 1.474                              | 107.4        | 172.2       | 167.6        | 17.4         | 21.6              | 40.0       |
| <b>BDPA-3Me</b> | 1.643 | 1.618              | 1.471                              | 105.5        | 171.0       | 165.8        | 18.1         | 20.7              | 35.4       |
| <b>BDPA-4Me</b> | 1.640 | 1.618              | 1.472                              | 105.4        | 171.0       | 165.6        | 18.2         | 21.1              | 35.8       |
| <b>BDPA-5Me</b> | 1.655 | 1.618              | 1.474                              | 105.7        | 168.8       | 167.3        | 20.9         | 25.6              | 42.2       |

[a]  $\alpha$  = C<sub>1,5</sub>-B-N angle; [b]  $\beta$  = Cent1-C<sub>1,5</sub>-B; [c]  $\gamma$  = Cent2-C<sub>9,10</sub>-C<sub>Py</sub>; [d]  $\delta$  = internal bending of central anthracene ring; [e]  $\varepsilon$  = Ph<sub>An,out</sub> // Ph<sub>An,out</sub>, dihedral angle between outer anthracene rings; [f]  $\phi$  = Ph<sub>An,in</sub> // Py, dihedral angle between inner anthracene ring and pendent pyridyl ring.

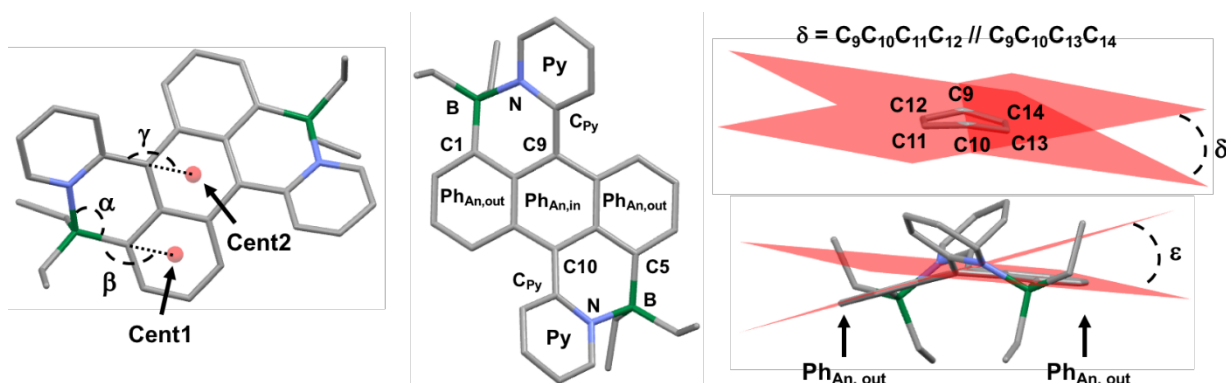


**Figure 3-3.** Illustration of geometric parameters discussed for BN-anthracenes.

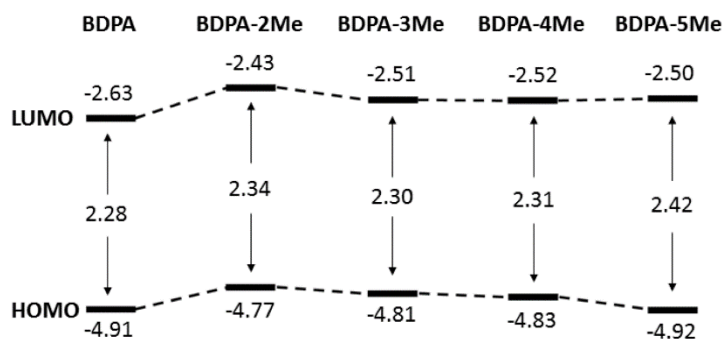
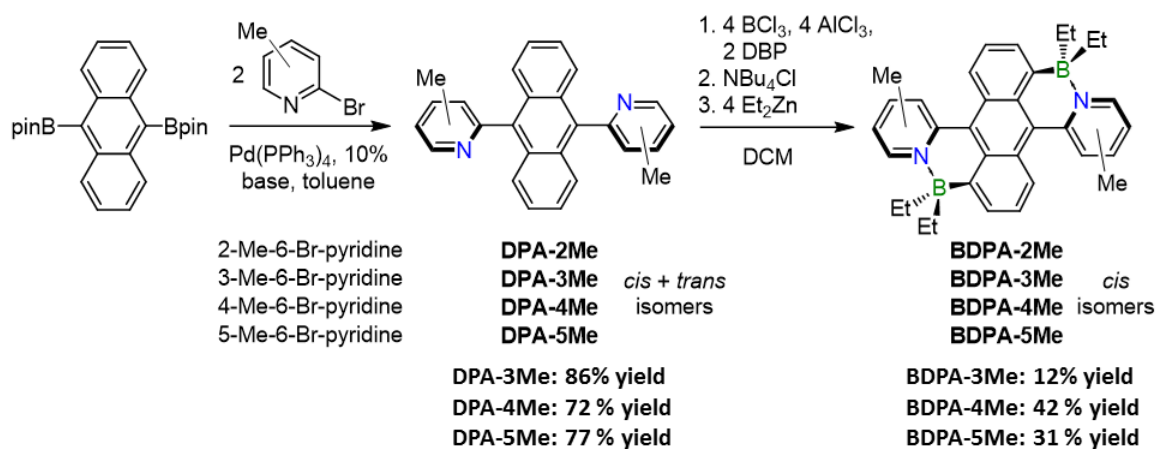


**Figure 3-4.** Comparison of HOMO and LUMO energies of BN-anthracenes

The effects on the electronic structure were assessed by examining the HOMO-LUMO energy levels (Figure 3-4). The electron-donating effect of the Me groups raises the HOMO and LUMO levels relative to the parent molecule **BDPA**. The LUMOs are very similar in energy, except for that the methyl groups in *ortho*-position to N (**BDPA-2Me**) raise the energy. Larger differences are found in the HOMO energies. Again, the methyl groups in *ortho*-position to N in **BDPA-2Me** lead to a significant elevation of the HOMO energy level. The methyl group in *ortho*-position to the anthracene moiety lowers the HOMO energy level and, consequently, the HOMO-LUMO gap is the largest for **BDPA-5Me** (2.42 eV). The increased HOMO-LUMO gap for **BDPA-5Me** is likely related to the severe structural distortions discussed earlier that limit  $\pi$ -conjugation.



**Scheme 3-1.** Synthesis of BN-Fused 9,10-Dipyridylanthracenes.

The BN-fused systems **BDPA-3Me**, **BDPA-4Me** and **BDPA-5Me** were synthesized using a similar procedure to that previously reported for compound **BDPA-2Me** (Scheme 3-1). The dipyridylanthracene precursors **DPA-3Me**, **DPA-4Me**, and **DPA-5Me** were obtained in 86%, 72%, and 77% yield by Suzuki-Miyaura coupling of 9,10-

bis(pinacolboryl)anthracene with the respective brominated methylpyridine derivative. For **DPA-3Me** a 2.1:1 mixture of isomers and for **DPA-4Me** a 2.7:1 mixture of isomers with the pyridyl groups in a *trans* or *cis*-arrangement was found, whereas the dipyridylanthracene **DPA-5Me** was obtained as a single isomer, presumably the sterically more favorable *trans*-derivative. Lewis base-directed electrophilic aromatic borylation with  $\text{BCl}_3$  and  $\text{AlCl}_3$  in the presence of 2,6-di-*tert*-butylpyridine (DBP)<sup>7g, 24</sup> and subsequent treatment with diethylzinc gave **BDPA-3Me** in 12%, **BDPA-4Me** in 42%, and **BDPA-5Me** in 31% yield. The products were isolated by recrystallization from  $\text{CH}_2\text{Cl}_2$ /hexanes and fully characterized by multinuclear NMR and high-resolution MALDI-TOF MS. The  $^{11}\text{B}$  NMR signals at -0.3 ppm (**BDPA-3Me**), -0.6 ppm (**BDPA-4Me**) and -0.7 ppm (**BDPA-5Me**) are slightly shifted upfield compared with that of **BDPA-2Me** (2.8 ppm), consistent with a stronger  $\text{B} \leftarrow \text{N}$  interaction. The  $^1\text{H}$  NMR data are in good agreement with the proposed structures and all the protons could be assigned by H,H-COSY and H,H-NOESY 2D NMR analyses.

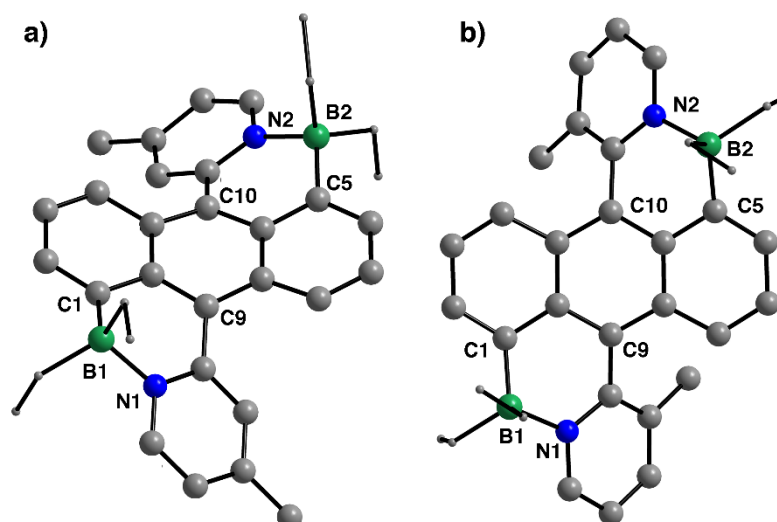


**Figure 3-5.** Ball-and-stick illustrations of the X-ray structures of a) **BDPA-4Me** and b) **BDPA-5Me**.

Single crystals of **BDPA-4Me** and **BDPA-5Me** were grown from CH<sub>2</sub>Cl<sub>2</sub>/hexanes mixture at -20 °C. The molecular structures are depicted in Figure 3-5 and the structural data summarized in Table 3-7. Compared with **BDPA-2Me**,<sup>22</sup> the B-N distances for **BDPA-4Me** and **BDPA-5Me** are significantly shorter, ranging from 1.628(8)-1.635(8) Å for **BDPA-4Me** and 1.637(2)-1.642(2) Å for **BDPA-5Me** (cf. **BDPA-2Me** 1.671(4)-1.685(3) Å), as expected for a stronger Lewis acid-base interaction. The molecular structures of **BDPA-4Me** and **BDPA-5Me** further confirm the predicted buckled anthracene backbone with interplanar angles between the outer benzene rings of  $\varepsilon = 17.4^\circ$  for **BDPA-4Me** and  $\varepsilon = 20.7^\circ$  for **BDPA-5Me**. They are slightly smaller than that of **BDPA-2Me** ( $\varepsilon = 21.5^\circ$ ), which may suggest less distortion. However, an increased strain is evident from the dislocation of the boron atom from the plane of the anthracene backbone. The Cent1-C<sub>1,5</sub>-B angles of  $\beta = 168.8, 170.5^\circ$  for **BDPA-4Me** and  $\beta = 168.0, 168.8^\circ$  for **BDPA-5Me** reveal much more pronounced distortions than for **BDPA-2Me** ( $\beta = 173.6, 174.8^\circ$ ). The steric effects of the 5-Me groups in **BDPA-5Me** also lead to the largest interplanar angle between anthracene and pyridyl (41.6 and 43.5°). Overall, these observations are consistent with the results of the DFT calculations, which suggested that shorter B-N distances result in enhanced steric strain and the presence of the Me group in 5-position in the most severe distortions. Crystal packing indicated intermolecular  $\pi$ - $\pi$  stacking of the anthracene main chain is prevented by the presence of the BEt<sub>2</sub> and contorted PAHs (Figure 3-6).

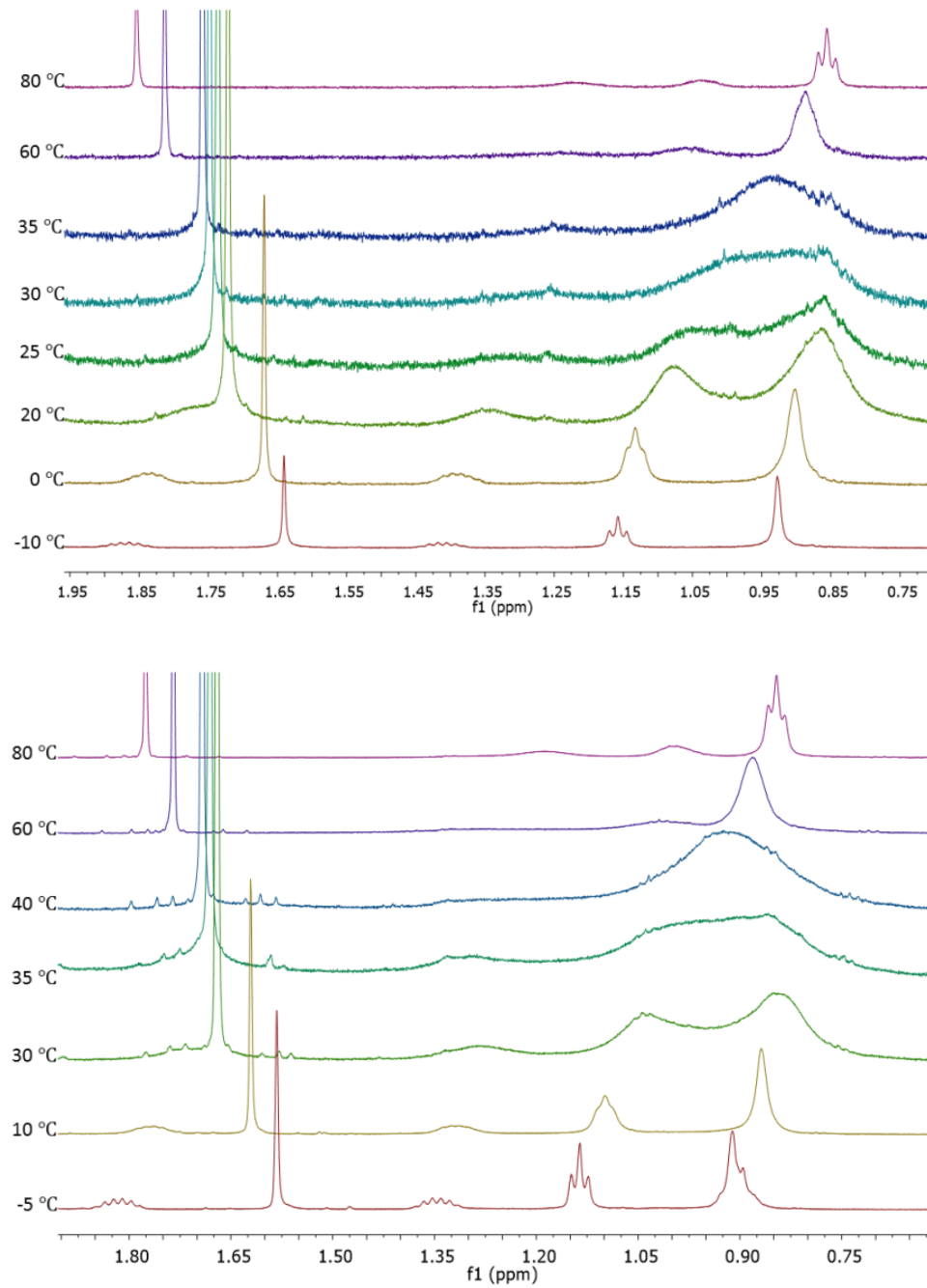


**Figure 3-6.** VT  $^1\text{H}$  NMR spectra of **BDPA-3Me** and **BDPA-4Me** (Et region,  $\text{d}_8\text{-tol}$ , 599.7 MHz)



**Table 3-2.** Summary of results from VT NMR spectroscopy studies

| Compound                        | Probe                | $T_c$ <sup>[a]</sup> [K] | $\Delta\nu$ [Hz] <sup>[b]</sup> | $\Delta G^\ddagger$ <sup>[a]</sup> [kJ mol <sup>-1</sup> ] |
|---------------------------------|----------------------|--------------------------|---------------------------------|--|
| <b>BDPA-2Me</b> <sup>[22]</sup> | CH <sub>3</sub> (Et) | 323 ± 3                  | 36 <sup>[c]</sup>               | 68.5 ± 0.7   |
| <b>BDPA-3Me</b>                 | CH <sub>3</sub> (Et) | 303 ± 3                  | 130 <sup>[c]</sup>              | 60.8 ± 0.6   |
| <b>BDPA-4Me</b>                 | CH <sub>3</sub> (Et) | 308 ± 3                  | 125 <sup>[c]</sup>              | 61.9 ± 0.7   |

[a] Data from coalescence temperature method by using the approximation  $\Delta G^\ddagger = 0.0194T_c [9.972 + \lg(T_c \Delta\nu)]$  for estimation of  $\Delta G^\ddagger$  at  $T_c$ ; <sup>[32]</sup> [b] an error of 5% in the line width determination is assumed; [c] values for  $\Delta\nu$  at  $T_c$  were estimated by linear extrapolation of chemical shift trends at low temperature (where exchange is negligible) to  $T_c$ .

The crystal structures confirm the formation of the *cis*-isomer with the pyridyl groups positioned on the same side relative to the anthracene backbone. However, our prior studies revealed that, while the *trans*-isomer is higher in energy, it may be involved as an intermediate in the interconversion of the *cis*-isomer, a process that can be monitored by the chemical exchange of the inequivalent ethyl substituents on boron. To further investigate this aspect, we performed VT <sup>1</sup>H NMR experiments that provide the free energy barrier to interconversion of the ethyl groups (Figures 3-6). From the coalescence temperatures the barrier was determined to  $\Delta G^\ddagger = 68.5 \pm 0.7$  kJ mol<sup>-1</sup> for **BDPA-2Me**,  $60.8 \pm 0.6$  kJ mol<sup>-1</sup> for **BDPA-3Me**, and  $61.9 \pm 0.7$  kJ mol<sup>-1</sup> for **BDPA-4Me** (Table 3-2), whereas for **BDPA-5Me** the barrier proved to be too high to observe any isomerization. Thus, despite the shorter B-N distances, the smallest energy barriers are found for **BDPA-3Me** and **BDPA-4Me**, and this indicates that the reorientation (rotation) of the pyridyl group is rate determining rather than the B-N bond cleavage.

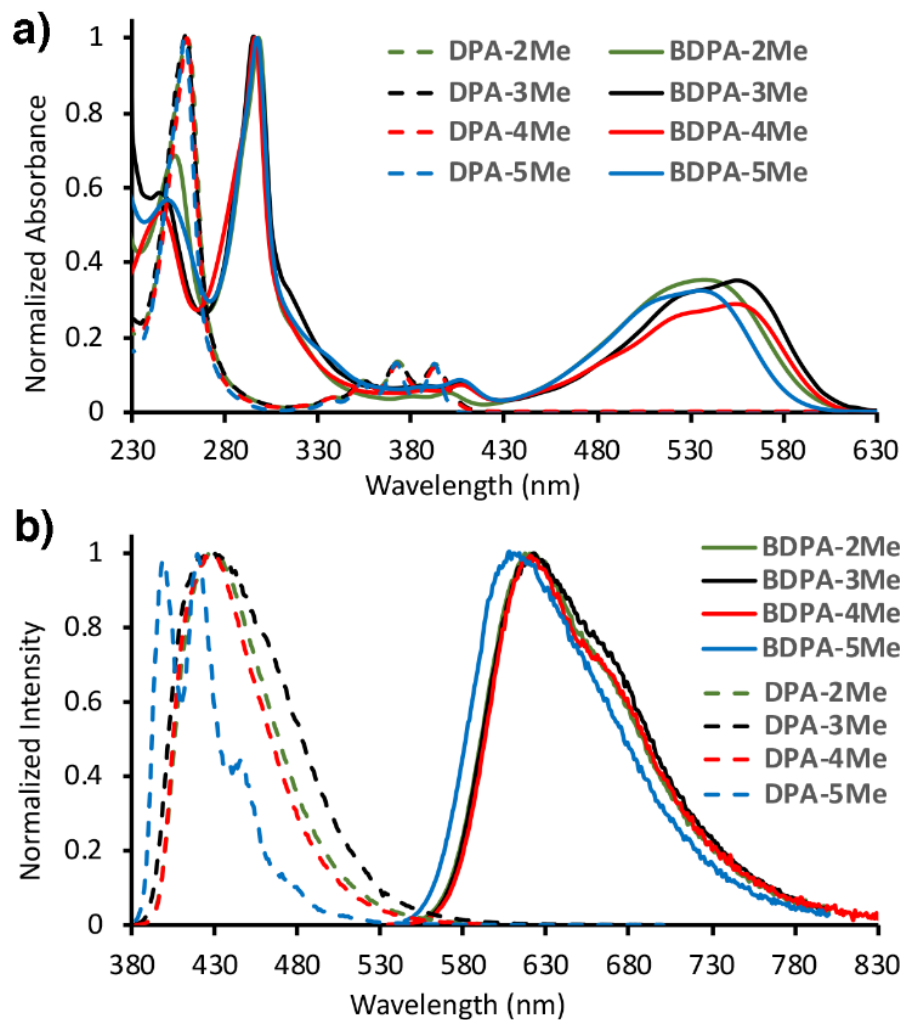


**Figure 3-7.** a) UV-vis absorption and b) emission spectra in  $\text{CH}_2\text{Cl}_2$  solution.

**Table 3-3.** Comparison of photophysical data of BN-functionalized anthracenes and their ligand precursors

| Compound                      | $\lambda_{\text{abs}}$ <sup>[a]</sup><br>[nm] | $\lambda_{\text{abs, TDDFT}}$<br>[nm] | $\lambda_{\text{Fl}}$ <sup>[b]</sup><br>[nm] | $\tau_{\text{Fl}}$ <sup>[c]</sup><br>[ns] | $\Phi_{\text{Fl}}$ <sup>[d]</sup> | $k_{\text{r}} / k_{\text{nr}}$ <sup>[e]</sup><br>[10 <sup>7</sup> s <sup>-1</sup> ] |
|-------------------------------|---|---------------------------------------|--|---|-----------------------------------|---|
| <b>DPA-2Me</b> <sup>22</sup>  | 393, 372, 354, 259                            | 359                                   | 428  | 6.0 ( $\chi^2 = 1.64$ )                   | 0.77                              | 12.8 / 3.8  |
| <b>DPA-3Me</b>                | 393, 372, 354, 259                            | 361                                   | 427  | 5.9 ( $\chi^2 = 1.46$ )                   | 0.59                              | 10.0 / 6.9  |
| <b>DPA-4Me</b>                | 393, 372, 354, 259                            | 359                                   | 428  | 6.1 ( $\chi^2 = 1.42$ )                   | 0.64                              | 10.5 / 5.9  |
| <b>DPA-5Me</b>                | 392, 372, 354, 258                            | 355                                   | 419, 397                                     | 6.9 ( $\chi^2 = 1.42$ )                   | 0.60                              | 8.7 / 5.8   |
| <b>BDPA-2Me</b> <sup>22</sup> | 538, 298, 293                                 | 523                                   | 620  | 11.1 ( $\chi^2 = 1.54$ )                  | 0.53                              | 4.8 / 4.2   |
| <b>BDPA-3Me</b>               | 555, 528 (sh), 295                            | 532                                   | 622  | 10.2 ( $\chi^2 = 1.53$ )                  | 0.43                              | 4.2 / 5.6   |
| <b>BDPA-4Me</b>               | 554, 525 (sh), 298                            | 533                                   | 621  | 10.9 ( $\chi^2 = 2.33$ ) <sup>[f]</sup>   | 0.60                              | 5.5 / 3.7   |
| <b>BDPA-5Me</b>               | 535, 297                                      | 512                                   | 612  | 11.5 ( $\chi^2 = 1.50$ )                  | 0.55                              | 4.8 / 3.9   |

[a] In CH<sub>2</sub>Cl<sub>2</sub> solution. [b] Excited at 372 nm (**DPA-2Me**, **DPA-3Me**, **DPA-4Me** and **DPA-5Me**), 538 nm (**BDPA-2Me**), 528 nm (**BDPA-3Me**), 525 nm (**BDPA-4Me**), 535 nm (**BDPA-5Me**); [c] excited with a nanoLED at 388 nm (ligands), or 450 nm (borylated species); [d] absolute quantum yield determined using an integrating sphere; [e] radiative ( $k_{\text{r}}$ ) and non-radiative ( $k_{\text{nr}}$ ) decay rate constants are calculated using the equations  $k_{\text{r}} = \Phi / \tau$ ,  $k_{\text{nr}} = (1 - \Phi) / \tau$ ; [f] for double-exponential fit:  $\tau_{\text{Fl}} = 1.3$  ns (3%), 11.1 ns (97%) ( $\chi^2 = 1.62$ ).

Formation of the B←N Lewis pairs results in strong bathochromic shifts of the absorption and emission bands relative to those of the 9,10-dipyridylanthracene precursors. The BN-fused species are obtained as red crystalline solids that display a very intense orange emission in solution. A comparison of the absorption and emission spectra in CH<sub>2</sub>Cl<sub>2</sub> is displayed in Figure 3-7 and the photophysical properties are summarized in Table 3-3. A longer wavelength absorption maximum for **BDPA-3Me** (555 nm) and **BDPA-4Me** (554 nm) in comparison to **BDPA-2Me** (538 nm) and **BDPA-5Me** (535 nm) is consistent with

our DFT data, which showed that the relatively larger HOMO-LUMO energy gap for **BDPA-2Me** is due primarily to an increase in the LUMO energy. The larger HOMO-LUMO energy gap for **BDPA-5Me** relative to those of **BDPA-3Me** and **BDPA-4Me** is owing to a lower HOMO energy level. The quantum yields are consistently very high, despite the relatively low energy of the emission, with the largest value determined for **BDPA-4Me** (60%), closely followed by **BDPA-5Me** (55%), **BDPA-2Me** (53%), and **BDPA-3Me** (43%). The fluorescence lifetimes are very similar to one another, in the range of 10.2 to 11.5 ns, and significantly longer than for the non-borylated precursors. These data are consistent with relatively small non-radiative decay constants ( $k_{nr}$ ) due to the more rigid molecular framework.

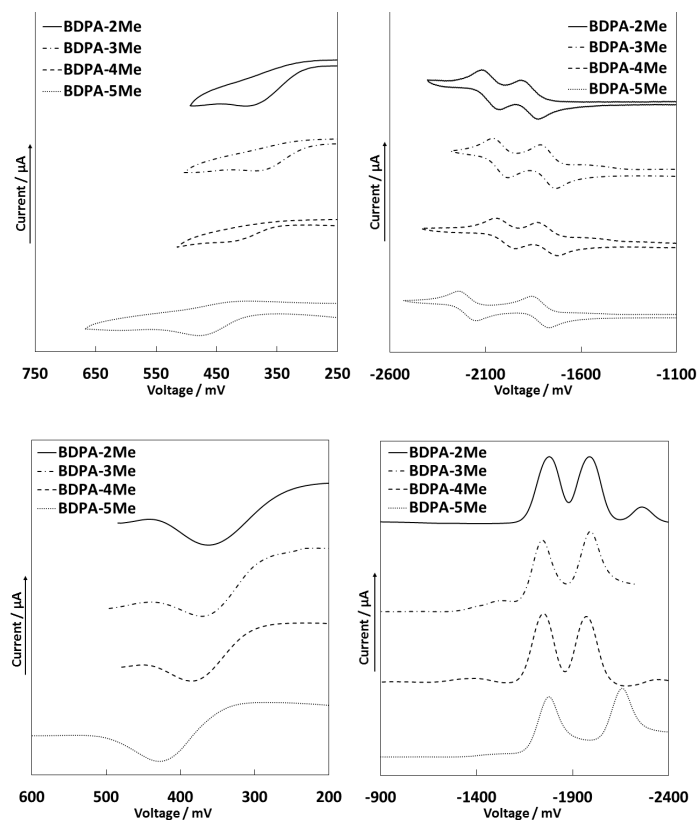


**Figure 3-8** Cyclic (CV, top) and square wave voltammetry (SWV, bottom) data. Oxidation in 0.1M Bu<sub>4</sub>N[PF<sub>6</sub>] in DCM, reduction in 0.1M Bu<sub>4</sub>N[PF<sub>6</sub>] in THF, reported vs Fc<sup>+/0</sup>,  $\nu = 100 \text{ mV s}^{-1}$ .

Cyclic (CV) and square wave voltammetry (SWV) data acquired in THF containing 0.1 M Bu<sub>4</sub>N[PF<sub>6</sub>] show two consecutive reversible reduction processes (Figure 3-8). As predicted by the DFT calculations, the first reduction occurs slightly more readily for **BDPA-3Me** ( $E_{\text{red}} = -1.77$  V vs. Fc<sup>+/0</sup>), **BDPA-4Me** ( $E_{\text{red}} = -1.77$  V) and **BDPA-5Me** ( $E_{\text{red}} = -1.81$  V) in comparison with **BDPA-2Me** ( $E_{\text{red}} = -1.87$  V) (Table 3-4). Of note is that the second reduction occurs at a much more negative potential for **BDPA-5Me** in comparison to the other isomers, resulting in an unusually large redox splitting of  $\Delta E = 0.38$  V. Considering that the LUMO orbitals show a quinoidal  $\pi$ -delocalization between the anthracene and pyridyl groups, this may be due to steric constraints that hinder the planarization of the pyridyl and anthracene groups in **BDPA-5Me**. Oxidative scans performed in CH<sub>2</sub>Cl<sub>2</sub> containing 0.1 M Bu<sub>4</sub>N[PF<sub>6</sub>] show irreversible waves with peak potentials of  $E_{\text{pa}} = 0.40$  V (**BDPA-2Me**), 0.39 V (**BDPA-3Me**), 0.42 V (**BDPA-4Me**), and 0.48 V (**BDPA-5Me**) (Figure 3-8). The derived electrochemical HOMO–LUMO gaps range from 2.16 eV (**BDPA-3Me**) to 2.29 eV (**BDPA-5Me**), in excellent agreement with the trends in the optical gaps deduced from the UV-vis absorption spectra.

**Table 3-4.** Electrochemical data of BN-functionalized anthracenes and comparison of HOMO-LUMO gaps with results from DFT calculations and UV-vis absorption spectroscopy

| Compound                      | $E_{\text{ox}}^{\text{CV}}$ [a] | $E_{\text{red}}^{\text{CV}}$ [b] | HOMO[c] | LUMO[c] | $E_{\text{g}}^{\text{CV}}$ [c] | $E_{\text{g}}^{\text{DFT[d]}}$ | $E_{\text{g, opt}}$ [e] |
|-------------------------------|---------------------------------|----------------------------------|---------|---------|--------------------------------|--------------------------------|-------------------------|
|                               | [V]                             | [V]                              | [eV]    | [eV]    | [eV]                           | [eV]                           | [eV]                    |
| <b>BDPA-2Me</b> <sup>22</sup> | 0.40                            | -1.87, -2.07                     | -5.20   | -2.93   | 2.27                           | 2.34                           | 2.30                    |
| <b>BDPA-3Me</b>               | 0.39                            | -1.77, -2.02                     | -5.19   | -3.03   | 2.16                           | 2.30                           | 2.23                    |
| <b>BDPA-4Me</b>               | 0.42                            | -1.77, -2.00                     | -5.22   | -3.03   | 2.19                           | 2.31                           | 2.24                    |
| <b>BDPA-5Me</b>               | 0.48                            | -1.81, -2.19                     | -5.28   | -2.99   | 2.29                           | 2.42                           | 2.32                    |

[a] Recorded using 0.1M Bu<sub>4</sub>N[PF<sub>6</sub>] in CH<sub>2</sub>Cl<sub>2</sub>,  $E_{\text{ox}} = E_{\text{pa}}$ ; [b] recorded using 0.1M Bu<sub>4</sub>N[PF<sub>6</sub>] in THF,  $E_{\text{red}} = 0.5 (E_{\text{pc}} + E_{\text{pa}})$ ; [c] determined from CV data using the equations  $E_{\text{LUMO}} = -(4.8 + E_{\text{red}})$  and  $E_{\text{HOMO}} = -(4.8 + E_{\text{ox}})$ ; [d] from DFT calculations at the rb3lyp/6-31g(d) level of theory; [e] estimated from absorption maxima in CH<sub>2</sub>Cl<sub>2</sub> solution.

Beyond the superior emissive properties, an intriguing characteristic of anthracenes is their ability to take up and release singlet oxygen via the reversible formation of endoperoxides. This behavior is not only of key importance to cancer treatment via photodynamic therapy,<sup>12-13</sup> but has also been exploited in materials science, for instance, in photolithography,<sup>14</sup> fluorescent anti-counterfeiting<sup>15</sup>, and the development of molecular switches<sup>16</sup>. Typically, an external sensitizer is added to promote the by conversion of triplet to singlet oxygen, which in turn reacts with the acene to yield the respective endoperoxides. In a very recent study Linker demonstrated that this is also the case for dipyridylanthracenes which are converted to the endoperoxides by sensitization with tetraphenylporphyrin.<sup>25</sup> While spontaneous self-sensitized reaction of higher acenes (e.g. pentacene) with oxygen is frequently encountered, relatively few examples of anthracene derivatives are known that display efficient self-sensitized endoperoxide formation with visible light, most notably systems in which the phenyl groups in 9,10-diphenylanthracene

are fused to the anthracene backbone via O, S, C=O, or aryl bridges that results in planarized structures and red-shifted absorptions.<sup>26</sup> We found that the BN-functionalized anthracene rapidly react with O<sub>2</sub> in the presence of visible light to selectively form the corresponding endoperoxide **BPO-2Me**, **BPO-3Me**, **BPO-4Me**, and **BPO-5Me** (Figure 3-9). The endoperoxides were fully characterized by multinuclear NMR and high-resolution MALDI-TOF MS.

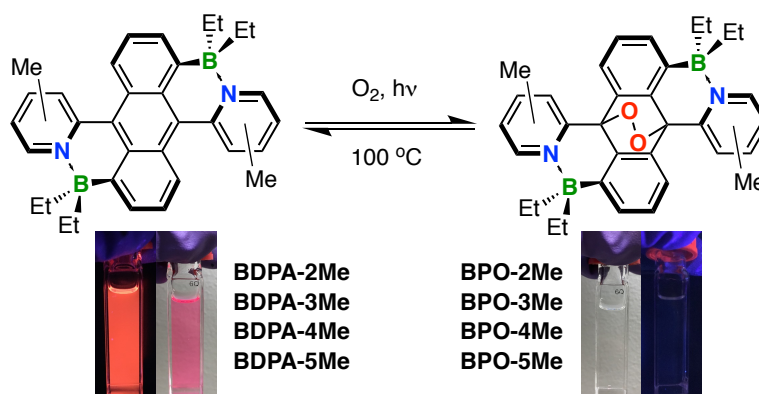


**Figure 3-9.** Self-sensitized formation of endoperoxides and photographs under ambient light and UV-irradiation illustrating color changes for the reversible conversion of **BDPA-5Me** to its endoperoxide **BPO-5Me**.

To explore differences in reactivity, solutions of the acenes in oxygen-saturated CH<sub>2</sub>Cl<sub>2</sub> (1 × 10<sup>-5</sup> M) were irradiated with a Xe lamp at room temperature (Figure 3-10a, see appendix for details). The kinetic data reveal a strong influence of substituent effects on the reactivity as **BDPA-5Me** with the Me groups in close proximity to the anthracene backbone reacts almost an order of magnitude more slowly than the other derivatives to give the corresponding endoperoxide **BPO-5Me**. In the case of diarylanthracenes, zwitterionic intermediates consisting of a C-9 attached peroxy anion and C10-centered carbocation have been proposed, and a correlation between the HOMO energy of diarylanthracenes with their reactivity towards O<sub>2</sub> has been postulated.<sup>27</sup> According to our calculations the HOMO

level decreases slightly in the order of **BDPA-2Me** > **BDPA-3Me**  $\approx$  **BDPA-4Me** > **BDPA-5Me** (Figure 3-4), which is consistent with their relative reactivity except for that **BDPA-2Me** reacts at a similar rate as **BDPA-3Me** and **BDPA-4Me**. However, the much lower rate for **BDPA-5Me** suggests that steric factors play a major role, most likely by preventing further planarization of the pyridyl group and the anthracene backbone, which is necessary to stabilize the proposed carbocation intermediate<sup>27</sup> in the peroxo intermediate for **BDPA-5Me** (Figure 3-10a). On the other hand, the fact that the rate for **BDPA-2Me** is similar to that of **BDPA-3Me** and **BDPA-4Me** suggests that the effect of the steric pressure of the Me group in 2-position and the ensuing weakening of the B←N interaction is less significant as it does not directly affect the ability of the pyridyl group to adopt a position that is coplanar with the anthracene backbone.



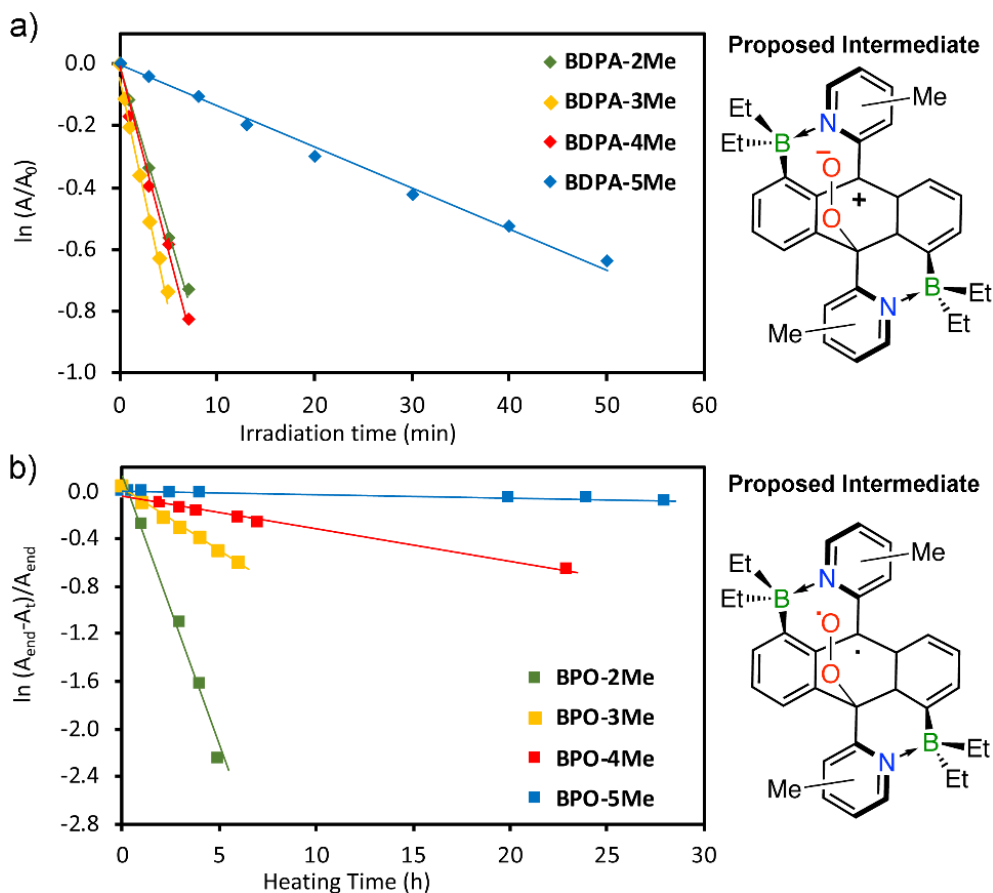


**Figure 3-10.** a) Pseudo first-order kinetics and structures of proposed intermediates for the reaction of BN-functionalized anthracenes with oxygen upon photoirradiation with a Xe lamp in CH<sub>2</sub>Cl<sub>2</sub> solution (BDPA-2Me:  $k = 1.8 \times 10^{-3} \text{ s}^{-1}$ , BDPA-3Me:  $k = 2.4 \times 10^{-3} \text{ s}^{-1}$ , BDPA-4Me:  $2.0 \times 10^{-3} \text{ s}^{-1}$ , BDPA-5Me:  $2.2 \times 10^{-4} \text{ s}^{-1}$ ). b) Kinetics for the thermolysis of the endoperoxides at 100 °C and structures of proposed intermediates; A<sub>end</sub>: final absorption intensity of BDPA, A<sub>t</sub>: absorption intensity of BDPA at a given time (BPO-2Me:  $k = 1.2 \times 10^{-4} \text{ s}^{-1}$ , BPO-3Me:  $2.9 \times 10^{-5} \text{ s}^{-1}$ , BPO-4Me:  $7.6 \times 10^{-6} \text{ s}^{-1}$ , BPO-5Me:  $7.5 \times 10^{-7} \text{ s}^{-1}$ ).

Another appealing aspect of diarylanthracene endoperoxides is their ability to thermally revert to the parent acenes with generation of singlet oxygen that can be delivered on demand.<sup>11b, 11c</sup> This process is believed to proceed through a diradical intermediate generated upon initial cleavage of one of the C-O bonds.<sup>27</sup> Indeed, when heated to 100 °C in toluene, the BPOs gradually revert back to the parent acenes (Figure 3-10b). The rate of cyclo-reversion for **BPO-2Me** is by far the highest, almost an order of magnitude higher than that of **BPO-3Me** and more than two orders of magnitude higher than that of **BPO-**

**5Me**. This suggests a relatively lower kinetic barrier for **BPO-2Me** and is in good agreement with the calculated C-O and O-O bond distances for the BPOs which increase in the order of **BPO-5Me** < **BPO-4Me**  $\approx$  **BPO-3Me** < **BPO-2Me** (Table 3-15). While not directly correlated, our results are also consistent with a comparison of the relative stability of the BN-anthracenes and their endoperoxides, where the regeneration of **BDPA-5Me** from its endoperoxide **BPO-5Me** is energetically least favorable (Table 3-5). **BDPA-2Me** is highest in energy among the acenes, presumably due to the weaker B $\leftarrow$ N interaction (B-N 1.690 Å), but the formation of its endoperoxide **BPO-2Me** is predicted to be relatively even less favorable (B-N 1.727, 1.745 Å). The elongated B-N bond distances for **BPO-2Me** and expected more facile bond dissociation could also be an indication that generation of a tricoordinate borane plays a role in promoting the release of oxygen from **BPO-2Me**. Indeed, the rate of cyclo-reversion for **BPO-2Me** ( $t_{1/2}$  = 105 mins) is higher than that reported for diphenylanthracene ( $t_{1/2}$  = 121 mins) and, interestingly, the parent non-borylated di-*o*-pyridylanthracene was reported to only release O<sub>2</sub> at a temperature of 135 °C at which other side reactions occur.<sup>25, 27a</sup> In a recent study, Linker and coworkers proposed that N-methylation of di(*o*-pyridyl)anthracene triggers very rapid O<sub>2</sub> release by interaction of the cationic methylpyridinium group with the peroxy bridge.<sup>28</sup> Although a direct interaction between the Lewis-acidic boron center generated upon B-N cleavage and the peroxy bridge is sterically not feasible, it is conceivable that the borane interacts with a lone pair on the peroxy group after the initial C-O bond cleavage.

**Table 3-5.** Relative computed energies for isomeric BN-anthracenes and their endoperoxides<sup>[a]</sup>

|                 | $\Delta E_{\text{BDPA}}^{\text{[b]}}$<br>(kJ/mol) | $\Delta E_{\text{BPO}}^{\text{[c]}}$<br>(kJ/mol) | $\Delta(E_{\text{BPO}} - E_{\text{BDPA}})$<br>(kJ/mol) |
|-----------------|---|--|--|
| <b>BDPA-2Me</b> | +77.8   | +99.4  | +21.6  |
| <b>BDPA-3Me</b> | +5.9  | +28.1  | +22.2  |
| <b>BDPA-4Me</b> | $\equiv 0$  | $\equiv 0$                                       | $\equiv 0$   |
| <b>BDPA-5Me</b> | +52.6   | +40.0  | -12.6  |

[a] Optimized at rb3lyp/6-31g(d) level of theory. [b] Comparison of total energy relative to sterically unhindered 4-methylated acene. [c] Comparison of total energy relative to sterically unhindered 4-methylated acene endoperoxide.

The results described above indicate that while compound **BDPA-2Me** reacts similarly fast as **BDPA-3Me** and **BDPA-4Me** with O<sub>2</sub> under photoirradiation it thermally releases singlet O<sub>2</sub> more readily. On the other hand, **BDPA-5Me** sluggishly reacts with O<sub>2</sub> and only very slowly releases singlet O<sub>2</sub>. This suggests that by simply varying the substitution pattern on the pyridyl moiety either a material (**BDPA-2Me**) that can be used for delivery of singlet oxygen on demand or a material (**BDPA-5Me**) that acts as a singlet oxygen sensitizer for oxygenation of other compounds can be achieved. To test the ability of the BN-fused dipyridylanthracenes to act as a singlet oxygen sensitizer and promote oxygenation of other substrates we performed competition experiments with 9,10-dimethylantracene (DMA) as a singlet oxygen acceptor. Indeed, all the compounds promote oxygenation of DMA as evidenced by a decrease in the characteristic absorptions between 300 to 400 nm. However, whereas **BDPA-2Me**, **BDPA-3Me** and **BDPA-4Me** undergo preferential self-sensitized oxygenation and the oxygenation of DMA occurs at a relatively lower rate (Figure 3-16), **BDPA-5Me** leads to preferential conversion of DMA into its endoperoxide. The oxidation of DMA using 10% of **BDPA-5Me** as a photosensitizer is illustrated in Figure 3-11. In the absence of **BDPA-5Me** as a photosensitizer only negligible amounts of DMA are converted

upon photoirradiation under otherwise identical conditions.

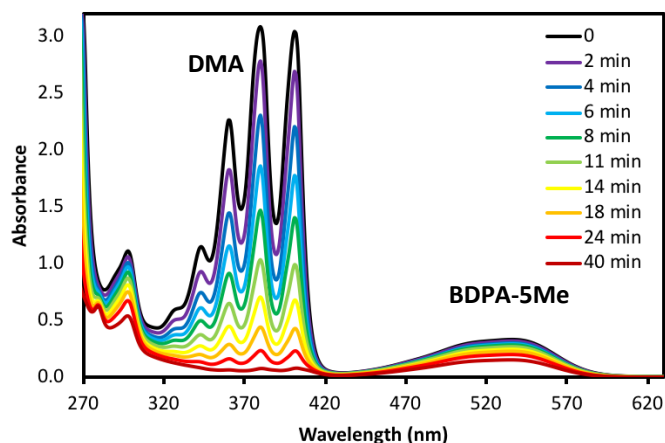


**Figure 3-11.** Photoirradiation of 9,10-dimethylantracene (DMA) in the presence of 10 mol% **BDPA-5Me** with a Xe lamp in oxygen-saturated  $\text{CH}_2\text{Cl}_2$  solution followed by UV-Vis spectroscopy. isolation of a specific desired cyclic product.

### 3.3 Experimental

**Materials and General Methods.** All reactions were carried out under an atmosphere of pre-purified nitrogen using either Schlenk techniques or an inert-atmosphere glovebox. THF was distilled from Na/benzophenone prior to use. Hydrocarbon and chlorinated solvents were purified using a solvent purification system (alumina/copper columns for hydrocarbon solvents), and the chlorinated solvents were subsequently distilled from  $\text{CaH}_2$  and degassed via several freeze-pump-thaw cycles. All chemicals were purchased from commercial sources and directly used without further purification unless noted otherwise.

NMR data were acquired at ambient temperature unless noted otherwise. 499.9 MHz  $^1\text{H}$  and 160.4 MHz  $^{11}\text{B}$  NMR data were recorded on a 500 MHz Bruker AVANCE spectrometer; 599.7 MHz  $^1\text{H}$ , 150.8 MHz  $^{13}\text{C}\{^1\text{H}\}$ , and 192.4 MHz  $^{11}\text{B}\{^1\text{H}\}$  NMR data were recorded on a Varian INOVA 600 spectrometer.  $^{11}\text{B}\{^1\text{H}\}$  NMR spectra were acquired with boron-

free quartz NMR tubes either on the Varian INOVA 600 with a boron-free 5 mm dual broadband gradient probe (Nalorac, Varian Inc., Martinez, CA) or the 500 MHz Bruker Auto Avance with a 5mm PH SEX 500S1 11B-H/F-D probe.  $^1\text{H}$  and  $^{13}\text{C}\{^1\text{H}\}$  NMR spectra were referenced internally to solvent signals ( $\text{CDCl}_3$ : 7.27 ppm for  $^1\text{H}$  NMR, 77.23 ppm for  $^{13}\text{C}$  NMR; d8-toluene: 2.08 ppm for  $^1\text{H}$  NMR) and all other NMR spectra externally to  $\text{SiMe}_4$  (0 ppm). Abbreviations used for signal assignments: An = anthracene, Ph = phenyl, Py = pyridyl, Me = methyl, s = singlet, d = doublet, t = triplet, vt = virtual triplet, dd = doublet of doublets, m = multiplet, br = broad. MALDI-TOF MS measurements were performed on a Bruker Ultraflex extreme in reflectron mode with delayed extraction. Red phosphorus was used for calibration.

UV-visible absorption data were acquired on a Varian Cary 5000 UV-Vis/NIR spectrophotometer or a Cary 60 UV-Vis spectrophotometer. The fluorescence data and lifetimes were measured using a Horiba Fluorolog-3 spectrofluorometer equipped with a 388 or 450 nm nanoLED and a FluoroHub R-928 detector. Absolute quantum yields ( $\Phi_F$ ) were measured on the HORIBA Fluorolog-3 using a pre-calibrated Quanta- $\phi$  integrating sphere. Light from the sample compartment is directed into the sphere via a fiber-optic cable and an F-3000 Fiber-Optic Adapter, and then returned to the sample compartment (and to the emission monochromator) via a second fiber-optic cable and an F-3000 Fiber-Optic Adapter.

Cyclic voltammetry (CV) and square wave voltammetry (SWV) experiments were carried out on a CV-50W analyzer from BASi. The three-electrode system consisted of an Au disk as working electrode, a Pt wire as counter electrode and an Ag wire as the pseudo-reference electrode. The voltammograms were recorded with ca.  $10^{-3}$  to  $10^{-4}$  M solutions in THF

(reduction scans) or DCM (oxidation scans) containing  $\text{Bu}_4\text{N}[\text{PF}_6]$  (0.1 M) as the supporting electrolyte. The scans were referenced after the addition of a small amount of ferrocene as internal standard. The potentials are reported relative to the ferrocene/ferrocenium couple.

DFT calculations were performed with the Gaussian09 suite of programs.<sup>29</sup> The input files were generated from single crystal structures when available or otherwise generated from Chem3D and pre-optimized in Spartan '08 V 1.2.0. Ground state geometries were then optimized in Gaussian09 using the hybrid density functional  $\text{rb3lyp}$  with a 6-31g(d) basis set. Frequency calculations were performed to confirm the presence of local minima (only positive frequencies). Vertical excitations were calculated by TD-DFT methods at the  $\text{rcam-b3lyp}/6\text{-}31\text{g(d)}$  level. First triplet excited state geometries were optimized by DFT methods at the  $\text{ub3lyp}/6\text{-}31\text{g(d)}$  level and first singlet excited state geometries were optimized by TD-DFT methods at the  $\text{b3lyp}/6\text{-}31\text{g(d)}$  level.

Single crystals of BDPA-4Me and BDPA-5Me suitable for X-ray analysis were grown from  $\text{CH}_2\text{Cl}_2$ /hexanes mixture at  $-20^\circ\text{C}$ . X-ray diffraction intensities on BDPA-4Me and BDPA-5Me were collected on a Bruker SMART APEX II CCD Diffractometer using  $\text{CuK}\alpha$  ( $1.54178\text{ \AA}$ ) radiation at  $100(2)\text{ K}$ . The structures were refined by full-matrix least squares based on  $F^2$  with all reflections (SHELXTL V5.10; G. Sheldrick, Siemens XRD, Madison, WI).<sup>30</sup> Non-hydrogen atoms were refined with anisotropic displacement coefficients, and hydrogen atoms were treated as idealized contribution. SADABS (Sheldrick, 12 G.M. SADABS (2.01), Bruker/Siemens Area Detector Absorption Correction Program; Bruker AXS: Madison, WI, 1998) absorption correction was applied.<sup>31</sup> Crystallographic data for both crystals have been deposited with the Cambridge Crystallographic Data Center as

supplementary publications CCDC 1898388-1898389. Copies of the data can be obtained free of charge on application to CCDC, 12 Union Road, Cambridge CB2 1EZ, UK (fax: (+44) 1223-336-033; email: deposit@ccdc.cam.ac.uk).

**Synthesis of Dipyridylanthracene DPA-3Me.** 9,10-Bis(pinacolboryl)anthracene (**1**) (3.00 g, 6.97 mmol), 2-bromo-5-methylpyridine (2.64 g, 15.3 mmol, 2.2 equiv) and sodium carbonate (5.9 g, 56 mmol, 8 equiv) were added to a Schlenk flask. Then 155 mL of toluene, ethanol and water in a ratio of v/v/v = 7:1.5:7 were added. Tetrakis(triphenylphosphine)palladium(0) (0.48 g, 0.42 mmol, 6 mol%) was added after degassing under nitrogen for 20 min. The reaction mixture was stirred at 80 °C for 3 days under nitrogen atmosphere, allowed to cool to room temperature, and then poured into water with stirring. The mixture was extracted with CH<sub>2</sub>Cl<sub>2</sub>, the organic layer was washed with brine and dried over anhydrous sodium sulfate. After rotary evaporation the crude product was redissolved in a small amount of CH<sub>2</sub>Cl<sub>2</sub> and layered with hexanes (v/v = 1:1) at room temperature. Diffusion and slow partial evaporation of the solvent resulted in light yellow crystals. Yield: 2.16 g (86%). <sup>1</sup>H NMR (599.7 MHz, CDCl<sub>3</sub>, 25 °C): δ (ppm) = Major isomer (68%) 8.77 (s, 2H; Py), 7.75 (dd, J = 7.2 Hz, J = 1.8 Hz, 2H; Py), 7.60 (m, 4H; An), 7.45 (d, J = 7.2 Hz, 2H; Py), 7.33 (m, 4H; An), 2.55 (s, 6H; Me). Minor isomer (32%) 8.80 (s, 2H; Py), 7.75 (dd, J = 7.2 Hz, J = 1.8 Hz, 2H; Py), 7.65 (m, 4H; An), 7.45 (d, J = 7.2 Hz, 2H; Py), 7.35 (m, 4H; An), 2.55 (s, 6H; Me). <sup>13</sup>C{<sup>1</sup>H} NMR (150.8 MHz, CDCl<sub>3</sub>, 25 °C): δ (ppm) = Major isomer 155.7, 150.7, 137.0, 136.2, 132.0, 130.2, 130.1, 126.6, 125.6, 18.7. Minor isomer 155.6, 150.8, 137.0, 136.3, 132.0, 130.1, 126.6, 125.6, 18.7. High-resolution MALDI-TOF mass spectrum (pos. mode, neat): m/z = 360.1619 ([M]<sup>+</sup>, 100 %, calcd for <sup>12</sup>C<sub>26</sub><sup>1</sup>H<sub>20</sub><sup>14</sup>N<sub>2</sub> 360.1621).

**Synthesis of Dipyridylanthracene DPA-4Me.** In a glovebox, 9,10-bis(pinacolboryl)anthracene (**1**) (5.50 g, 12.8 mmol) and 2-bromo-4-methylpyridine (3.1 mL, 28 mmol, 2.2 equiv) were dissolved in toluene, followed by the addition of tetrakis(triphenylphosphine)palladium(0) (1.48 g, 1.29 mmol, 10 mol%) and cesium carbonate (25 g, 77 mmol, 6 equiv). The reaction mixture was stirred at 100 °C for 11 days under nitrogen atmosphere, allowed to cool to room temperature, and then filtered through a fritted funnel. The solid that was collected, redissolved in a small amount of CH<sub>2</sub>Cl<sub>2</sub>, and layered with hexanes (v/v = 1:1) at room temperature. Diffusion and slow partial evaporation of the solvent resulted in light yellow crystals. Yield: 3.29 g (72%). <sup>1</sup>H NMR (599.7 MHz, CDCl<sub>3</sub>, 25 °C): δ (ppm) = Major isomer (71%) 8.78 (d, J = 4.8 Hz, 2H; Py), 7.59 (m, 4H; An), 7.36 (s, 2H; Py), 7.34 (m, 4H; An), 7.31 (d, J = 4.8 Hz, 2H; Py), 2.52 (s, 6H; Me). Minor isomer (29%) 8.81 (d, J = 5.4 Hz, 2H; Py), 7.63 (m, 4H; An), 7.37-7.30 (overlapped, 8H; An, Py), 2.51 (s, 6H; Me). <sup>13</sup>C {<sup>1</sup>H} NMR (150.8 MHz, CDCl<sub>3</sub>, 25 °C): δ (ppm) = Major isomer 158.5, 150.0, 147.7, 136.4, 130.0, 127.9, 126.5, 125.6, 123.6, 21.4. Minor isomer 158.5, 150.1, 147.5, 136.5, 129.9, 127.9, 126.6, 125.6, 123.6, 21.4. High-resolution MALDI-TOF mass spectrum (pos. mode, neat): m/z = 360.1616 ([M]<sup>+</sup>, 100 %, calcd for <sup>12</sup>C<sub>26</sub><sup>1</sup>H<sub>20</sub><sup>14</sup>N<sub>2</sub> 360.1621).

**Synthesis of Dipyridylanthracene DPA-5Me.** 9,10-bis(pinacolboryl)anthracene (**1**) (3.00 g, 6.97 mmol), 2-bromo-3-methylpyridine (1.7 mL, 15 mmol, 2.2 equiv) and sodium carbonate (5.9 g, 56 mmol, 8 equiv) were added to a Schlenk flask. Then 155 mL of toluene, ethanol and water in a ratio of v/v/v = 7:1.5:7 were added. Tetrakis(triphenylphosphine)palladium(0) (0.48 g, 0.42 mmol, 6 mol%) was added after degassing under nitrogen for 20 min. The reaction mixture was stirred at 80 °C for 2 days



under nitrogen atmosphere, allowed to cool to room temperature, and then poured into water with stirring. The mixture was extracted with  $\text{CH}_2\text{Cl}_2$ , the organic layer was washed with brine and dried over anhydrous sodium sulfate. After rotary evaporation the crude product was purified by column chromatography (silica gel) with hexanes/ $\text{CH}_2\text{Cl}_2$ /triethylamine (v/v/v = 10:1:1) as eluent. The volatile components were then removed under high vacuum to give the product as a yellow solid. Yield: 1.93 g (77 %).  $^1\text{H}$  NMR (499.9 MHz,  $\text{CDCl}_3$ , 25 °C):  $\delta$  (ppm) = 8.76 (d,  $J$  = 5.0 Hz, 2H; Py), 7.80 (d,  $J$  = 8.0 Hz, 2H; Py), 7.43 (m, 6H; Py, An), 7.34 (m, 4H; An), 1.97 (s, 6H; Me).  $^{13}\text{C}\{^1\text{H}\}$  NMR (125.8 MHz,  $\text{CDCl}_3$ , 25 °C):  $\delta$  (ppm) = 157.9, 147.6, 138.0, 135.4, 134.5, 129.6, 126.1, 125.9, 123.0, 19.0. High-resolution MALDI-TOF mass spectrum (pos. mode, neat):  $m/z$  = 360.1612 ( $[\text{M}]^+$ , 100 %, calcd for  $^{12}\text{C}_{26}^{1}\text{H}_{20}^{14}\text{N}_2$  360.1621).

**Synthesis of Bis-Borane Complex BDPA-3Me.** In a glovebox,  $\text{BCl}_3$  (7.2 mL, 1M solution in hexane, 7.2 mmol, 4 equiv) was added to a bright yellow solution of **DPA-3Me** (0.64 g, 1.78 mmol) in  $\text{CH}_2\text{Cl}_2$ . The solution instantly changed color to orange red. 2,6-Di-*tert*-butylpyridine (0.683 g, 3.57 mmol, 2 equiv) and  $\text{AlCl}_3$  (0.715 g, 5.36 mmol, 3 equiv) were added to the reaction mixture. After stirring for 16 hours, an additional portion of  $\text{AlCl}_3$  (0.238 g, 1.78 mmol, 1 equiv) was added and the mixture was stirred for a further 16 hours whereupon it turned dark green. Addition of  $\text{Bu}_4\text{NCl}$  (0.993 g, 3.57 mmol, 2 equiv) resulted in a dark purple suspension to which  $\text{ZnEt}_2$  (0.77 mL, 7.32 mmol, 4.1 equiv) was added dropwise. The reaction mixture was then stirred for 16 hours at room temperature, followed by removal of the solvent under reduced pressure. The dark residue was redissolved in toluene and insoluble components were removed by filtration through a fritted funnel. The solution was concentrated under reduced pressure. Recrystallization in

dichloromethane/hexanes at -20 °C gave **BDPA-3Me** as red crystals. Yield: 0.11 g (12 %). Yield: 0.11 g (12 %).  $^1\text{H}$  NMR (499.9 MHz,  $\text{CDCl}_3$ , -10 °C):  $\delta$  (ppm) = 8.60 (s, 2H; Py), 8.22 (d,  $J$  = 8.5 Hz, 2H; Py), 8.10 (d,  $J$  = 8.0 Hz, 2H; An), 7.74 (br d,  $J$  = 7.5 Hz, 2H; Py), 7.58 (d,  $J$  = 6.5 Hz, 2H; An), 7.49 (dd,  $J$  = 8.5 Hz,  $J$  = 7.0 Hz, 2H; An), 2.54 (s, 6H; Me), 1.34 (m, 2H; Et), 1.02 (m, 2H; Et), 0.76 (t,  $J$  = 7.5 Hz, 6H; Et), 0.41 (overlapped, 10H; Et).  $^{13}\text{C}\{^1\text{H}\}$  NMR (150.8 MHz,  $\text{CDCl}_3$ , 25 °C):  $\delta$  (ppm) = 150.7, 150.2 (br), 144.9, 138.6, 132.8, 132.3, 129.4, 128.5, 128.0, 127.2, 120.7, 23.7 (br), 18.8, 14.0 (br), 10.4 (br), 9.4 (br).  $^{11}\text{B}\{^1\text{H}\}$  NMR (160.4 MHz,  $\text{CDCl}_3$ , 25 °C):  $\delta$  (ppm) = -0.3 ( $w_{1/2}$  = 390 Hz). High-resolution MALDI-TOF MS (neg. mode, neat):  $m/z$  = 496.3163 ( $[\text{M}]^-$ , 15 %, calcd for  $^{12}\text{C}_{34}^{1}\text{H}_{38}^{11}\text{B}_2^{14}\text{N}_2$  496.3227), 467.2821 ( $[\text{M-Et}]^-$ , 100 %, calcd for  $^{12}\text{C}_{32}^{1}\text{H}_{33}^{11}\text{B}_2^{14}\text{N}_2$  467.2835).

**Synthesis of Bis-Borane Complex BDPA-4Me.** In a glovebox,  $\text{BCl}_3$  (8.7 mL, 1M solution in hexane, 8.7 mmol, 4 equiv) was added to a bright yellow solution of **DPA-4Me** (0.79 g, 2.18 mmol) in  $\text{CH}_2\text{Cl}_2$ . The solution instantly changed color to orange red. 2,6-Di-*tert*-butylpyridine (0.835 g, 4.37 mmol, 2 equiv) and  $\text{AlCl}_3$  (0.874 g, 6.55 mmol, 3 equiv) were added to the reaction mixture. After stirring for 16 hours, an additional portion of  $\text{AlCl}_3$  (0.291 g, 2.18 mmol, 1 equiv) was added and the mixture was stirred for a further 16 hours whereupon it turned dark green. Addition of  $\text{Bu}_4\text{NCl}$  (386 mg, 1.387 mmol, 2 equiv) resulted in a dark purple suspension to which  $\text{ZnEt}_2$  (0.95 mL, 8.96 mmol, 4.1 equiv) was added dropwise. The reaction mixture was then stirred for 16 hours at room temperature, followed by removal of the solvent under reduced pressure. The dark residue was redissolved in toluene and insoluble components were removed by filtration through a fritted funnel. The solution was concentrated under reduced pressure. Recrystallization in

dichloromethane/hexanes at -20 °C gave **BDPA-4Me** as red crystals that were suitable for X-ray analysis. Yield: 0.45 g (42%).  $^1\text{H}$  NMR (599.7 MHz,  $\text{CDCl}_3$ , -5 °C):  $\delta$  (ppm) = 8.65 (d,  $J$  = 6.6 Hz, 2H; Py), 8.13 (m, 4H; Py, An), 7.59 (d,  $J$  = 6.0 Hz, 2H; An), 7.51 (vt,  $J$  = 7.8 Hz, 2H; An), 7.29 (d,  $J$  = 6.6 Hz, 2H; Py), 2.49 (s, 6H; Me), 1.32 (m, 2H; Et), 1.01 (m, 2H; Et), 0.75 (t,  $J$  = 7.2 Hz, 6H; Et), 0.45 (t,  $J$  = 7.2 Hz, 6H; Et), 0.36 (m, 4H; Et).  $^{13}\text{C}\{^1\text{H}\}$  NMR (150.8 MHz,  $\text{CDCl}_3$ , 25 °C):  $\delta$  (ppm) = 152.5, 150.4 (br), 149.6, 144.7, 133.0, 130.3, 128.7, 128.7, 127.9, 127.3, 123.2, 120.6, 23.5 (br), 21.6, 13.7 (br), 10.5, 9.3.  $^{11}\text{B}\{^1\text{H}\}$  NMR (160.4 MHz,  $\text{CDCl}_3$ , 25 °C):  $\delta$  (ppm) = -0.6 ( $w_{1/2}$  = 400 Hz). High-resolution MALDI-TOF MS (neg. mode, neat):  $m/z$  = 496.3214 ( $[\text{M}]^-$ , 13 %, calcd for  $^{12}\text{C}_{34}^{11}\text{H}_{38}^{11}\text{B}_2^{14}\text{N}_2$  496.3227), 467.2804 ( $[\text{M-Et}]^-$ , 100 %, calcd for  $^{12}\text{C}_{32}^{11}\text{H}_{33}^{11}\text{B}_2^{14}\text{N}_2$  467.2835).

**Synthesis of Bis-Borane Complex BDPA-5Me.** In a glovebox,  $\text{BCl}_3$  (11.1 mL, 1M solution in hexane, 11.1 mmol, 4 equiv) was added to a bright yellow solution of **DPA-5Me** (1.00 g, 2.77 mmol) in  $\text{CH}_2\text{Cl}_2$ . The solution instantly changed color to orange red. 2,6-Di-*tert*-butylpyridine (1.06 g, 5.55 mmol, 2 equiv) and  $\text{AlCl}_3$  (1.11 g, 8.32 mmol, 3 equiv) were added to the reaction mixture. After stirring for 16 hours, an additional portion of  $\text{AlCl}_3$  (0.37 g, 2.77 mmol, 1 equiv) was added and the mixture was stirred for a further 16 hours whereupon it turned purple. Addition of  $\text{Bu}_4\text{NCl}$  (1.54 g, 5.55 mmol, 2 equiv) resulted in a dark orange suspension to which  $\text{ZnEt}_2$  (1.20 mL, 11.37 mmol, 4.1 equiv) was added dropwise. The reaction mixture was then stirred for 16 hours at room temperature, followed by removal of the solvent under reduced pressure. The dark residue was redissolved in toluene and insoluble components were removed by filtration through a fritted funnel. The solution was concentrated under reduced pressure. Recrystallization in dichloromethane/hexanes at -20 °C gave **BDPA-5Me** as red crystals that were suitable for

X-ray analysis. Yield: 0.42 g (31 %).  $^1\text{H}$  NMR (500.2 MHz,  $\text{CDCl}_3$ , 25 °C):  $\delta$  (ppm) = 8.79 (d,  $J$  = 5.5 Hz, 2H; Py), 7.85 (d,  $J$  = 8.0 Hz, 2H; An), 7.47 (m, 6H; Py, An), 7.36 (d,  $J$  = 8.0 Hz, 2H; Py), 2.06 (s, 6H; Me), 1.33 (m, 2H; Et), 0.98 (m, 2H; Et), 0.73 (t,  $J$  = 7.5 Hz, 6H; Et), 0.30 (m, 10H; Et).  $^{13}\text{C}\{^1\text{H}\}$  NMR (125.8 MHz,  $\text{CDCl}_3$ , 25 °C):  $\delta$  (ppm) = 152.9, 150.1 (br), 143.0, 141.5, 136.0, 134.0, 128.7, 127.5, 127.3, 127.0, 121.7, 119.9, 23.8, 22.9 (br), 14.5 (br), 10.5, 9.6.  $^{11}\text{B}\{^1\text{H}\}$  NMR (160.4 MHz,  $\text{CDCl}_3$ , 25 °C):  $\delta$  (ppm) = -0.7 ( $w_{1/2}$  = 360 Hz). High-resolution MALDI-TOF MS (neg. mode, neat):  $m/z$  = 496.3194 ( $[\text{M}]^-$ , 11 %, calcd for  $^{12}\text{C}_{34}\text{H}_{38}^{11}\text{B}_2^{14}\text{N}_2$  496.3227), 467.2816 ( $[\text{M-Et}]^-$ , 100 %, calcd for  $^{12}\text{C}_{32}\text{H}_{33}^{11}\text{B}_2^{14}\text{N}_2$  467.2835).

**Synthesis of Endoperoxide BPO-3Me.** Compound **BDPA-3Me** (15.8 mg) was dissolved in  $\text{CH}_2\text{Cl}_2$  (8 mL) in a vial. The solution was irradiated under sunlight for one day. After the removal of solvent, the crude product was dissolved in a minimum amount of  $\text{CH}_2\text{Cl}_2$  and carefully layered with hexanes ( $v/v$  = 1:1) at room temperature. Diffusion and slow partial evaporation of the solvents gave **BPO-3Me** as colorless crystals. Yield: 16.0 mg (95 %).  $^1\text{H}$  NMR (599.7 MHz,  $\text{CDCl}_3$ , 25 °C):  $\delta$  (ppm) = 8.71 (s, 2H; Py), 8.13 (d,  $J$  = 8.4 Hz, 2H; Py), 7.97 (d,  $J$  = 8.4 Hz, 2H; Py), 7.29 (d,  $J$  = 7.8 Hz, 2H; An), 7.08 (vt,  $J$  = 7.5 Hz, 2H; An), 6.46 (d,  $J$  = 7.8 Hz, 2H; An), 2.62 (s, 6H; Me), 0.97 (m, 2H; Et), 0.80 (m, 2H; Et), 0.62 (m, 4H; Et), 0.41 (t,  $J$  = 7.5 Hz, 6H; Et), 0.22 (t,  $J$  = 7.5 Hz, 6H; Et).  $^{13}\text{C}\{^1\text{H}\}$  NMR (150.8 MHz,  $\text{CDCl}_3$ , 25 °C):  $\delta$  (ppm) = 148.4, 147.3 (br), 145.4, 140.0, 138.4, 136.4, 135.8, 129.9, 129.2, 126.2, 118.6, 82.0, 22.5 (br), 19.6 (br), 19.1, 10.4, 10.0.  $^{11}\text{B}\{^1\text{H}\}$  NMR (160.4 MHz,  $\text{CDCl}_3$ , 25 °C):  $\delta$  (ppm) = 1.2 ( $w_{1/2}$  = 490 Hz). High-resolution MALDI-TOF MS (neg. mode, neat):  $m/z$  = 499.2736 ( $[\text{M-Et}]^-$ , 100 %, calcd for  $^{12}\text{C}_{32}\text{H}_{33}^{11}\text{B}_2^{14}\text{N}_2^{16}\text{O}_2$  499.2733).

**Synthesis of Endoperoxide BPO-4Me.** Compound **BDPA-4Me** (10.0 mg) was dissolved in CH<sub>2</sub>Cl<sub>2</sub> in a vial. The solution was irradiated under sunlight for one day. After the removal of solvent, the crude product was dissolved in a minimum amount of CH<sub>2</sub>Cl<sub>2</sub> and carefully layered with hexanes (v/v = 1:1) at room temperature. Diffusion and slow partial evaporation of the solvents gave **BPO-4Me** as white crystals. Yield: 9.0 mg (85 %). <sup>1</sup>H NMR (499.9 MHz, CDCl<sub>3</sub>, 25 °C): δ (ppm) = 8.75 (d, J = 6.5 Hz, 2H; Py), 8.06 (s, 2H; Py), 7.58 (dd, J = 6.0 Hz, J = 2.0 Hz, 2H; Py), 7.30 (d, J = 7.5 Hz, 2H; An), 7.10 (vt, J = 7.5 Hz, 2H; An), 6.48 (d, J = 7.5 Hz, 2H; An), 2.62 (s, 6H; Me), 0.96 (m, 2H; Et), 0.79 (m, 2H; Et), 0.60 (m, 4H; Et), 0.41 (t, J = 8.0 Hz, 6H; Et), 0.22 (t, J = 7.5 Hz, 6H; Et). <sup>13</sup>C{<sup>1</sup>H} NMR (150.8 MHz, CDCl<sub>3</sub>, 25 °C): δ (ppm) = 151.7, 150.4, 147.5 (br), 145.0, 138.5, 135.9, 130.2, 130.0, 126.9, 126.2, 118.6, 82.1, 22.3 (br), 21.6, 19.5 (br), 10.4, 10.0. <sup>11</sup>B{<sup>1</sup>H} NMR (160.4 MHz, CDCl<sub>3</sub>, 25 °C): δ (ppm) = 0.8 (w<sub>1/2</sub> = 490 Hz). High-resolution MALDI-TOF MS (neg. mode, neat): m/z = 499.2732 ([M-Et]<sup>-</sup>, 100 %, calcd for <sup>12</sup>C<sub>32</sub><sup>1</sup>H<sub>33</sub><sup>11</sup>B<sub>2</sub><sup>14</sup>N<sub>2</sub><sup>16</sup>O<sub>2</sub> 499.2733).

**Synthesis of Endoperoxide BPO-5Me.** Compound **BDPA-5Me** (11.0 mg) was dissolved in CH<sub>2</sub>Cl<sub>2</sub> in a vial. The solution was irradiated under sunlight for one day. After the removal of solvent, the crude product was dissolved in a minimum amount of CH<sub>2</sub>Cl<sub>2</sub> and carefully layered with hexanes (v/v = 1:1) at room temperature. Diffusion and slow partial evaporation of the solvents gave **BPO-5Me** as white crystals. Yield: 5.0 mg (43 %). <sup>1</sup>H NMR (500.2 MHz, CDCl<sub>3</sub>, 25 °C): δ (ppm) = 8.85 (d, J = 5.5 Hz, 2H; Py), 7.98 (d, J = 7.5 Hz, 2H; Py), 7.67 (vt, J = 6.5 Hz, 2H; Py), 7.23 (d, J = 7.5 Hz, 2H; An), 7.03 (vt, J = 7.5 Hz, 2H; An), 6.42 (d, J = 7.5 Hz, 2H; An), 2.59 (s, 6H; Me), 0.93 (m, 2H; Et), 0.77 (m, 2H; Et), 0.64 (m, 4H; Et), 0.39 (t, J = 7.5 Hz, 6H; Et), 0.23 (t, J = 7.5 Hz, 6H; Et). <sup>13</sup>C{<sup>1</sup>H}

NMR (125.8 MHz, CDCl<sub>3</sub>, 25 °C):  $\delta$  (ppm) = 149.3, 146.2 (br), 144.1, 143.4, 140.8, 138.7, 135.1, 129.4, 125.6, 125.2, 119.3, 82.6, 22.7, 22.3 (br), 20.4 (br), 10.5, 9.8. <sup>11</sup>B{<sup>1</sup>H} NMR (160.4 MHz, CDCl<sub>3</sub>, 25 °C):  $\delta$  (ppm) = 2.3 ( $w_{1/2}$  = 470 Hz). High-resolution MALDI-TOF MS (neg. mode, neat):  $m/z$  = 528.3117 ([M]<sup>-</sup>, 10 %, calcd for <sup>12</sup>C<sub>34</sub><sup>1</sup>H<sub>38</sub><sup>11</sup>B<sub>2</sub><sup>14</sup>N<sub>2</sub><sup>16</sup>O<sub>2</sub> 528.3125), 499.2717 ([M-Et]<sup>-</sup>, 100 %, calcd for <sup>12</sup>C<sub>32</sub><sup>1</sup>H<sub>33</sub><sup>11</sup>B<sub>2</sub><sup>14</sup>N<sub>2</sub><sup>16</sup>O<sub>2</sub> 499.2733).

### 3.4 Conclusions

We have synthesized a series of BN-fused 9,10-dipyridylanthracenes with Me groups in different positions of the pyridyl ring to investigate in detail steric and electronic effects on the structural parameters, the optical and electronic properties, and the reactivity towards oxygen. Single crystal X-ray structures and DFT calculations reveal the most pronounced structural distortions for **BDPA-5Me** as reflected in a strong buckling and dislocation of the boron atoms from the anthracene backbone, whereas for **BDPA-2Me** a lengthening of the B-N bonds allows for some relaxation of the overall steric strain. The dynamic nature of the B←N Lewis pair formation was verified by variable temperature NMR spectroscopy and the barrier to the structural inversion correlated to the hindered rotation of the pyridyl group relative to the anthracene backbone. The substitution pattern also influences the HOMO and LUMO energy levels as evidenced by electrochemical, UV-Vis and fluorescence spectroscopy measurements. The most dramatic effect of the substitution pattern is seen in the reactivity toward oxygen to give the respective endoperoxides and their cyclo-reversion with release of singlet oxygen. **BDPA-2Me**, **BDPA-3Me** and **BDPA-4Me** rapidly react with O<sub>2</sub> under photoirradiation, whereas the rate for **BDPA-5Me** is one order of magnitude lower. The difference in reactivity is attributed to kinetic factors where

the Me groups in 5-position prevent effective planarization and therefore limit carbocation stabilization of the generally accepted zwitterionic intermediate in the oxygenation reaction. The substitution pattern also has a dramatic effect on the rate of thermal release of singlet oxygen from the endoperoxides with almost an order of magnitude difference in reactivity between each compound, **BDPA-5Me** < **BDPA-4Me** < **BDPA-3Me** < **BDPA-2Me**. We speculate that the much higher rate of cyclo-reversion for **BDPA-2Me** may relate to the weaker B←N dative bond and possibly an involvement of the borane Lewis acid sites in stabilizing the radical intermediate.

The demonstrated ability to alter the reactivity of the BN-anthracenes through relatively minor structural modifications has important ramifications in respect to potential applications as singlet oxygen sensitizers and on-demand delivery of singlet oxygen from the respective endoperoxides. With respect to singlet oxygen sensitization it is desirable to avoid self-sensitized reactivity with formation of endoperoxides. Our studies clearly indicate that further enhanced bulk in 5-position will be beneficial in this respect. A lower reactivity towards oxygen is also beneficial for applications in organic electronics and fluorescent imaging. Conversely, a high propensity for self-sensitized endoperoxide formation and subsequent cyclo-reversion is of interest for on-demand delivery of singlet O<sub>2</sub>. In this respect, the favorable reactivity of **BDPA-2Me** suggests that further weakening of the B-N bond, possibly even a fully ring-opened “frustrated” Lewis pair structure, could provide superior singlet oxygen release properties and might also result in unusual reactivity towards other substrates.

### 3.5 References

1. (a) He, X. M.; Baumgartner, T., Conjugated main-group polymers for optoelectronics. *RSC Adv.* **2013**, *3*, 11334-11350; (b) Priegert, A. M.; Rawe, B. W.; Serin, S. C.; Gates, D. P., Polymers and the p-block elements. *Chem. Soc. Rev.* **2016**, *45*, 922-953; (c) Stępień, M.; Gońka, E.; Żyła, M.; Sprutta, N., Heterocyclic Nanographenes and Other Polycyclic Heteroaromatic Compounds: Synthetic Routes, Properties, and Applications. *Chem. Rev.* **2017**, *117*, 3479-3716; (d) Zhang, G. Y.; Zhao, J. B.; Chow, P. C. Y.; Jiang, K.; Zhang, J. Q.; Zhu, Z. L.; Zhang, J.; Huang, F.; Yan, H., Nonfullerene Acceptor Molecules for Bulk Heterojunction Organic Solar Cells. *Chem. Rev.* **2018**, *118*, 3447-3507; (e) Gon, M.; Tanaka, K.; Chujo, Y., Recent progress in the development of advanced element-block materials. *Polym. J.* **2018**, *50*, 109-126; (f) Baumgartner, T.; Jäkle, F., *Main group strategies towards functional hybrid materials*. John Wiley & Sons: Hoboken, NJ, 2018; (g) Vidal, F.; Jäkle, F., Functional Polymeric Materials Based on Main Group Elements. *Angew. Chem. Int. Ed.* **2019**, *58*, 5846-5870.
2. (a) Entwistle, C. D.; Marder, T. B., Applications of Three-Coordinate Organoboron Compounds and Polymers in Optoelectronics. *Chem. Mat.* **2004**, *16*, 4574-4585; (b) Jäkle, F., Advances in the Synthesis of Organoborane Polymers for Optical, Electronic and Sensory Applications. *Chem. Rev.* **2010**, *110*, 3985-4022; (c) Escande, A.; Ingleson, M. J., Fused polycyclic aromatics incorporating boron in the core: fundamentals and applications. *Chem. Commun.* **2015**, *51*, 6257-6274; (d) Wakamiya, A.; Yamaguchi, S., Designs of Functional pi-Electron Materials based on the Characteristic Features of Boron. *B. Chem. Soc. Jpn.* **2015**, *88*, 1357-1377; (e) Wang, X. Y.; Wang, J. Y.; Pei, J., BN Heterosuperbenzenes: Synthesis and Properties. *Chem. Eur. J.* **2015**, *21*, 3528-3539; (f) Ji, L.; Griesbeck, S.; Marder, T. B., Recent developments in and perspectives on three-coordinate boron materials: a bright future. *Chem. Sci.* **2017**, *8*, 846-863; (g) Giustra, Z. X.; Liu, S. Y., The State of the Art in Azaborine Chemistry: New Synthetic Methods and Applications. *J. Am. Chem. Soc.* **2018**, *140*, 1184-1194; (h) von Grotthuss, E.; John, A.; Kaese, T.; Wagner, M., Doping Polycyclic Aromatics with Boron for Superior Performance in Materials Science and Catalysis. *Asian J. Org. Chem.* **2018**, *7*, 37-53; (i) Huang, J. H.; Li, Y. Q., BN Embedded Polycyclic pi-Conjugated Systems: Synthesis, Optoelectronic Properties, and Photovoltaic Applications. *Front. Chem.* **2018**, *6*; (j) Saito, S.; Matsuo, K.; Yamaguchi, S., Polycyclic pi-Electron System with Boron at Its Center. *J. Am. Chem. Soc.* **2012**, *134*, 9130-9133; (k) Reus, C.; Weidlich, S.; Bolte, M.; Lerner, H. W.; Wagner, M., C-Functionalized, Air- and Water-Stable 9,10-Dihydro-9,10-diboraanthracenes: Efficient Blue to Red Emitting Luminophores. *J. Am. Chem. Soc.* **2013**, *135*, 12892-12907; (l) Neue, B.; Araneda, J. F.; Piers, W. E.; Parvez, M., BN-Dibenzo[a,o]picenes: Analogues of an Unknown Polycyclic Aromatic Hydrocarbon. *Angew. Chem. Int. Ed.* **2013**, *52*, 9966-9969; (m) Sarkar, S. K.; Mukherjee, S.; Thilagar,



P., Going beyond Red with a Tri- and Tetracoordinate Boron Conjugate: Intriguing Near-IR Optical Properties and Applications in Anion Sensing. *Inorg. Chem.* **2014**, *53*, 2343-2345; (n) Wang, X. Y.; Zhuang, F. D.; Wang, R. B.; Wang, X. C.; Cao, X. Y.; Wang, J. Y.; Pei, J., A Straightforward Strategy toward Large BN-Embedded  $\pi$ -Systems: Synthesis, Structure, and Optoelectronic Properties of Extended BN Heterosuperbenzenes. *J. Am. Chem. Soc.* **2014**, *136*, 3764-3767; (o) Levine, D. R.; Siegler, M. A.; Tovar, J. D., Thiophene-Fused Borepins As Directly Functionalizable Boron-Containing  $\pi$ -Electron Systems. *J. Am. Chem. Soc.* **2014**, *136*, 7132-7139; (p) Kushida, T.; Shuto, A.; Yoshio, M.; Kato, T.; Yamaguchi, S., A Planarized Triphenylborane Mesogen: Discotic Liquid Crystals with Ambipolar Charge-Carrier Transport Properties. *Angew. Chem. Int. Ed.* **2015**, *54*, 6922-6925; (q) Yin, X. D.; Liu, K. L.; Ren, Y.; Lalancette, R. A.; Loo, Y. L.; Jäkle, F., Pyridalithiadiazole acceptor-functionalized triarylboranes with multi-responsive optoelectronic characteristics. *Chem Sci* **2017**, *8*, 5497-5505; (r) Yang, Z. Y.; Mao, Z.; Xie, Z. L.; Zhang, Y.; Liu, S. W.; Zhao, J.; Xu, J. R.; Chi, Z. G.; Aldred, M. P., Recent advances in organic thermally activated delayed fluorescence materials. *Chem. Soc. Rev.* **2017**, *46*, 915-1016; (s) Meng, B.; Ren, Y.; Liu, J.; Jäkle, F.; Wang, L. X., p- $\pi$  Conjugated Polymers Based on Stable Triarylborane with n-Type Behavior in Optoelectronic Devices. *Angew. Chem. Int. Ed.* **2018**, *57*, 2183-2187; (t) Cai, X. Y.; Su, S. J., Marching Toward Highly Efficient, Pure-Blue, and Stable Thermally Activated Delayed Fluorescent Organic Light-Emitting Diodes. *Adv. Funct. Mater.* **2018**, *28*; (u) John, A.; Bolte, M.; Lerner, H. W.; Meng, G. Y.; Wang, S. N.; Peng, T.; Wagner, M., Doubly boron-doped pentacenes as emitters for OLEDs. *J. Mater. Chem. C* **2018**, *6*, 10881-10887; (v) Wu, T. L.; Huang, M. J.; Lin, C. C.; Huang, P. Y.; Chou, T. Y.; Chen-Cheng, R. W.; Lin, H. W.; Liu, R. S.; Cheng, C. H., Diboron compound-based organic light-emitting diodes with high efficiency and reduced efficiency roll-off. *Nat. Photonics* **2018**, *12*, 235; (w) Liang, X.; Yan, Z. P.; Han, H. B.; Wu, Z. G.; Zheng, Y. X.; Meng, H.; Zuo, J. L.; Huang, W., Peripheral Amplification of Multi-Resonance Induced Thermally Activated Delayed Fluorescence for Highly Efficient OLEDs. *Angew. Chem. Int. Ed.* **2018**, *57*, 11316-11320.

3. (a) Ma, K.; Scheibitz, M.; Scholz, S.; Wagner, M., Applications of boron-nitrogen and boron-phosphorus adducts in organometallic chemistry. *J. Organomet. Chem.* **2002**, *652*, 11-19; (b) Li, D.; Zhang, Z. L.; Zhao, S. S.; Wang, Y.; Zhang, H. Y., Diboron-containing fluorophores with extended ladder-type  $\pi$ -conjugated skeletons. *Dalton Trans.* **2011**, *40*, 1279-1285; (c) Cao, Y.; Nagle, J. K.; Wolf, M. O.; Patrick, B. O., Tunable Luminescence of Bithiophene-Based Flexible Lewis Pairs. *J. Am. Chem. Soc.* **2015**, *137*, 4888-4891; (d) Dou, C. D.; Ding, Z. C.; Zhang, Z. J.; Xie, Z. Y.; Liu, J.; Wang, L. X., Developing Conjugated Polymers with High Electron Affinity by Replacing a C-C Unit with a B - N Unit. *Angew. Chem. Int. Ed.* **2015**, *54*, 3648-3652; (e) Yusuf, M.; Liu, K. L.; Guo, F.; Lalancette, R. A.; Jäkle, F., Luminescent organoboron ladder compounds via directed electrophilic aromatic C-H borylation. *Dalton Trans.* **2016**, *45*, 4580-4587; (f) Zhu, C.

Z.; Guo, Z. H.; Mu, A. U.; Liu, Y.; Wheeler, S. E.; Fang, L., Low Band Gap Coplanar Conjugated Molecules Featuring Dynamic Intramolecular Lewis Acid-Base Coordination. *J. Org. Chem.* **2016**, *81*, 4347-4352; (g) Shimogawa, H.; Yoshikawa, O.; Aramaki, Y.; Murata, M.; Wakamiya, A.; Murata, Y., 4,7-Bis[3-(dimesitylboryl)thien-2-yl]benzothiadiazole: Solvato-, Thermo-, and Mechanochromism Based on the Reversible Formation of an Intramolecular B-N Bond. *Chem. Eur. J.* **2017**, *23*, 3784-3791; (h) Schraff, S.; Sun, Y.; Pammer, F., Tuning of electronic properties via labile N → B-coordination in conjugated organoboranes. *J. Mater. Chem. C* **2017**, *5*, 1730-1741; (i) Grandl, M.; Sun, Y.; Pammer, F., Electronic and structural properties of N → B-ladder boranes with high electron affinity. *Org. Chem. Front.* **2018**, *5*, 336-352; (j) Zhu, C. Z.; Fang, L., Locking the Coplanar Conformation of pi-Conjugated Molecules and Macromolecules Using Dynamic Noncovalent Bonds. *Macromol. Rapid Comm.* **2018**, *39*; (k) Zeng, C.; Yuan, K.; Wang, N.; Peng, T.; Wu, G.; Wang, S., The opposite and amplifying effect of B ← N coordination on photophysical properties of regioisomers with an unsymmetrical backbone. *Chem. Sci.* **2019**, *10*, 1724-1734.

4. (a) Ros, A.; Estepa, B.; Lopez-Rodriguez, R.; Alvarez, E.; Fernandez, R.; Lassaletta, J. M., Use of Hemilabile N,N Ligands in Nitrogen-Directed Iridium-Catalyzed Borylations of Arenes. *Angew. Chem. Int. Ed.* **2011**, *50*, 11724-11728; (b) Kuninobu, Y.; Iwanaga, T.; Omura, T.; Takai, K., Palladium-Catalyzed ortho-Selective C-H Borylation of 2-Phenylpyridine and Its Derivatives at Room Temperature. *Angew. Chem. Int. Ed.* **2013**, *52*, 4431-4434; (c) Keske, E. C.; Moore, B. D.; Zenkina, O. V.; Wang, R. Y.; Schatte, G.; Crudden, C. M., Highly selective directed arylation reactions via back-to-back dehydrogenative C-H borylation/arylation reactions. *Chem. Commun.* **2014**, *50*, 9883-9886; (d) Kondrashov, M.; Raman, S.; Wendt, O. F., Metal controlled regioselectivity in the cyclometallation of 2-(1-naphthyl)-pyridine. *Chem. Commun.* **2015**, *51*, 911-913.

5. Grandl, M.; Kaese, T.; Krautsieder, A.; Sun, Y.; Pammer, F., Hydroboration as an Efficient Tool for the Preparation of Electronically and Structurally Diverse N → B-Heterocycles. *Chem.-Eur. J.* **2016**, *22*, 14373-14382.

6. (a) Ishida, N.; Moriya, T.; Goya, T.; Murakami, M., Synthesis of Pyridine-Borane Complexes via Electrophilic Aromatic Borylation. *J. Org. Chem.* **2010**, *75*, 8709-8712; (b) Wong, H.-L.; Wong, W.-T.; Yam, V. W.-W., Photochromic Thienylpyridine Bis(alkynyl)borane Complexes: Toward Readily Tunable Fluorescence Dyes and Photoswitchable Materials. *Org. Lett.* **2012**, *14*, 1862-1865; (c) Niu, L.; Yang, H.; Wang, R.; Fu, H., Metal-Free Ortho C H Borylation of 2-Phenoxypyridines under Mild Conditions. *Org. Lett.* **2012**, *14*, 2618-2621; (d) Dhanunjayarao, K.; Sa, S.; Aradhyula,

B. P. R.; Venkatasubbaiah, K., Synthesis of phenanthroimidazole-based four coordinate organoboron compounds. *Tetrahedron* **2018**, *74*, 5819-5825.

7. (a) Rao, Y. L.; Amarne, H.; Wang, S. N., Photochromic four-coordinate N,C-chelate boron compounds. *Coord. Chem. Rev.* **2012**, *256*, 759-770; (b) Zhao, Z. J.; Chang, Z. F.; He, B. R.; Chen, B.; Deng, C. M.; Lu, P.; Qiu, H. Y.; Tang, B. Z., Aggregation-Induced Emission and Efficient Solid-State Fluorescence from Tetraphenylethene-Based N,C-Chelate Four-Coordinate Organoborons. *Chem. Eur. J.* **2013**, *19*, 11512-11517; (c) Rao, Y. L.; Hörl, C.; Braunschweig, H.; Wang, S. N., Reversible Photochemical and Thermal Isomerization of Azaboratabisnorcaradiene to Azaborabenzotropilidene. *Angew. Chem. Int. Ed.* **2014**, *53*, 9086-9089; (d) Baranov, M. S.; Solntsev, K. M.; Baleeva, N. S.; Mishin, A. S.; Lukyanov, S. A.; Lukyanov, K. A.; Yampolsky, I. V., Red-Shifted Fluorescent Aminated Derivatives of a Conformationally Locked GFP Chromophore. *Chem.-Eur. J.* **2014**, *20*, 13234-13241; (e) Shaikh, A. C.; Ranade, D. S.; Thorat, S.; Maity, A.; Kulkarni, P. P.; Gonnade, R. G.; Munshi, P.; Patil, N. T., Highly emissive organic solids with remarkably broad color tunability based on N,C-chelate, four-coordinate organoborons. *Chem. Commun.* **2015**, *51*, 16115-16118; (f) Pais, V. F.; Alcaide, M. M.; Lopez-Rodriguez, R.; Collado, D.; Najera, F.; Perez-Inestrosa, E.; Alvarez, E.; Lassaletta, J. M.; Fernandez, R.; Ros, A.; Pischel, U., Strongly Emissive and Photostable Four-Coordinate Organoboron N,C Chelates and Their Use in Fluorescence Microscopy. *Chem. - Eur. J.* **2015**, *21*, 15369-15376; (g) Crossley, D. L.; Vitorica-Yrezabal, I.; Humphries, M. J.; Turner, M. L.; Ingleson, M. J., Highly Emissive Far Red/Near-IR Fluorophores Based on Borylated Fluorene-Benzothiadiazole Donor-Acceptor Materials. *Chem. Eur. J.* **2016**, *22*, 12439-12448; (h) Wong, B. Y. W.; Wong, H. L.; Wong, Y. C.; Chan, M. Y.; Yam, V. W. W., Air-Stable Spirofluorene-Containing Ladder-Type Bis(alkynyl)borane Compounds with Readily Tunable Full Color Emission Properties. *Chem.-Eur. J.* **2016**, *22*, 15095-15106; (i) Zhao, R. Y.; Dou, C. D.; Xie, Z. Y.; Liu, J.; Wang, L. X., Polymer Acceptor Based on BN Units with Enhanced Electron Mobility for Efficient All-Polymer Solar Cells. *Angew. Chem. Int. Ed.* **2016**, *55*, 5313-5317; (j) Shiu, Y. J.; Chen, Y. T.; Lee, W. K.; Wu, C. C.; Lin, T. C.; Liu, S. H.; Chou, P. T.; Lu, C. W.; Cheng, I. C.; Lien, Y. J.; Chi, Y., Efficient thermally activated delayed fluorescence of functional phenylpyridinato boron complexes and high performance organic light-emitting diodes. *J. Mater. Chem. C* **2017**, *5*, 1452-1462; (k) Matsuo, K.; Yasuda, T., Enhancing thermally activated delayed fluorescence characteristics by intramolecular B-N coordination in a phenylpyridine-containing donor-acceptor pi-system. *Chem. Commun.* **2017**, *53*, 8723-8726; (l) Hecht, R.; Kade, J.; Schmidt, D.; Nowak-Krol, A., n-Channel Organic Semiconductors Derived from Air-Stable Four-Coordinate Boron Complexes of Substituted Thienylthiazoles. *Chem.-Eur. J.* **2017**, *23*, 11620-11628; (m) Møllerup, S. K.; Li, C.; Peng, T.; Wang, S. N., Regioselective Photoisomerization/C-C Bond Formation of Asymmetric B(ppy)(Mes)(Ar): The Role of the Aryl Groups on Boron. *Angew. Chem. Int. Ed.* **2017**, *56*, 6093-6097; (n) Alahmadi,

A. F.; Lalancette, R. A.; Jäkle, F., Highly Luminescent Ladderized Fluorene Copolymers Based on B-N Lewis Pair Functionalization. *Macromol. Rapid Comm.* **2018**, *39*; (o) Stanoppi, M.; Lorbach, A., Boron-based donor-spiro-acceptor compounds exhibiting thermally activated delayed fluorescence (TADF). *Dalton Trans.* **2018**, *47*, 10394-10398; (p) Mellerup, S. K.; Wang, S., Chapter 3: Photoresponsive Organoboron Systems. In *Main Group Strategies towards Functional Hybrid Materials*, Baumgartner, T.; Jäkle, F., Eds. 2018; pp 47-77; (q) Pang, S.; Más-Montoya, M.; Manjun Xiao; Duan, C.; Wang, Z.; Liu, X.; Janssen, R.; Yu, G.; Huang, F.; Cao, Y., Adjusting Aggregation Modes, Photophysical and Photovoltaic Properties of Diketopyrrolopyrrole-Based Small Molecules by Introducing B←N Bonds. *Chem.-Eur. J.* **2019**, *25*, 564-572.

8. (a) Wu, J. S.; Pisula, W.; Müllen, K., Graphenes as potential material for electronics. *Chem. Rev.* **2007**, *107*, 718-747; (b) Vadrucchi, R.; Weder, C.; Simon, Y. C., Organogels for low-power light upconversion. *Mater. Horiz.* **2015**, *2*, 120-124; (c) Smith, J. N.; Hook, J. M.; Lucas, N. T., Superphenylphosphines: Nanographene-Based Ligands That Control Coordination Geometry and Drive Supramolecular Assembly. *J. Am. Chem. Soc.* **2018**, *140*, 1131-1141; (d) Huang, Z. Y.; Tang, M. L., Semiconductor Nanocrystal Light Absorbers for Photon Upconversion. *J. Phys. Chem. Lett.* **2018**, *9*, 6198-6206; (e) Krishnapriya, K. C.; Musser, A. J.; Patil, S., Molecular Design Strategies for Efficient Intramolecular Singlet Exciton Fission. *ACS Energy Lett.* **2019**, *4*, 192-202.

9. (a) Narita, A.; Wang, X. Y.; Feng, X. L.; Müllen, K., New advances in nanographene chemistry. *Chem. Soc. Rev.* **2015**, *44*, 6616-6643; (b) Li, G.; Yoon, K. Y.; Zhong, X. J.; Wang, J. C.; Zhang, R.; Guest, J. R.; Wen, J. G.; Zhu, X. Y.; Dong, G. B., A modular synthetic approach for band-gap engineering of armchair graphene nanoribbons. *Nat. Commun.* **2018**, *9*; (c) Wang, X. Y.; Urgel, J. I.; Barin, G. B.; Eimre, K.; Di Giovannantonio, M.; Milani, A.; Tommasini, M.; Pignedoli, C. A.; Ruffieux, P.; Feng, X. L.; Fasel, R.; Müllen, K.; Narita, A., Bottom-Up Synthesis of Heteroatom-Doped Chiral Graphene Nanoribbons. *J. Am. Chem. Soc.* **2018**, *140*, 9104-9107.

10. Sun, H.; Kabb, C. P.; Dai, Y. Q.; Hill, M. R.; Ghiviriga, I.; Bapat, A. P.; Sumerlin, B. S., Macromolecular metamorphosis via stimulus-induced transformations of polymer architecture. *Nature Chem.* **2017**, *9*, 817-823.

11. (a) Aubry, J. M.; Pierlot, C.; Rigaudy, J.; Schmidt, R., Reversible binding of oxygen to aromatic compounds. *Acc. Chem. Res.* **2003**, *36*, 668-675; (b) Fudickar, W.; Linker, T., Release of Singlet Oxygen from Organic Peroxides under Mild Conditions. *ChemPhotoChem* **2018**, *2*, 548-558; (c) Pibiri, I.; Buscemi, S.; Piccionello, A. P.; Pace, A., Photochemically Produced Singlet Oxygen: Applications and Perspectives. *ChemPhotoChem* **2018**, *2*, 535-547.

12. (a) Martins, S.; Farinha, J. P. S.; Baleizao, C.; Berberan-Santos, M. N., Controlled release of singlet oxygen using diphenylanthracene functionalized polymer nanoparticles. *Chem. Commun.* **2014**, *50*, 3317-3320; (b) Klaper, M.; Linker, T., Intramolecular Transfer of Singlet Oxygen. *J. Am. Chem. Soc.* **2015**, *137*, 13744-13747; (c) Yuan, Z.; Yu, S.; Cao, F. Y.; Mao, Z. W.; Gao, C. Y.; Ling, J., Near-infrared light triggered photothermal and photodynamic therapy with an oxygen-shuttle endoperoxide of anthracene against tumor hypoxia. *Polym. Chem.* **2018**, *9*, 2124-2133.
  
13. (a) Wu, H. Y.; Song, Q. J.; Ran, G. X.; Lu, X. M.; Xu, B. G., Recent developments in the detection of singlet oxygen with molecular spectroscopic methods. *Trend Analyt. Chem.* **2011**, *30*, 133-141; (b) Altinok, E.; Smith, Z. C.; Thomas, S. W., Two-Dimensional, Acene-Containing Conjugated Polymers That Show Ratiometric Fluorescent Response to Singlet Oxygen. *Macromolecules* **2015**, *48*, 6825-6831.
  
14. Fudickar, W.; Fery, A.; Linker, T., Reversible light and air-driven lithography by singlet oxygen. *J. Am. Chem. Soc.* **2005**, *127*, 9386-9387.
  
15. Gao, Z.; Han, Y. F.; Wang, F., Cooperative supramolecular polymers with anthracene. endoperoxide photo-switching for fluorescent anti-counterfeiting. *Nat. Commun.* **2018**, *9*, 3977.
  
16. (a) Zehm, D.; Fudickar, W.; Linker, T., Molecular switches flipped by oxygen. *Angew. Chem. Int. Ed.* **2007**, *46*, 7689-7692; (b) Zehm, D.; Fudickar, W.; Hans, M.; Schilde, U.; Kelling, A.; Linker, T., 9,10-Diarylanthracenes as Molecular Switches. Syntheses, Properties, Isomerisations and Their Reactions with Singlet Oxygen. *Chem. - Eur. J.* **2008**, *14*, 11429-11441.
  
17. (a) Møllerup, S. K.; Hafele, L.; Lorbach, A.; Wang, X.; Wang, S. N., Triplet Energy and pi-Conjugation Effects on Photoisomerization of Chiral N,C-Chelate Organoborons with PAH Substituents. *Org. Lett.* **2017**, *19*, 3851-3854; (b) Wang, S. N.; Yuan, K.; Hu, M. F.; Wang, X.; Peng, T.; Wang, N.; Li, Q. S., Cleavage of Unstrained C-C Bonds in Acenes by Boron and Light: Transformation of Naphthalene into Benzoborepin. *Angew. Chem. Int. Ed.* **2018**, *57*, 1073-1077.
  
18. (a) Pais, V. F.; Lineros, M.; Lopez-Rodriguez, R.; El-Sheshtawy, H. S.; Fernandez, R.; Lassaletta, J. M.; Ros, A.; Pischel, U., Preparation and pH-Switching of Fluorescent Borylated Arylisoquinolines for Multilevel Molecular Logic. *J. Org. Chem.* **2013**, *78*, 7949-7961; (b) Pais, V. F.; El-Sheshtawy, H. S.; Fernandez, R.; Lassaletta, J. M.; Ros, A.; Pischel, U., Borylated Arylisoquinolines: Photophysical Properties and Switching Behavior of Promising Tunable Fluorophores. *Chem-Eur J* **2013**, *19*, 6650-6661; (c) Pais, V. F.; Lassaletta, J. M.; Fernandez, R.; El-Sheshtawy, H. S.; Ros, A.; Pischel, U., Organic Fluorescent Thermometers Based on Borylated Arylisoquinoline Dyes. *Chem.-*

*Eur. J.* **2014**, *20*, 7638-7645; (d) Bosca, F.; Cuquerella, M. C.; Pais, V. F.; Ros, A.; Pischel, U., Excited-State Pathways of Four-Coordinate N,C-Chelate Organoboron Dyes. *ChemPhotoChem* **2018**, *2*, 34-41.

19. (a) Shen, C. S.; Srebro-Hooper, M.; Jean, M.; Vanthuyne, N.; Toupet, L.; Williams, J. A. G.; Torres, A. R.; Riives, A. J.; Muller, G.; Autschbach, J.; Crassous, J., Synthesis and Chiroptical Properties of Hexa-, Octa-, and Deca-azaborahelicenes: Influence of Helicene Size and of the Number of Boron Atoms. *Chem.-Eur. J.* **2017**, *23*, 407-418; (b) Dominguez, Z.; Lopez-Rodriguez, R.; Alvarez, E.; Abbate, S.; Longhi, G.; Pischel, U.; Ros, A., Azabora[5]helicene Charge-Transfer Dyes Show Efficient and Spectrally Variable Circularly Polarized Luminescence. *Chem.-Eur. J.* **2018**, *24*, 12660-12668.

20. Stolar, M.; Baumgartner, T., Functional conjugated pyridines via main-group element tuning. *Chem. Commun.* **2018**, *54*, 3311-3322.

21. (a) 9- or 9,10-borylated anthracenes are more common; see: ; (b) Yamaguchi, S.; Akiyama, S.; Tamao, K., Tri-9-anthrylborane and its Derivatives: New Boron-Containing  $\pi$ -Electron Systems with Divergently Extended  $\pi$ -Conjugation through Boron. *J. Am. Chem. Soc.* **2000**, *122*, 6335-6336; (c) Uchida, M.; Ono, Y.; Yokoi, H.; Nakano, T.; Furukawa, K., Undoping Type of Highly Efficient Organic Light Emitting Diodes. *J. Photopolym. Sci. Technol.* **2001**, *14*, 305-310.

22. Liu, K. L.; Lalancette, R. A.; Jäkle, F., B-N Lewis Pair Functionalization of Anthracene: Structural Dynamics, Optoelectronic Properties, and O<sub>2</sub> Sensitization. *J. Am. Chem. Soc.* **2017**, *139*, 18170-18173.

23. Yang, C.; Jacob, J.; Müllen, K., Synthesis and photochromic properties of ladderized poly(p-phenylene-alt-9,10-anthrylene)s. *Macromolecules* **2006**, *39*, 5696-5704.

24. Ingleson, M. J., A perspective on direct electrophilic arene borylation. *Synlett* **2012**, *23*, 1411-1415.

25. Fudickar, W.; Linker, T., Synthesis of Pyridylanthracenes and Their Reversible Reaction with Singlet Oxygen to Endoperoxides. *J. Org. Chem.* **2017**, *82*, 9258-9262.

26. (a) Schaffner, K.; Schmidt, R.; Brauer, H.-D., Photochromism based on the reversible reaction of singlet oxygen with aromatic compounds. *Mol. Cryst. Liq. Cryst.* **1994**, *246*, 119-125; (b) Seip, M.; Brauer, H. D., Endoperoxide Formation of Helianthrene with Triplet Molecular-Oxygen - a Spin-Forbidden Reaction. *J. Am. Chem. Soc.* **1992**, *114*, 4486-4490.

27. (a) Fudickar, W.; Linker, T., Remote substituent effects on the photooxygenation of 9,10-diarylanthracenes: strong evidence for polar intermediates. *Chem. Commun.* **2008**,

1771-1773; (b) Fudickar, W.; Linker, T., Why Triple Bonds Protect Acenes from Oxidation and Decomposition. *J. Am. Chem. Soc.* **2012**, *134*, 15071-15082.

28. Fudickar, W.; Linker, T., Release of Singlet Oxygen from Aromatic Endoperoxides by Chemical Triggers. *Angew. Chem. Int. Ed.* **2018**, *57*, 12971-12975.

29. Gaussian 09, Revision B.01, M. J. Frisch, G. W. Trucks, H. B. Schlegel, G. E. Scuseria, M. A. Robb, J. R. Cheeseman, G. Scalmani, V. Barone, B. Mennucci, G. A. Petersson, H. Nakatsuji, M. Caricato, X. Li, H. P. Hratchian, A. F. Izmaylov, J. Bloino, G. Zheng, J. L. Sonnenberg, M. Hada, M. Ehara, K. Toyota, R. Fukuda, J. Hasegawa, M. Ishida, T. Nakajima, Y. Honda, O. Kitao, H. Nakai, T. Vreven, J. A. Montgomery, Jr., J. E. Peralta, F. Ogliaro, M. Bearpark, J. J. Heyd, E. Brothers, K. N. Kudin, V. N. Staroverov, T. Keith, R. Kobayashi, J. Normand, K. Raghavachari, A. Rendell, J. C. Burant, S. S. Iyengar, J. Tomasi, M. Cossi, N. Rega, J. M. Millam, M. Klene, J. E. Knox, J. B. Cross, V. Bakken, C. Adamo, J. Jaramillo, R. Gomperts, R. E. Stratmann, O. Yazyev, A. J. Austin, R. Cammi, C. Pomelli, J. W. Ochterski, R. L. Martin, K. Morokuma, V. G. Zakrzewski, G. A. Voth, P. Salvador, J. J. Dannenberg, S. Dapprich, A. D. Daniels, O. Farkas, J. B. Foresman, J. V. Ortiz, J. Cioslowski, and D. J. Fox, Gaussian, Inc., Wallingford CT, 2010.

30. Bruker (2005). *SAINT* Version 7.23a. Bruker AXS Inc., Madison, Wisconsin, USA. Bruker (2006). *APEX 2* Version 2.0-2. Bruker AXS Inc., Madison, Wisconsin, USA.

31. G. M. Sheldrick (2008). SADABS. University of Göttingen, Germany. G. M. Sheldrick, *Acta Cryst.* **2008**, A64, 112-122. G. M. Sheldrick, SHELXL, *Acta Cryst.* **2015**, C71, 3-8.

32. J. Sandström, *Dynamic NMR Spectroscopy*, Academic Press, London, **1982**.

33. Liu, K. L.; Lalancette, R. A.; Jäkle, F., Tuning the Structure and Electronic Properties of B-N Fused Dipyridylanthracene and Implications on the Self-Sensitized Reactivity with Singlet Oxygen. *J. Am. Chem. Soc.* 2019, *141*, 7453-7462.

## Appendix

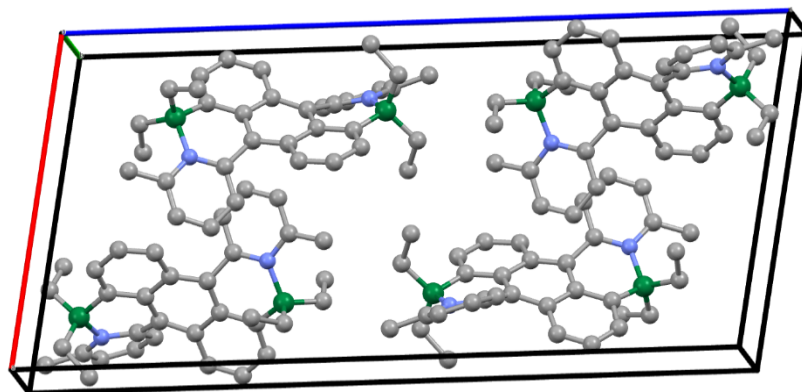


Figure 3-12. Crystal packing of **BDPA-2Me**

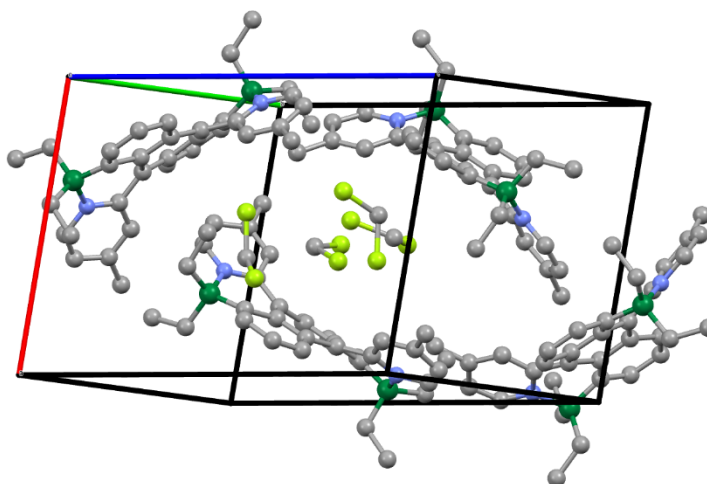


Figure 3-13. Crystal packing of **BDPA-4Me**

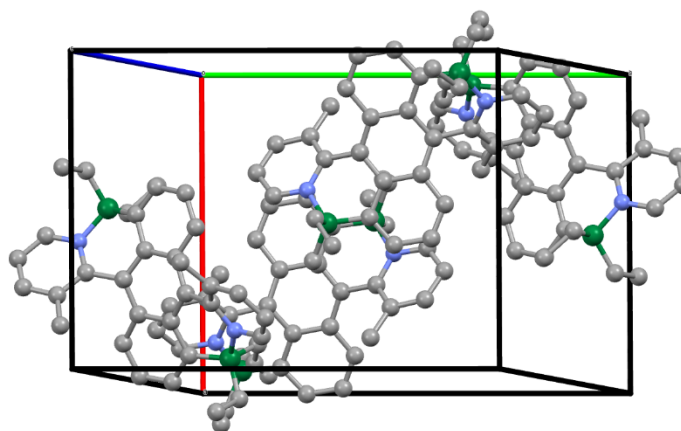


Figure 3-14. Crystal packing of **BDPA-5Me**



**Table 3-6.** Comparison of computed total energies for *cis*- and *trans*-isomers.

|                 | <i>cis</i> -isomer | <i>trans</i> -isomer | <i>cis</i> -isomer                       | <i>trans</i> -isomer                     | $\Delta E$  |
|-----------------|--------------------|----------------------|--|--|-------------|
|                 | $E(\text{rb3lyp})$ | $E(\text{rb3lyp})$   | $\Sigma_{\text{el \& th free energies}}$ | $\Sigma_{\text{el \& th free energies}}$ | (kJ/mol)    |
|                 | (Hartree)          | (Hartree)            | (Hartree)                                | (Hartree)                                |             |
| <b>BDPA-2Me</b> | -1477.7984         | -1477.7851           | -1477.2161                               | -1477.200133                             | 35.0 / 42.0 |
| <b>BDPA-3Me</b> | -1477.8258         | -1477.8163           | -1477.2462                               | -1477.235471                             | 25.0 / 28.1 |
| <b>BDPA-4Me</b> | -1477.8280         | -1477.8184           | -1477.2487                               | -1477.238861                             | 25.3 / 25.9 |
| <b>BDPA-5Me</b> | -1477.8080         | -1477.7947           | -1477.2258                               | -1477.213080                             | 34.8 / 33.5 |

**Table 3-7.** Comparison of geometric parameters (distances in Å, angles in °) obtained from X-ray crystal structure analyses and **DFT calculations** (Gaussian 09; rb3lyp/6-31g(d))

|  | B-N                   | B-C <sub>1,5</sub>     | C <sub>9,10</sub> -C <sub>Py</sub> | $\alpha$ [a]          | $\beta$ [b]     | $\gamma$ [c]    | $\delta$ [d] | $\varepsilon$ [e] | $\phi$ [f]    |
|--|-----------------------|------------------------|------------------------------------|-----------------------|-----------------|-----------------|--------------|-------------------|---------------|
| <b>BDPA</b>                                    | 1.642                 | 1.619                  | 1.471                              | 105.3                 | 171.2           | 165.4           | 18.4         | 21.3              | 36.2          |
| <b>BDPA-2Me</b> <sub>X-ray</sub> <sup>22</sup> | 1.685(3),<br>1.671(4) | 1.616(4),<br>1.626(4)  | 1.479(3),<br>1.479(3)              | 106.5(2),<br>107.6(2) | 173.6,<br>174.8 | 164.7,<br>166.4 | 18.6         | 21.5              | 39.0,<br>38.8 |
| <b>BDPA-2Me</b>                                | 1.690                 | 1.626                  | 1.474                              | 107.4                 | 172.2           | 167.6           | 17.4         | 21.6              | 40.0          |
| <b>BDPA-3Me</b>                                | 1.643                 | 1.618                  | 1.471                              | 105.5                 | 171.0           | 165.8           | 18.1         | 20.7              | 35.4          |
| <b>BDPA-4Me</b> <sub>X-ray</sub>               | 1.628(8),<br>1.635(8) | 1.584(10),<br>1.610(9) | 1.492(8),<br>1.459(8)              | 106.2(5),<br>106.4(5) | 168.8,<br>170.5 | 166.2,<br>167.3 | 16.5         | 17.4              | 34.9,<br>32.2 |
| <b>BDPA-4Me</b>                                | 1.640                 | 1.618                  | 1.472                              | 105.4                 | 171.0           | 165.6           | 18.2         | 21.1              | 35.8          |
| <b>BDPA-5Me</b> <sub>X-ray</sub>               | 1.637(2),<br>1.642(2) | 1.611(2),<br>1.615(2)  | 1.480(2),<br>1.479(2)              | 106.6(1),<br>106.0(1) | 168.0,<br>168.8 | 169.6,<br>168.1 | 17.8         | 20.7              | 41.6,<br>43.5 |
| <b>BDPA-5Me</b>                                | 1.655                 | 1.618                  | 1.474                              | 105.7                 | 168.8           | 167.3           | 20.9         | 25.6              | 42.2          |

[a]  $\alpha$  = C<sub>1,5</sub>-B-N angle; [b]  $\beta$  = Cent1-C<sub>1,5</sub>-B; [c]  $\gamma$  = Cent2-C<sub>9,10</sub>-C<sub>Py</sub>; [d]  $\delta$  = internal twist of central anthracene ring; [e]  $\varepsilon$  = Ph<sub>An,out</sub> // Ph<sub>An,out</sub>, dihedral angle between outer anthracene rings; [f]  $\phi$  = Ph<sub>An,in</sub> // Py, dihedral angle between inner anthracene ring and pendent pyridyl ring.

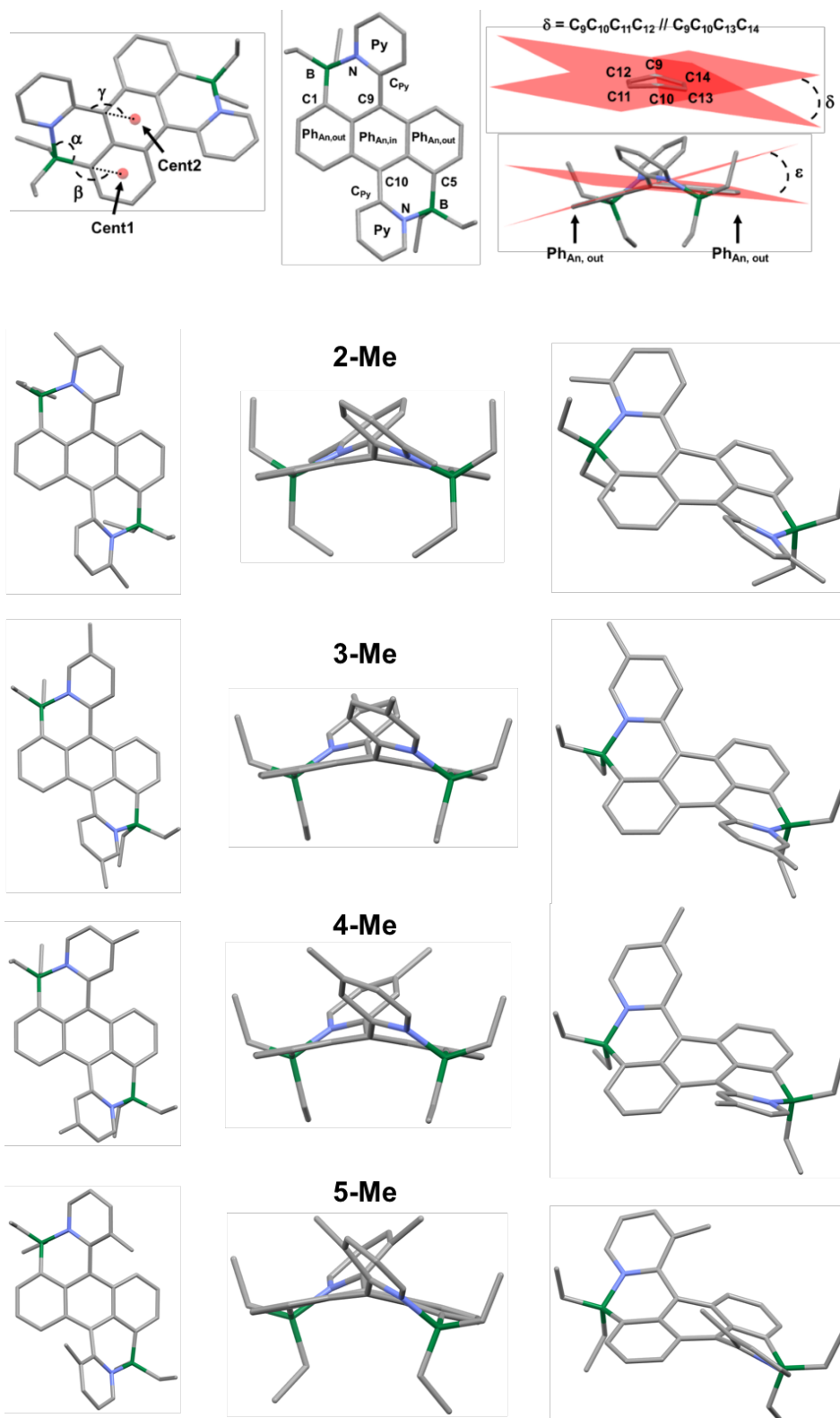


**Figure 3-15.** Different views of the optimized structures of **BDPA-2Me**, **BDPA-3Me**, **BDPA-4Me**, and **BDPA-5Me** (Gaussian 09; rb3lyp/6-31g(d)). C grey, B green, N blue.

**Table 3-8.** Electrochemical data of BN-functionalized anthracenes.

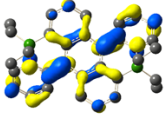
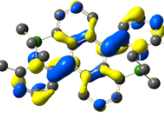
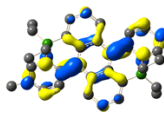
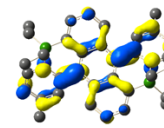
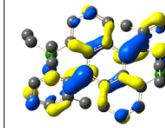
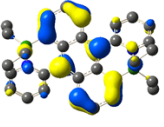
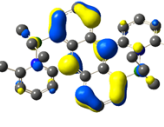
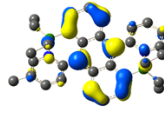
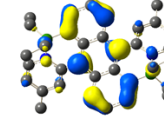
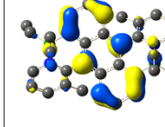
| Compound                     | $E_{\text{ox}}^{\text{CV}}$ [a]<br>[V] | $E_{\text{ox}}^{\text{SWV}}$ [a]<br>[V] | $E_{\text{red}}^{\text{CV}}$ [b]<br>[V] | $E_{\text{red}}^{\text{SWV}}$ [b]<br>[V] |
|------------------------------|--|---|---|--|
| <b>BDPA-2Me<sup>22</sup></b> | 0.40                                   | 0.36                                    | -1.87, -2.07                            | -1.78, -1.99                             |
| <b>BDPA-3Me</b>              | 0.39                                   | 0.37                                    | -1.77, -2.02                            | -1.74, -1.99                             |
| <b>BDPA-4Me</b>              | 0.42                                   | 0.38                                    | -1.77, -2.00                            | -1.75, -1.97                             |
| <b>BDPA-5Me</b>              | 0.48                                   | 0.43                                    | -1.81, -2.19                            | -1.78, -2.16                             |

[a] Recorded using 0.1M Bu<sub>4</sub>N[PF<sub>6</sub>] in CH<sub>2</sub>Cl<sub>2</sub>,  $E_{\text{ox}} = E_{\text{pa}}$ ; [b] recorded using 0.1M Bu<sub>4</sub>N[PF<sub>6</sub>] in THF,  $E_{\text{red}} = 0.5 (E_{\text{pc}} + E_{\text{pa}})$ .

**Table 3-9.** Comparison of calculated orbital energy levels (rb3lyp/6-31g(d)) for differently substituted B-N Lewis-pairs (*cis*-isomers)

| Compound        | LUMO (eV) | HOMO (eV) | $E_{\text{gap}}$ (eV) |
|-----------------|-----------|-----------|-----------------------|
| <b>BDPA</b>     | -2.63     | -4.91     | 2.28                  |
| <b>BDPA-2Me</b> | -2.43     | -4.77     | 2.34                  |
| <b>BDPA-3Me</b> | -2.51     | -4.81     | 2.30                  |
| <b>BDPA-4Me</b> | -2.52     | -4.83     | 2.31                  |
| <b>BDPA-5Me</b> | -2.51     | -4.93     | 2.42                  |

**Table 3-10.** Kohn-Sham HOMO and LUMO orbital plots for differently substituted BN-functionalized anthracenes (rb3lyp/6-31g(d), scaling radii of 75%, isovalue = 0.04)

|      | BDPA   | BDPA-2Me   | BDPA-3Me   | BDPA-4Me   | BDPA-5Me   |
|------|--|--|--|--|--|
| LUMO | <br>- 2.63 eV | <br>- 2.43 eV | <br>- 2.51 eV | <br>- 2.52 eV | <br>- 2.51 eV |
| HOMO | <br>- 4.91 eV | <br>- 4.77 eV | <br>- 4.81 eV | <br>- 4.83 eV | <br>- 4.93 eV |

**Table 3-11.** TD-DFT data for **BDPA-2Me**, **BDPA-3Me**, **BDPA-4Me** and **BDPA-5Me** (rcam-b3lyp/6-31g(d))

| Compound        | Transition <sup>[a]</sup> | $E_{\text{ex}}$<br>(eV) | $\lambda$ (nm) | Oscillator<br>strength $f$ | Assignment  |
|-----------------|---------------------------|-------------------------|----------------|----------------------------|---|
| <b>BDPA-2Me</b> | $S_0 \rightarrow S_1$     | <b>2.37</b>             | <b>522.8</b>   | <b>0.359</b>               | <b>H <math>\rightarrow</math> L (0.70)</b>  |
|                 | $S_0 \rightarrow S_8$     | 4.40                    | 282.1          | 0.181                      | H-8 $\rightarrow$ L+1 (-0.13),<br>H-7 $\rightarrow$ L (0.17)<br>H-3 $\rightarrow$ L (0.62),<br>H-1 $\rightarrow$ L+1 (-0.18)  |
|                 | $S_0 \rightarrow S_{10}$  | 4.64                    | 267.1          | 0.204                      | H-7 $\rightarrow$ L (-0.11),<br>H-6 $\rightarrow$ L (0.44),<br>H-2 $\rightarrow$ L (0.24),<br>H-2 $\rightarrow$ L+4 (0.11),<br>H-1 $\rightarrow$ L+1 (-0.15),<br>H $\rightarrow$ L+5 (0.39) |
|                 | $S_0 \rightarrow S_{11}$  | 4.69                    | 264.6          | 0.169                      | H-7 $\rightarrow$ L (0.15),<br>H-6 $\rightarrow$ L (0.49),<br>H-4 $\rightarrow$ L+1 (0.11),<br>H-2 $\rightarrow$ L (0.19),<br>H $\rightarrow$ L+5 (0.37)                                    |
|                 | $S_0 \rightarrow S_1$     | <b>2.33</b>             | <b>532.2</b>   | <b>0.409</b>               | <b>H <math>\rightarrow</math> L (0.70)</b>  |
| <b>BDPA-3Me</b> | $S_0 \rightarrow S_6$     | 4.30                    | 288.1          | 0.107                      | H-7 $\rightarrow$ L (-0.11),<br>H-6 $\rightarrow$ L (-0.22),<br>H-3 $\rightarrow$ L (0.34),<br>H $\rightarrow$ L+2 (-0.15),<br>H $\rightarrow$ L+4 (0.52)                                   |
|                 | $S_0 \rightarrow S_{13}$  | 4.74                    | 261.3          | 0.569                      | H-7 $\rightarrow$ L (-0.25),<br>H-6 $\rightarrow$ L (-0.20),<br>H-2 $\rightarrow$ L (-0.25),<br>H-2 $\rightarrow$ L+4 (-0.13),<br>H $\rightarrow$ L+5 (0.53)                                |
|                 | $S_0 \rightarrow S_1$     | <b>2.33</b>             | <b>532.5</b>   | <b>0.365</b>               | <b>H <math>\rightarrow</math> L (0.70)</b>  |
| <b>BDPA-4Me</b> | $S_0 \rightarrow S_{12}$  | 4.67                    | 265.7          | 0.109                      | H-7 $\rightarrow$ L (0.45),<br>H-6 $\rightarrow$ L (-0.33),<br>H-2 $\rightarrow$ L (-0.14),<br>H-1 $\rightarrow$ L+1 (-0.11),<br>H $\rightarrow$ L+5 (-0.31)                                |
|                 | $S_0 \rightarrow S_{13}$  | 4.75                    | 261.0          | 0.535                      | H-7 $\rightarrow$ L (0.38),<br>H-3 $\rightarrow$ L (-0.11),<br>H-2 $\rightarrow$ L (0.23),<br>H-2 $\rightarrow$ L+4 (0.12),   |
|                 | $S_0 \rightarrow S_1$     | <b>2.33</b>             | <b>532.5</b>   | <b>0.365</b>               | <b>H <math>\rightarrow</math> L (0.70)</b>  |

|                 |                          |             |              |              |   |
|-----------------|--------------------------|-------------|--------------|--------------|---|
| H → L+5 (0.49)  |                          |             |              |              |   |
| <b>BDPA-5Me</b> | $S_0 \rightarrow S_1$    | <b>2.42</b> | <b>512.0</b> | <b>0.310</b> | <b>H → L (0.70)</b>   |
|                 | $S_0 \rightarrow S_6$    | 4.28        | 289.5        | 0.147        | H-7 → L (0.24),<br>H-3 → L (0.60),<br>H-1 → L+1 (0.11),<br>H → L+2 (-0.16)                        |
|                 | $S_0 \rightarrow S_{13}$ | 4.74        | 261.6        | 0.445        | H-7 → L (0.38),<br>H-2 → L (-0.23),<br>H-2 → L+2 (-0.10),<br>H-2 → L+4 (-0.11),<br>H → L+5 (0.50) |

[a] Only transitions with oscillator strengths >0.1 are presented.

**Table 3-12.** Comparison of the calculated singlet state and triplet state energies for **BDPA-2Me**, **BDPA-3Me**, **BDPA-4Me**, and **BDPA-5Me**

|                 | $S_0$ <sup>[a]</sup> | $T_1$ <sup>[a]</sup> | $S_1$ <sup>[b]</sup> | $\Delta E_{ad}(S_0-S_1)$   | $\Delta E_{ad}(S_0-T_1)$   | $\Delta E_{ad}(S_1-T_1)$   |
|-----------------|----------------------|----------------------|----------------------|----------------------------|----------------------------|----------------------------|
|                 | (Hartree)            | (Hartree)            | (Hartree)            | (eV/kJ mol <sup>-1</sup> ) | (eV/kJ mol <sup>-1</sup> ) | (eV/kJ mol <sup>-1</sup> ) |
| <b>BDPA-2Me</b> | -1477.7984           | -1477.7620           | -1477.7322           | 1.803/174.0                | 0.990/95.5                 | 0.813/78.5                 |
| <b>BDPA-3Me</b> | -1477.8258           | -1477.7901           | -1477.7598           | 1.797/173.4                | 0.972/93.8                 | 0.825/79.6                 |
| <b>BDPA-4Me</b> | -1477.8280           | -1477.7922           | -1477.7621           | 1.793/173.0                | 0.974/94.0                 | 0.819/79.0                 |
| <b>DPA-5Me</b>  | -1477.8080           | -1477.7703           | -1477.7389           | 1.881/181.5                | 1.026/99.0                 | 0.855/82.5                 |

[a]  $S_0$  optimized a rb3lyp/6-31g(d),  $T_1$  optimized a ub3lyp/6-31g(d) level of theory. [b] From TD-DFT optimization of  $S_1$  state at b3lyp/6-31g(d) level of theory.

**Table 3-13.** Comparison of total energies for **BDPA-2Me**, **BDPA-3Me**, **BDPA-4Me**, **BDPA-5Me** and their endoperoxides

|                 | $E_{acene}$ <sup>[a]</sup> | $\Delta E_{acene}$ <sup>[b]</sup> | $E_{BPO}$ <sup>[a]</sup> | $\Delta E_{BPO}$ <sup>[c]</sup> | $\Delta (E_{BPO} - E_{acene})$ |
|-----------------|----------------------------|-----------------------------------|--------------------------|---------------------------------|--------------------------------|
|                 | (Hartree)                  | (kJ/mol)                          | (Hartree)                | (kJ/mol)                        | (kJ/mol)                       |
| <b>BDPA-2Me</b> | -1477.798416               | +77.8                             | -1628.10648366           | +99.4                           | +21.6                          |
| <b>BDPA-3Me</b> | -1477.825777               | +5.9                              | -1628.14161416           | +28.1                           | +22.2                          |
| <b>BDPA-4Me</b> | -1477.828041               | ≡ 0                               | -1628.14433321           | ≡ 0                             | ≡ 0                            |
| <b>BDPA-5Me</b> | -1477.808001               | +52.6                             | -1628.12908112           | +40.0                           | -12.6                          |

[a]  $S_0$  optimized with rb3lyp/6-31g(d). [b] Comparison of total energy relative to sterically unhindered 4-methylated acene. [c] Comparison of total energy relative to sterically unhindered 4-methylated endoperoxide.

**Table 3-14.** Comparison of calculated geometric parameters (distances in Å, angles in °) for **Singlet Ground State ( $S_0$ )**, **First Singlet Excited State ( $S_1$ )**, and **First Triplet Excited State ( $T_1$ )** for B-N anthracenes **BDPA-2Me**, **BDPA-3Me**, **BDPA-4Me** and **BDPA-5Me**. Derived from DFT calculations; for  $S_0$ : rb3lyp/6-31g(d);  $S_1$ : TD-DFT, b3lyp/6-31g(d);  $T_1$ : ub3lyp/6-31g(d).

|                                    | B-N             | B-C <sub>1,5</sub> | C <sub>9,10</sub> -C <sub>Py</sub> | $\alpha$ [a]    | $\beta$ [b]     | $\gamma$ [c]    | $\delta$ [d] | $\varepsilon$ [e] | $\phi$ [f] |
|------------------------------------|-----------------|--------------------|------------------------------------|-----------------|-----------------|-----------------|--------------|-------------------|------------|
| <b>BDPA-2Me (<math>S_0</math>)</b> | 1.690           | 1.626              | 1.474                              | 107.4           | 172.2           | 167.6           | 17.4         | 21.6              | 40.0       |
| <b>BDPA-2Me (<math>S_1</math>)</b> | 1.649,<br>1.652 | 1.610,<br>1.613    | 1.448                              | 109.2,<br>108.9 | 176.8,<br>175.8 | 169.2,<br>167.9 | 20.6         | 28.5              | 31.4       |
| <b>BDPA-2Me (<math>T_1</math>)</b> | 1.675           | 1.619              | 1.440,<br>1.439                    | 108.3           | 177.7           | 166.1           | 25.7         | 35.1              | 31.7       |
| <b>BDPA-3Me (<math>S_0</math>)</b> | 1.643           | 1.618              | 1.471                              | 105.4           | 171.0           | 165.8           | 18.1         | 20.7              | 35.4       |
| <b>BDPA-3Me (<math>S_1</math>)</b> | 1.616           | 1.608              | 1.444                              | 107.1           | 174.9           | 166.2           | 22.0         | 29.0              | 32.6       |
| <b>BDPA-3Me (<math>T_1</math>)</b> | 1.633           | 1.613              | 1.436                              | 106.3           | 176.1           | 164.7           | 24.8         | 30.4              | 34.5       |
| <b>BDPA-4Me (<math>S_0</math>)</b> | 1.640           | 1.618              | 1.472                              | 105.4           | 171.0           | 165.6           | 18.2         | 21.1              | 35.8       |
| <b>BDPA-4Me (<math>S_1</math>)</b> | 1.614,<br>1.615 | 1.607              | 1.443                              | 107.1           | 174.9           | 166.2           | 22.2         | 29.3              | 32.7       |
| <b>BDPA-4Me (<math>T_1</math>)</b> | 1.631           | 1.614              | 1.438                              | 106.3           | 176.2           | 164.6           | 24.9         | 30.8              | 34.6       |
| <b>BDPA-5Me (<math>S_0</math>)</b> | 1.655           | 1.618              | 1.474                              | 105.7           | 168.8           | 167.3           | 20.9         | 25.6              | 42.2       |
| <b>BDPA-5Me (<math>S_1</math>)</b> | 1.625           | 1.606              | 1.447                              | 107.3           | 172.6           | 167.7           | 25.5         | 34.0              | 38.6       |
| <b>BDPA-5Me (<math>T_1</math>)</b> | 1.647           | 1.611              | 1.443                              | 106.7           | 174.8           | 166.2           | 29.5         | 35.6              | 39.1       |

[a]  $\alpha$  = C<sub>1,5</sub>-B-N angle; [b]  $\beta$  = Cent1-C<sub>1,5</sub>-B; [c]  $\gamma$  = Cent2-C<sub>9,10</sub>-C<sub>Py</sub>; [d]  $\delta$  = internal twist of central anthracene ring; [e]  $\varepsilon$  = Ph<sub>An,out</sub> // Ph<sub>An,out</sub>, dihedral angle between outer anthracene rings; [f]  $\phi$  = Ph<sub>An,in</sub> // Py, dihedral angle between inner anthracene ring and pendent pyridyl ring.

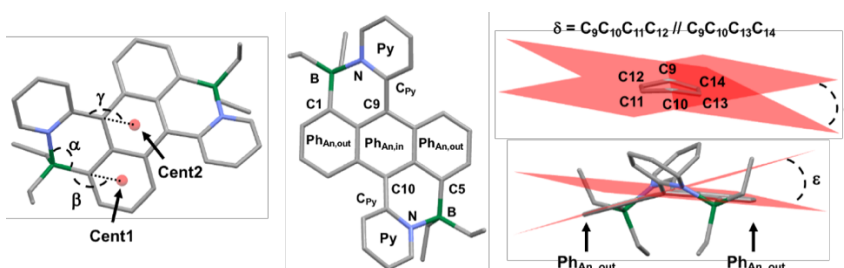


**Table 3-15.** Comparison of calculated geometric parameters (distances in Å, angles in °) for endoperoxides obtained from DFT calculations (Gaussian 09; rb3lyp/6-31g(d))

|                                   | B-N    | B-C <sub>1,5</sub> | C <sub>9,10</sub> -C <sub>Py</sub> | C-O    | O-O   | $\alpha$ [a] | $\beta$ [b] | $\gamma$ [c] | $\delta$ [d] | $\varepsilon$ [e] | $\phi$ [f] |
|-----------------------------------|--------|--------------------|------------------------------------|--------|-------|--------------|-------------|--------------|--------------|-------------------|------------|
| <b>BPO-2Me<sub>th</sub></b><br>22 | 1.727, | 1.617,             | 1.517,                             | 1.491, | 1.465 | 107.5,       | 175.1,      | 170.3,       | 57.7         | 58.4              | 40.0,      |
|                                   | 1.745  | 1.619              | 1.515                              | 1.490  |       | 107.7        | 176.0       | 169.8        |              |                   | 41.9       |
| <b>BPO-3Me<sub>th</sub></b>       | 1.678, | 1.612,             | 1.510,                             | 1.489, | 1.466 | 106.9,       | 176.4,      | 170.2,       | 58.0         | 60.8              | 37.8,      |
|                                   | 1.692  | 1.616              | 1.509                              | 1.486  |       | 107.0        | 179.0       | 168.9        |              |                   | 36.7       |
| <b>BPO-4Me<sub>th</sub></b>       | 1.674, | 1.612,             | 1.511,                             | 1.488, | 1.467 | 106.9,       | 176.4,      | 170.1,       | 58.1         | 61.0              | 38.1,      |
|                                   | 1.689  | 1.615              | 1.511                              | 1.486  |       | 107.0        | 178.9       | 168.9        |              |                   | 36.9       |
| <b>BPO-5Me<sub>th</sub></b>       | 1.690, | 1.606,             | 1.519,                             | 1.483, | 1.462 | 107.0,       | 175.6,      | 169.8,       | 60.3         | 66.6              | 41.1,      |
|                                   | 1.703  | 1.610              | 1.517                              | 1.480  |       | 107.2        | 179.0       | 168.3        |              |                   | 40.1       |

[a]  $\alpha$  = C<sub>1,5</sub>-B-N angle; [b]  $\beta$  = Cent1-C<sub>1,5</sub>-B; [c]  $\gamma$  = Cent2-C<sub>9,10</sub>-C<sub>Py</sub>; [d]  $\delta$  = internal twist of central anthracene ring; [e]  $\varepsilon$  = Ph<sub>An,out</sub> // Ph<sub>An,out</sub>, dihedral angle between outer anthracene rings; [f]  $\phi$  = Ph<sub>An,in</sub> // Py, dihedral angle between inner anthracene ring and pendent pyridyl ring.

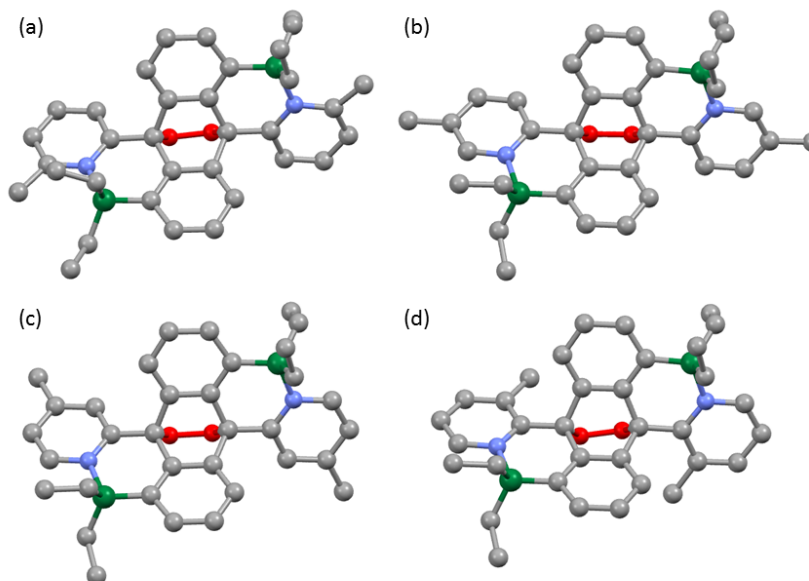


**Figure 3-16.** Optimized structures of (a) **BPO-2Me**, (b) **BPO-3Me**, (c) **BPO-4Me**, (d) **BPO-5Me** (Gaussian 09; rb3lyp/6-31g(d)). C grey, B green, N blue, O red.

### Kinetics of Photo-Induced Endoperoxide Formation

Solutions of the acene (0.01 mM) in oxygen-saturated DCM were prepared. The solutions were irradiated by a Xe lamp at room temperature (34 Watt, the distance to the light source was kept constant at 10 cm). The decrease in the acene concentration during irradiation was measured by UV-Vis spectroscopy at constant time intervals. The wavelengths for recording the absorbances  $A$  were as follows: **BDPA-2Me** (538 nm), **BDPA-3Me** (555 nm), **BDPA-4Me** (554 nm), **BDPA-5Me** (535 nm). The corresponding endoperoxides do not absorb at these wavelengths. The kinetics were determined three times for each substance and the absorbance averaged at each time point.

The bimolecular rate constants ( $k$ ) were derived using the equation  $\ln A = \ln A_0 - kt$ , where a plot of  $\ln[A/A_0]$  vs  $t$  will be linear with a slope of  $-k$ .

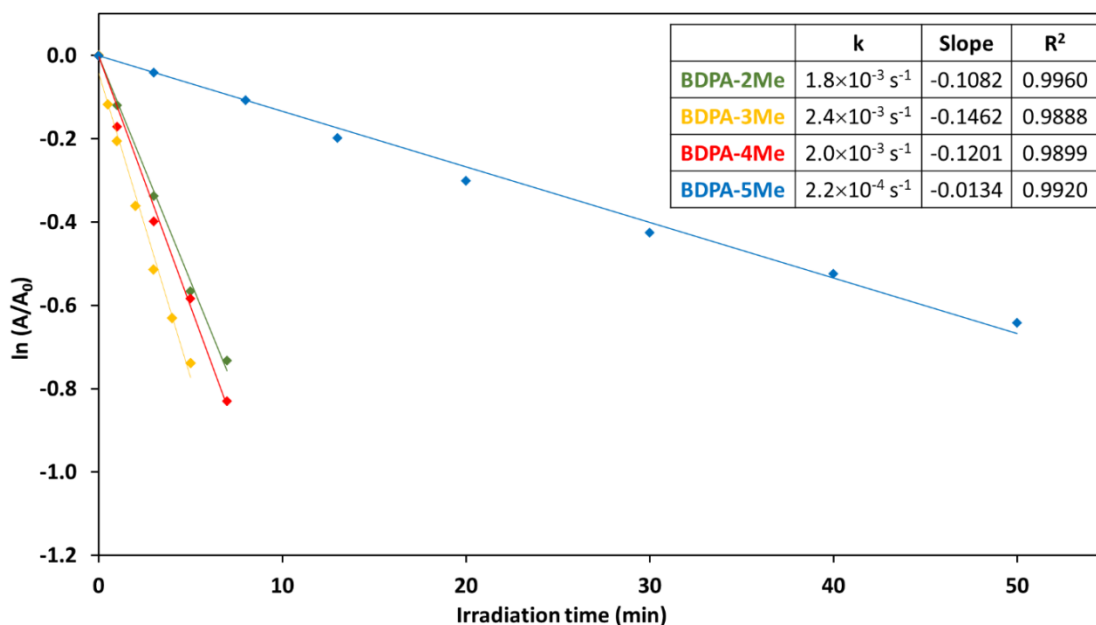
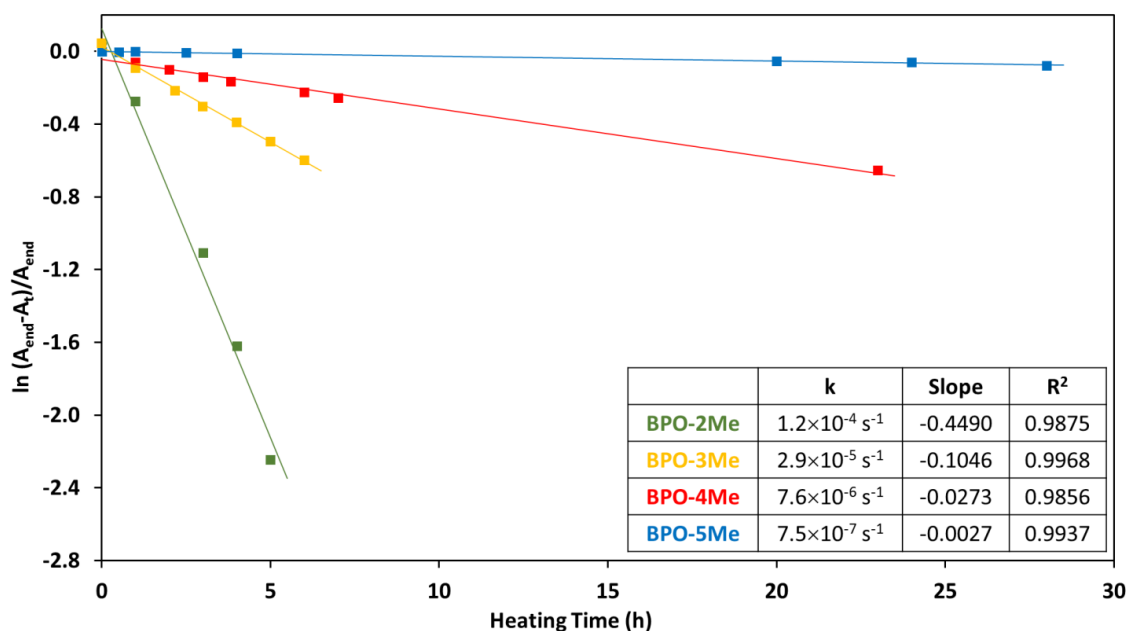


**Figure 3-17.** Pseudo first-order kinetics for the reaction of BN-functionalized anthracenes with oxygen upon photoirradiation to give the respective endoperoxides in DCM.



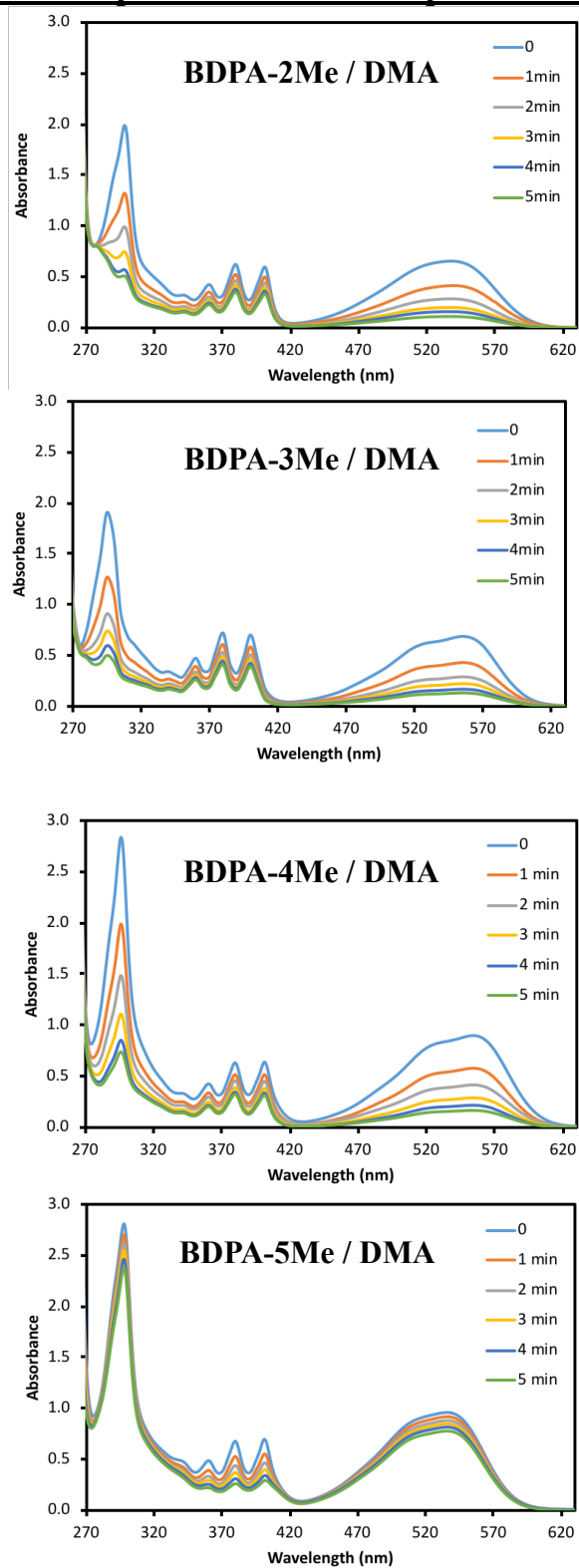
### Kinetics of the Endoperoxide Thermolysis

For measurements of the values of  $k_{-1}$ , solutions of the BPOs in toluene (0.1 mM) were heated to 100 °C. The appearance of the oxygen-free acene species was recorded by UV-vis spectroscopy. The wavelengths for recording the absorbances  $A$  were as follows: **BDPA-2Me** (548 nm), **BDPA-3Me** (565 nm), **BDPA-4Me** (566 nm), **BDPA-5Me** (544 nm). The rate constant  $k_{-1}$  was determined from the plot of  $\ln (A_{\text{end}}-A_t)/A_{\text{end}}$  versus time.



**Figure 3-18.** Thermolysis of the endoperoxides at 100 °C;  $A_{\text{end}}$ : final absorption intensity of **BDPA**,  $A_t$ : absorption intensity of **BDPA** at a given time.

## Competition Experiments for Endoperoxide Formation



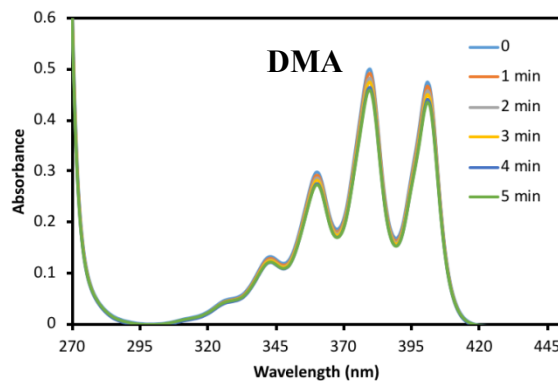


**Figure 3-19.** Competition of BN-functionalized anthracenes ( $5 \times 10^{-5}$  M in DCM) and dimethyl-anthracene (DMA) ( $5 \times 10^{-5}$  M in DCM) in the reaction with oxygen upon photoirradiation by a Xe lamp at room temperature (34 Watt). to give the respective endoperoxides in DCM.

### Spectral Data for Isolated Compounds

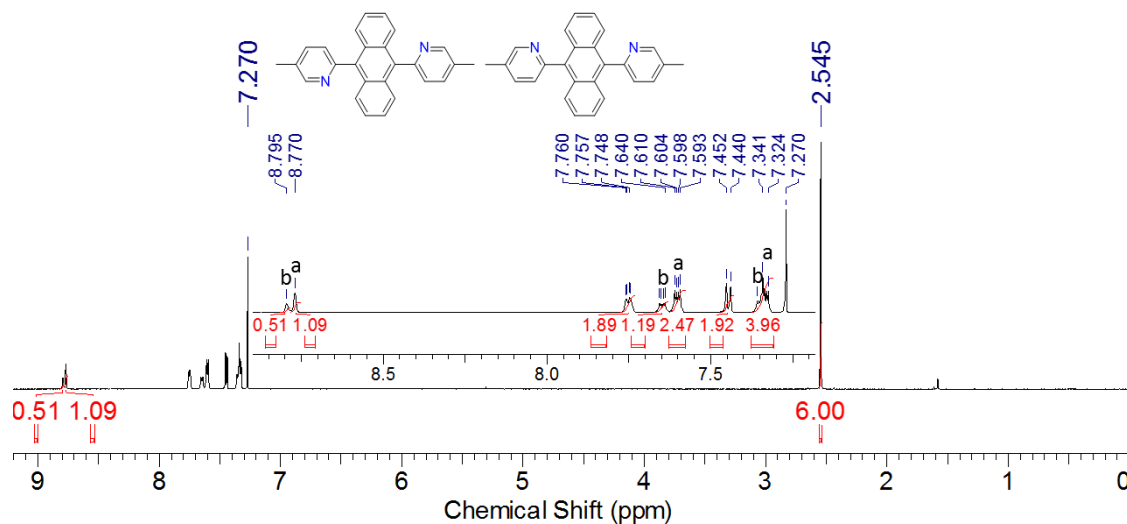


**Figure 3-20.**  $^1\text{H}$  NMR spectrum of 9,10-bis(3-methylpyrid-2-yl)anthracene (DPA-3Me) in  $\text{CDCl}_3$ , a and b correspond to two distinct isomers

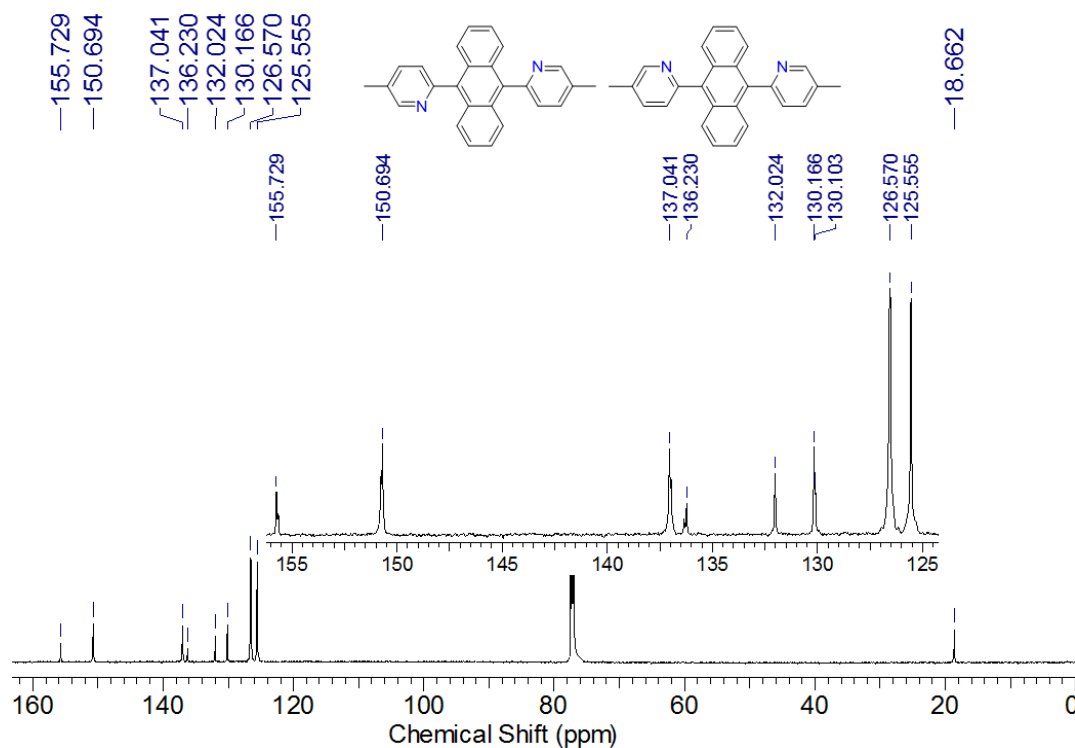


**Figure 3-21.**  $^{13}\text{C}\{^1\text{H}\}$  NMR spectrum of 9,10-bis(3-methylpyrid-2-yl)anthracene (DPA-3Me) in  $\text{CDCl}_3$

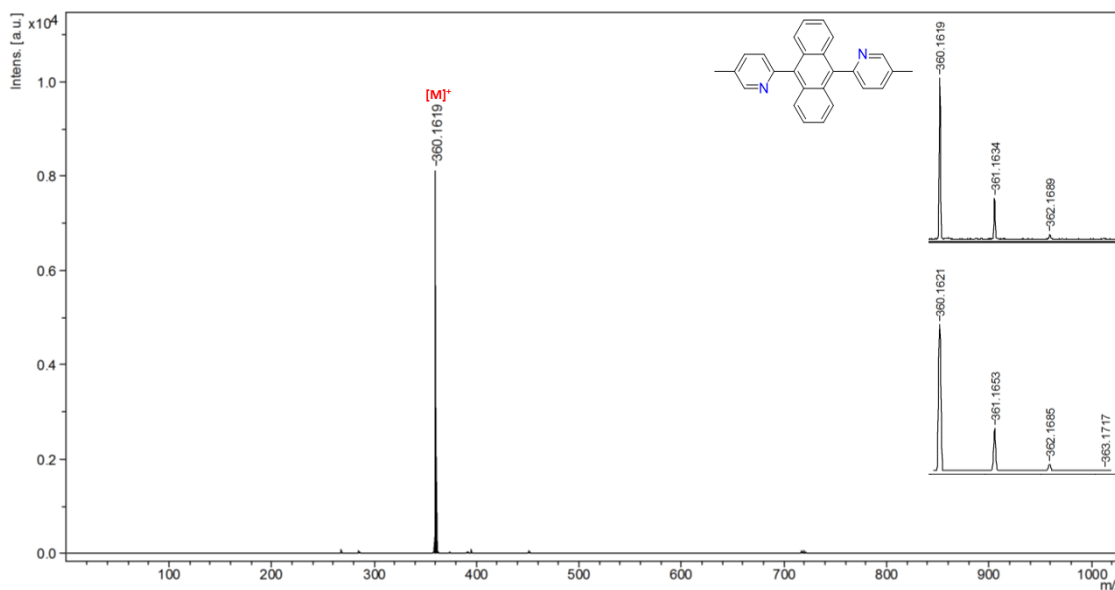


**Figure 3-22.** MALDI-TOF mass spectrum (pos. mode) of 9,10-bis(3-methylpyrid-2-yl)anthracene (DPA-3Me)

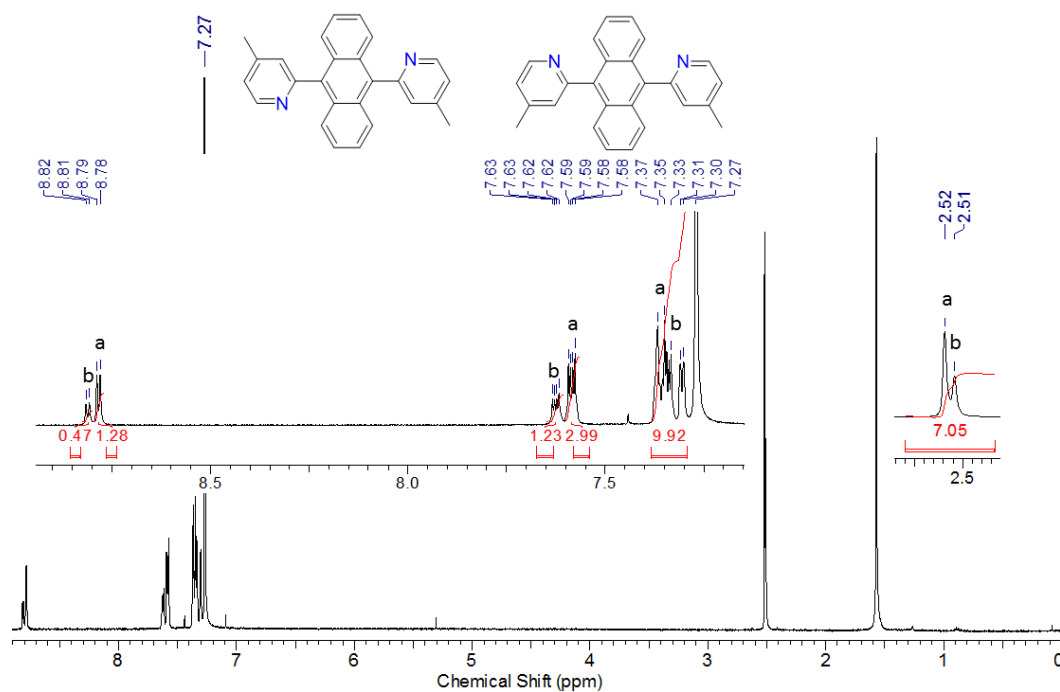


**Figure 3-23.** <sup>1</sup>H NMR spectrum of 9,10-bis(4-methylpyrid-2-yl)anthracene (DPA-4Me) in CDCl<sub>3</sub>, a and b correspond to two distinct isomers

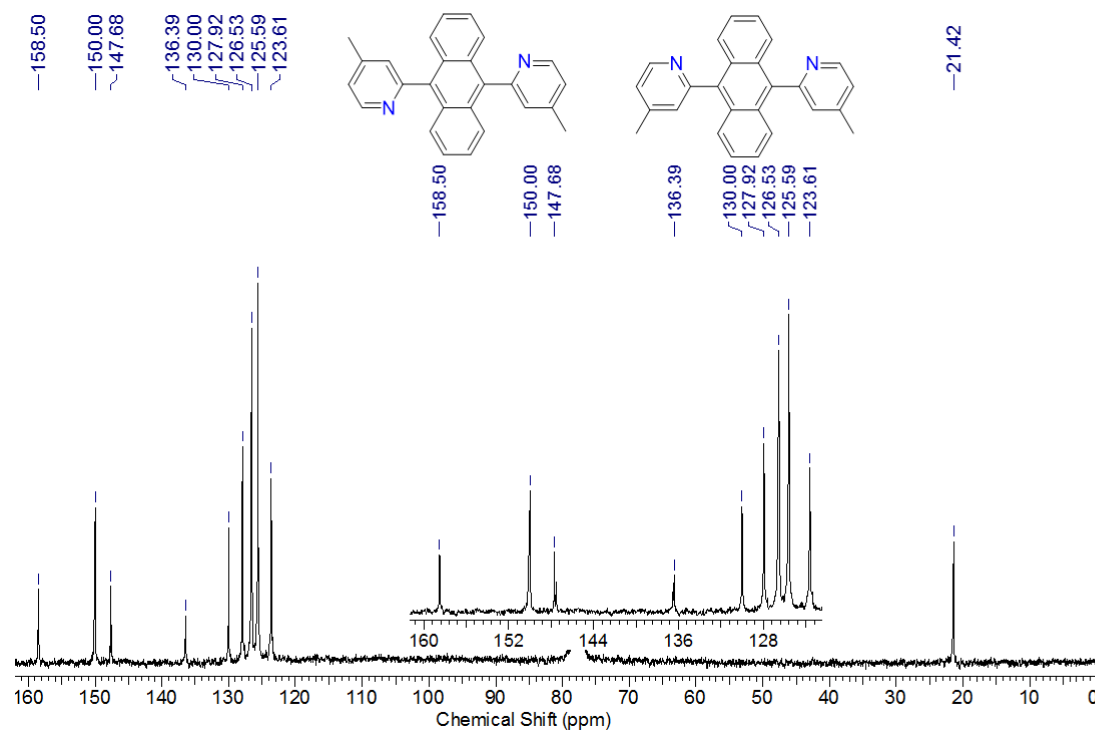


**Figure 3-24.**  $^{13}\text{C}\{^1\text{H}\}$  NMR spectrum of 9,10-bis(4-methylpyrid-2-yl)anthracene (DPA-4Me) in  $\text{CDCl}_3$

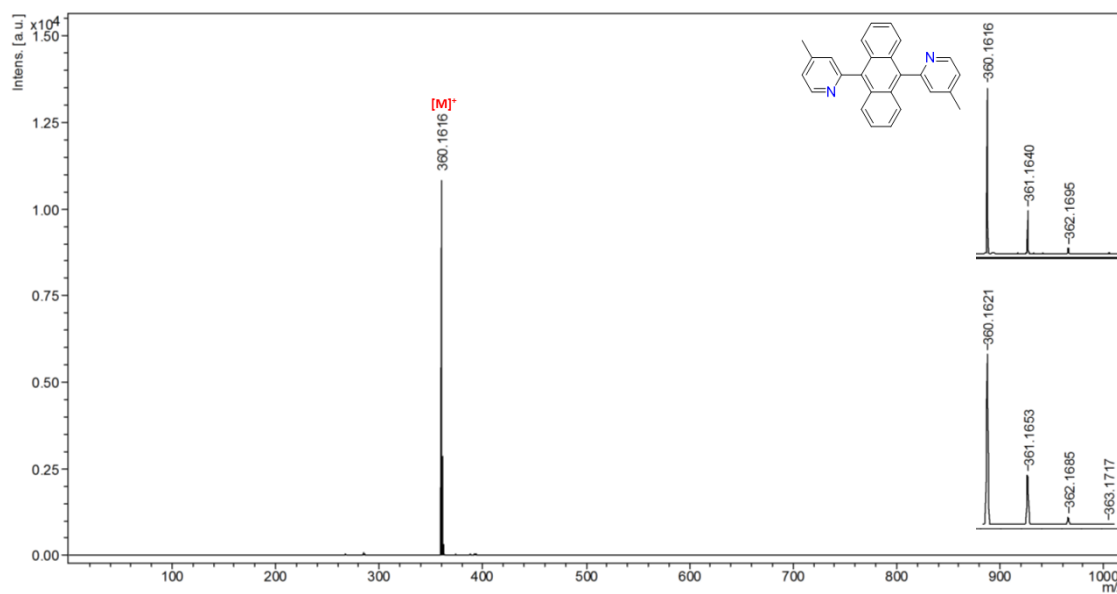


**Figure 3-25.** MALDI-TOF mass spectrum (pos. mode) of 9,10-bis(4-methylpyrid-2-yl)anthracene (DPA-4Me)

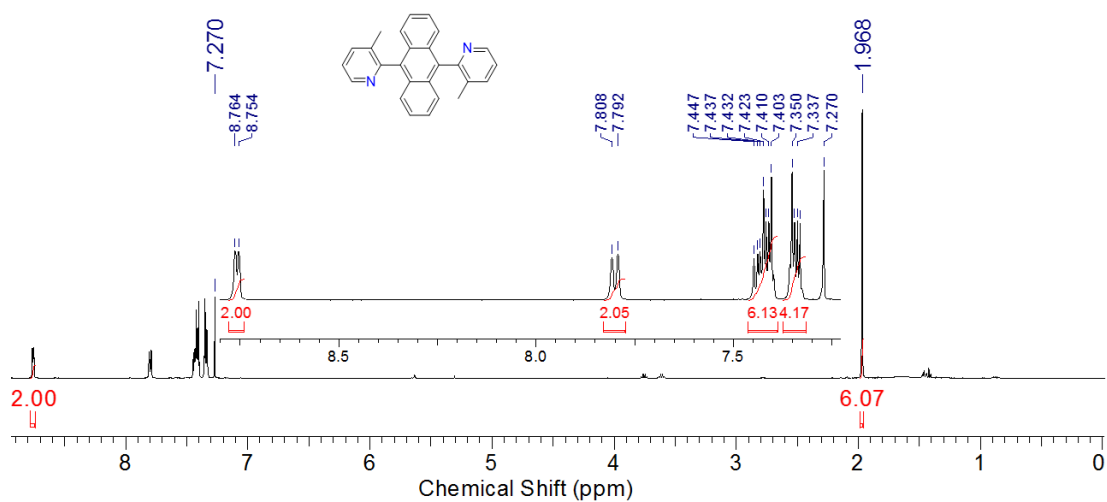


**Figure 3-26.** <sup>1</sup>H NMR spectrum of 9,10-bis(5-methylpyrid-2-yl)anthracene (DPA-5Me) in CDCl<sub>3</sub>

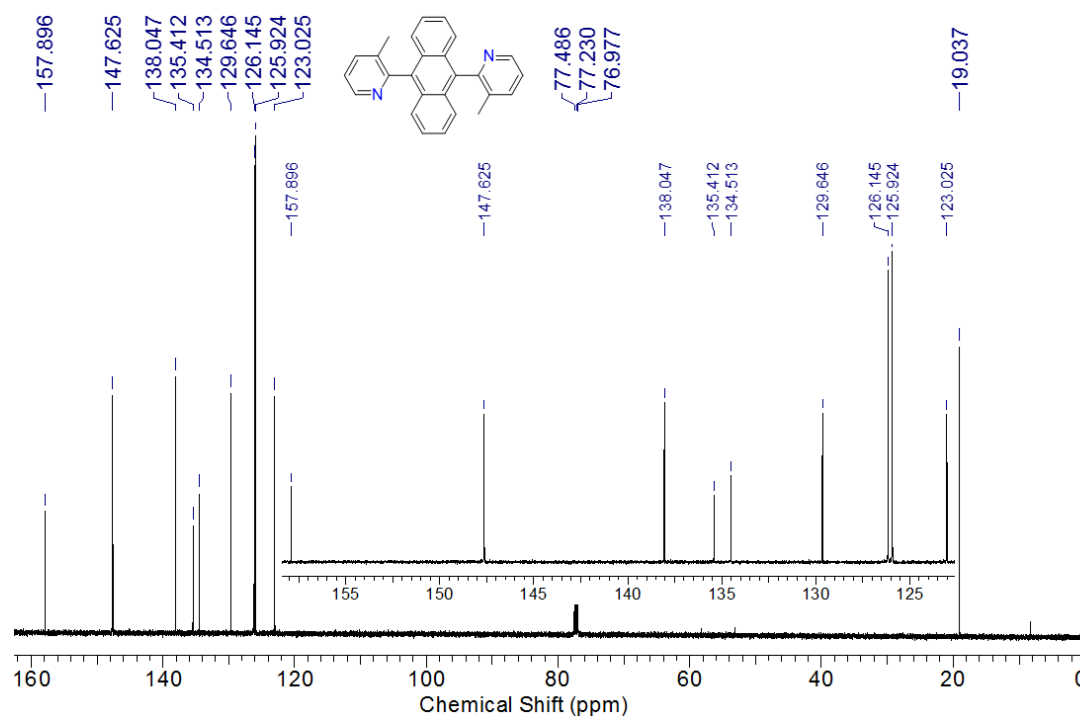


**Figure 3-27.** <sup>13</sup>C {<sup>1</sup>H} NMR spectrum of 9,10-bis(5-methylpyrid-2-yl)anthracene (DPA-5Me) in CDCl<sub>3</sub>

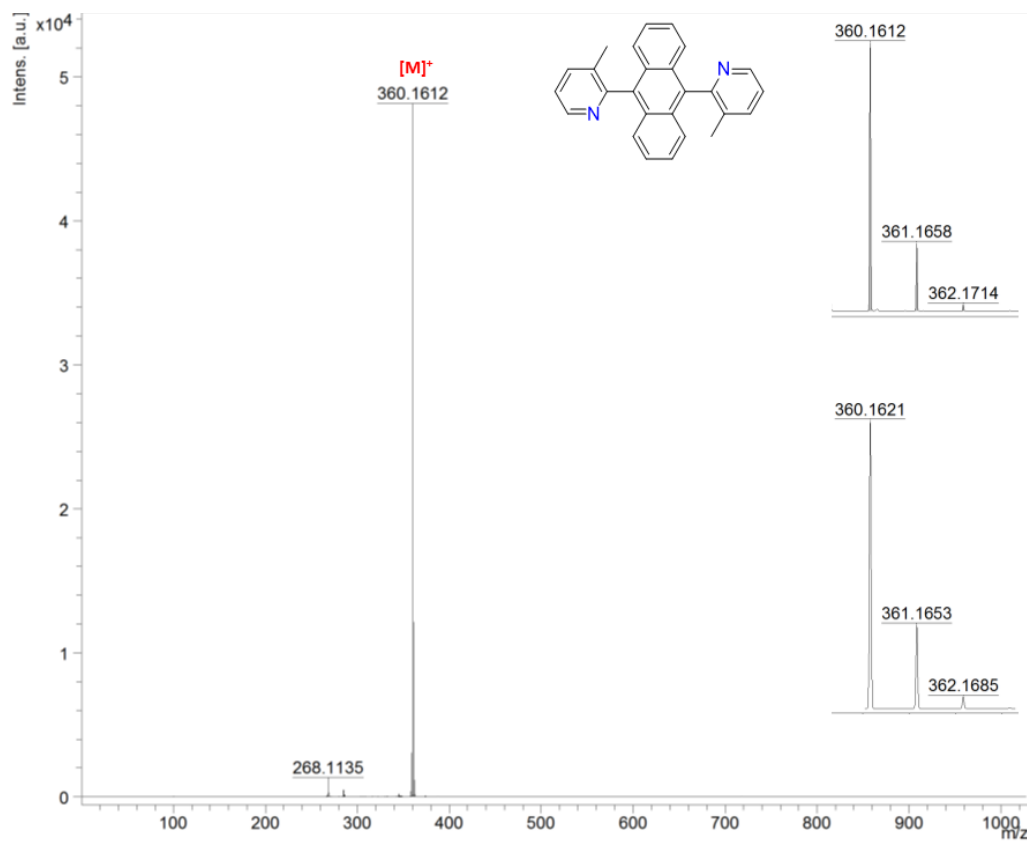


**Figure 3-28.** MALDI-TOF mass spectrum (pos. mode) of 9,10-bis(5-methylpyrid-2-yl)anthracene (**DPA-5Me**)



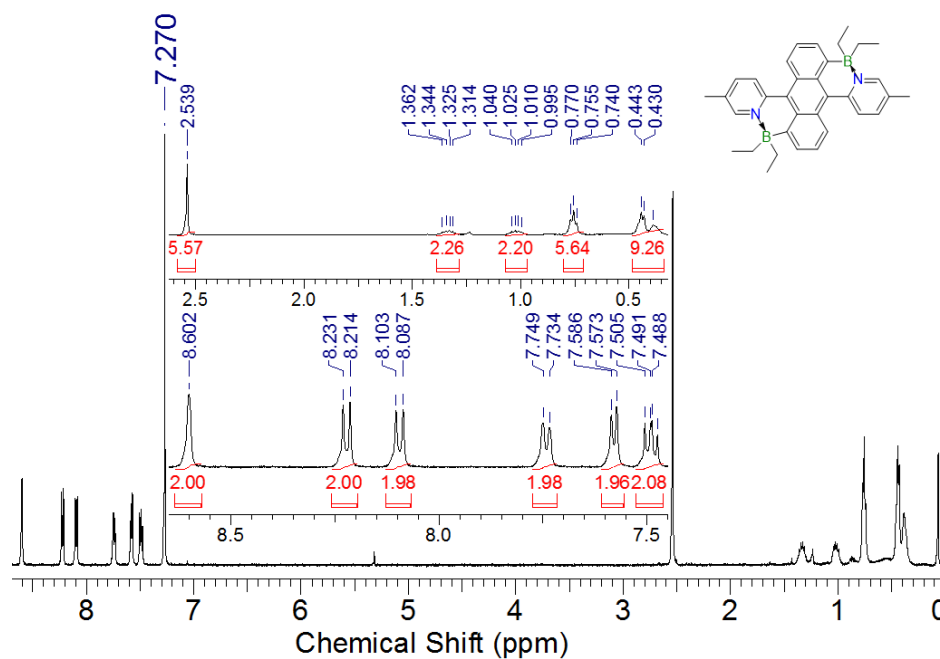


**Figure 3-29.** <sup>1</sup>H NMR spectrum of **BDPA-3Me** in  $\text{CDCl}_3$  at  $-10\text{ }^\circ\text{C}$

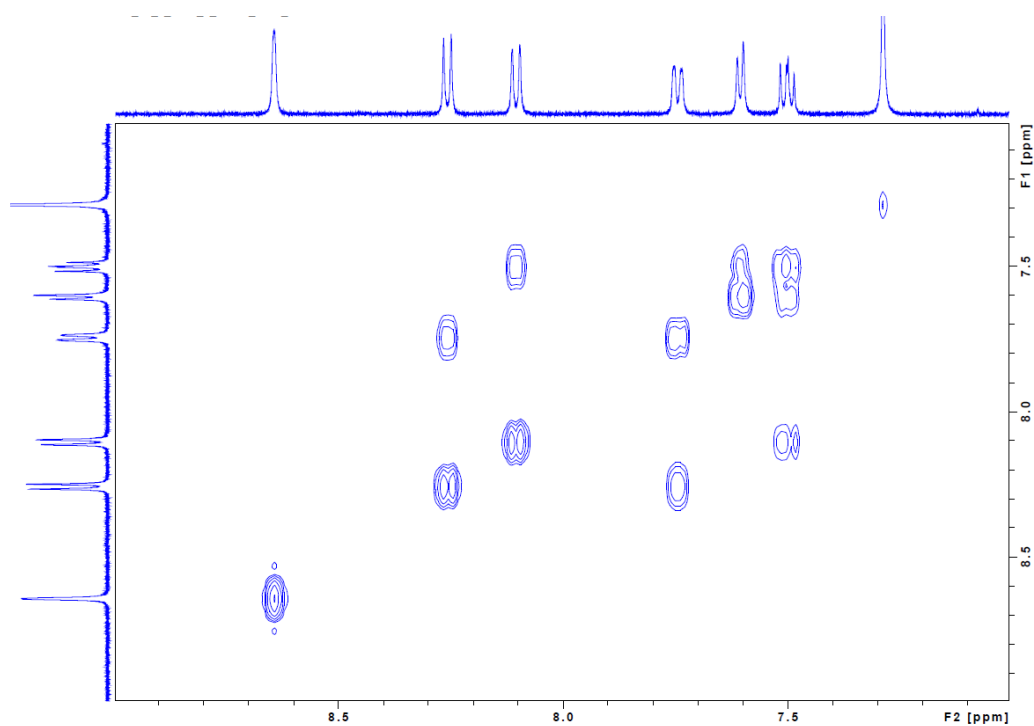


**Figure 3-30.** Aromatic region of the gCOSY NMR spectrum of **BDPA-3Me** in  $\text{CDCl}_3$  at RT

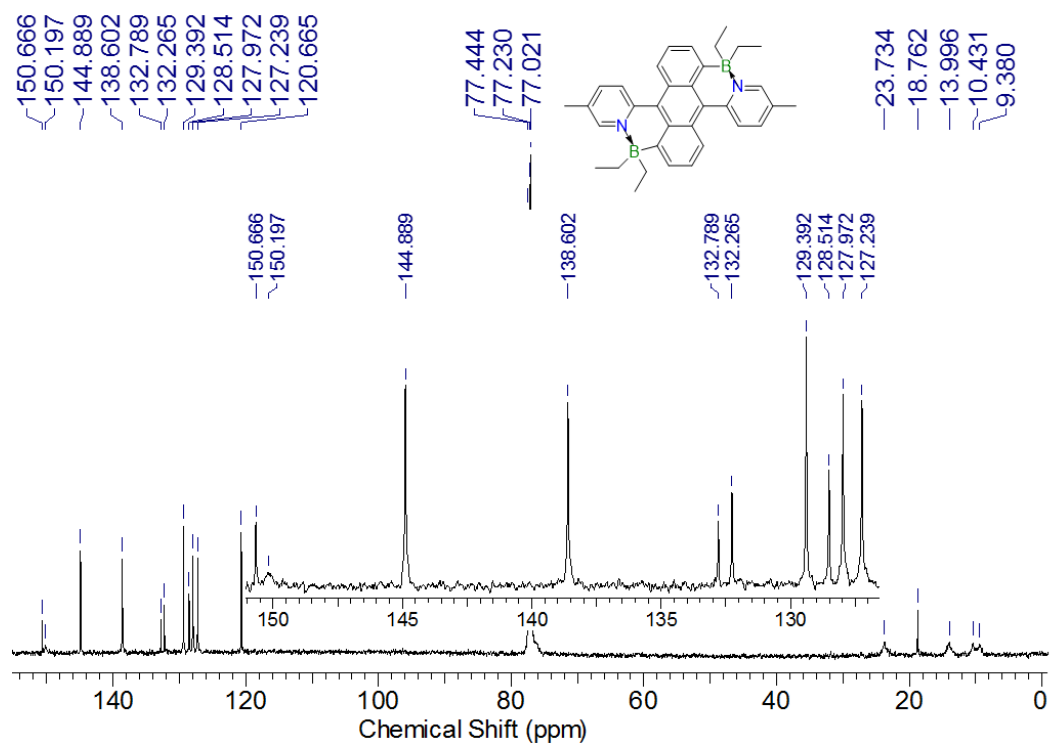


**Figure 3-31.**  $^{13}\text{C}\{^1\text{H}\}$  NMR spectrum of **BDPA-3Me** in  $\text{CDCl}_3$

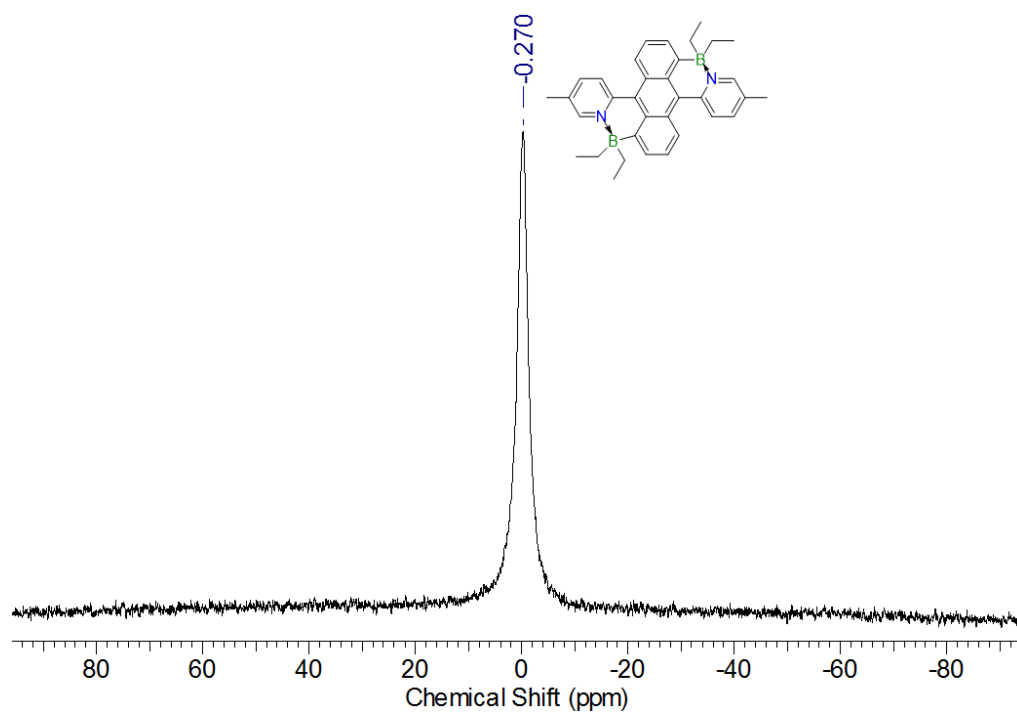


**Figure 3-32.**  $^{11}\text{B}\{^1\text{H}\}$  NMR spectrum of **BDPA-3Me** in  $\text{CDCl}_3$

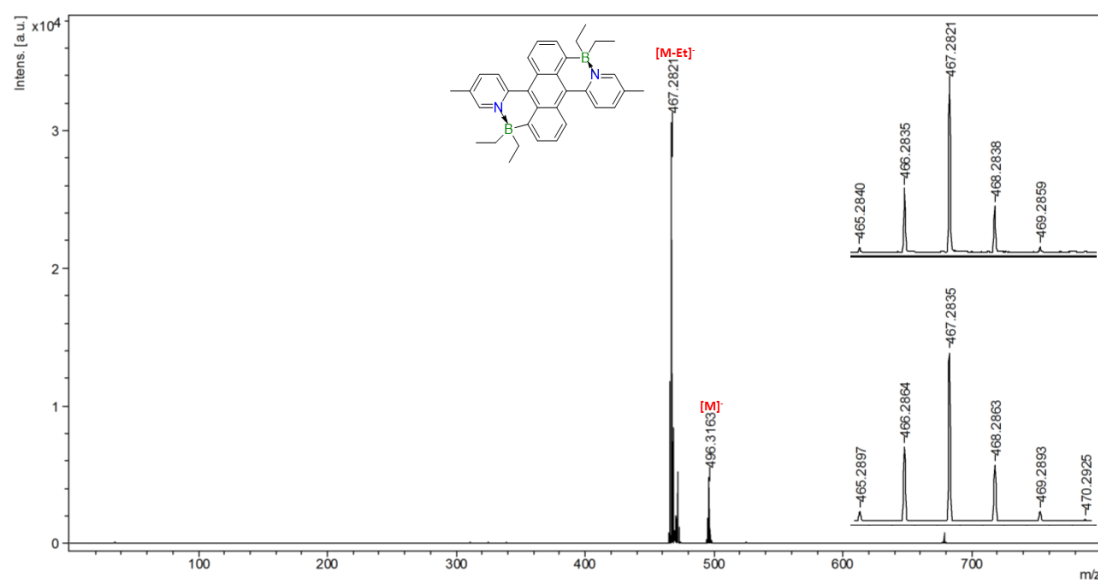


**Figure 3-33.** MALDI-TOF mass spectrum (neg. mode) of **BDPA-3Me**

**Figure 3-35.** Aromatic region of the gCOSY NMR spectrum of **BDPA-4Me** in CDCl<sub>3</sub> at RT

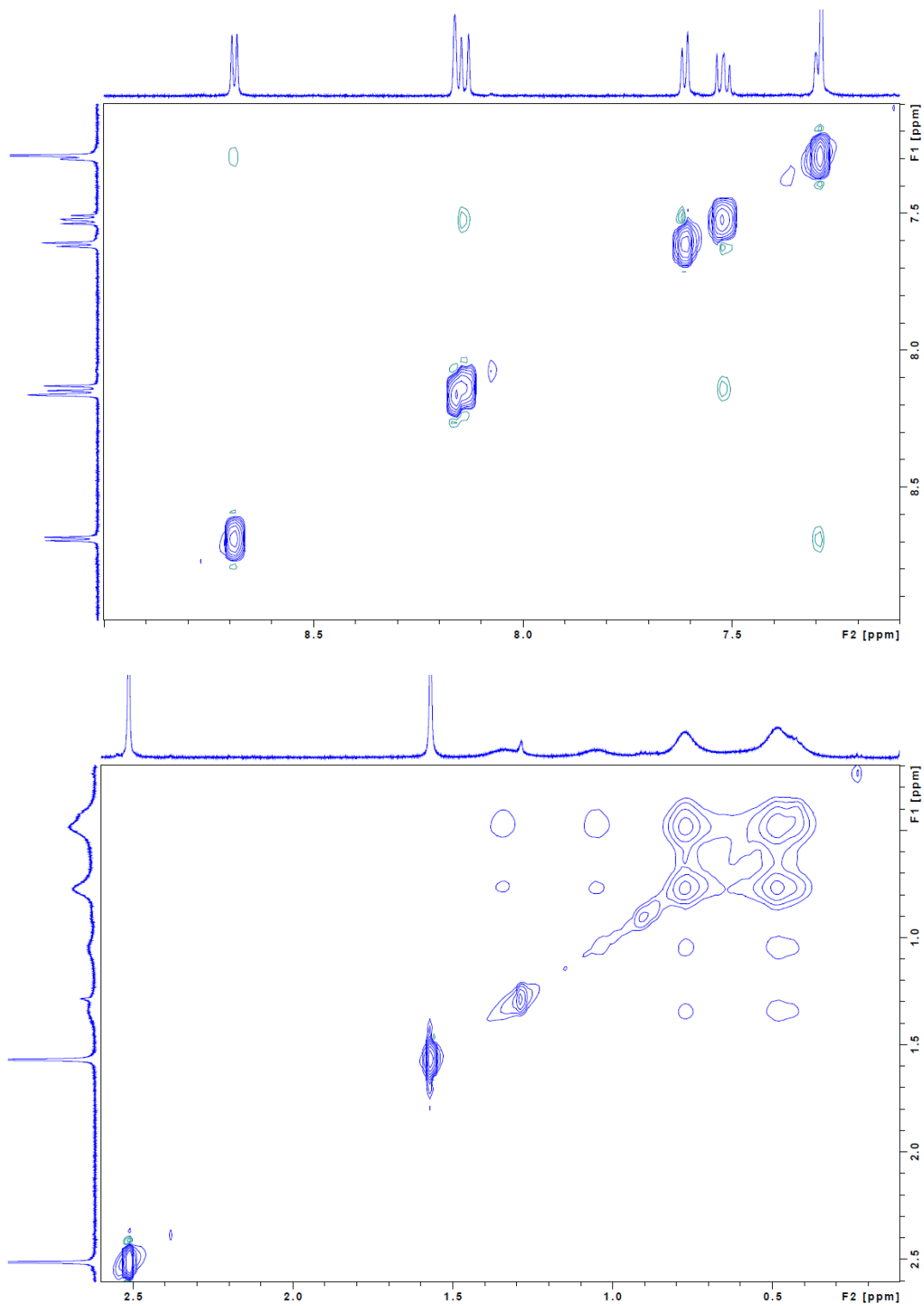


**Figure 3-36a.** Expansions of the HH-NOESY NMR spectrum of **BDPA-4Me** in CDCl<sub>3</sub> at RT

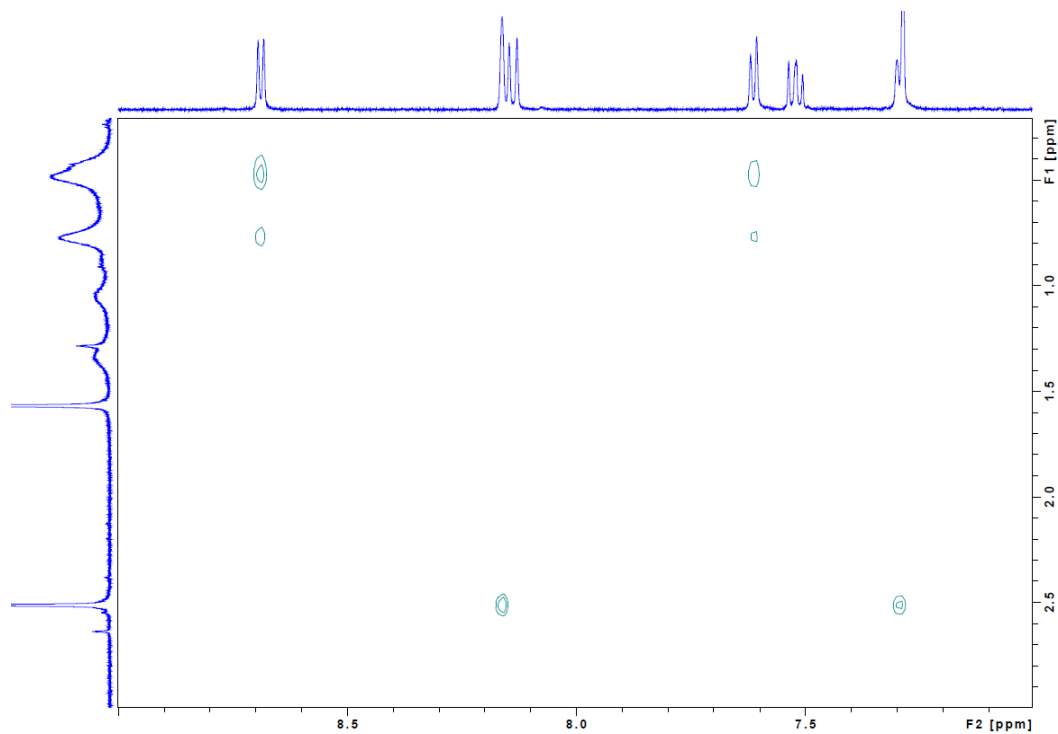


**Figure 3-36b.** Expansion of the HH-NOESY NMR spectrum of **BDPA-4Me** in CDCl<sub>3</sub> at RT

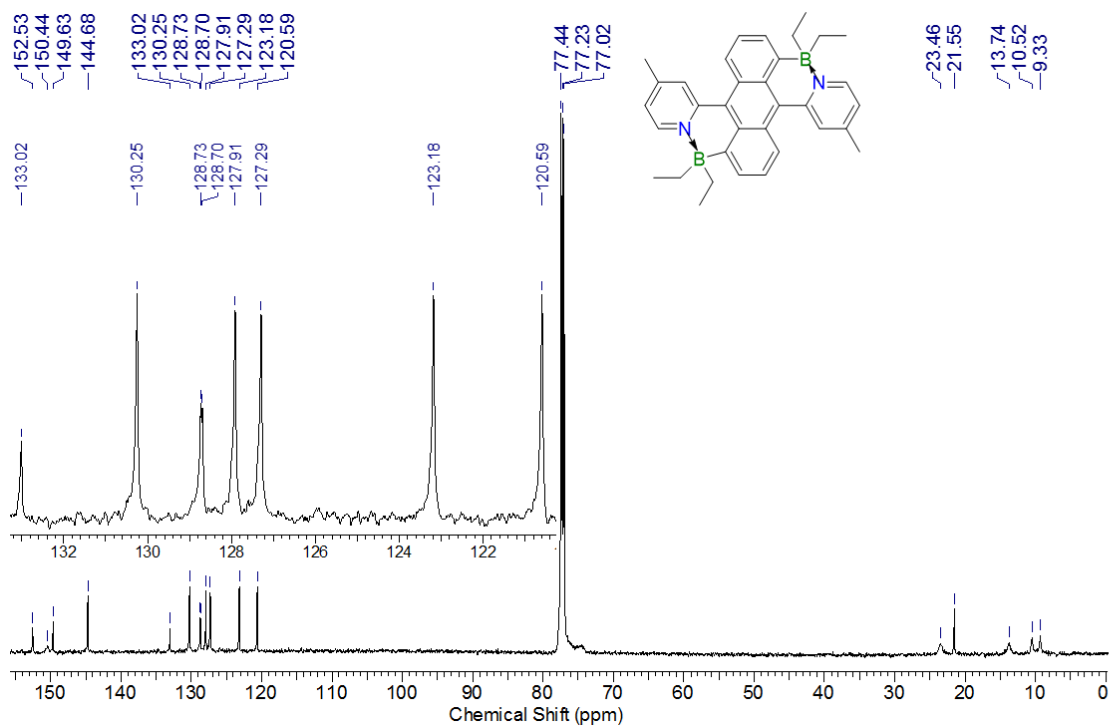


**Figure 3-37.** <sup>13</sup>C{<sup>1</sup>H} NMR spectrum of **BDPA-4Me** in CDCl<sub>3</sub>

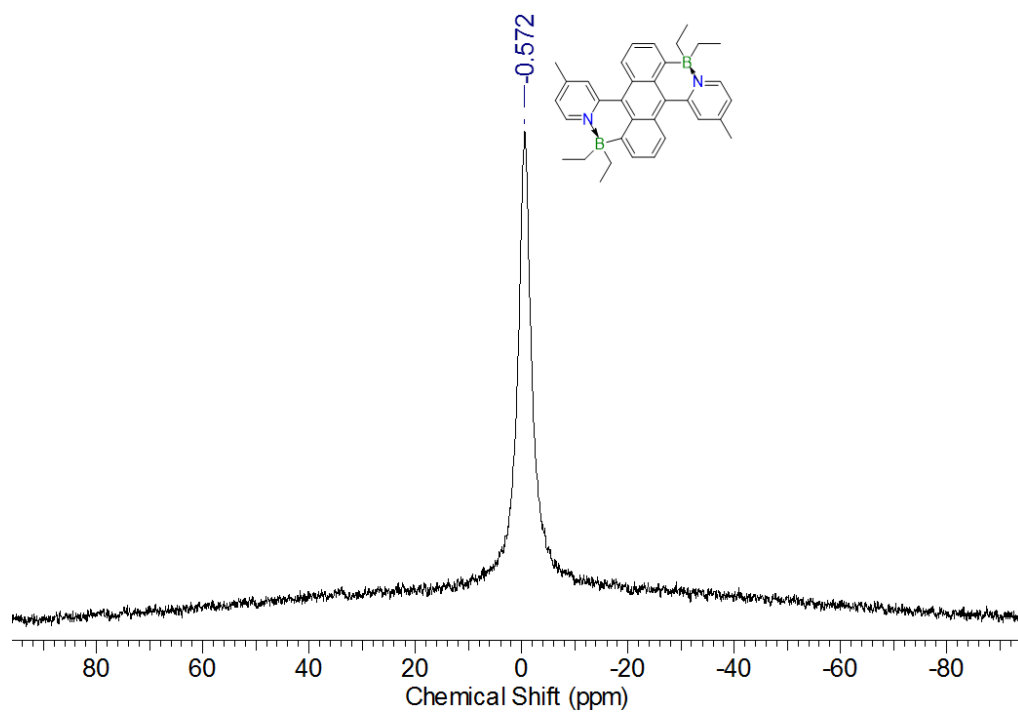


**Figure 3-38.**  $^{11}\text{B}\{^1\text{H}\}$  NMR spectrum of **BDPA-4Me** in  $\text{CDCl}_3$

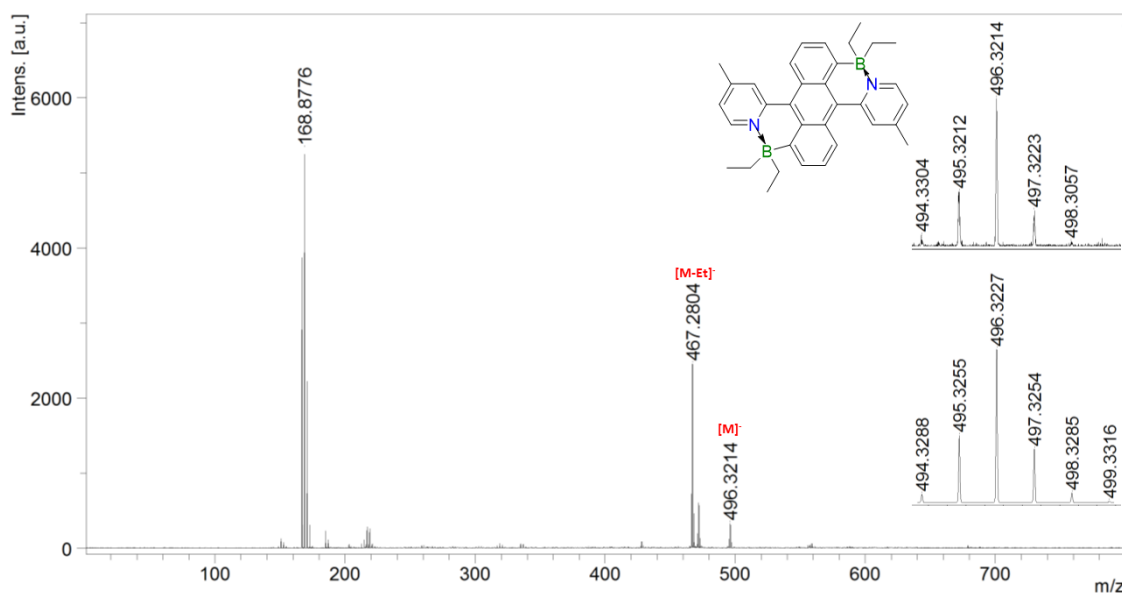


**Figure 3-39.** MALDI-TOF mass spectrum (neg. mode) of **BDPA-4Me**

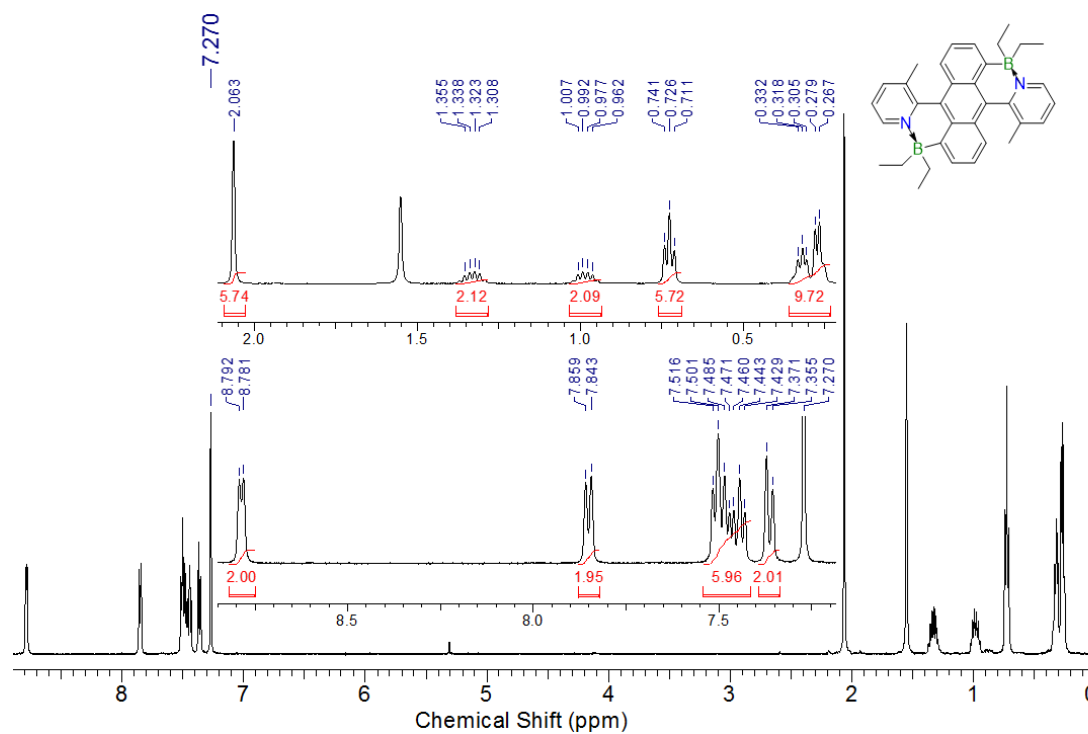


**Figure 3-40.**  $^1\text{H}$  NMR spectrum of **BDPA-5Me** in  $\text{CDCl}_3$

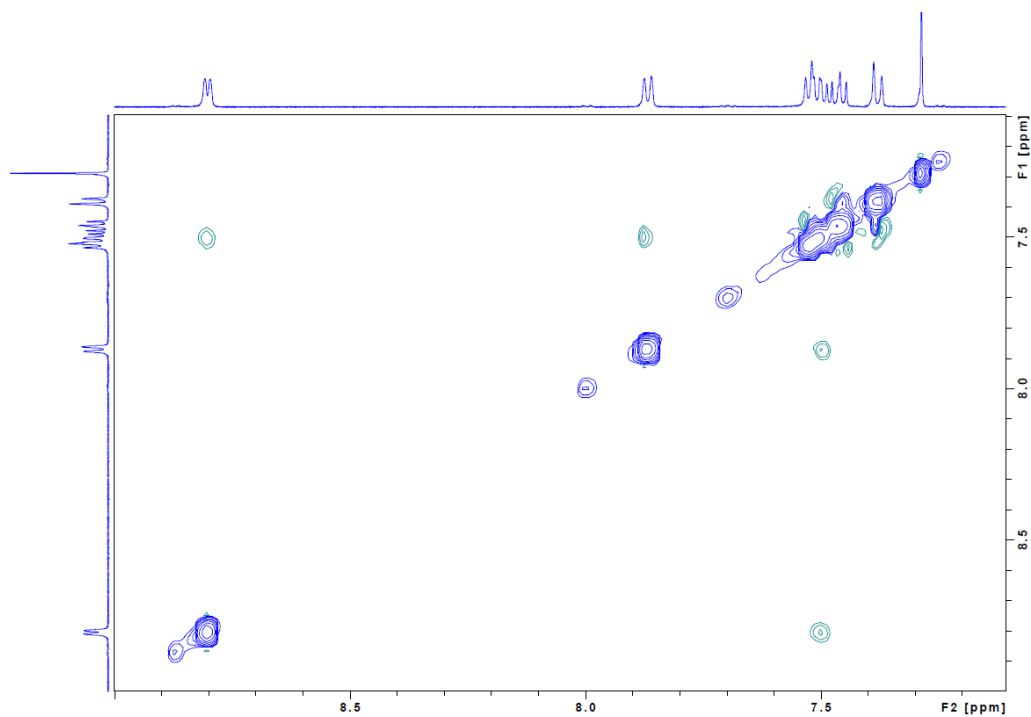


**Figure 3-41a.** Expansion of the HH-NOESY NMR spectrum of **BDPA-5Me** in  $\text{CDCl}_3$



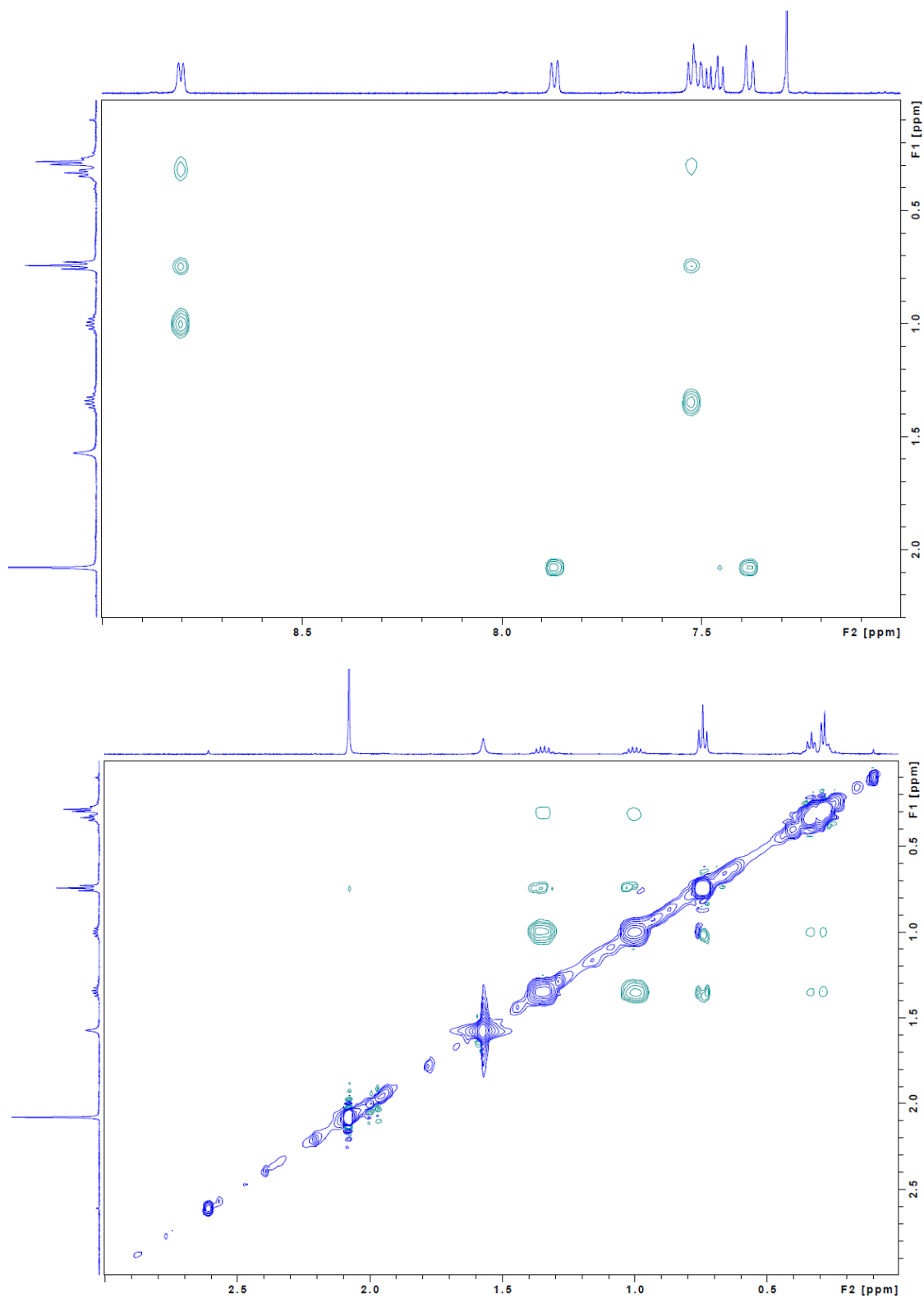


**Figure 3-41b.** Expansions of the HH-NOESY NMR spectrum of **BDPA-5Me** in CDCl<sub>3</sub>

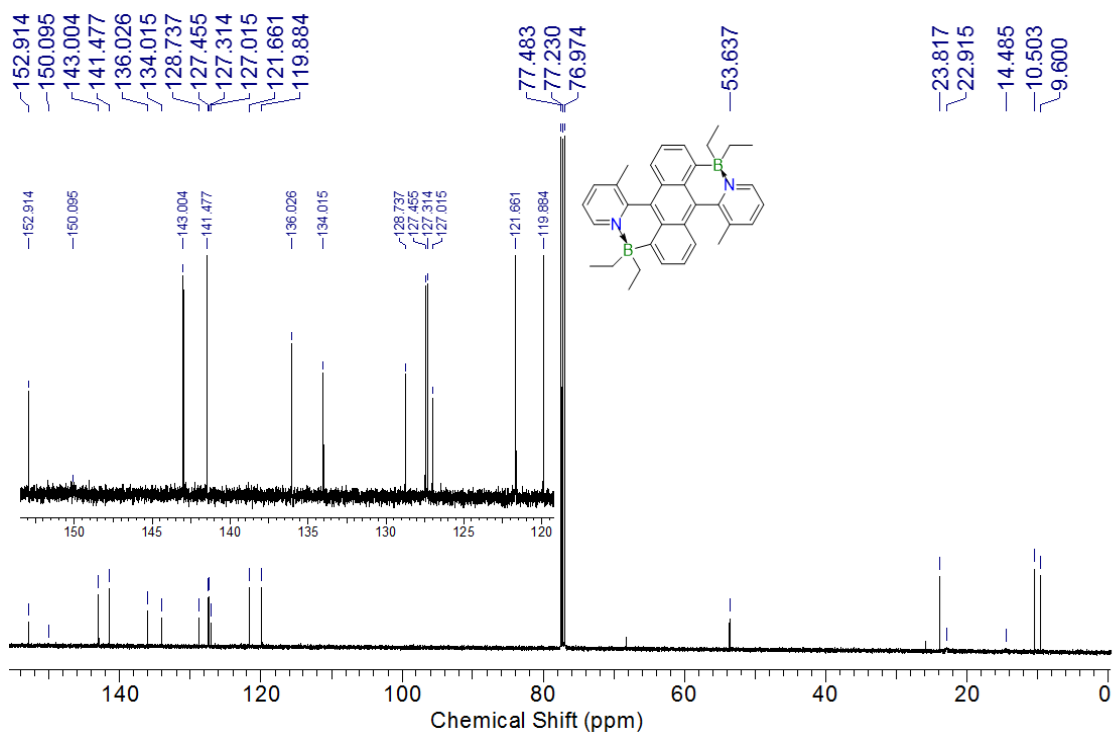


**Figure 3-42.**  $^{13}\text{C}\{^1\text{H}\}$  NMR spectrum of BDPA-5Me in  $\text{CDCl}_3$

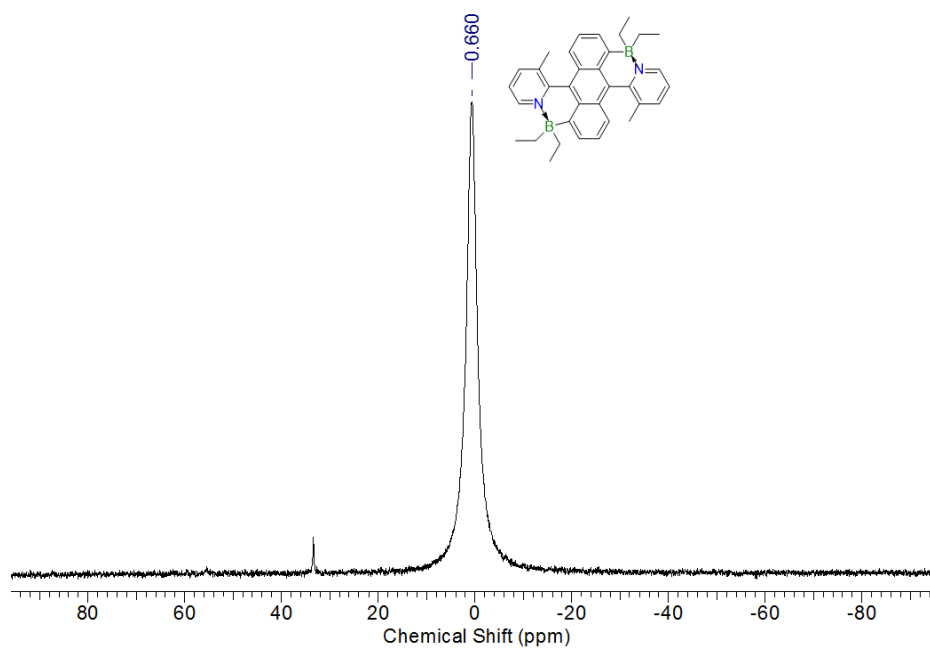


**Figure 3-43.**  $^{11}\text{B}\{^1\text{H}\}$  NMR spectrum of BDPA-5Me in  $\text{CDCl}_3$

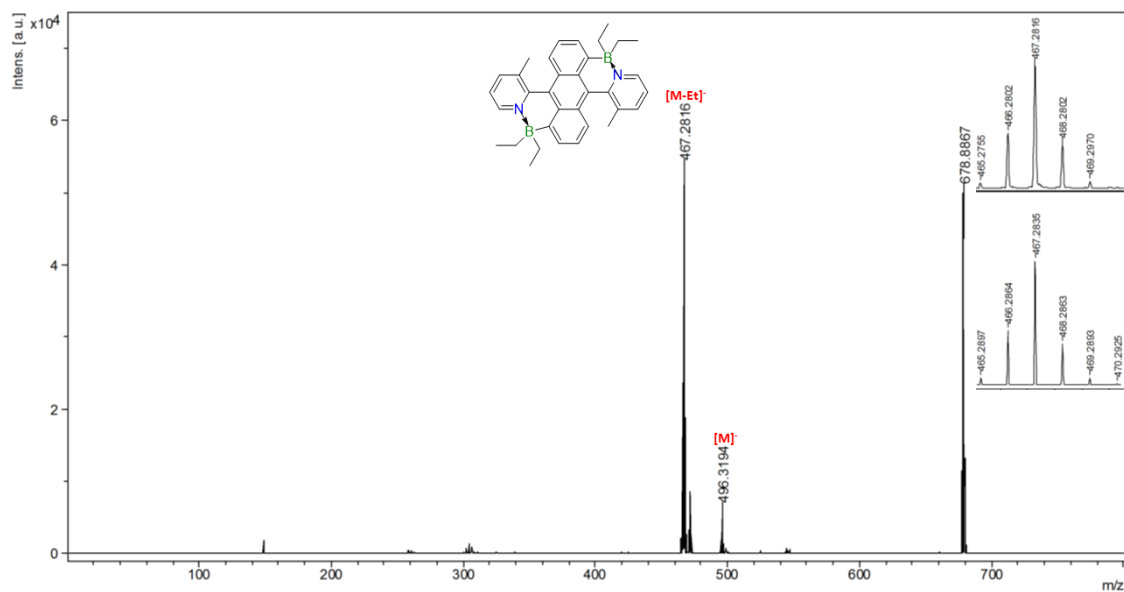


**Figure 3-44.** MALDI-TOF mass spectrum (neg. mode) of **BDPA-5Me** in CDCl<sub>3</sub>

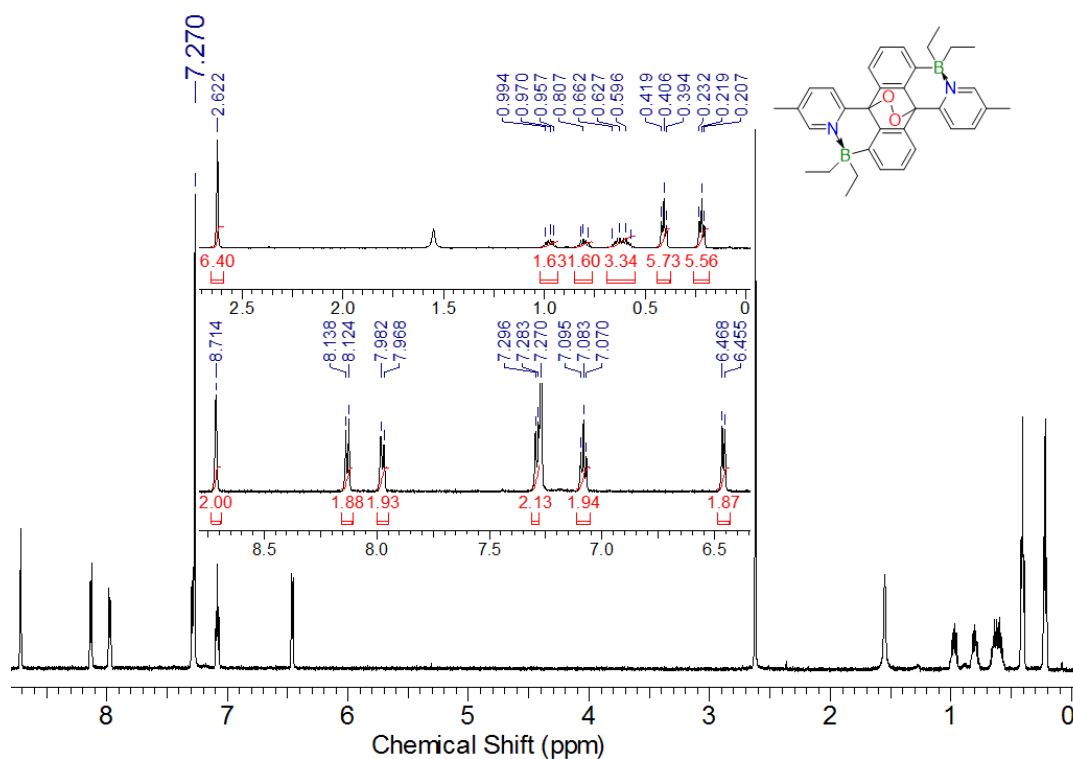


Figure 3-45. <sup>1</sup>H NMR spectrum of BPO-3Me in CDCl<sub>3</sub>

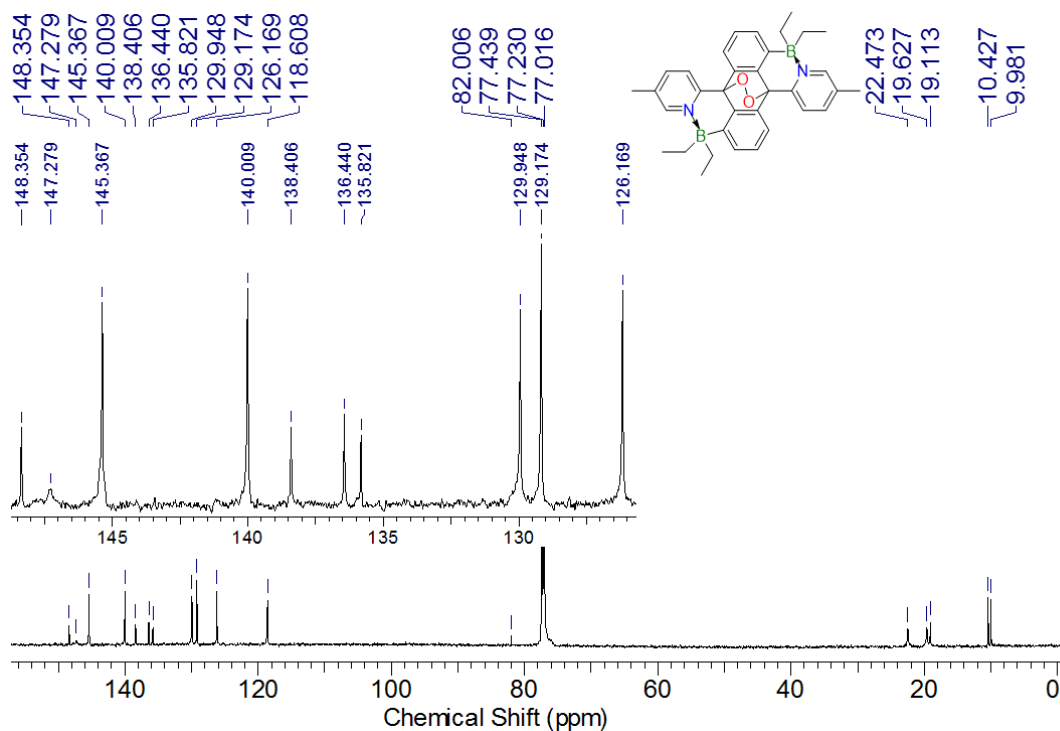
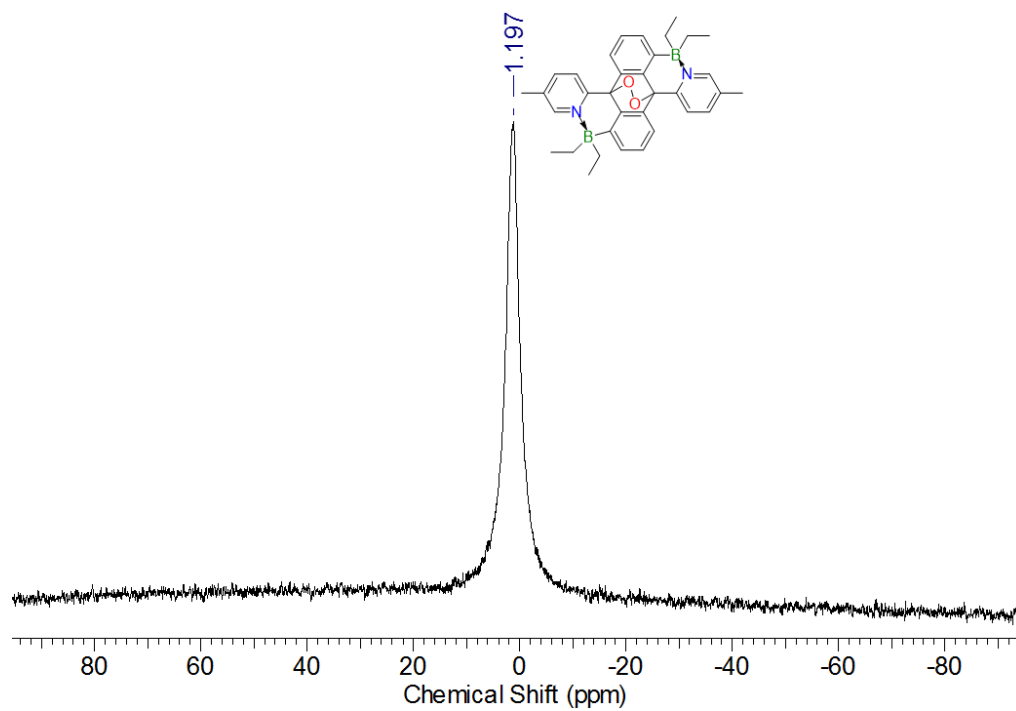
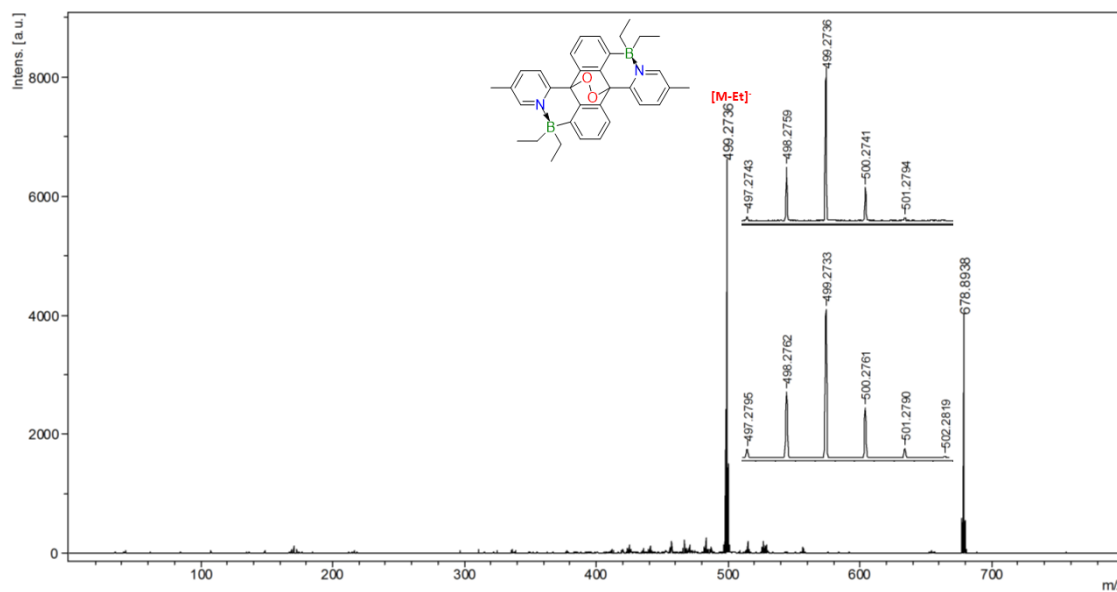


Figure 3-46. <sup>13</sup>C{<sup>1</sup>H} NMR spectrum of BPO-3Me in CDCl<sub>3</sub>



**Figure 3-47.**  $^{11}\text{B}\{^1\text{H}\}$  NMR spectrum of **BPO-3Me** in  $\text{CDCl}_3$



**Figure 3-48.** MALDI-TOF mass spectrum (neg. mode) of **BPO-3Me**

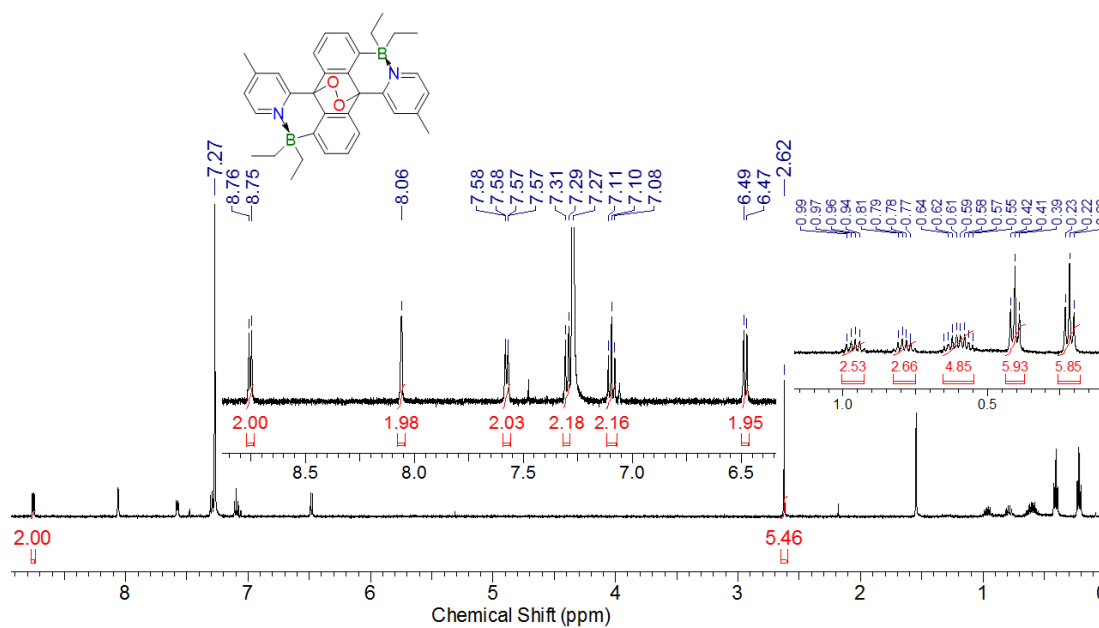


**Figure 3-49.**  $^1\text{H}$  NMR spectrum of **BPO-4Me** in  $\text{CDCl}_3$

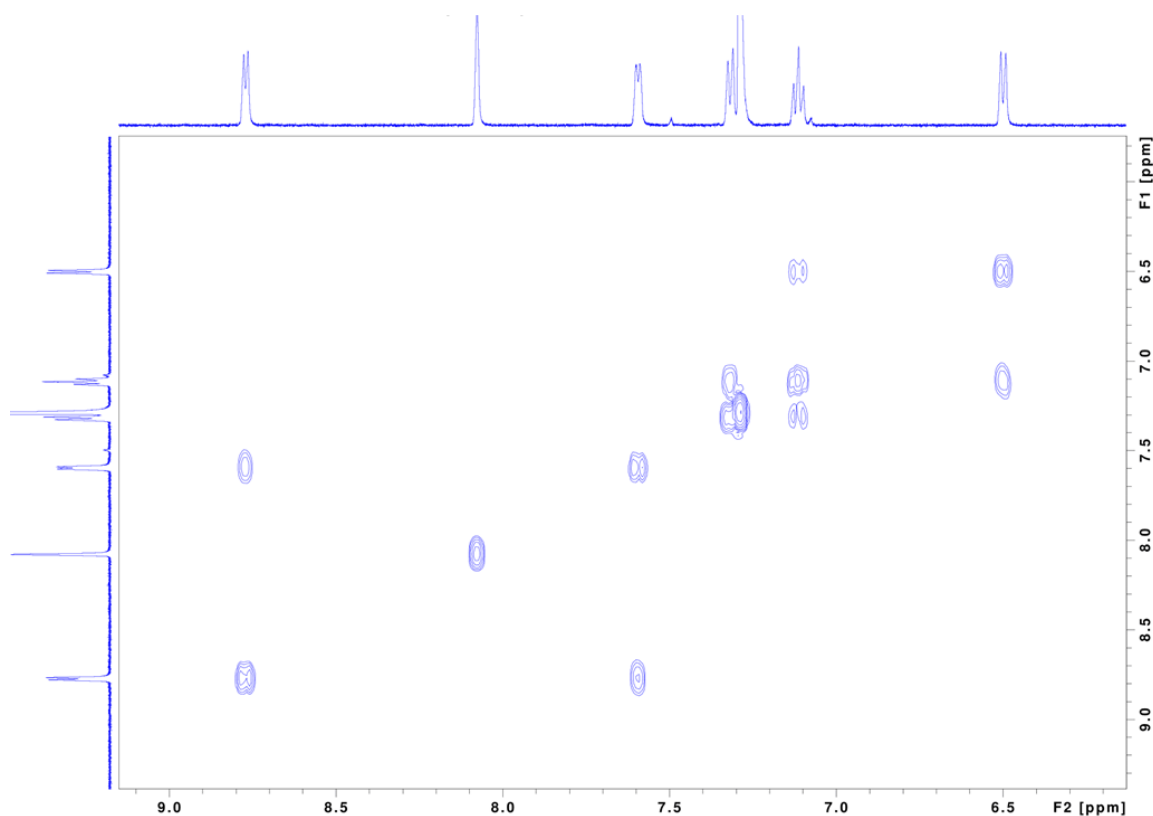


**Figure 3-50.** Aromatic region of the gCOSY NMR spectrum of **BPO-4Me** in  $\text{CDCl}_3$

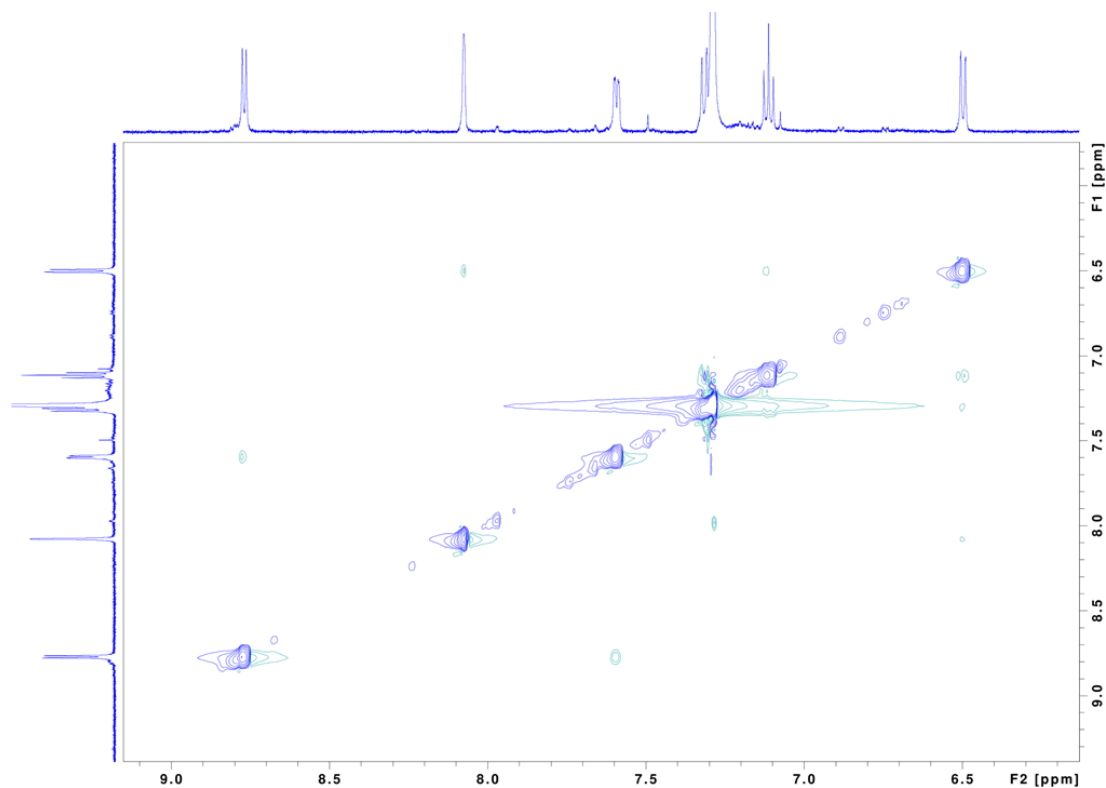


**Figure 3-51.** Aromatic region of the HH-NOESY NMR spectrum of **BPO-4Me** in  $\text{CDCl}_3$

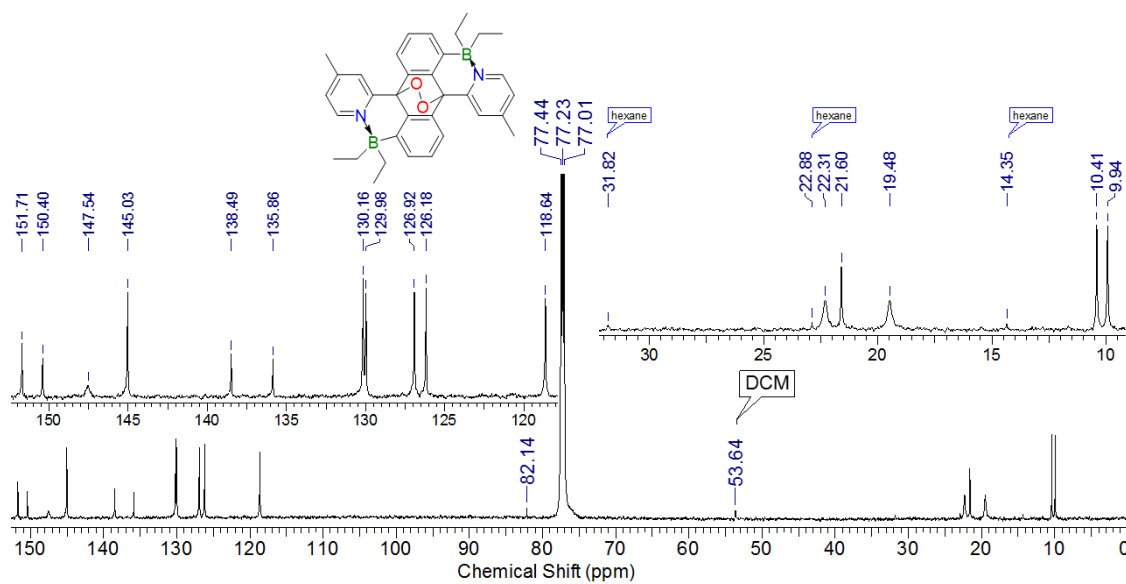


**Figure 3-52.**  $^{13}\text{C}\{^1\text{H}\}$  NMR spectrum of **BPO-4Me** in  $\text{CDCl}_3$

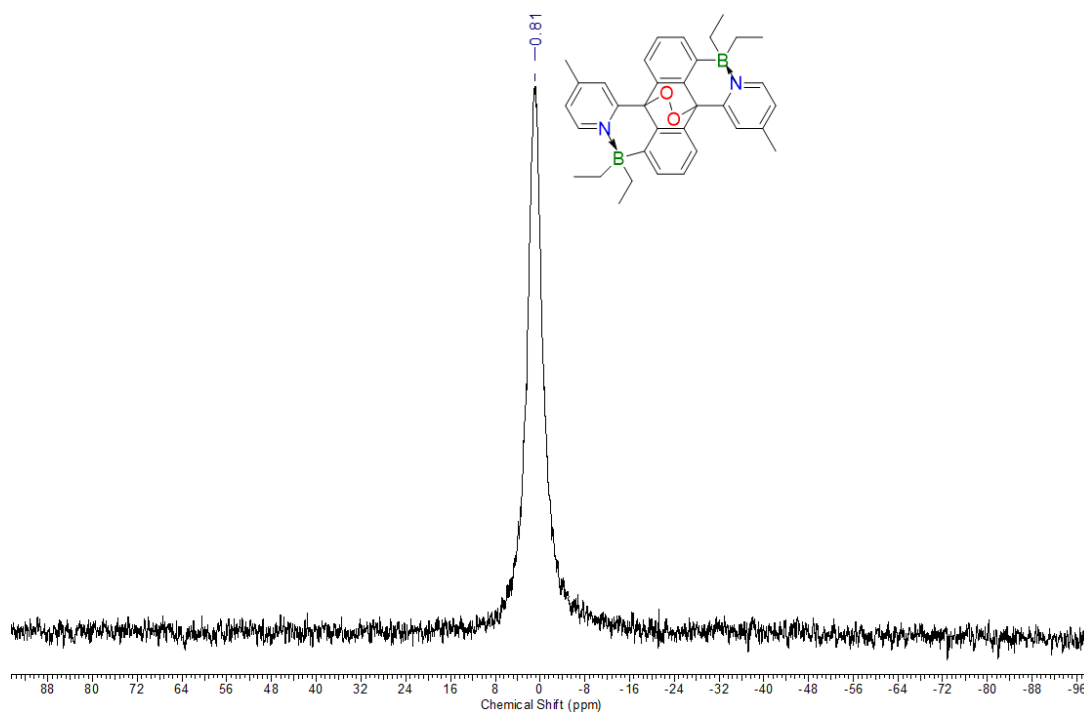


Figure 3-53.  $^{11}\text{B}\{^1\text{H}\}$  NMR spectrum of **BPO-4Me** in  $\text{CDCl}_3$

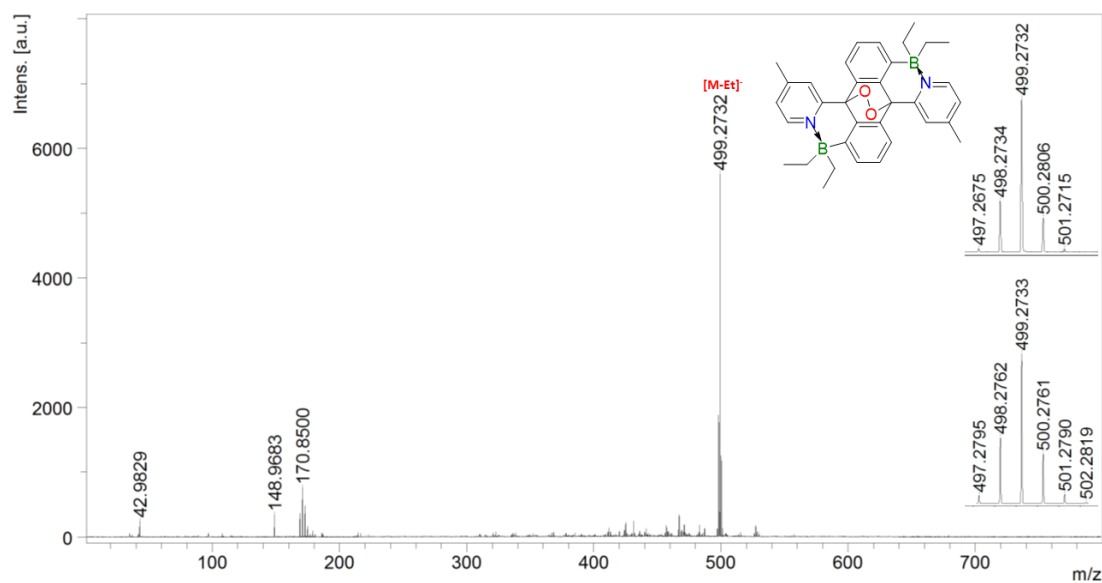


Figure 3-54. MALDI-TOF mass spectrum (neg. mode) of **BPO-4Me**



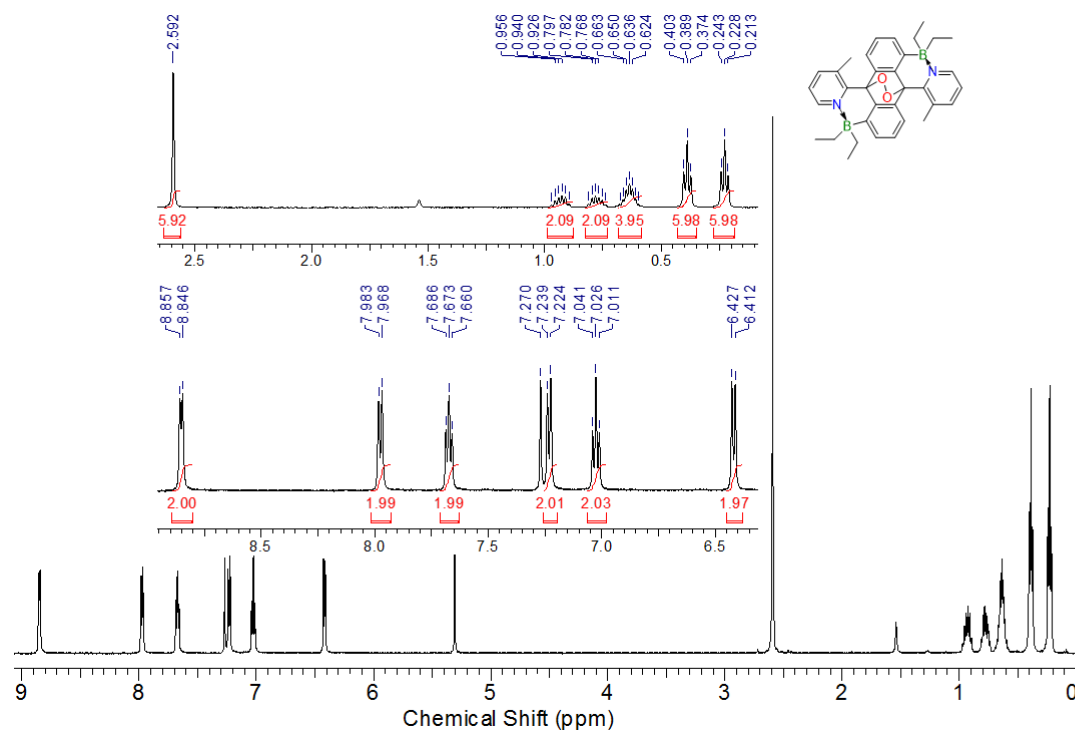


Figure 3-55. <sup>1</sup>H NMR spectrum of BPO-5Me in CDCl<sub>3</sub>

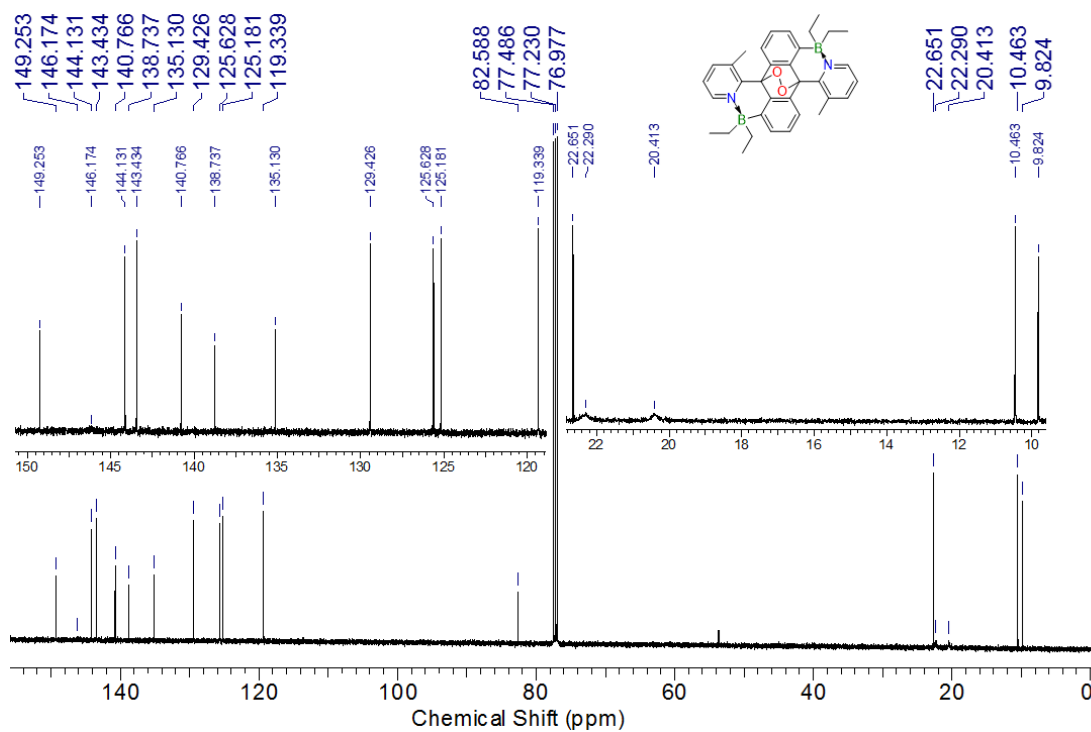
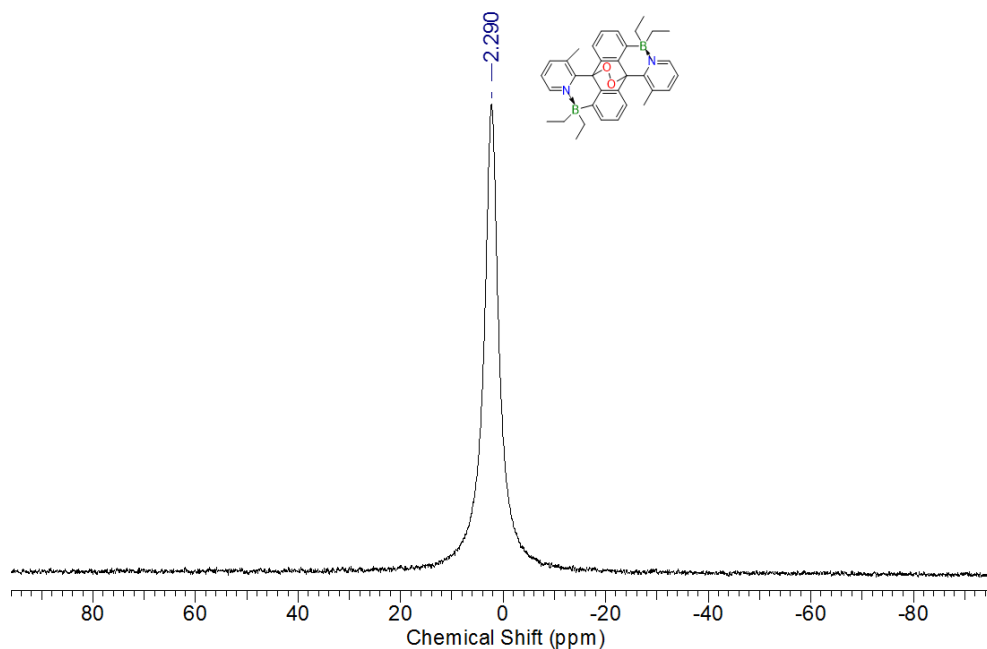
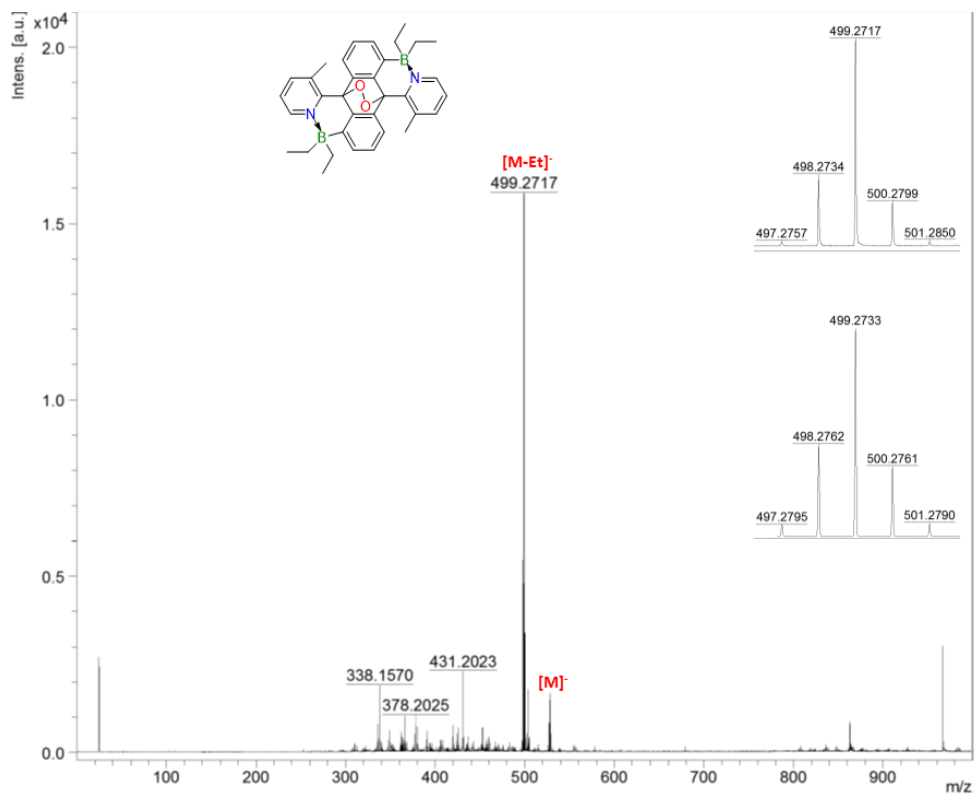


Figure 3-56. <sup>13</sup>C{<sup>1</sup>H} NMR spectrum of BPO-5Me in CDCl<sub>3</sub>



**Figure 3-57.**  $^{11}\text{B}\{^1\text{H}\}$  NMR spectrum of **BPO-5Me** in  $\text{CDCl}_3$



**Figure 3-58.** MALDI-TOF mass spectrum (neg. mode) of **BPO-5Me**

## Chapter 4 Boron Complexes of a Pyrazine-Bridged Anthracene

### Dimer as Low Band Gap Materials

#### 4.1 Introduction

Conjugated organic materials are important because of their wide applications ranging from electronic and optoelectronic devices, such as organic photovoltaic devices (OPVs), organic field effect transistors (OFETs) and organic light emitting diodes (OLEDs) to chemical sensors and biological imaging materials.<sup>1-5</sup> Recently, low band gap materials with strong near-infrared (NIR) absorption or emission have gained interest for use in photovoltaic devices and biological imaging applications.<sup>6-9</sup> In this respect, the functionalization of  $\pi$ -conjugated systems with main group elements such as boron is particularly attractive because it offers a means to easily tune the electronic structures and optoelectronic properties.<sup>10-12</sup> Substitution of the carbon-carbon covalent bond (C-C) with an isoelectronic B $\leftarrow$ N unit has emerged as a general strategy to adjust the energy levels and bandgaps of conjugated materials. However, so far only a limited number of low band gap molecules containing B $\leftarrow$ N units have been introduced.<sup>13-19</sup> In late 2017, we reported a new class of BN-fused dipyridylanthracenes with unique structural features and electronic properties. We found that the formation of the B $\leftarrow$ N Lewis pairs at the periphery of anthracene results in dramatically lowered LUMO energy levels, which leads to large bathochromic shifts in the absorption and emission relative to the all-carbon analogs. To achieve a further decrease in the HOMO-LUMO gap of BN Lewis pair-functionalized anthracenes, we designed the borane-modified dianthracenylpyrazine derivatives shown in Figure 4-1. We chose the pyrazine unit as a linker because it is an inherently highly

electron-deficient heterocycle and binding of boron to the N atoms is expected to further decrease the LUMO energy levels. Fang and Pammer demonstrated that the borylation of pyrazine-derived substrates results in low-lying LUMO levels (Figure 4-1).<sup>15, 20</sup> Indeed, our theoretical studies indicated that BN-fused dianthracenylpyrazine compounds show very low-lying LUMO levels and a dramatically decreased HOMO-LUMO gap relative to the previously described BN-fused dipyridylanthracenes. Modification of the boryl substituents provides an additional opportunity for LUMO tuning.<sup>14</sup> Thus, the attachment of electron-withdrawing groups, such as C<sub>6</sub>F<sub>5</sub> to boron further lowers the HOMO-LUMO gap, potentially offering access to near-infrared (NIR) emitting materials. In this Chapter we report the BN-fusion of a pyrazine-bridged anthracene dimer to generate new low band gap materials.

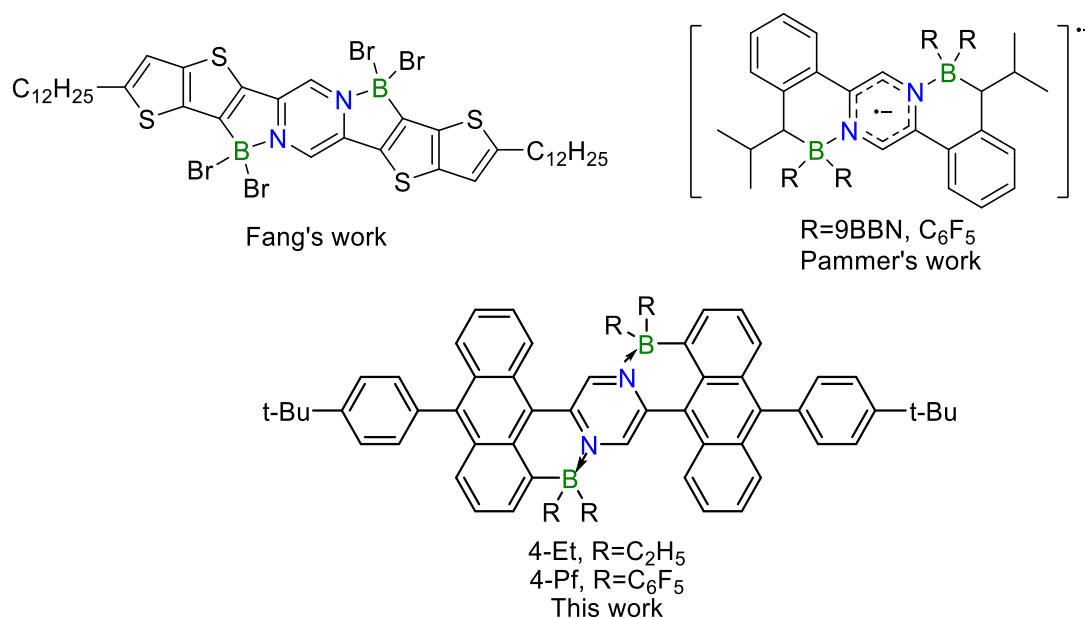
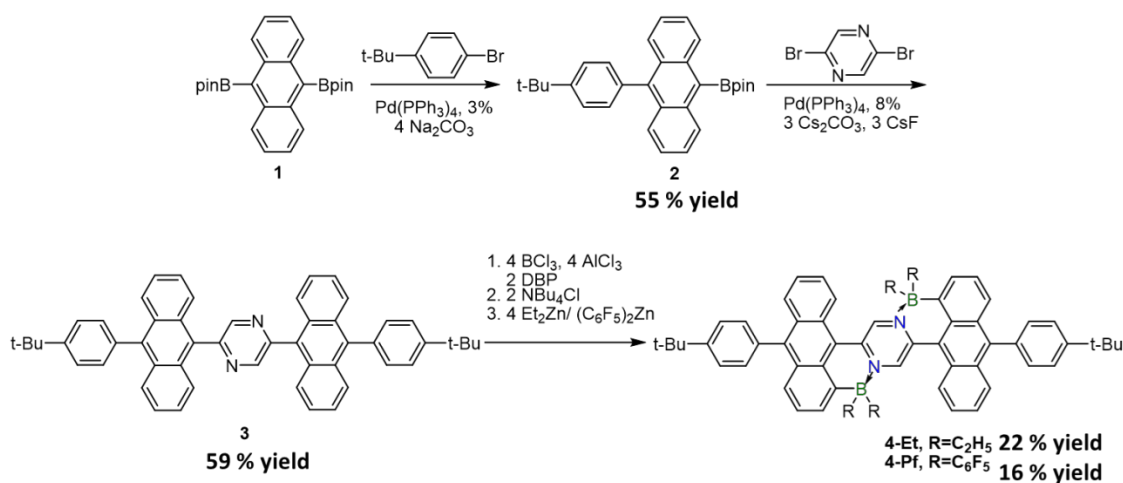


**Figure 4-1.** Examples of borylation of pyrazine-derived substrates.

## 4.2 Result and Discussion

The synthetic route to the targeted boron-complexed dianthracenylpyrazines is shown in Scheme 4-1. The unsymmetrically substituted anthracene **2** was obtained in 55% yield by reaction of **1**<sup>21</sup> with 1-bromo-4-*tert*-butylbenzene. The *tert*-butylphenyl group was introduced to increase the solubility and stability of the final products. Suzuki-Miyaura cross coupling of **2** with dibromopyrazine furnished the pyrazine-bridged anthracene dimer **3** in a yield of 59 %. The addition of BCl<sub>3</sub>, AlCl<sub>3</sub> and the bulky base 2,6-di-*tert*-butylpyridine (DBP) to a DCM solution of **3** gave the fused boracyclic species. Subsequent treatment with Et<sub>2</sub>Zn or (C<sub>6</sub>F<sub>5</sub>)<sub>2</sub>Zn produced the targeted planarized B-N doped polycyclic species **4-Et** and **4-Pf** in low yields.



**Scheme 4-1.** Synthesis of BN-fused dianthracenylpyrazines **4-Et** and **4-Pf**

The B-N fused products were fully characterized by multinuclear NMR and high-resolution MALDI-TOF mass spectrometry. <sup>11</sup>B NMR data in CDCl<sub>3</sub> revealed signals at 1.7 ppm (**4-Et**) and -2.6 ppm (**4-Pf**) that suggest a tetra-coordinate configuration for the boron centers.

The  $^{11}\text{B}$  NMR signal of **4-Pf** is slightly shifted upfield compared with that of **4-Et**, consistent with the expected stronger  $\text{B} \leftarrow \text{N}$  interaction for the more electron-deficient bis(pentafluorophenyl)borane derivative. The  $^{19}\text{F}$  NMR spectrum of **4-Pf** showed strongly broadened signals at room temperature. At  $-30\text{ }^{\circ}\text{C}$  in  $\text{D}_8$ -toluene they split into four signals for the *ortho*- and *meta*- and two signals for the *para*-fluorine atoms of the  $\text{C}_6\text{F}_5$  rings. A VT NMR study showed gradual coalescence into one set of signals and at  $80\text{ }^{\circ}\text{C}$  all the signals became sharp except for the *ortho*-fluorines. The coalescence phenomena are attributed to two distinct processes, the hindered rotation of the  $\text{C}_6\text{F}_5$  rings and the exchange of the  $\text{C}_6\text{F}_5$  rings. The latter presumably occurs through B-N bond dissociation followed by rotation of the  $\text{B}(\text{C}_6\text{F}_5)_2$  group about the B-C(pyrazine) bond. The free energy barrier for exchange of the  $\text{C}_6\text{F}_5$  rings was calculated to be  $52\text{ kJ mol}^{-1}$  based on the coalescence for the *para*-fluorine signals. The energy required for rotation of the  $\text{C}_6\text{F}_5$  groups themselves is in a similar range, preventing accurate determination due to simultaneous coalescence events.

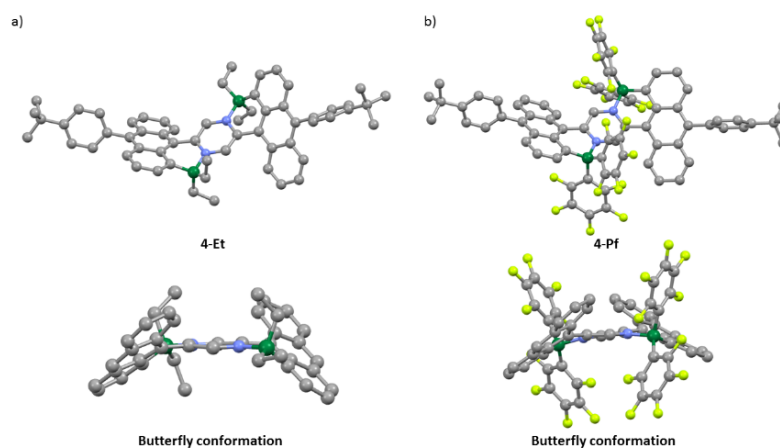


**Figure 4-2.** Optimized structures of (a) **4-Et** and (b) **4-Pf**(Gaussian 09; rb3lyp/6-31g(d)). C grey, B green, N blue, F yellow.

Geometry optimization of **4-Et** and **4-Pf** predicts the formation of highly distorted PAHs. The results are in Figure 4-2 and Table 4-10. The two anthracene backbones of **4-Et** and **4-Pf** both are strongly distorted with butterfly conformation, indicating the incorporation of tetrahedral boron centers into the B–N heterocycles contributes to structural distortion. The largest distortions are found for **4-Et** with an interplanar angle between the two inner benzene rings of anthracene of  $70.7^\circ$ .

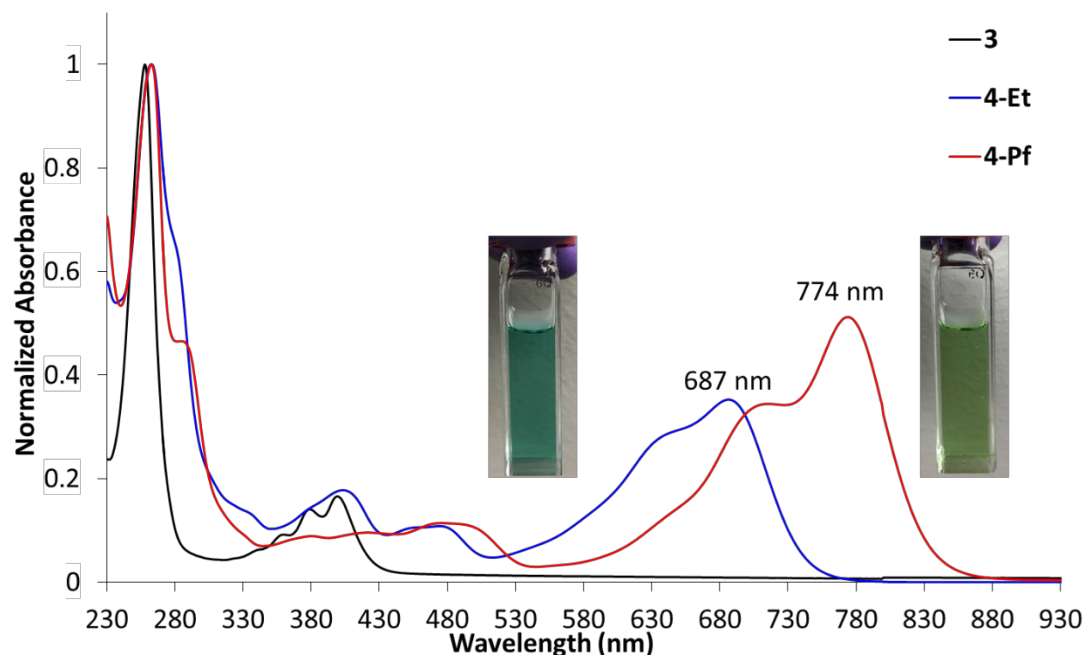


**Figure 4-3.** UV-vis absorption spectra of **3**, **4-Et** and **4-Pf** in DCM

The UV-vis-NIR absorption data of **4-Et** and **4-Pf** were measured in DCM and are illustrated in Figure 4-3. Compared to the precursor **3**, the absorption spectra of **4-Et** and **4-Pf** in dichloromethane were dramatically redshifted, approaching the NIR region. The larger shift was observed for **4-Pf**, which shows a broad band with a maximum at 774 nm in DCM with relatively little absorption throughout the visible region (400-700 nm). These results are indicative of a very narrow HOMO-LUMO gap. The observed intense NIR absorptions were well reproduced by TDDFT calculations (CAM-B3LYP/6-31G(d), Table 5-1) on optimized DCM-solution structures. According to these calculations the longest wavelength absorption is assigned to a HOMO→LUMO transition and exhibits a large oscillator strength ( $f = 0.9028$  for **4-Et** and  $0.8333$  for **4-Pf**).



**Table 4-1.** Summary of photophysical data in DCM solution

| Compound    | $\lambda_{\text{abs}}$ / nm | $\lambda_{\text{abs}}$ (TDDFT) / nm         | $E_{\text{g}}^{\text{opt}}$ / eV |
|-------------|-----------------------------|---|----------------------------------|
| <b>3</b>    | 399<br>379<br>358<br>258    | 376.6<br>(S <sub>0</sub> → S <sub>1</sub> ) | 3.11                             |
| <b>4-Et</b> | 687<br>637 (sh)<br>263      | 596.5<br>(S <sub>0</sub> → S <sub>1</sub> ) | 1.80                             |
| <b>4-Pf</b> | 774<br>708 (sh)<br>263      | 663.4<br>(S <sub>0</sub> → S <sub>1</sub> ) | 1.60                             |

Significant negative solvatochromic shifts were found when varying the polarity of the solvent. The absorption maxima change from  $\lambda_{\text{max}} = 698$  nm (**4-Et**) and 777 nm (**4-Pf**) in toluene to  $\lambda_{\text{max}} = 648$  nm (**4-Et**) and 733 nm (**4-Pf**) in acetonitrile (Figure 4-4), indicative of a more polar ground state that is better stabilized by polar solvents in comparison to the first excited state.

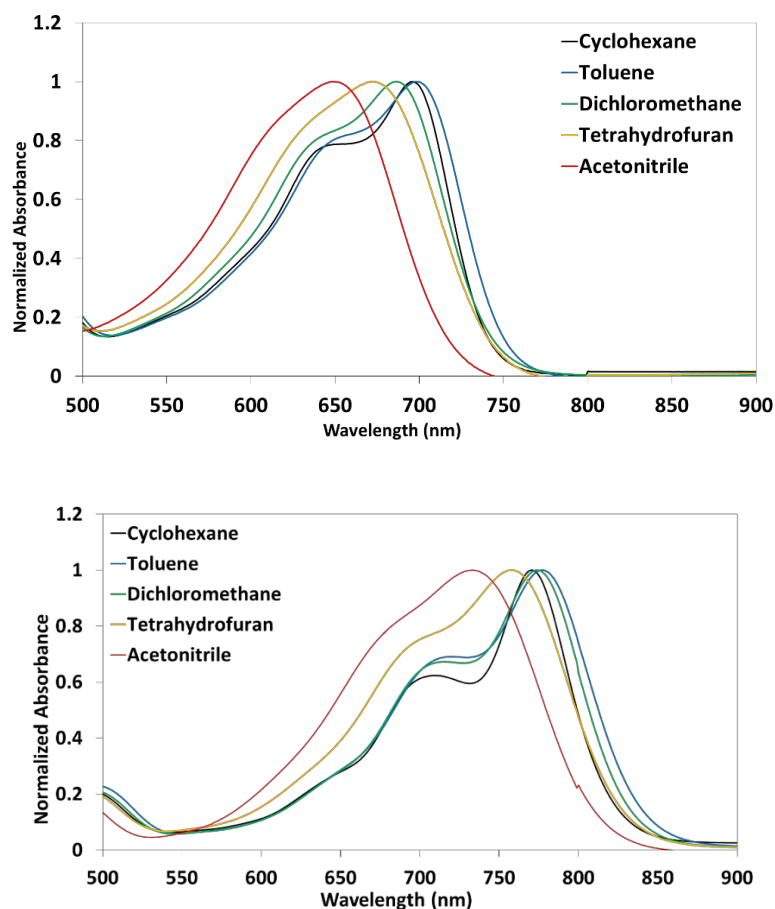


**Figure 4-4.** UV-vis absorption spectra of (a) **4-Et** and (b) **4-Pf** in solvents of varying polarity

To experimentally verify the electronic features of the BN-fused dianthracenylpyrazine unit, we acquired cyclic (CV) and square wave voltammograms (SWV) for **4-Et** and **4-Pf** in THF containing 0.1 M Bu<sub>4</sub>N[PF<sub>6</sub>]. The electrochemical data are summarized in Table 4-6. **4-Pf** exhibits two consecutive reversible reduction processes at  $E_{\text{red}} = -0.74$  and  $-1.75$  V, which appear at much less negative potential than those of **4-Et** ( $E_{\text{red}} = -1.23, -2.10$  V; vs Fc<sup>+/0</sup>) (Figure 4-5). The far less negative potentials for **4-Pf** are due to the electron withdrawing nature of the C<sub>6</sub>F<sub>5</sub> substituents that dramatically increase the electron-deficient character of **4-Pf**. Oxidative scans were performed in CH<sub>2</sub>Cl<sub>2</sub> containing 0.1 M

Bu<sub>4</sub>N[PF<sub>6</sub>]. **4-Pf** undergoes two reversible oxidations, whereas **4-Et** shows only irreversible processes. The HOMO and LUMO levels were estimated from these redox potentials and are given in Table 4-2. The HOMO-LUMO gaps are in good agreement with the trends from our DFT results (vide infra) and the optical gaps deduced from UV-Vis absorption spectroscopy.

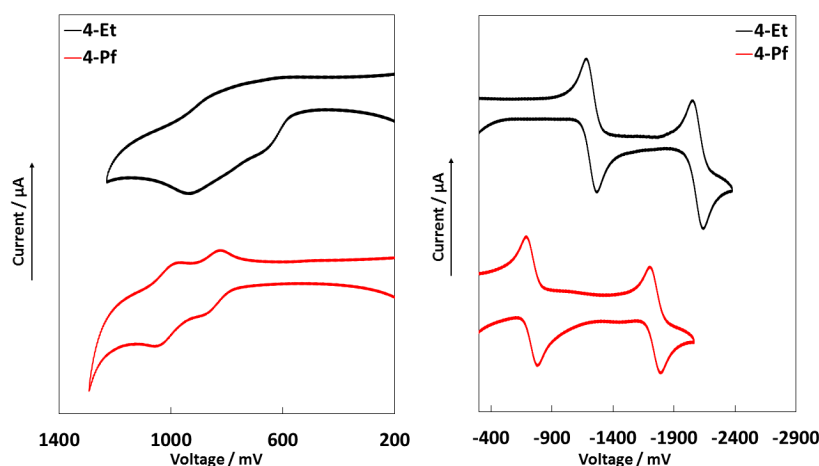


**Figure 4-5.** Cyclic voltammetry (CV) data. Oxidation in 0.1M Bu<sub>4</sub>N[PF<sub>6</sub>] in DCM, reduction in 0.1M Bu<sub>4</sub>N[PF<sub>6</sub>] in THF, reported vs Fc<sup>+/0</sup>,  $\nu = 250 \text{ mV s}^{-1}$ .

**Table 4-2.** Electrochemical data of BN-fused dianthracenylpyrazine and comparison of HOMO-LUMO gaps with results from DFT calculations and UV-Vis absorption spectroscopy

| Compound    | $E_{\text{ox}}^{\text{CV}}$<br>(V) | $E_{\text{red}}^{\text{CV}}$<br>(V) | HOMO <sup>c</sup><br>(eV) | LUMO <sup>c</sup><br>(eV) | $E_{\text{g}}^{\text{CV c}}$<br>(eV) | $E_{\text{g}}^{\text{DFT d}}$<br>(eV) | $E_{\text{g}}^{\text{opt e}}$<br>(eV) |
|-------------|------------------------------------|-------------------------------------|---------------------------|---------------------------|--------------------------------------|---------------------------------------|---------------------------------------|
| <b>4-Et</b> | 0.65, 0.93 <sup>b</sup>            | -1.23, -2.10 <sup>a</sup>           | -5.45                     | -3.57                     | 1.88                                 | 2.05                                  | 1.80                                  |
| <b>4-Pf</b> | 0.85, 1.02 <sup>a</sup>            | -0.74, -1.75 <sup>a</sup>           | -5.65                     | -4.06                     | 1.59                                 | 1.84                                  | 1.60                                  |

[a] Quasi-reversible or reversible ( $E_{\text{red}}$  or  $E_{\text{ox}} = 0.5 (E_{\text{pc}} + E_{\text{pa}})$ ); [b] Irreversible ( $E_{\text{ox}} = E_{\text{pa}}$ ;  $E_{\text{red}} = E_{\text{pc}}$ ); [c] Determined from CV data using the equations  $E_{\text{LUMO}} = -(4.8 + E_{\text{red}})$  and  $E_{\text{HOMO}} = -(4.8 + E_{\text{ox}})$ ; [d] From DFT calculations at the rb3lyp/6-31g(d) level of theory; [e] Estimated from absorption maxima in CH<sub>2</sub>Cl<sub>2</sub> solution.

In order to gain a deeper understanding into the effects of the B-N coordination on the electronic structure in the central building block, calculations were performed using a rb3lyp/6-31g(d) basis set and the calculated energy levels are illustrated in Figure 4-6 and summarized in Table 4-3. The BN-fused dianthracenylpyrazine compounds show slightly decreased HOMO energy levels and a dramatically decreased LUMO energy levels relative to the all-carbon analogs **4-Et-C** and **4-Pf-C**. This leads to small HOMO-LUMO energy gaps for BN-fused dianthracenylpyrazine compounds. The HOMO and LUMO orbitals for the all-carbon analogs **4-Et-C** and **4-Pf-C** are delocalized into the pyrazine groups. However, dramatic differences are apparent for the BN-fused dianthracenylpyrazine compounds. The electron densities of the HOMOs of **4-Et** and **4-Pf** are mainly localized on the two anthracene groups and the LUMOs on the pyrazine units. The spatial separation of the HOMO and LUMO illustrates the D-A-D character of this class of molecules. The HOMO-LUMO energy gaps ( $E_g$ ) for **4-Et** and **4-Pf** are 2.05 and 1.84 eV, respectively. The attachment of electron-withdrawing groups  $C_6F_5$  groups to boron further lowers the HOMO-LUMO gap, in good agreement with the redshift of the absorption of **4-Pf** in comparison to **4-Et**.

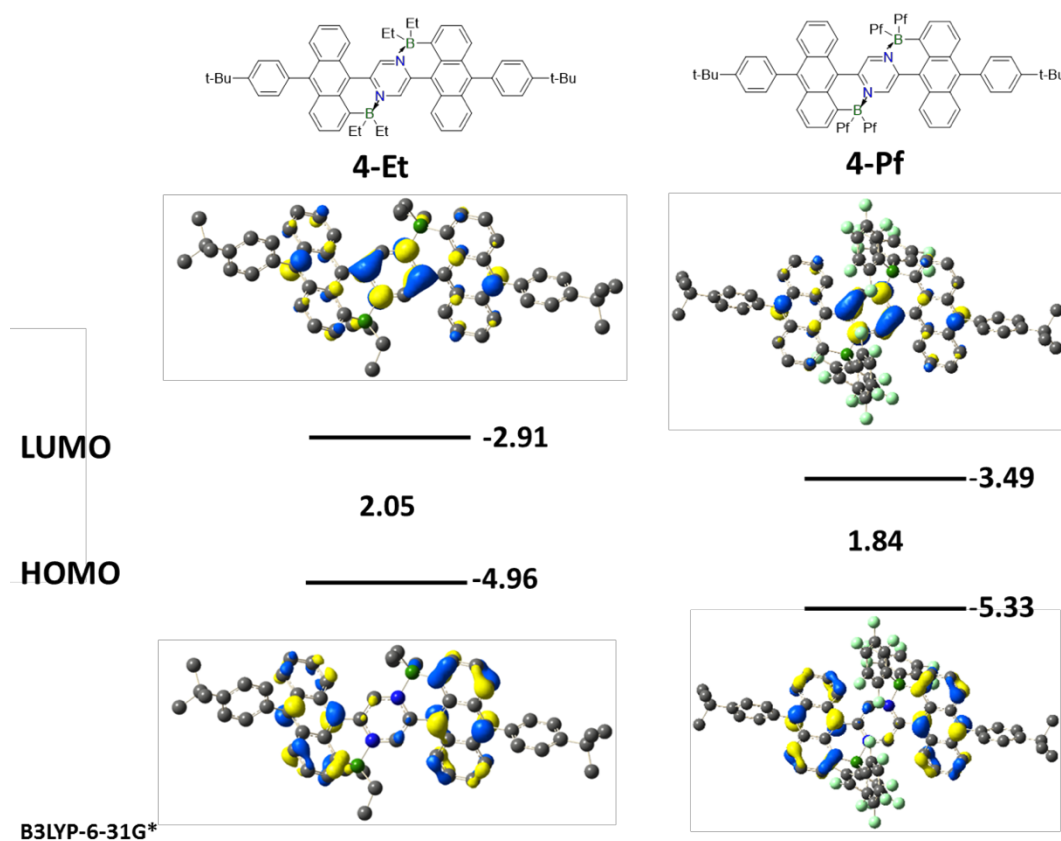


**Figure 4-6.** Calculated frontier orbital energy levels and HOMO/LUMO orbital plots of **4-Et** and **4-Pf** (DFT, B3LYP/6-31G(d)).

**Table 4-3.** Comparison of calculated orbital energy levels (rb3lyp/6-31g(d)) for differently substituted B-N Lewis-pairs

| Compound    | LUMO (eV) | HOMO (eV) | $E_{\text{gap}}$ (eV) |
|-------------|-----------|-----------|-----------------------|
| <b>3</b>    | -1.84     | -5.12     | 3.28                  |
| <b>4-Et</b> | -2.91     | -4.96     | 2.05                  |
| <b>4-Pf</b> | -3.49     | -5.33     | 1.84                  |

### 4.3 Experimental

**Materials and General Methods.** All reactions were carried out under an atmosphere of pre-purified nitrogen using either Schlenk techniques or an inert-atmosphere glovebox.

DCM was distilled from  $\text{CaH}_2$  and degassed via several freeze-pump-thaw cycles. THF was distilled from Na/K and degassed via several freeze-pump-thaw cycles. All chemicals were purchased from commercial sources and directly used without further purification unless noted otherwise.

NMR data were acquired at ambient temperature unless noted otherwise. 499.9 MHz  $^1\text{H}$  and 160.4 MHz  $^{11}\text{B}$  NMR data were recorded on a 500 MHz Bruker AVANCE spectrometer; 599.7 MHz  $^1\text{H}$ , 150.8 MHz  $^{13}\text{C}$  and 192.4 MHz  $^{11}\text{B}$  NMR data were recorded on a Varian INOVA 600 spectrometer.  $^{11}\text{B}$  NMR spectra were acquired with boron-free quartz NMR tubes either on the Varian INOVA 600 with a boron-free 5 mm dual broadband gradient probe (Nalorac, Varian Inc., Martinez, CA) or the 500 MHz Bruker Auto Avance with a 5mm PH SEX 500S1 11B-H/F-D probe.  $^1\text{H}$  and  $^{13}\text{C}$  NMR spectra were referenced internally to solvent signals ( $\text{CDCl}_3$ : 7.27 ppm for  $^1\text{H}$  NMR, 77.23 ppm for  $^{13}\text{C}$  NMR) and all other NMR spectra externally to  $\text{SiMe}_4$  (0 ppm). Abbreviations used for signal assignments: An = anthracene, Ph = phenyl, Py = pyrazinyl, Me = methyl, s = singlet, d = doublet, t = triplet, m = multiplet, br = broad.

MALDI-TOF MS measurements were performed on a Bruker Ultraflex extreme in reflectron mode with delayed extraction. Red phosphorus was used for calibration.

UV-visible absorption data were acquired on a Varian Cary 5000 UV-Vis/NIR spectrophotometer.

Cyclic voltammetry (CV) and square wave voltammetry (SWV) experiments were carried out on a CV-50W analyzer from BASi. The three-electrode system consisted of an Au disk as working electrode, a Pt wire as counter electrode and an Ag wire as the pseudo-reference electrode. The voltammograms were recorded with ca.  $10^{-3}$  to  $10^{-4}$  M solutions in THF

(reduction scans) or DCM (oxidation scans) containing Bu<sub>4</sub>N[PF<sub>6</sub>] (0.1 M) as the supporting electrolyte. The scans were referenced after the addition of a small amount of ferrocene as internal standard. The potentials are reported relative to the ferrocene/ferrocenium couple.

DFT calculations were performed with the Gaussian09 suite of programs.<sup>[S1]</sup> The input files were generated from Chem3D and pre-optimized in Spartan '08 V 1.2.0. Ground state geometries were then optimized in Gaussian09 using the hybrid density functional rb3lyp with a 6-31g(d) basis set. Frequency calculations were performed to confirm the presence of local minima (only positive frequencies). Vertical excitations were calculated by TD-DFT methods at the rcam-b3lyp/6-31g(d) level. DCM solution phase calculations were performed. First triplet excited state geometries were optimized by DFT methods at the ub3lyp/6-31g(d) level and first singlet excited state geometries were optimized by TD-DFT methods at the b3lyp/6-31g(d) level.

**Synthesis of 2-(10-(4-(*tert*-butylphenyl)anthracen-9-yl)-4,4,5,5-tetramethyl-1,3,2-dioxaborolane (2).** 9,10-Bis(pinacolboryl)anthracene (5.00 g, 11.6 mmol, 1.4 equiv), 1-bromo-4-*tert*-butylbenzene (1.44 mL, 8.30 mmol) and sodium carbonate (3.52 g, 33.2 mmol, 4 equiv) were added to a Schlenk flask. Then a mixture of toluene (210 mL), ethanol (45 mL) and water (210 mL) was added. The mixture was degassed by bubbling nitrogen for 20 min and then tetrakis(triphenylphosphine) palladium(0) (0.288 g, 0.249 mmol, 3 mol%) was added as the catalyst. The reaction mixture was stirred at 80 °C for 2 days under nitrogen atmosphere, allowed to cool to room temperature, and then poured into water with stirring. The mixture was extracted with DCM, the organic layer was washed with brine and dried over anhydrous sodium sulfate. After rotary evaporation the crude product was

purified by column chromatography (silica gel) with hexanes/DCM (v/v = 3:1) as eluent. Recrystallization in ethanol/dichloromethane (1:1) gave the product as yellow crystals. Yield: 2.0 g (55%). <sup>1</sup>H NMR (499.9 MHz, CDCl<sub>3</sub>, 25 °C): δ (ppm) = 8.44 (d, J = 9.0 Hz, 2H; An), 7.69 (d, J = 8.5 Hz, 2H; An), 7.58 (d, J = 8.0 Hz, 2H; Ph), 7.47 (td, <sup>2</sup>J = 7.5 Hz, <sup>3</sup>J = 1.5 Hz, 2H; An), 7.34-7.30 (overlapped, 4H; Ph, An), 1.61 (s, 12H; Me), 1.47 (s, 9H; Me). <sup>13</sup>C NMR (150.8 MHz, CDCl<sub>3</sub>, 25 °C): δ (ppm) = 150.4, 140.0, 136.1, 135.6, 130.9, 130.1, 128.6, 127.8, 125.6, 125.3, 124.9, 84.6, 34.9, 31.8, 25.5. High-resolution MALDI-TOF mass spectrum (pos. mode, neat): m/z = 436.2562 ([M]<sup>+</sup>, 100 %, calcd for <sup>12</sup>C<sub>30</sub><sup>1</sup>H<sub>33</sub><sup>11</sup>B<sub>1</sub><sup>16</sup>O<sub>2</sub> 436.2573).

**Synthesis of 2,5-bis(10-(4-*tert*-butylphenyl)anthracen-9-yl)pyrazine (3).** 2,5-Dibromopyrazine (0.39 g, 1.64 mmol), 2-(10-(4-(*tert*-butylphenyl)anthracen-9-yl)-4,4,5,5-tetramethyl-1,3,2-dioxaborolane (2.00 g, 4.58 mmol, 2.8 equiv), cesium carbonate (1.60 g, 4.92 mmol, 3 equiv) and cesium fluoride (0.75 g, 4.92 mmol, 3 equiv) were added to a Schlenk flask. Then a mixture of toluene (80 mL) and DMF (40 mL) was added. The mixture was degassed by bubbling nitrogen for 20 min and then tetrakis(triphenylphosphine) palladium(0) (0.152 g, 0.131 mmol, 8 mol%) was added as the catalyst. The reaction mixture was stirred at 90 °C for 3 days under nitrogen atmosphere, allowed to cool to room temperature, and then poured into water with stirring. The mixture was extracted with DCM, the organic layer was washed with brine and dried over anhydrous sodium sulfate. After removal of the solvent under vacuum, the residue was purified by column chromatography (silica gel) with hexanes/ethyl acetate (v/v = 10:1) as eluent to afford the desired product as a yellow solid. Yield: 0.67 g (59 %). <sup>1</sup>H NMR (499.9 MHz, CDCl<sub>3</sub>, 25 °C): δ (ppm) = 9.22 (s, 2H; Py), 7.86-7.83 (overlapped, 8H; An), 7.66 (d,



$J = 7.5$  Hz, 4H; Ph), 7.56 (t,  $J = 7.5$  Hz, 4H; An), 7.46-7.43 (overlapped, 8H; Ph, An), 1.51 (s, 18H; Me).  $^{13}\text{C}$  NMR (125.8 MHz,  $\text{CDCl}_3$ , 25 °C):  $\delta$  (ppm) = 153.0, 150.8, 147.7, 140.0, 135.7, 131.2, 131.0, 130.6, 130.4, 128.0, 126.6, 125.6, 125.6, 125.4, 35.0, 31.8. High-resolution MALDI-TOF mass spectrum (pos. mode, neat):  $m/z = 696.3533$  ( $[\text{M}]^+$ , 100 %, calcd for  $^{12}\text{C}_{52}^{1}\text{H}_{44}^{14}\text{N}_2$  696.3499).

**Synthesis of 4-Et.** In a glovebox,  $\text{BCl}_3$  (3.9 mL, 1M solution in hexane, 3.83 mmol, 4 equiv) was added to a bright yellow solution of 2,5-bis(10-(4-*tert*-butylphenyl)-anthracen-9-yl)pyrazine (0.67 g, 0.96 mmol) in DCM (20 mL). The solution instantly changed color to dark yellow. 2,6-Di-*tert*-butylpyridine (0.37 g, 1.92 mmol, 2 equiv) and  $\text{AlCl}_3$  (0.383 g, 2.87 mmol, 3 equiv) were added to the reaction mixture. After stirring for 16 hours, an additional portion of  $\text{AlCl}_3$  (0.128 g, 0.96 mmol, 1 equiv) was added and the mixture was stirred for a further 16 hours whereupon it turned dark blue. Addition of  $\text{Bu}_4\text{NCl}$  (0.533 g, 1.92 mmol, 2 equiv) resulted in a dark purple suspension to which  $\text{ZnEt}_2$  (0.44 mL, 3.93 mmol, 4.1 equiv) was added dropwise. The reaction mixture was stirred for 16 hours at room temperature and the solvent was then removed under reduced pressure. The dark green residue was redissolved in toluene and insoluble components were removed by filtration through a fritted funnel. The solution was concentrated under reduced pressure. The residue was dissolved in dichloromethane, layered with hexanes, and stored at -37 °C. The product was collected as a dark green crystalline solid. Yield: 0.18 g (22 %).  $^1\text{H}$  NMR (599.7 MHz,  $\text{CDCl}_3$ , 25 °C):  $\delta$  (ppm) = 9.50 (s, 2H; Py), 8.60 (d,  $J = 9.0$  Hz, 2H; na), 7.88 (d,  $J = 9.0$  Hz, 2H; An), 7.70-7.62 (overlapped, 8H; Ph, An), 7.56 (d,  $J = 8.4$  Hz, 2H; An), 7.51-7.47 (overlapped, 4H; An), 7.45 (d,  $J = 7.8$  Hz, 4H; Ph), 1.51 (s, 18H; Me), 1.02 (m, 4H; Et), 0.80 (m, 4H; Et), 0.66 (t,  $J = 7.8$  Hz, 12H; Et).  $^{13}\text{C}$  NMR (150.8 MHz,  $\text{CDCl}_3$ ,

25 °C):  $\delta$  (ppm) = 151.1, 147.2 (br), 146.0, 144.7, 143.7, 135.5, 133.5, 131.2, 130.8, 130.7, 130.2, 129.4, 129.3, 128.1, 127.3, 125.8, 125.6, 124.1, 124.0, 121.1, 35.1, 31.8, 18.9 (br), 10.0.  $^{11}\text{B}$  NMR (160.4 MHz,  $\text{CDCl}_3$ , 25 °C):  $\delta$  (ppm) = 1.7 ( $w_{1/2}$  = 1040 Hz). High-resolution MALDI-TOF mass spectrum (pos. mode, neat):  $m/z$  = 832.5061 ( $[\text{M}]^+$ , 5%, calcd for  $^{12}\text{C}_{60}^{1}\text{H}_{62}^{11}\text{B}_2^{14}\text{N}_2$  832.5112), 803.4689 ( $[\text{M-Et}]^+$ , 3%, calcd for  $^{12}\text{C}_{58}^{1}\text{H}_{57}^{11}\text{B}_2^{14}\text{N}_2$  803.4720), 774.4325 ( $[\text{M-2Et}]^+$ , 100 %, calcd for  $^{12}\text{C}_{56}^{1}\text{H}_{52}^{11}\text{B}_2^{14}\text{N}_2$  774.4329).

**Synthesis of 4-Pf.** In a glovebox,  $\text{BCl}_3$  (1.15 mL, 1M solution in hexane, 1.15 mmol, 4 equiv) was added to a bright yellow solution of 2,5-bis(10-(4-*tert*-butylphenyl)- anthracen-9-yl)pyrazine (0.200 g, 0.287 mmol) in DCM (50 mL). The solution instantly changed color to dark yellow. 2,6-Di-*tert*-butylpyridine (0.110 g, 0.574 mmol, 2 equiv) and  $\text{AlCl}_3$  (0.115 g, 0.861 mmol, 3 equiv) were added to the reaction mixture. After stirring for 16 hours, an additional portion of  $\text{AlCl}_3$  (0.0383 g, 0.287 mmol, 1 equiv) was added and the mixture was stirred for a further 16 hours whereupon it turned dark blue. Addition of  $\text{Bu}_4\text{NCl}$  (0.160 g, 0.574 mmol, 2 equiv) resulted in a dark red suspension. After evaporation of the solvent under high vacuum, the dark residue was redissolved in toluene (50 mL) and insoluble components were removed by filtration through a fritted funnel. A solution of  $(\text{C}_6\text{F}_5)_2\text{Zn}$  (0.287 g, 0.718 mmol, 2.5 equiv) in toluene (10 mL) was added dropwise. The reaction mixture was kept stirring overnight, and then heated to 80 °C for 2 h. The dark green solution was allowed to cool to room temperature and filtered through a plug of silica gel with toluene as the eluent. The solution was concentrated using a rotary evaporator. The residue was redissolved in dichloromethane, the solution layered with hexanes, and stored at -37 °C. The product was collected as a dark green crystalline solid. Yield: 65 mg (16 %).  $^1\text{H}$  NMR (499.9 MHz,  $\text{CDCl}_3$ , 25 °C):  $\delta$  (ppm) = 9.42 (s, 2H; Py), 7.97 (d,  $J$  = 7.5

Hz, 2H; An), 7.88 (d,  $J = 8.0$  Hz, 2H; An), 7.73 (d,  $J = 8.5$  Hz, 2H; An), 7.64 (d,  $J = 8.0$  Hz, 4H; Ph), 7.54-7.40 (overlapped, 12H; Ph, An), 1.49 (s, 18H; Me).  $^{13}\text{C}$  NMR (150.8 MHz,  $\text{CDCl}_3$ , 25 °C):  $\delta$  (ppm) = 151.8, 149.5, 148.8 (br d,  $^1J(^{13}\text{C}, ^{19}\text{F}) = 254$  Hz), 145.6, 143.4, 140.6 (br d,  $^1J(^{13}\text{C}, ^{19}\text{F}) = 250$  Hz), 137.6 (br d,  $^1J(^{13}\text{C}, ^{19}\text{F}) = 261$  Hz), 134.3, 131.5, 131.4, 130.6, 130.2, 129.8, 129.7, 129.1, 127.9, 127.5, 126.7, 125.6, 122.7, 120.4, 117.3 (br), 35.1, 31.7.  $^{11}\text{B}$  NMR (160.4 MHz,  $\text{CDCl}_3$ , 25 °C):  $\delta$  (ppm) = -2.6 ( $w_{1/2} = 750$  Hz).  $^{19}\text{F}$  NMR (470.2 MHz,  $d_8\text{-tol}$ , 80 °C):  $\delta$  (ppm) = -131.0 (8F, o-Pf), -155.4 (4F, p-Pf), -162.4 (8F, m-Pf). High-resolution MALDI-TOF mass spectrum (neg. mode, neat):  $m/z = 1384.3260$  ( $[\text{M}]^-$ , 100 %, calcd for  $^{12}\text{C}_{76}^{1}\text{H}_{42}^{11}\text{B}_2^{19}\text{F}_{20}^{14}\text{N}_2$  1384.3231).

## 4.4 Conclusions

In summary, we have successfully synthesized two new BN-fused dianthracenylpyrazine derivatives with narrow band gap. Incorporation of the B-N units into the conjugated systems leads to dramatic changes in the electronic structure compared to the C-C analogs, most importantly a large decrease in the HOMO-LUMO gap. Thus, the borylated dianthracenylpyrazine derivatives have significant absorbance at greater than 700 nm. DFT calculations reveal the D-A-D character of these BN-fused dianthracenylpyrazines as seen in the spatial separation of the HOMO and LUMO orbitals. These results indicate that the borylative fusion of the dianthracenylpyrazine donor-acceptor-donor structure is a promising strategy toward materials with low band gap. Thus, the products will be investigated as low band gap materials for organic electronics and imaging applications.

## 4.5 References

1. Anthony, J. E., Functionalized Acenes and Heteroacenes for Organic Electronics. *Chem. Rev.* **2006**, *106* (12), 5028-5048.
2. Wu, J.; Pisula, W.; Müllen, K., Graphenes as Potential Material for Electronics. *Chem. Rev.* **2007**, *107* (3), 718-747.
3. Shirota, Y.; Kageyama, H., Charge Carrier Transporting Molecular Materials and Their Applications in Devices. *Chem. Rev.* **2007**, *107* (4), 953-1010.
4. Anthony, J. E.; Facchetti, A.; Heeney, M.; Marder, S. R.; Zhan, X., n-Type organic semiconductors in organic electronics. *Adv. Mater.* **2010**, *22* (34), 3876-3892.
5. Ding, D.; Li, K.; Liu, B.; Tang, B. Z., Bioprobes Based on AIE Fluorogens. *Acc. Chem. Res.* **2013**, *46* (11), 2441-2453.
6. Bundgaard, E.; Krebs, F., Low band gap polymers for organic photovoltaics. *Sol. Energ. Mat. Sol. C.* **2007**, *91* (11), 954-985.
7. Qian, G.; Wang, Z. Y., Near-infrared organic compounds and emerging applications. *Chem. Asian. J.* **2010**, *5* (5), 1006-1029.
8. Yuan, L.; Lin, W.; Zheng, K.; He, L.; Huang, W., Far-red to near infrared analyte-responsive fluorescent probes based on organic fluorophore platforms for fluorescence imaging. *Chem. Soc. Rev.* **2013**, *42* (2), 622-661.
9. Guo, Z.; Park, S.; Yoon, J.; Shin, I., Recent progress in the development of near-infrared fluorescent probes for bioimaging applications. *Chem. Soc. Rev.* **2014**, *43* (1), 16-29.
10. He, X.; Baumgartner, T., Conjugated main-group polymers for optoelectronics. *RSC Adv.* **2013**, *3* (29), 11334-11350.
11. Stepień, M.; Gonka, E.; Zyla, M.; Sprutta, N., Heterocyclic Nanographenes and Other Polycyclic Heteroaromatic Compounds: Synthetic Routes, Properties, and Applications. *Chem. Rev.* **2017**, *117* (4), 3479-3716.
12. Zhang, G.; Zhao, J.; Chow, P. C. Y.; Jiang, K.; Zhang, J.; Zhu, Z.; Zhang, J.; Huang, F.; Yan, H., Nonfullerene Acceptor Molecules for Bulk Heterojunction Organic Solar Cells. *Chem. Rev.* **2018**, *118* (7), 3447-3507.

13. Crossley, D. L.; Vitorica-Yrezabal, I.; Humphries, M. J.; Turner, M. L.; Ingleson, M. J., Highly Emissive Far Red/Near-IR Fluorophores Based on Borylated Fluorene-Benzothiadiazole Donor-Acceptor Materials. *Chem. - Eur. J.* **2016**, *22* (35), 12439-12448.
14. Nakamura, T.; Furukawa, S.; Nakamura, E., Benzodipyrrole-based Donor-Acceptor-type Boron Complexes as Tunable Near-infrared-Absorbing Materials. *Chem. Asian. J.* **2016**, *11* (14), 2016-2020.
15. Zhu, C.; Guo, Z. H.; Mu, A. U.; Liu, Y.; Wheeler, S. E.; Fang, L., Low Band Gap Coplanar Conjugated Molecules Featuring Dynamic Intramolecular Lewis Acid-Base Coordination. *J. Org. Chem.* **2016**, *81* (10), 4347-4352.
16. Crossley, D. L.; Goh, R.; Cid, J.; Vitorica-Yrezabal, I.; Turner, M. L.; Ingleson, M. J., Borylated Arylamine-Benzothiadiazole Donor-Acceptor Materials as Low-LUMO, Low-Band-Gap Chromophores. *Organometallics* **2017**, *36* (14), 2597-2604.
17. Li, Y.; Meng, H.; Yan, D.; Li, Y.; Pang, B.; Zhang, K.; Luo, G.; Huang, J.; Zhan, C., Synthesis of B←N embedded indacenodithiophene chromophores and effects of bromine atoms on photophysical properties and energy levels. *Tetrahedron* **2018**, *74* (32), 4308-4314.
18. Dash, B. P.; Hamilton, I.; Tate, D. J.; Crossley, D. L.; Kim, J.-S.; Ingleson, M. J.; Turner, M. L., Benzoselenadiazole and benzotriazole directed electrophilic C-H borylation of conjugated donor-acceptor materials. *J. Mater. Chem. C* **2019**, *7* (3), 718-724.
19. Min, Y.; Dou, C.; Tian, H.; Liu, J.; Wang, L., A disk-type polyarene containing four B←N units. *Chem. Commun.* **2019**, *55* (25), 3638-3641.
20. Grandl, M.; Rudolf, B.; Sun, Y.; Bechtel, D. F.; Pierik, A. J.; Pammer, F., Intramolecular N→B Coordination as a Stabilizing Scaffold for  $\pi$ -Conjugated Radical Anions with Tunable Redox Potentials. *Organometallics* **2017**, *36* (14), 2527-2535.
21. Zhu, Y.; Rabindranath, A. R.; Beyerlein, T.; Tieke, B., Highly Luminescent 1,4-Diketo-3,6-diphenylpyrrolo[3,4-c]pyrrole(DPP-) Based Conjugated Polymers Prepared Upon Suzuki Coupling. *Macromolecules* **2007**, *40*, 6981-6989.

## Appendix

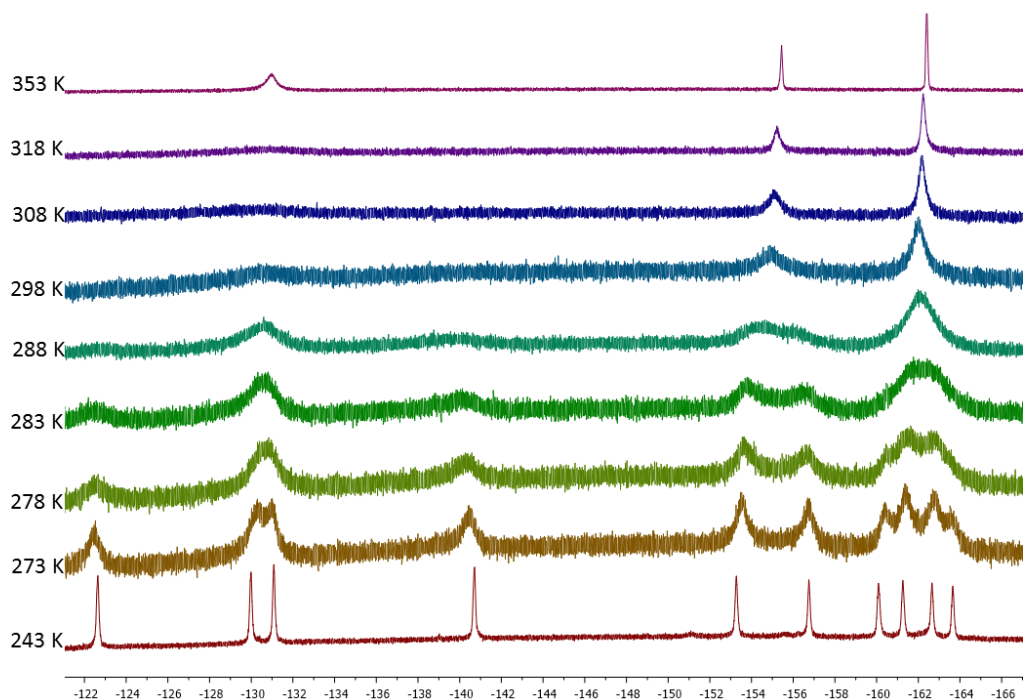


**Figure 4-7.** VT  $^{19}\text{F}$  NMR spectra of **4-Pf** (d8-tol, 470.2 MHz)

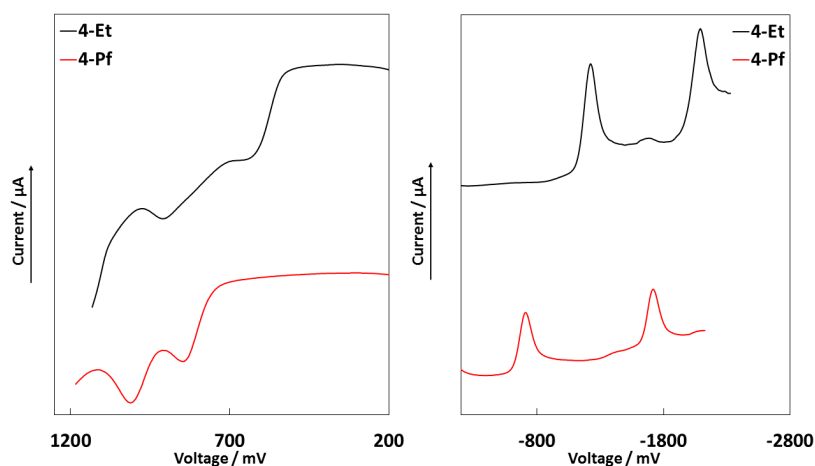
**Table 4-4.** Summary of results from VT NMR spectroscopy studies

| Compound    | Probe                | $T_c$ <sup>[a]</sup> [K] | $\Delta\nu$ [Hz] <sup>[b]</sup> | $\Delta G^\ddagger_{T_c}$ <sup>[a]</sup> [kJ mol <sup>-1</sup> ] |
|-------------|----------------------|--------------------------|---------------------------------|--|
| <b>4-Pf</b> | p-Pf                 | $293 \pm 3$              | 1636                            | $52.4 \pm 0.6$   |
| <b>4-Pf</b> | o-Pf (-130.0/-131.1) | $278 \pm 3$              | 513                             | $52.3 \pm 0.6$   |
| <b>4-Pf</b> | o-Pf (-122.6/-140.7) | $308 \pm 3$              | 8497                            | $51.0 \pm 0.5$   |

[a] Data from coalescence temperature method by using the approximation  $\Delta G^\ddagger = 0.0194T_c [9.972 + \lg(T_c \Delta\nu)]$  for estimation of  $\Delta G^\ddagger$  at  $T_c$ ; [b] an error of 5% in the line width determination is assumed.

**Table 4-5.** Comparison of UV-Vis spectra of boron complexes **4-Et** and **4-Pf** in different solvents

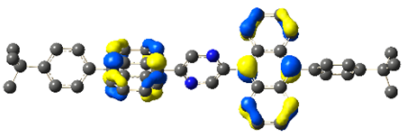
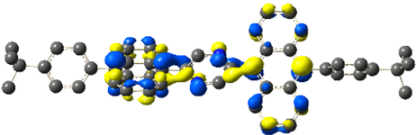
|             | Cyclohexane | Toluene | DCM | THF | Acetonitrile |
|-------------|-------------|---------|-----|-----|--------------|
| <b>4-Et</b> | 695         | 698     | 687 | 672 | 648          |
| <b>4-Pf</b> | 771         | 777     | 774 | 758 | 733          |

**Figure 4-8.** Square wave voltammetry (SWV) data. Oxidation in 0.1M Bu<sub>4</sub>N[PF<sub>6</sub>] in DCM, reduction in 0.1M Bu<sub>4</sub>N[PF<sub>6</sub>] in THF, reported vs Fc<sup>+0</sup>,  $\nu = 250 \text{ mV s}^{-1}$ .**Table 4-6.** Electrochemical Data of BN-fused Dianthracenylpyrazines.

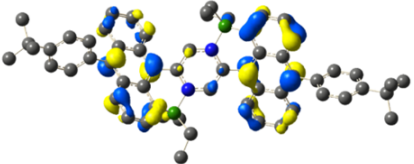
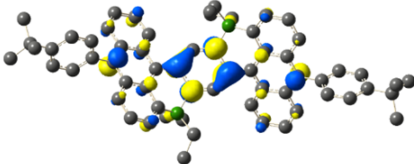
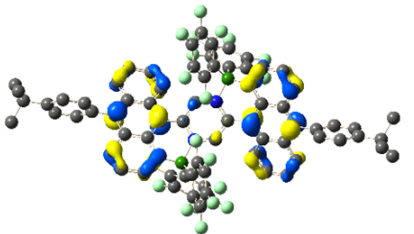
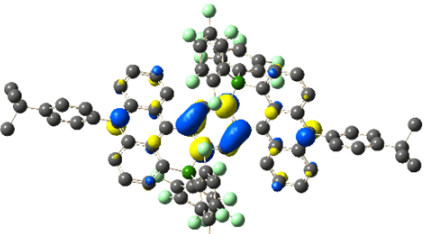
| Compound    | $E_{\text{ox}}^{\text{CV}}$<br>[V] | $E_{\text{ox}}^{\text{SWV}}$<br>[V] | $E_{\text{red}}^{\text{CV}}$<br>[V] | $E_{\text{red}}^{\text{SWV}}$<br>[V] |
|-------------|------------------------------------|-------------------------------------|-------------------------------------|--------------------------------------|
| <b>4-Et</b> | 0.65, 0.93 <sup>b</sup>            | 0.63, 0.91                          | -1.23, -2.10 <sup>a</sup>           | -1.22, -2.09                         |
| <b>4-Pf</b> | 0.85, 1.02 <sup>a</sup>            | 0.85, 1.01                          | -0.74, -1.75 <sup>a</sup>           | -0.71, -1.72                         |

[a] Quasi-reversible or reversible ( $E_{\text{red}}$  or  $E_{\text{ox}} = 0.5 (E_{\text{pc}} + E_{\text{pa}})$ ); [b] Irreversible ( $E_{\text{ox}} = E_{\text{pa}}$ ;  $E_{\text{red}} = E_{\text{pc}}$ ).

**Table 4-7.** Kohn-Sham HOMO and LUMO orbital plots for precursor **3** (rb3lyp/6-31g(d), scaling radii of 75%, isovalue = 0.04)

|          | HOMO  | LUMO   |
|----------|---|--|
| <b>3</b> |  <p>-5.12 eV</p> |  <p>-1.84 eV</p> |

**Table 4-8.** Kohn-Sham HOMO and LUMO orbital plots for differently substituted BN-functionalized anthracenes (rb3lyp/6-31g(d), scaling radii of 75%, isovalue = 0.04)

|             | HOMO  | LUMO  |
|-------------|---|---|
| <b>4-Et</b> |  <p>-4.96 eV</p> |  <p>-2.91 eV</p> |
| <b>4-Pf</b> |  <p>-5.33 eV</p> |  <p>-3.49 eV</p>  |



**Table 4-9.** Comparison of calculated geometric parameters (distances in Å, angles in °) for BN-fused dianthracenylpyrazines **4-Et** and **4-Pf** from DFT calculations (Gaussian 09; rb3lyp/6-31g(d))

|             | B-N             | B-C <sub>An</sub> | C <sub>An</sub> -C <sub>Py</sub> | C <sub>An</sub> -B-N | Cent <sub>An</sub> -<br>C-B | Cent <sub>An</sub> -<br>C-C <sub>Py</sub> | Ph <sub>An,inner</sub> //<br>Ph <sub>An,inner</sub> | Ph <sub>An,inner</sub> //<br>Py |
|-------------|-----------------|-------------------|----------------------------------|----------------------|-----------------------------|---|---|---------------------------------|
| <b>4-Et</b> | 1.639,<br>1.652 | 1.619,<br>1.624   | 1.462,<br>1.463                  | 104.8,<br>102.2      | 170.6,<br>170.3             | 167.2,<br>164.8                           | 70.7  | 33.0,<br>37.8                   |
| <b>4-Pf</b> | 1.645           | 1.612,<br>1.613   | 1.456                            | 107.2                | 174.6                       | 168.5                                     | 62.2  | 31.1                            |

**Table 4-10.** TD-DFT data for precursors **3** (rcam-b3lyp/6-31g(d))

| Compound | Transition <sup>[a]</sup>            | <i>E</i> <sub>ex</sub> (eV) | λ (nm)        | Oscillator strength <i>f</i> | Assignment                                      |
|----------|--------------------------------------|-----------------------------|---------------|------------------------------|---|
| <b>3</b> | <b>S<sub>0</sub> → S<sub>1</sub></b> | <b>3.29</b>                 | <b>376.57</b> | <b>0.8599</b>                | <b>H → L (0.57)</b><br><b>H-1 → L+1 (-0.41)</b> |

[a] Only transitions with oscillator strengths &gt;0.1 are presented.

**Table 4-11.** TD-DFT data for **4-Et** and **4-Pf** (rcam-b3lyp/6-31g(d))

| Compound    | Transition <sup>[a]</sup>            | <i>E</i> <sub>ex</sub> (eV) | λ (nm)        | Oscillator strength <i>f</i> | Assignment                                      |
|-------------|--------------------------------------|-----------------------------|---------------|------------------------------|---|
| <b>4-Et</b> | <b>S<sub>0</sub> → S<sub>1</sub></b> | <b>2.08</b>                 | <b>596.54</b> | <b>0.9028</b>                | <b>H → L (0.69)</b><br><b>H-1 → L+1 (-0.13)</b> |
|             | S <sub>0</sub> → S <sub>3</sub>      | 3.20                        | 387.76        | 0.1650                       | H-1 → L+1 (-0.21)                               |
|             |                                      |                             |               |                              | H → L+1 (-0.10)                                 |
|             |                                      |                             |               |                              | H → L+2 (0.66)                                  |
|             |                                      |                             |               |                              | H-8 → L (-0.14)                                 |
|             |                                      |                             |               |                              | H-6 → L (0.37)                                  |
| <b>4-Pf</b> | S <sub>0</sub> → S <sub>7</sub>      | 3.78                        | 328.34        | 0.2048                       | H-4 → L (-0.24)                                 |
|             |                                      |                             |               |                              | H-3 → L+1 (0.13)                                |
|             |                                      |                             |               |                              | H-2 → L (0.44)                                  |
|             |                                      |                             |               |                              |   |
|             | <b>S<sub>0</sub> → S<sub>1</sub></b> | <b>1.87</b>                 | <b>663.37</b> | <b>0.8333</b>                | <b>H → L (0.69)</b><br><b>H-1 → L+2 (0.11)</b>  |
|             | S <sub>0</sub> → S <sub>3</sub>      | 3.00                        | 413.19        | 0.2425                       | H-1 → L+2 (0.18)                                |
|             |                                      |                             |               |                              | H → L+1 (0.68)                                  |
|             |                                      |                             |               |                              | H-8 → L (0.31)                                  |
|             |                                      |                             |               |                              | H-5 → L (0.43)                                  |
|             |                                      |                             |               |                              | H-4 → L+2 (-0.15)                               |
|             | S <sub>0</sub> → S <sub>5</sub>      | 3.52                        | 352.53        | 0.1006                       | H-3 → L (-0.28)                                 |
|             |                                      |                             |               |                              | H-2 → L+2 (-0.13)                               |
|             |                                      |                             |               |                              | H-1 → L+4 (0.12)                                |
|             |                                      |                             |               |                              | H → L+5 (0.17)                                  |

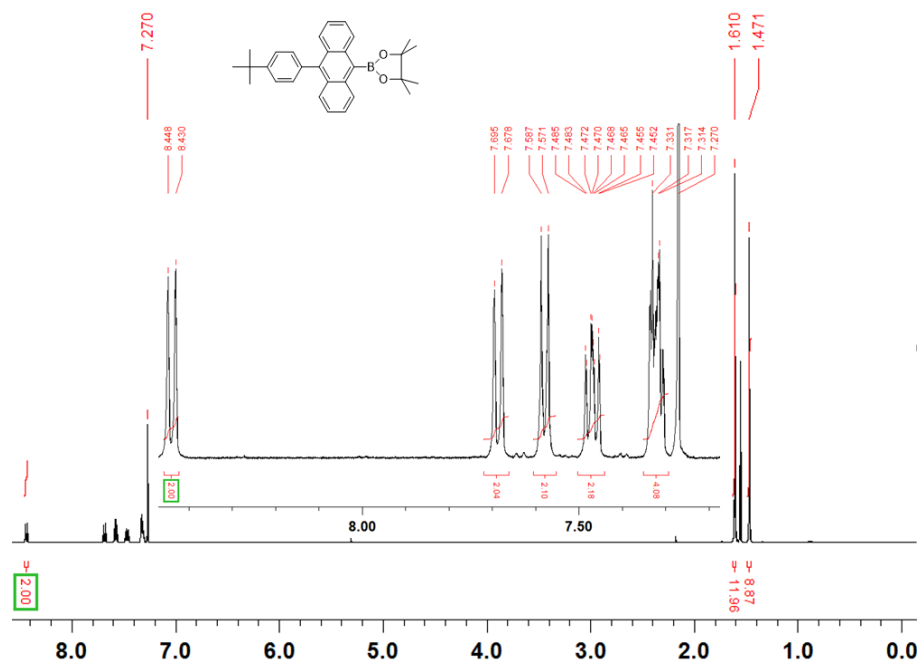
[a] Only transitions with oscillator strengths &gt;0.1 are presented.

**Table 4-12.** The calculated singlet and triplet state energies for **4-Et**

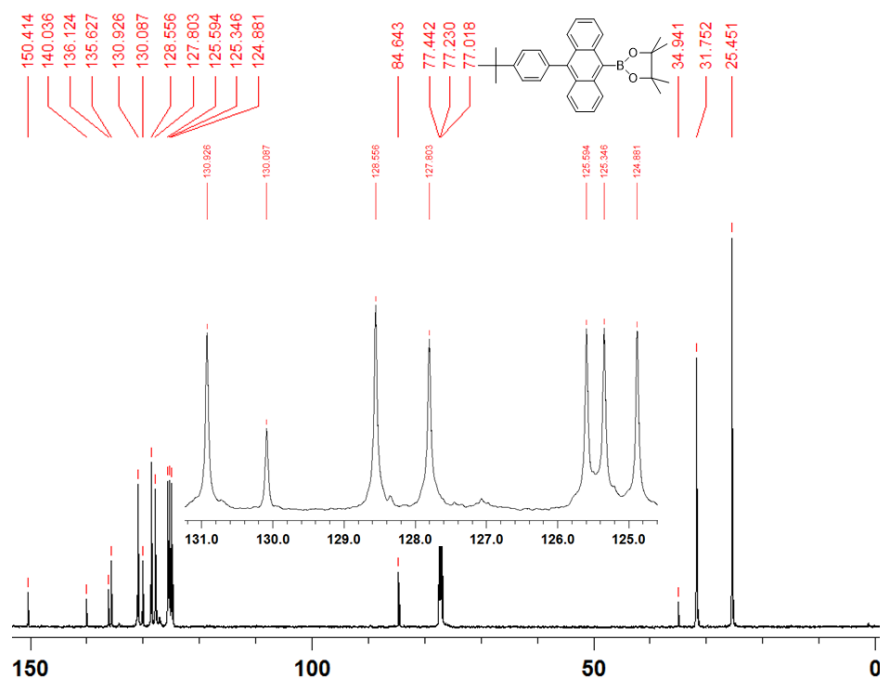
|             | $S_0$ <sup>[a]</sup> | $T_1$ <sup>[a]</sup> | $S_1$ <sup>[b]</sup> | $\Delta E_{ad}(S_0-S_1)$     | $\Delta E_{ad}(S_0-T_1)$     | $\Delta E_{ad}(S_1-T_1)$     |
|-------------|----------------------|----------------------|----------------------|------------------------------|------------------------------|------------------------------|
|             | (Hartree)            | (Hartree)            | (Hartree)            | (eV / kJ mol <sup>-1</sup> ) | (eV / kJ mol <sup>-1</sup> ) | (eV / kJ mol <sup>-1</sup> ) |
| <b>4-Et</b> | -2483.0657           | -2483.0274           | -2483.0075           | 1.582/152.6                  | 1.042/100.5                  | 0.540/52.1                   |

[a]  $S_0$  optimized with rb3lyp/6-31g(d),  $T_1$  optimized with ub3lyp/6-31g(d). [b] From TD-DFT optimization of  $S_1$  state with b3lyp/6-31g(d).

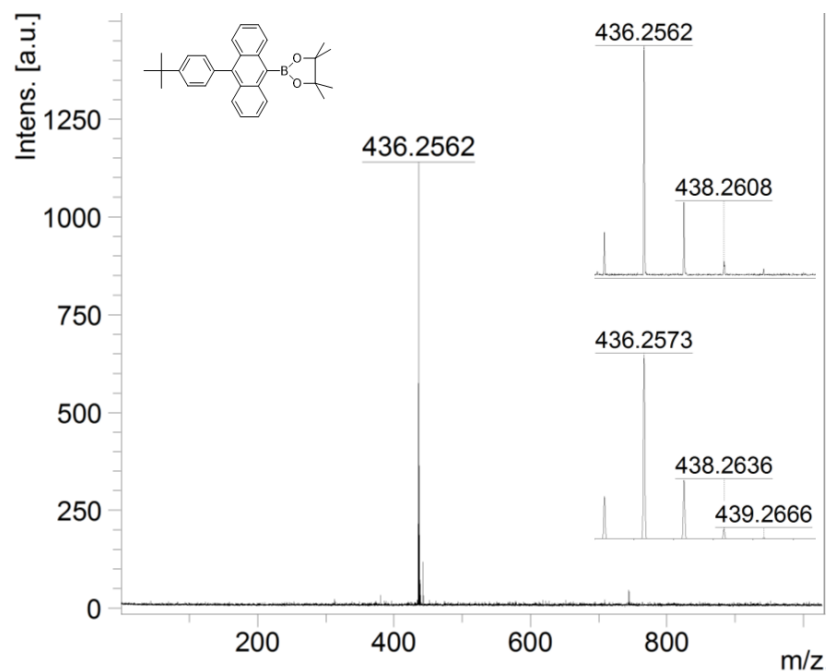
### Spectral Data for Isolated Compounds



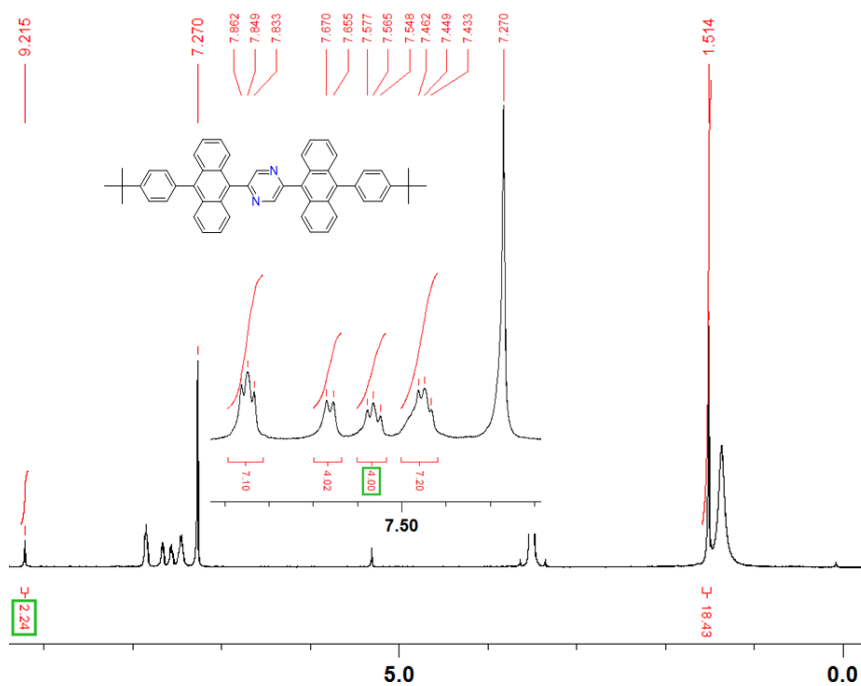
**Figure 4-9.** <sup>1</sup>H NMR spectrum of 2-(10-(4-*tert*-butylphenyl)anthracen-9-yl)-4,4,5,5-tetramethyl-1,3,2-dioxaborolane (**2**) in CDCl<sub>3</sub>



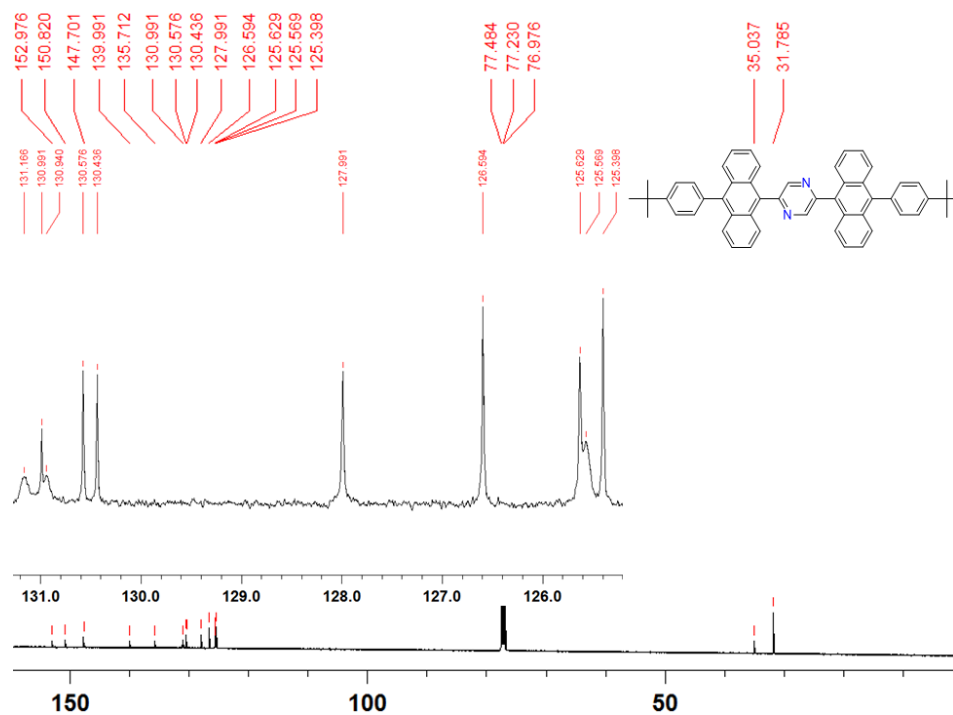
**Figure 4-10.** <sup>13</sup>C NMR spectrum of 2-(10-(4-*tert*-butylphenyl)anthracen-9-yl)-4,4,5,5-tetramethyl-1,3,2-dioxaborolane (**2**) in CDCl<sub>3</sub>



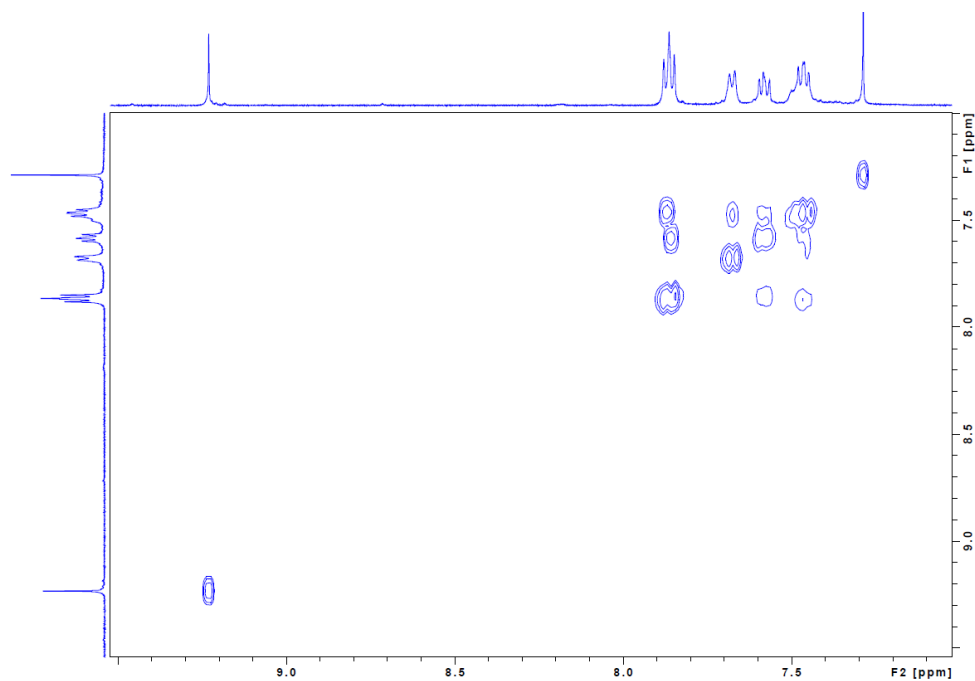
**Figure 4-11.** MALDI-TOF mass spectrum (pos. mode) of 2-(10-(4-tert-butylphenyl)anthracen-9-yl)-4,4,5,5-tetramethyl-1,3,2-dioxaborolane (**2**)



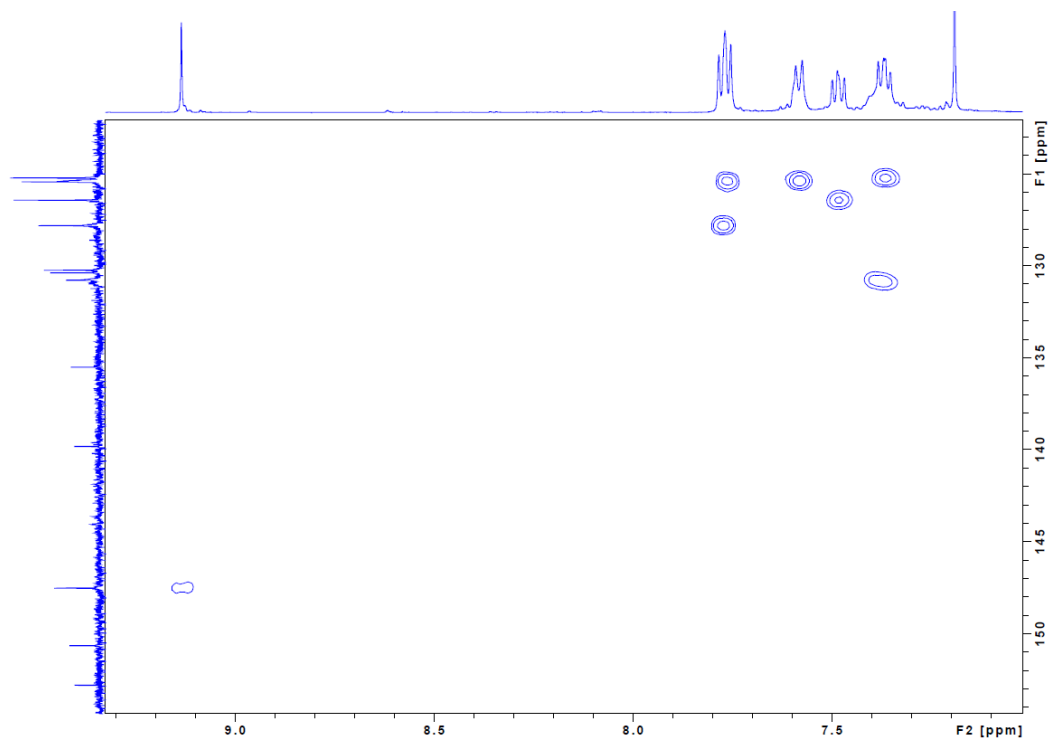
**Figure 4-12.** <sup>1</sup>H NMR spectrum of 2,5-bis(10-(4-tert-butylphenyl)anthracen-9-yl)pyrazine (**3**) in CDCl<sub>3</sub>



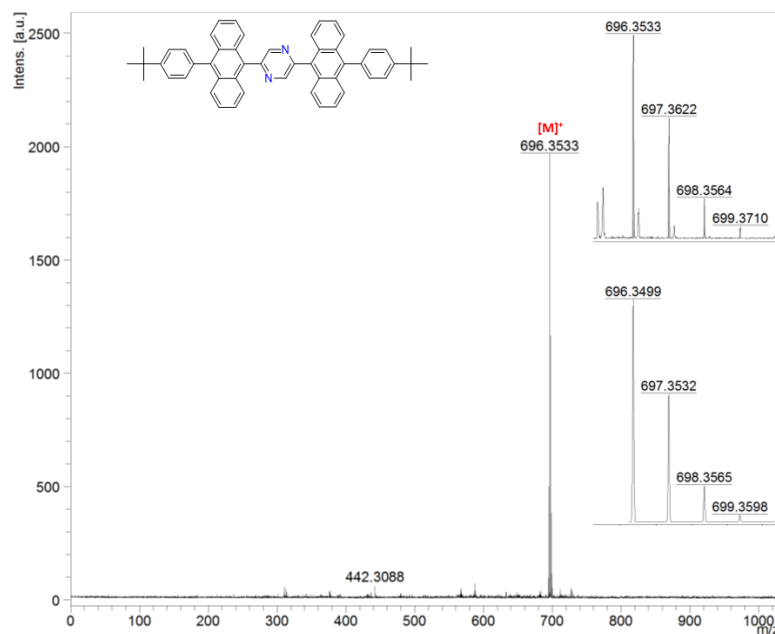
**Figure 4-13.**  $^{13}\text{C}$  NMR spectrum of 2,5-bis(10-(4-tert-butylphenyl)anthracen-9-yl)pyrazine (**3**) in  $\text{CDCl}_3$



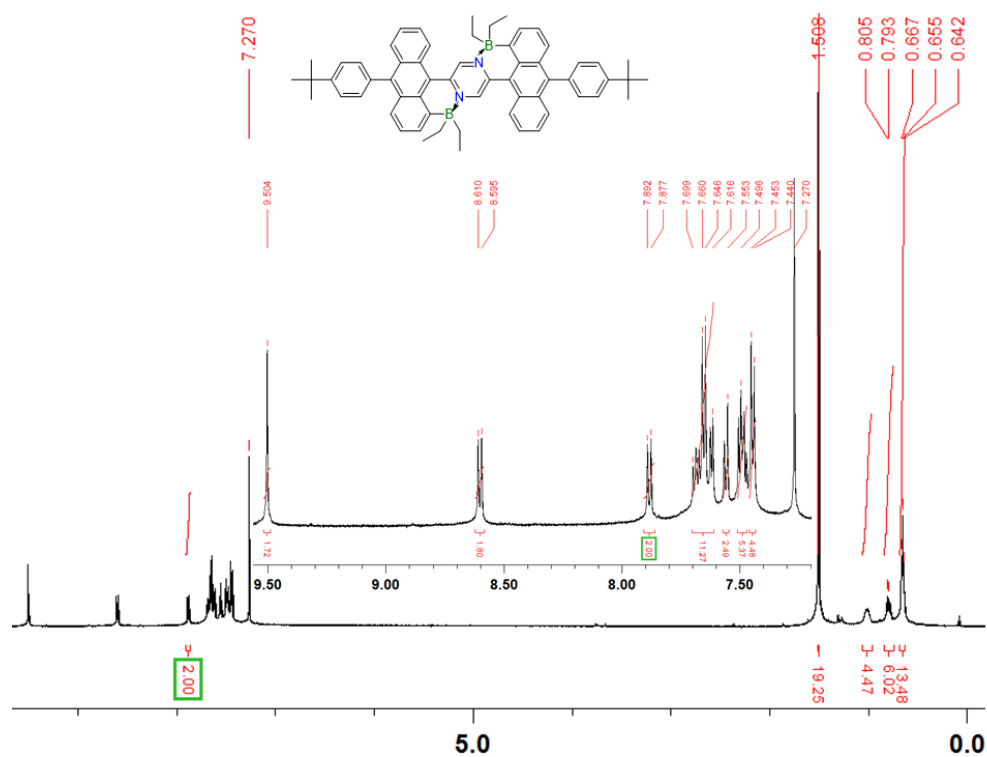
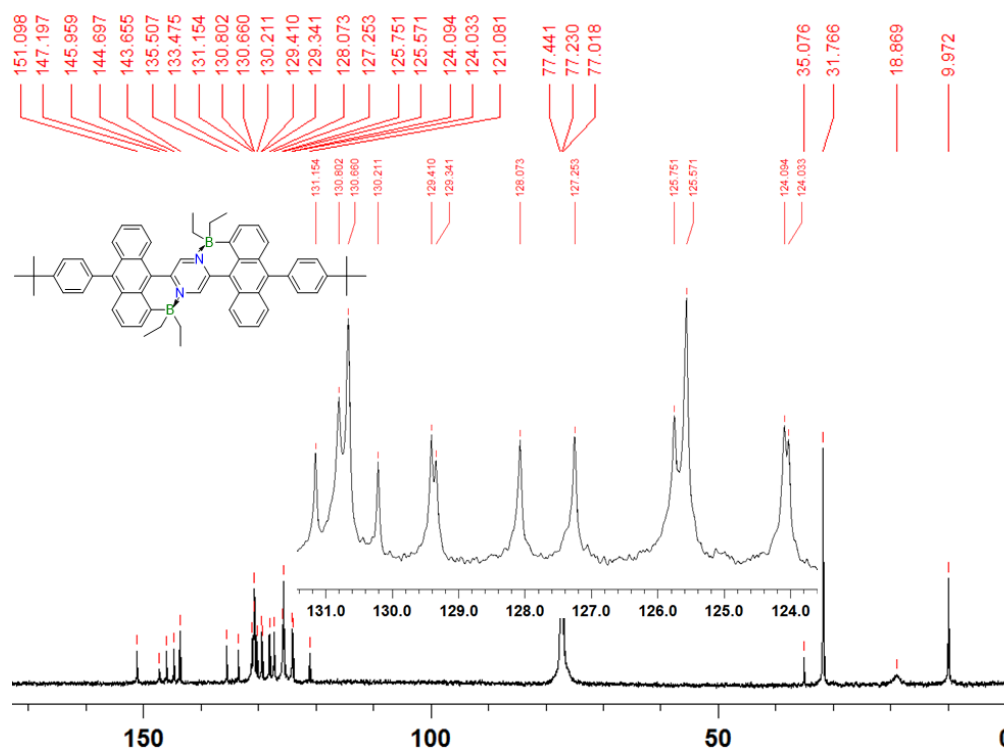
**Figure 4-14.** Aromatic region of the gCOSY NMR spectrum of 2,5-bis(10-(4-tert-butylphenyl)anthracen-9-yl)pyrazine (**3**) in  $\text{CDCl}_3$

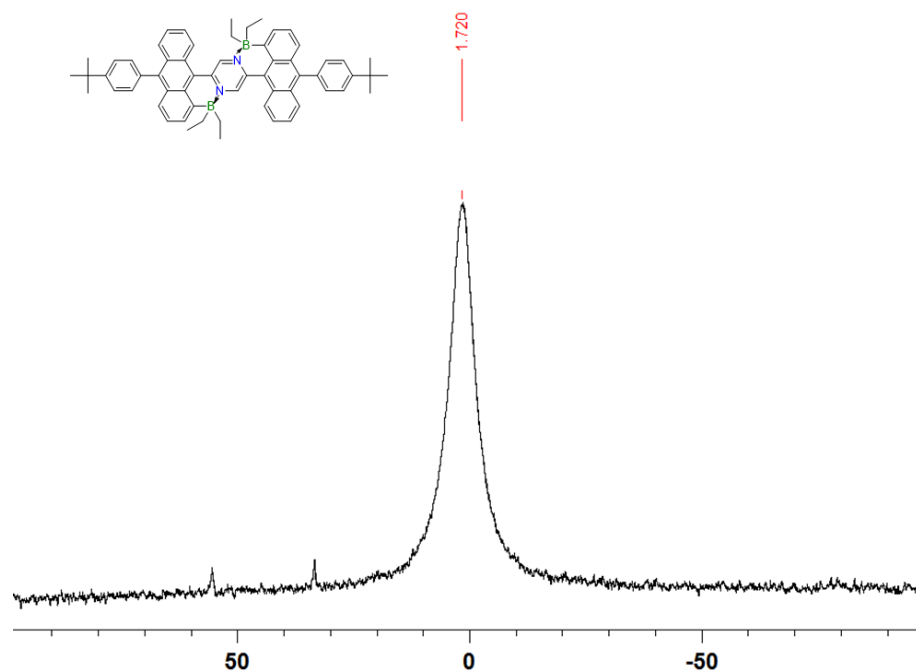


**Figure 4-15.** Aromatic region of the HSQC NMR spectrum of 2,5-bis(10-(4-tert-butylphenyl)anthracen-9-yl)pyrazine (**3**) in  $\text{CDCl}_3$

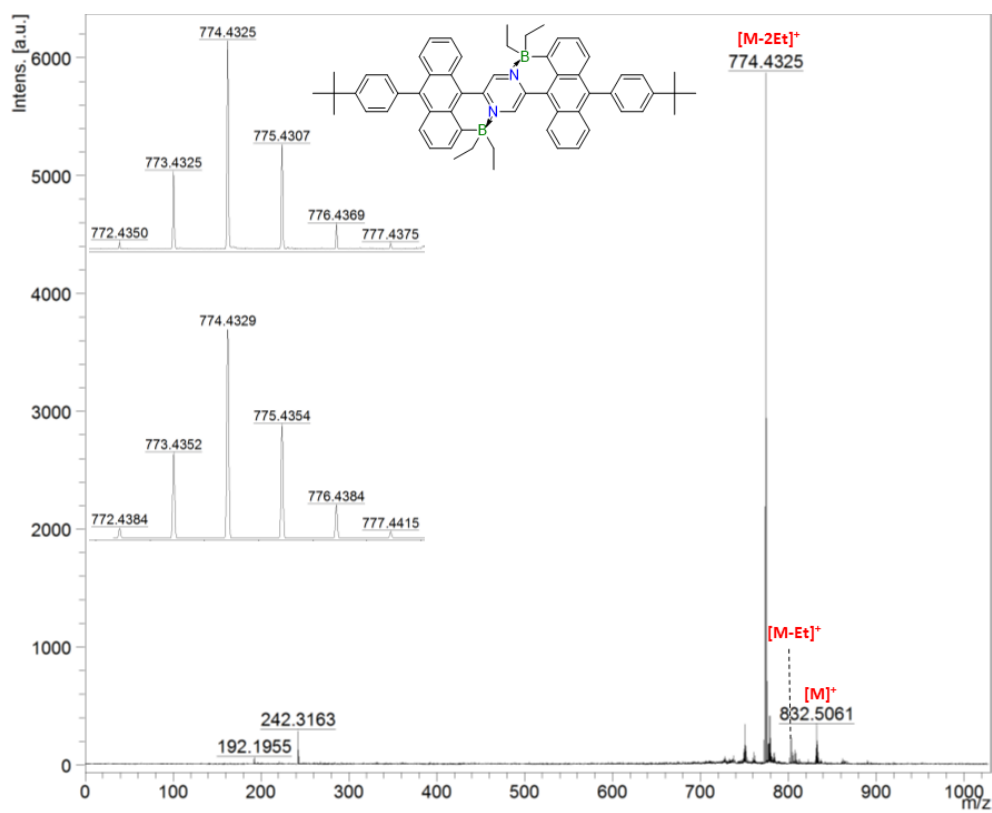


**Figure 4-16.** MALDI-TOF mass spectrum (pos. mode) of 2,5-bis(10-(4-tert-butylphenyl)anthracen-9-yl)pyrazine (**3**)

Figure 4-17. <sup>1</sup>H NMR spectrum of 4-Et in CDCl<sub>3</sub>Figure 4-18. <sup>13</sup>C NMR spectrum of 4-Et in CDCl<sub>3</sub>

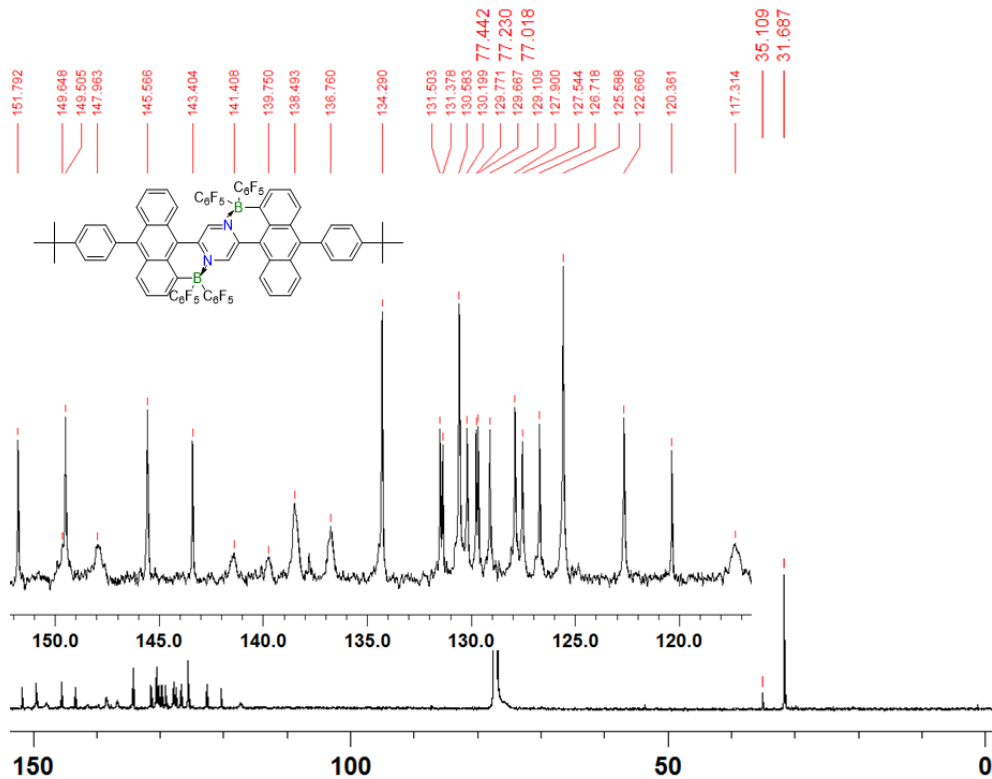
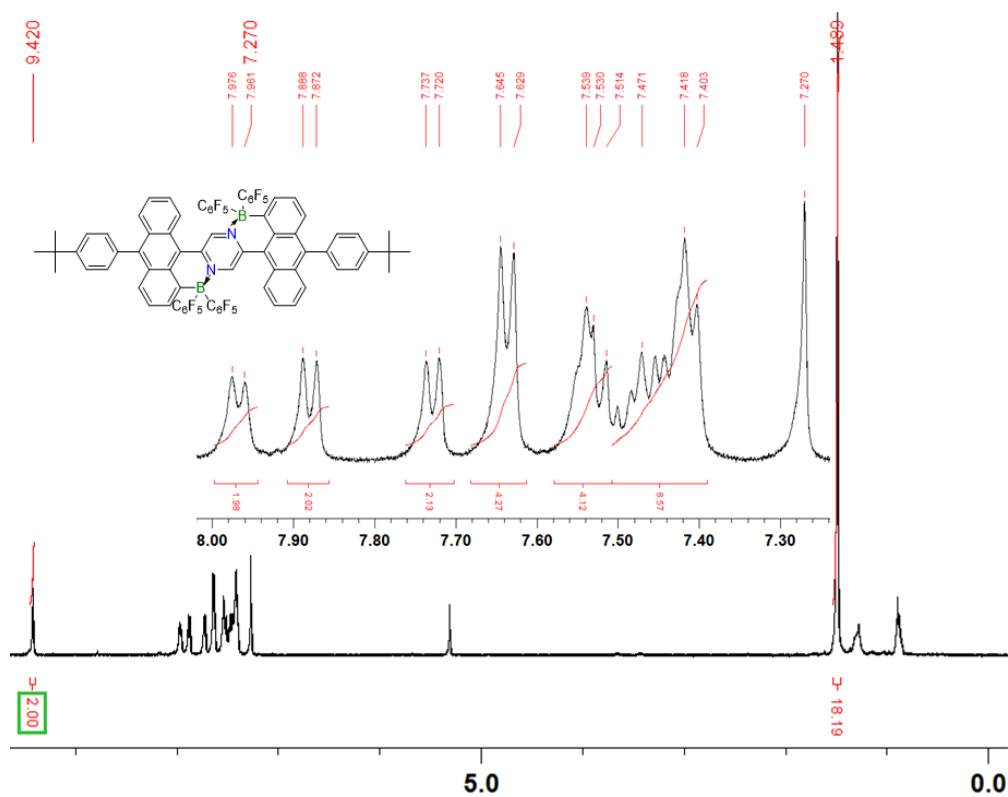


**Figure 4-19.**  $^{11}\text{B}$  NMR spectrum of 4-Et in  $\text{CDCl}_3$



**Figure 4-20.** MALDI-TOF mass spectrum (pos. mode) of 4-Et





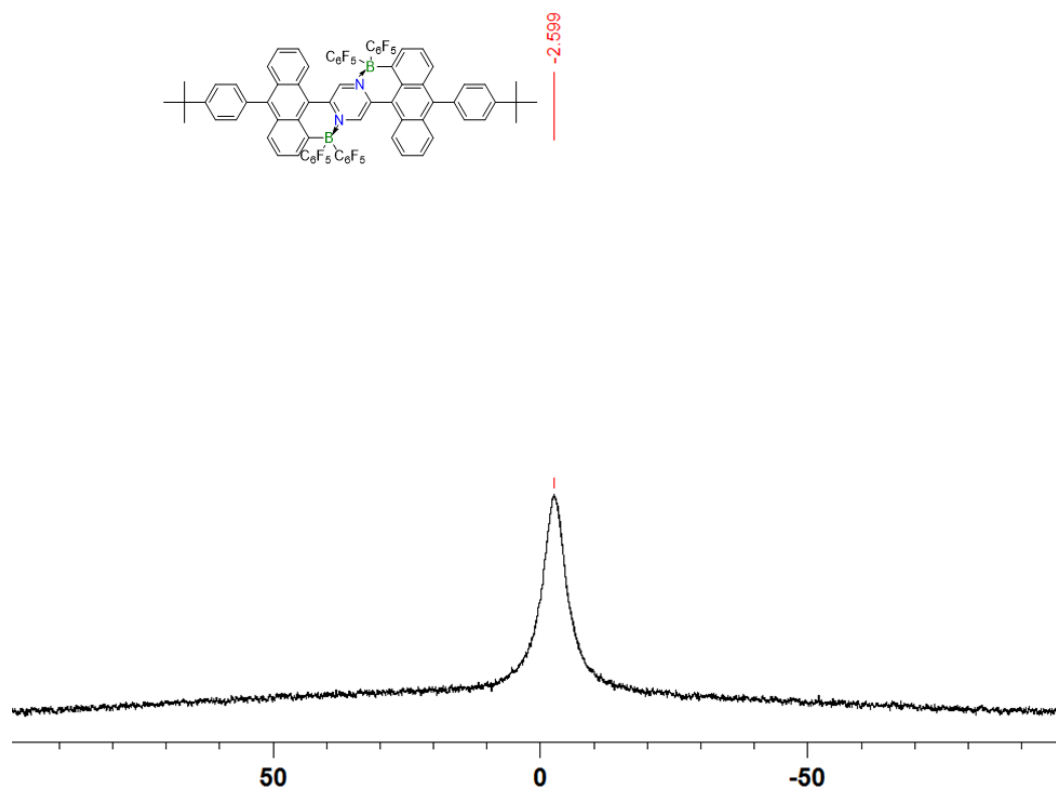


Figure 4-23. <sup>11</sup>B NMR spectrum of 4-Pf in CDCl<sub>3</sub>

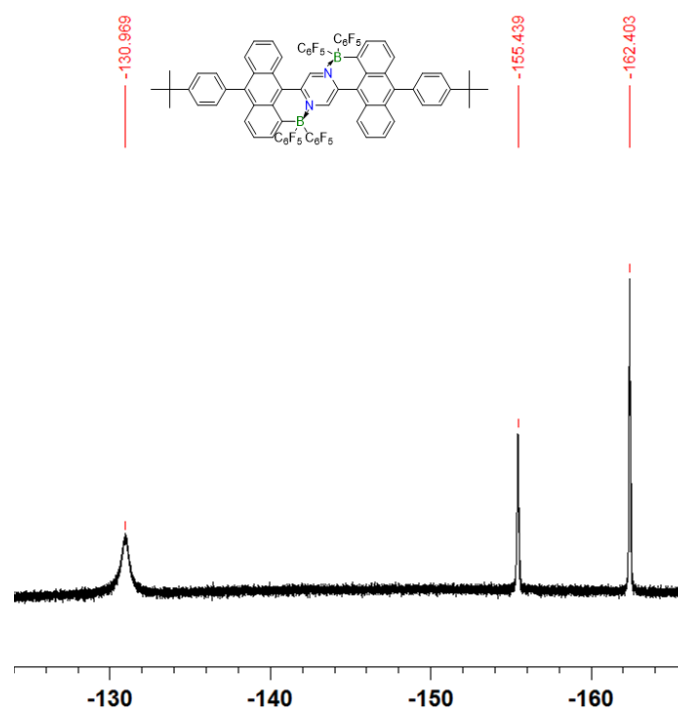
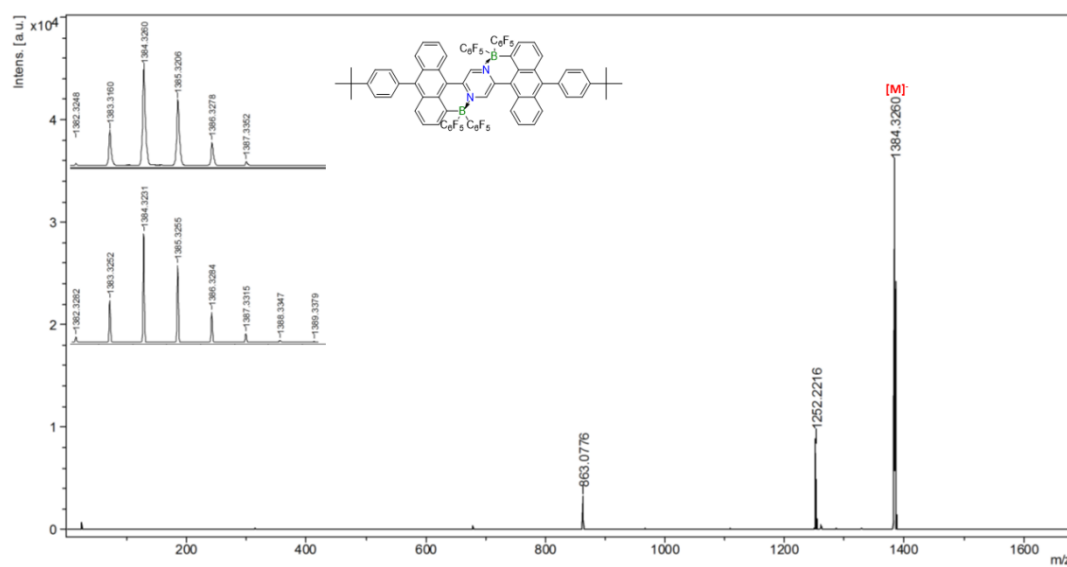


Figure 4-24. <sup>19</sup>F NMR spectrum of 4-Pf in CDCl<sub>3</sub>



**Figure 4-25.** MALDI-TOF mass spectrum (neg. mode) of **4-Pf**

## Overall Conclusions

In this thesis, we explored the effects of peripheral functionalization of larger  $\pi$ -conjugated scaffolds based on anthracene via Lewis base-directed electrophilic C-H borylation. Several new types of BN-substituted anthracene were synthesized with unique structural features and electronic properties.

In Chapter 2, we prepared a new class of B-N fused dipyridylanthracenes via electrophilic aromatic borylation. We demonstrated that this B-N Lewis pair functionalization of anthracene leads to severe distortions due to steric strain and results in substantially decreased LUMO energy. In the presence of light, the BN-fused anthracene rapidly react with  $O_2$  to form endoperoxide compound without an external photosensitizer. Endoperoxide compounds also can thermally revert to the parent acenes when heating in toluene under  $N_2$ . This study presented a new way to prepare conjugated materials, especially for structurally distorted systems. The facile reactivity with oxygen opens the possibility for applications in photodynamic therapy (PDT) and sensing.

Chapter 3 continued our studies on tuning the structure and electronic properties of B-N fused dipyridylanthracene and the self-sensitized reactivity with singlet oxygen. Four isomeric derivatives of BN-fused dipyridylanthracene with Me groups in different positions of the pyridyl ring were synthesized. The impact of the substituents in different positions on the photophysical and electrochemical properties of this class of compounds have been examined. The most dramatic effect of the substitution pattern is in the reactivity of the acenes toward oxygen and the respective endoperoxides thermal release of singlet oxygen. These results demonstrated that small changes in the substitution pattern on the

pyridyl moiety can dramatically alter the reactivity patterns, allowing for applications as highly effective sensitizers on one hand and materials for delivery of singlet oxygen on demand on the other hand. Further work on avoiding self-sensitized reactivity with formation of endoperoxides is expected to improve performance as singlet oxygen sensitizers. On the other hand, further weakening of the B-N bond, possibly even “open” the B-N bonds, could provide excellent singlet oxygen release performance and might offer the broader field of small molecule activation.

Chapter 4 introduced a series of BN fused dianthracenylpyrazines as new low band gap materials. DFT calculations revealed BN fused dianthracenylpyrazines show a small band gap. The electron withdrawing groups  $C_6F_5$  further decrease the HOMO-LUMO gap. Photophysical and electrochemical studies indicated a dramatic effect of borane functionalization on the electronic structure, as well as the substitution pattern attached boron influencing the HOMO and LUMO energy levels. These results demonstrated that boron-doped dianthracenylpyrazine derivatives are promising compounds as low band gap materials. Therefore, for the future work the device performance in organic solar cells may be investigated.